Pectora roborant cultus recti

Nuclear medium effects on analyzing power investigated with a proton knockout reaction

Retief Neveling

Dissertation presented for the Degree of Doctor of Philosophy at the University of Stellenbosch

Promoter: Prof. A. A. Cowley

October 2001

Declaration

I, the undersigned, hereby declare that the work contained in this dissertation is my own original work and that I have not previously in its entirety or in part submitted it at any university for a degree.

Signature Date

Abstract

Nuclear medium effects on analyzing power investigated with a proton knockout reaction

Quasi-free proton scattering provides a direct mechanism to study modifications of the free nucleon-nucleon interaction in the nuclear medium. It is known that due to the density dependence of the nucleon-nucleon interaction, quasi-free proton scattering from light targets (A$\leq$40) at medium energies ($\geq$200 MeV) yields analyzing powers that are substantially reduced with regards to theoretical calculations, based on the Distorted Wave Impulse Approximation (DWIA), that utilize the free nucleon-nucleon interaction. However, no analyzing power results for proton knockout from heavier targets exist, since it is traditionally expected that the severe distortion effects would defy accurate theoretical description. This dissertation represents an extension of the study of proton knockout to a heavier target nuclei. High resolution exclusive measurements of cross-sections and analyzing powers for the $^{208}Pb(\overrightarrow{p},2p)^{207}Tl$ proton knockout reaction at 200 MeV were performed for three quasi-free angle pairs. Coincident protons were detected in a magnetic spectrometer and a detector telescope consisting of a Si surface barrier detector and a high purity planar Ge-detector.

Energy-sharing cross-section distributions are found to be in excellent agreement with DWIA calculations, yielding spectroscopic factors that are in reasonable agreement with $(e,e'p)$ studies. This indicates that the distortions, which are quite severe due to the heavy target, are introduced in a reliable manner. However, the measured analyzing powers are significantly suppressed with regards to standard DWIA calculations that utilize the free nucleon-nucleon interaction. Analyzing power calculations are found to be insensitive to variations in the distorting potentials, different descriptions of the bound state, different energy prescriptions of the two-body interaction as well as non-locality effects. Agreement between theory and experiment is shown to improve only when density dependence of the nucleon-nucleon interaction is incorporated within the DWIA.

Samevatting

Die invloed van die kernmedium op analiseervermoë soos bestudeer met 'n proton uitslaan reaksie

Inligting aangaande die wysiging van die nukleon-nukleon wisselwerking binne kernmedium vanaf die bekende vrye nukleon-nukleon wisselwerking kan verkry word deur kwasi-vrye proton verstrooiing te bestudeer. Dit is welbekend dat digtheidsafhanklikheid van die nukleon-nukleon wisselwerking tot gevolg het dat kwasi-vrye proton verstrooiing vanaf ligte teikens (A$\leq$40) teen medium projektiel energië ($\geq$200 MeV) analiseervermoë resultate oplewer wat dramaties afwyk van standaard teoretiese berekeninge, gebaseer op die sg. Vervormde Golf Impuls Benadering (VGIB). Daar bestaan egter geen analiseervermoë resultate vir die proton uitslaan reaksie vanaf swaarder teikens nie, in welke geval die vervorming van die proton golffunksie tradisioneel beskou word as té drasties om sinvolle studie van die nukleon-nukleon wisselwerking moontlik te maak. In hierdie verhandeling word die studie van kwasi-vrye proton verstrooiing tot 'n swaarder teikenkern uitgebrei. Hoë resolusie kansvlak en analiseervermoë metings van die $^{208}Pb(\overrightarrow{p},2p)^{207}Tl$ proton uitslaan reaksie vir 'n projektiel energie van 200 MeV is vir drie kwasi-vrye hoekpare uitgevoer. Protone is in koïnsidens gemeet met behulp van 'n magnetiese spektrometer en 'n detektor teleskoop bestaande uit 'n Si oppervlaklaag detektor en 'n Ge-detektor.

Eksperimentele kansvlakke toon uitstekende ooreenstemming met VGIB berekeninge, en lewer spektroskopiese faktore op wat goed ooreenstem met resultate van $(e,e'p)$ studies. Dit dui daarop dat die vervorming van die proton golffunksie, wat besonder groot is a.g.v die swaar ^{208}Pb teikenkern, op 'n betroubare manier in die teorie vervat word. In teenstelling met die suksesvolle kansvlak berekeninge word gevind dat gemete analiseervermoë resultate heelwat verlaag is ten opsigte van die teoretiese berekeninge waarin die vrye nukleon-nukleon interaksie vervat is. Analiseervermoë berekeninge blyk verder onsensitief te wees vir veranderings aan die optiese potensiale, verskillende beskrywings van die gebonde proton, verskillende energie preskripsies vir die nukleon-nukleon interaksie asook nie-lokaliteits effekte. Ooreenstemming tussen teoretiese en eksperimentele analiseervermoë verbeter slegs wanneer digtheidsafhanklikheid van die nukleon-nukleon interaksie in die VGIB berekeninge in ag geneem word.

Acknowledgements

I wish to express my sincere gratitude to Prof. A.A. Cowley for his guidance and supervision of this work. I consider myself privileged to have been one of his students. I also owe a great debt of gratitude to Dr Deon Steyn, my unofficial advisor, whose contribution to this work is considerable. Thanks is due to Drs Ricky Smit, Siegfried Förtsch, Kobus Lawrie and Richard Newman of the National Accelerator Center, for their guidance and considerable help during the experimental phases of this study, which meant spending many a sleepless night in the data-room. Together we walked several kilometers back and forth between the data-room and the spectrometer vault! I am also grateful to members of the Nuclear Physics Group at the University of Stellenbosch, Drs Gillian Arendse, Greg Hillhouse, A. Stander, Prof. W.A. Richter and Mr Jacques Bezuidenhout, for their assistance in the experimental phases of this project.

Without the financial assistance of the National Research Foundation and the National Accelerator Center it would not have been possible for me to pursue this study. For this I am deeply grateful.

To all my fellow students and distinguished members of FINSMIC, especially the old guard: Shaun, Faith, Andrew, Dawid and Christine; thank you for ensuring that being a postgraduate student at the Stellenbosch physics department was such a pleasant experience. Especially thanks to Shaun for teaching me the finer points of the DWIA and of the game of squash. I am also grateful to Ingrid for assisting me in the tedious task of converting *PLOTDATA* files to *PHYSICA* files. And without them knowing it, Marius and the rest of the staff at the Bagel shop helped me through many a day with their excellent coffee.

I owe a lot to friends who helped me not lose sight of the other side of life. Thank you for your friendship and camaraderie, even thought most of you do not understand why I chose to walk this 'useless' road of science. I am privileged to have three brothers who share my passion for science: Johann the paleontologist, Arno the chemist and Jaco the engineer. May you satisfy your curiosities, and may the battle of the *real science* versus the *butterfly collections* never end! To Sanri: thank you for understanding. For courage. En dat ons saam kan drentel. My last word of thanks goes to my parents: Ronnie and Rita Neveling. The completion of this dissertation is the direct result of the inspiration, love and support that always flowed from your hearts through these 27 years.

God could cause us considerable embarrassment by revealing all the secrets of nature to us: we should not know what to do for sheer apathy and boredom. - Goethe

Contents

Chapter 1

Introduction

A proton knockout reaction in the context of this investigation refers to the process where an incident proton of medium energy (~100-1000 MeV) knocks out a bound proton from a nucleus, which recoils in a one-hole state. Both protons are consequently ejected from the nucleus, with no further violent interaction occuring between the residual nucleus and the two outgoing protons [Jac66]. The resulting three-body final state can be determined experimentally through momentum and energy conservation by the measurement of the momenta of the two outgoing protons. This process, also referred to as quasi-free scattering, has a strong relationship with the free scattering of protons, and only differs from the analogous free process because one of the participants in the reaction is bound inside the target nucleus. Such events are deemed to be reasonably probable, since the mean free path of medium energy protons in nuclear matter is of the same order of magnitude as the nuclear radius [Jac66]. Initially only the $(p, 2p)$ reaction was investigated, but eventually the study has been extended to other quasi-free scattering processes such as $(e, e'p)$, $(\pi, \pi'p)$, (p, pn), (p, pd) and $(\alpha, 2\alpha)$ [Kit85].

Over the past half century quasi-free scattering proved a valuable tool for the determination of the single-particle properties of the nucleus, such as single-nucleon separation energies, wave functions and spectroscopic factors [Kit85]. The first indications of the existence of such a process was obtained from an experiment performed at Berkeley in 1952. Chamberlain and Segrè [Cha52] bombarded a ^7Li target with 340 MeV protons, and studied proton pairs emitted in coincidence as a function of the angle between the two protons. The strong directional correlations found for such pairs was shown to be peaked when the angle between the two detectors approximately corresponds to that of free nucleon-nucleon (NN) scattering. By assuming that the incident proton interacted with a nuclear proton as if both particles were free, the observed spread in the angular correlation around the free scattering angle could be explained by modeling the momentum distribution of the nuclear protons by a Fermi-gas distribution of nucleons

confined to the nuclear volume.

The significance of the initial proton knockout experiments [Cha52, Wil55, McE57] was however limited due to the generally poor energy resolution, and because they yielded mainly estimates of the *average* nucleon momentum distribution inside the nucleus. With the development of the shell model it became clear that nucleon knockout reactions could also be used to establish single-particle separation energies, as well as the momentum distribution of protons in individual shells. Experimental evidence supporting this view was first obtained in 1958 by Tyŕen *et al.* [Tyr58], when measurements of the $(p, 2p)$ reaction at 185 MeV on various targets (^{7}Li, ^{9}Be, ^{11}B, ^{12}C, ^{14}N, ^{16}O, ^{40}Ca) clearly resolved the shell structure in the summed energy spectrum of the two outgoing protons. Such experiments have made it possible to investigate the inner shells in light and medium nuclei, and have given results which agree remarkably well with the shell model [Ber62].

The theoretical model used to describe the $(p, 2p)$ reaction, the Distorted Wave Impulse Approximation (DWIA), was first proposed by Maris *et al.* in the late 1950's [Mar58, Mar59]. The DWIA combines the impulse approximation, used to describe the violent quasi-free collision, with the distortion effects of multiple scattering on the incoming and outgoing protons. Among its earliest successes was the successful prediction of the momentum distribution of the p-shell knockout from a ^{7}Li target [Hil60]. The theory has since been refined and extended in numerous ways [Ber62, Lim64b, Lim66, Jack76, Cha77, Cha83], and successfully predicts angle and energy-sharing correlation cross-sections for knockout from various targets (e.g. ^{2}H, ^{4}He, ^{6}Li, ^{12}C, ^{16}O, ^{40}Ca, ^{208}Pb) at projectile energies ranging from 76 to 600 MeV [Kul71, Bho74, Kit80, Ant81, Oer82, Sam86, Cow91, Cow95, Car99a].

Whereas the initial studies of quasi-free proton knockout reactions were performed with the basic purpose of establishing the single-particle properties of the nucleus, the focus in recent years shifted from the study of nuclear structure towards the study of the nature of the strong interaction in nuclear matter. Because the process involves NN scattering in the nuclear field, quasi-free scattering provides a direct mechanism to investigate the NN interaction inside the nuclear medium [Hat97]. Although this was recognized early in the history of quasi-free scattering [Lim64a], such investigations only became viable with progress made in the theoretical description of the effective NN interaction in the 1980's [Kan90], as well as with the increasing

availability of high quality polarized beams. Such particle beams enables the measurement of spin observables, considered a more stringent test of reaction models than cross-sections. Renewed interest into nucleon knockout studies also followed from the enticing results obtained for quasi-elastic[1] (p,p') polarization observables [Car84], that has been interpreted as evidence of the modification of the NN interaction in the nuclear medium [Hor86].

This dissertation is concerned with the high resolution investigation of the $^{208}Pb(\overrightarrow{p},2p)^{207}Tl$ quasi-free proton knockout reaction[2] at 200 MeV, and the manifestation of medium modifications of the NN interaction in the analyzing power (A_y) results. It must be stressed that in our context we consider *quasi-free* to refer to a process close to zero-recoil of the residual nucleus, corresponding to knockout of bound protons virtually at rest in the target nucleus. At higher recoil momentum ($p_{recoil} > 200$ MeV/c) complications due to nucleon-nucleon correlations [Ma91] obscures interpretation of data in terms of the simple quasi-free reaction mechanism.

1.1 Spin Observables in $(p,2p)$ Studies

Initial experimental studies of quasi-free $(p,2p)$ scattering were performed with unpolarized proton beams, which yielded only summed energy spectra, angle correlation cross-sections and energy-sharing correlation cross-sections. Experiments utilizing polarized beams opened up interesting new possibilities, as illustrated by Kitching *et al.* [Kit76] in a study of the $^{16}O(\overrightarrow{p},2p)$ reaction at 200 MeV. It was observed that the asymmetry in the cross-section results between different polarization states for the projectile beam has the expected j-dependence as predicted by DWIA calculations.

Due to the non-trivial nature of the measurement of other spin observables, the asymmetry, or analyzing power, remains by far the best studied spin observable for knockout studies. The first extensive survey of analyzing power energy-sharing distributions was performed at TRIUMF for proton knockout from ^{16}O [Kit80] and ^{40}Ca [Ant81] for a 200 MeV polarized proton beam. It was concluded that while the strong j-dependence caused by the distorting optical potentials

[1] Quasi-elastic scattering, or *inclusive* quasi-free scattering, refers to an inclusive measurement of scattering from single protons and neutrons averaged over all bound states, and is characterized by a broad peak in the nuclear excitation spectrum, the centroid of which roughly corresponds to free NN scattering.

[2] $\overrightarrow{p}$ indicates a polarized incident proton beam.

and the nuclear spin-orbit coupling is demonstrated in the analyzing power data, the DWIA is capable of successful analyzing power predictions *only* in restricted angular regions, deteriorating for the more unsymmetrical angle pairs [Ant81]. Indications of failure of the DWIA to predict A_y was also found for the $^4He(p,2p)^3H$ reaction at 250 and 500 MeV for $p_{recoil} \leq 150$ MeV/c [Mar82], where the analyzing power was found to be consistently lower than the theoretical calculations, even though the study of energy-sharing cross-sections at 250, 350 and 500 MeV revealed good agreement with DWIA calculations [Eps80, Oer82].

Lack of accurate knowledge about the optical model potential, possible problems with the NN interaction and questions about the validity of the factorization assumption within the DWIA framework were cited as possible reasons for the failure of the DWIA to provide good analyzing power predictions [Kud86]. This prompted refinements in the theory, such as the incorporation of more advanced effective NN interactions in the t-matrix. Good agreement was consequently found between the refined non-relativistic DWIA calculations of Kudo and co-workers [Kud86, Kud88, Kud89, Kan90], and the experimental cross-section and analyzing power energy-sharing distributions for the $^{16}O(p,2p)^{15}N$ and $^{40}Ca(p,2p)^{39}K$ reactions at 76.1, 101.3 and 200 MeV [Kit80, Ant81, Sam86], and the $^{12}C(p,2p)^{11}B$ reaction at 84 MeV [Nor86]. However, for the $^{40}Ca(p,2p)^{39}K$ reaction at 300 MeV [Kit82] and the $^4He(p,2p)^3H$ reaction at 250 and 500 MeV [Mar82] the significant discrepancies initially reported could not be resolved.

In 1989 Cooper and Maxwell [Coo89] introduced a fully relativistic DWIA formalism, where the distortions are described by relativistic optical potentials with complex vector and scalar potentials, and Dirac-Hartree-like meson field potentials are used for nuclear structure. With the subsequent development of a finite-range relativistic DWIA, they were able to give good account of the TRIUMF data for the $^{16}O(p,2p)^{15}N$ and the $^{40}Ca(p,2p)^{39}K$ reactions at 200 MeV [Max93, Max96]. However, similar to the non-relativistic calculations by the Osaka group, the relativistic DWIA calculations [Ike95, Max96] could not solve the A_y problems for the $^{40}Ca(p,2p)^{39}K$ reaction at 300 MeV. It was furthermore shown that neither the non-relativistic or relativistic DWIA could adequately describe A_y for the $^{16}O(p,2p)^{15}N$ reaction at 500 MeV [Mil90, Mil98].

Since a total relativistic description also fails to provide an adequate description of quasi-free proton knockout, the next series of refinements within the DWIA framework concerns the

question of density dependence of the NN interaction. This would make the reaction sensitive to the location of the interaction within the target nucleus, since the relative strengths of the various amplitudes contributing to the NN t-matrix could in principle differ quite extensively between the nuclear surface and nuclear interior [Max96].

1.2 Evidence of Medium Effects

Evidence of the medium modification of the NN interaction was first seen in measurements of the polarization transfer observables for quasi-elastic scattering from ^{208}Pb at 500 MeV [Car84], where the analyzing power was shown to be substantially reduced with regards to the free NN scattering values. Various instances of this so-called 'quenching' effect of the analyzing power for quasi-elastic (p,p') scattering are known [Hau91, Li94, Car99]. While standard non-relativistic theoretical models fail to predict this effect, the relativistic treatment of quasi-elastic scattering, first examined by Horowitz and Iqbal [Hor86], succeeded in predicting the reduction in analyzing power data for (p,p') scattering from ^{12}C, ^{40}Ca and ^{208}Pb [Hor88] between 300 MeV and 800 MeV. Although similar successful prediction was not attained for the other five spin observables, this reduction in analyzing power was attributed to the inclusion of nuclear medium effects, naturally incorporated in the Dirac formalism as an enhancement of the lower components of the projectile and target nucleon Dirac spinors resulting from strong scalar potentials [Hil99]. This success in accessing medium modifications to the NN interaction by means of quasi-elastic proton scattering, combined with the fact that various exclusive quasi-free scattering studies confirm that the inclusive yield is primarily composed of a single-step quasi-free scattering process [Whi90, Li94, Car99a], prompted the consideration of quasi-free $(\overrightarrow{p},2p)$ scattering in investigations of the medium modification of the NN interaction.

Exclusive quasi-free scattering measurements are advantageous because the ambiguities in nuclear structure and reaction mechanisms present in the description of quasi-elastic scattering are minimized. While quasi-elastic scattering deals with the superposition of scattering amplitudes of all nucleons of the nucleus, quasi-free knockout deals basically with the scattering amplitude of a single nucleon [Kre95]. An additional advantage of exclusive over inclusive quasi-free scattering is that the two-body kinematics can be specified through the experimental setup. Knockout from s-states, the dominant knockout process at zero recoil geometry [Ber62], is espe-

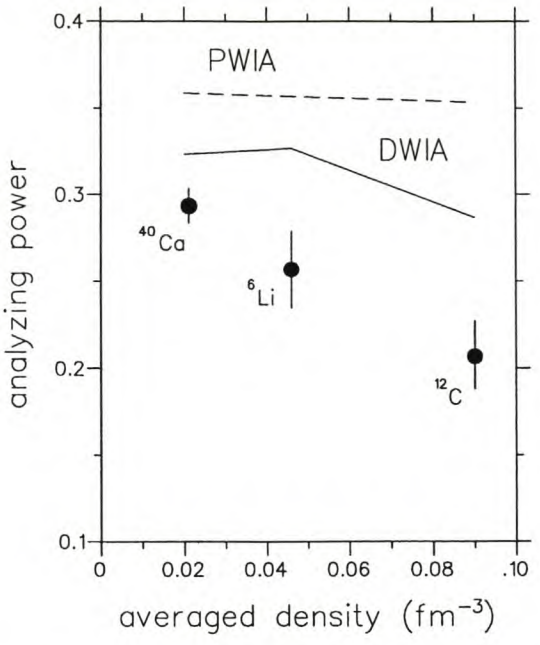

Figure 1.1: Analyzing powers for quasi-free proton knockout from $s_{1/2}$ orbits of various targets at 392 MeV, as obtained from Hatanaka *et al.* [Hat97].

cially illuminating since the bound nucleons can be regarded as being unpolarized, which is not the case for knockout from $l \neq 0$ states [Jac76]. A simple relation is thus expected between the spin observables of the $(p, 2p)$ reaction and the free NN scattering [Nor98]. In the case of $l \neq 0$ states the effective polarization of the bound nucleons [Jac73] makes this relation ambiguous.

Experimental evidence of the reduction of A_y in exclusive $(p, 2p)$ measurements was reported as early as 1982 by Margaziotis *et al.* [Mar82] for the $^4He(p, 2p)^3H$ reaction at 250 and 500 MeV, although it was not at the time associated with the possible medium modification of the t-matrix. A study of the knockout of $1s_{1/2}$ protons from ^{16}O [Mil90] at 500 MeV reported similar findings. Li and Huffman [Li94, Huf96] illustrated that the energy-sharing analyzing power for the very light targets $^{3,4}He$ at 200 MeV is also substantially reduced from the free space value. This reduction, very similar to the reduction in the associated inclusive yields, varies systematically with target mass and proton scattering angle. Likewise Carmen [Car99] showed that the magnitude of the suppression in $^{12}C(p, p')$ data for an incident beam of 200 MeV protons is consistent with the angle-integrated exclusive data.

In 1997 Hatanaka *et al.* [Hat97] presented experimental results that strongly suggests the existence of a nuclear medium effect on the NN interaction. In a measurement of proton knockout

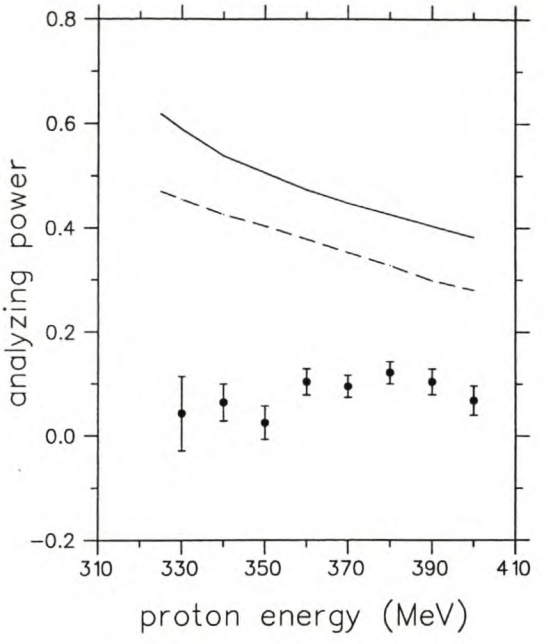

Figure 1.2: Experimental and theoretical analyzing powers, obtained from Miller *et al.* [Mil98], for proton knockout to the $1s_{1/2}$ state in the $^{16}O(p,2p)^{15}N$ reaction at 504 MeV. The results shown are for the angle pair $(20°, -52°)$, and are plotted as a function of the kinetic energy of the forward angle proton. The solid curve represents DWIA calculations for the free NN interaction, while the dashed curve represents calculations where an empirical density dependent interaction [Ray90] is employed.

(for the zero recoil condition) at 392 MeV from the $1s_{1/2}$ orbital from ^{6}Li and ^{12}C, and from the $2s_{1/2}$ orbital from the ^{40}Ca nucleus, it was shown that A_y is a monotonically decreasing function of the averaged density as seen through the knockout reaction (see Fig. (1.1)). In an attempt to reproduce this trend Noro *et al.* [Nor99] performed DWIA calculations employing various density dependent NN interactions, succeeding only in a qualitative reproduction of the reduction in A_y. Similarly Miller *et al.* [Mil98] included medium modified NN interactions in the DWIA description of the $^{16}O(p,2p)$ reaction at 500 MeV. He illustrated, as shown in Fig. (1.2), that although the inclusion of density dependent interactions in the DWIA improves agreement with the data, satisfactory description of the data is still not attained. And finaly it can be mentioned that Huffman [Huf96] included a Horowitz-type medium modified NN interaction [Hor86] in his analysis of proton knockout from $^{3,4}He$, and found improved although still inadequate agreement with experimental results.

1.3 Aim of this Experiment

Although the quasi-free proton knockout reaction has been studied quite extensively over the last five decades, measurements were carried out almost exclusively for light and medium targets up to ^{40}Ca. The DWIA formalism has been used successfully in this lower mass region to describe energy-sharing cross-sections and analyzing powers for projectile energies < 200 MeV (with the exception of quasi-free scattering from $^{3,4}He$ [Li94, Huf96] and ^{12}C [Car99]). The avoidance of the use of heavier targets follows from the expectation that the severe distortion effects would defy accurate theoretical description. In the first study of quasi-free proton knockout from a heavier target, Cowley *et al.* [Cow95] showed that the DWIA formalism appears to be a valid theoretical treatment of the $^{208}Pb(p,2p)^{207}Tl$ reaction at 200 MeV. Good shape agreement between the energy-sharing cross-section results and DWIA calculations were obtained, and reliable spectroscopic factors were extracted. This implies that the reaction is indeed a one-step process, and that the distortions are introduced reliably. However, the energy resolution of this experimental study was such that the ground-state and first three excited states of ^{207}Tl could not be resolved.

In order to provide a clearer picture with which the DWIA can be compared, one that does not involve a mixture of states, a high resolution coincidence measurement of energy-sharing cross-section and analyzing power of the $^{208}Pb(\vec{p},2p)^{207}Tl$ knockout reaction is performed in this investigation with the aim to separate the $3s_{1/2}$ ground state from the first three excited states of ^{207}Tl. If it is then assumed that distortions are modeled in a reliable manner, this reaction can also be used as a probe for the study of NN interactions in the nuclear medium. Pronounced differences between the experimental A_y and theoretical calculations for the free NN interaction, a process not seen at the projectile energy of 200 MeV for knockout from any but the lightest targets, could possibly indicate a density dependent modification of the NN interaction.

The theoretical framework used to describe a quasi-free proton knockout reaction is presented in Chapter 2. Chapters 3 and 4 elaborate on the detail related to the experimental method and the data analysis. The results are presented in Chapter 5, followed by the conclusion in Chapter 6.

Chapter 2

Theoretical Background

The Distorted Wave Impulse Approximation (DWIA) serves as the theoretical framework used to describe quasi-free knockout reactions at medium energies. Review articles by Jacob and Maris [Jac66, Jac73a] and Kitching *et al.* [Kit85] serve as useful introductions to the theory. Augmenting these articles are the complete theoretical descriptions of the DWIA formalism as found in [Cha77, Wyn98] and references therein.

Within the DWIA, the quasi-free knockout process is reduced to the following outline through various simplifying assumptions and approximations. The incident projectile nucleon travels through the nuclear medium before interacting with a bound nucleon. The wave function describing the projectile nucleon is distorted by interaction with the target nucleus. An interaction between the projectile nucleon and a bound nucleon results in the bound nucleon being knocked out of the nucleus and the projectile nucleon being scattered out of the nucleus. The impulse approximation now requires that this interaction has essentially the same form as the interaction between two nucleons [Hor91], with the rest of the nucleons acting as spectators. On traversing the residual nucleus on the way out, the wave functions of the knocked-out and scattered nucleons are distorted by interaction with the residual nucleus.

Given this outline, the ability to construct a theoretical formalism that yields theoretical values which can quantitatively be compared with experimental data depends on an accurate description of the distortion mechanism affecting the incoming and two outgoing nucleons, an accurate description of the bound nucleon and also a sound understanding of the nucleon-nucleon (NN) interaction inside the nuclear field. The following sections serve as a brief review of these and other aspects that make up the DWIA description of quasi-free knockout reactions.

The DWIA formalism presented here largely follows the non-relativistic treatment of quasi-free knockout as presented by Chant and Roos [Cha77, Cha83]. Although this approach treats

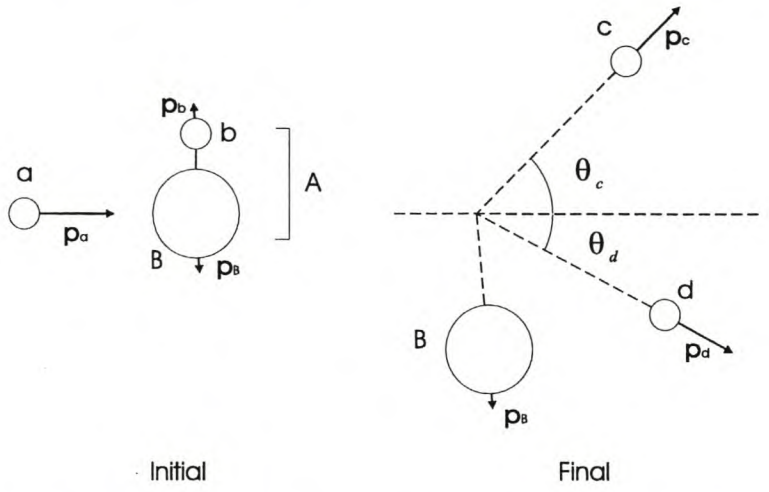

Figure 2.1: A diagram depicting the kinematics of the coplanar $A(a, cd)B$ reaction.

the NN interaction non-relativistically, utilizing the Schrödinger equation as opposed to the Dirac equation, the kinematics of the knockout process is nevertheless treated relativistically. A few general remarks on a full relativistic approach can be found in section 2.6.

2.1 Kinematics of Quasi-free Knockout

The initial state of a quasi-free proton knockout reaction, viewed in the laboratory reference frame as shown in Fig. (2.1), consists of a projectile proton a and target nucleus A with respective four momenta of $(T_a + m_a, \vec{p}_a)$ and $(T_A + m_A, \vec{p}_A)$. Target nucleus A consists of the to-be-knocked-out proton b and residual nucleus B such that $A = b + B$. Energy Q is required to separate proton b from the residual target, resulting in a final state represented by the two outgoing protons c and d and residual nucleus B in an excited state E_x. The two protons in the initial state, a and b, are thus relabelled in the final state as protons c and d. These two outgoing protons have four-momentum $(T_c + m_c, \vec{p}_c)$ and $(T_d + m_d, \vec{p}_d)$ respectively.

Since the target nucleus A is stationary in the laboratory system, energy and momentum conservation requires that

$$(T_a + m_a) + m_A = (T_c + m_c) + (T_d + m_d) + (T_B + m_B) + Q + E_x \ , \tag{2.1}$$

and that the recoil momentum of the residual nucleus is written as

$$\vec{p}_{recoil} = \vec{p}_B = \vec{p}_a - \vec{p}_c - \vec{p}_d \ . \tag{2.2}$$

T_a (MeV)	θ_c	θ_d	p_{recoil} (MeV/c)	T_c (MeV)	T_d (MeV)
202	22°	62.3°	0.81	163	31
200.5	28°	54.6°	8.04	143	49.5
202	33°	49.7°	8.476	127	67

Table 2.1: Kinematic quantities for minimum recoil for knockout to the ground state in the $^{208}Pb(p,2p)^{207}Tl$ reaction.

Since the assumption is made that the residual nucleus acts as a spectator, its momentum remains unchanged by the $(p,2p)$ reaction, and

$$\vec{p}_B = -\vec{p}_b \ . \tag{2.3}$$

Kinematically speaking there are two main aspects that separate quasi-free knockout from free scattering, viz. the non-zero separation energy required to liberate the nucleon from the nucleus, and the momentum distribution possessed by the nuclear proton. In order to view a *pure* quasi-free process, i.e. a process differing from free NN scattering *only* in terms of the role of the nuclear medium surrounding the nuclear nucleon, only knockout of a nucleon that has zero momentum at the moment of interaction, the so-called quasi-free point, should be considered.

Subject to the experimental constraints as outlined in Chapter 3, the kinematic quantities relevant to this study for knockout to the ground state for the minimum recoil condition are summarized in table (2.1).

2.2 The DWIA

This section is concerned with establishing theoretical expressions for the triple differential cross-section and analyzing power describing the proton knockout reaction $A(a,cd)B$. We start with Fermi's Golden Rule which states that [Sak94]

$$\sigma_{fi} = \frac{2\pi\varpi_f}{v} |T_{fi}|^2 \ , \tag{2.4}$$

where v is the relative velocity of the projectile and target in the entrance channel, ϖ_f represents the energy density of the final states and T_{fi} represents the transition amplitude from initial state

i to final state f. This is a general equation and must be rewritten in terms of the exclusive $(p, 2p)$-reaction. The energy density of final states (in the laboratory coordinate system) is written as

$$\varpi_B = \frac{d^3\overrightarrow{p_c}}{(2\pi\hbar)^3}\frac{d^3\overrightarrow{p_d}}{(2\pi\hbar)^3}\frac{1}{dE} \ . \tag{2.5}$$

Substituting $d^3\overrightarrow{p} = p^2 dp d\Omega$ and $E_c dE_c = c^2 p_c dp_c$ in Eq. (2.5) yields

$$\varpi_B = \frac{p_c E_c dE_c d\Omega_c p_d^2 dp_d d\Omega_d}{(2\pi\hbar)^6 c^2 dE} \ . \tag{2.6}$$

Substituting Eq. (2.6) in Eq. (2.4) yields

$$\sigma_{fi} = \frac{2\pi}{v}\frac{p_c E_c dE_c d\Omega_c p_d^2 dp_d d\Omega_d}{(2\pi\hbar)^6 c^2 dE}|T_{fi}|^2 \ . \tag{2.7}$$

Rewriting the above provides us with the so-called triple differential cross-section

$$\frac{d^3\sigma}{d\Omega_c d\Omega_d dE_c} = \frac{2\pi}{v}\frac{p_c E_c p_d^2 dp_d}{(2\pi\hbar)^6 c^2 dE}|T_{fi}|^2 \ . \tag{2.8}$$

Thus for a certain energy of outgoing proton c the associated cross-section of the knockout reaction can be calculated, also referred to as the energy-sharing cross-section. The total energy E can be written as

$$E = \sqrt{p_c^2c^2 + m_c^2c^2} + \sqrt{p_d^2c^2 + m_d^2c^2} + \sqrt{(\vec{p}_c + \vec{p}_d - \vec{p}_a)^2c^2 + m_B^2c^2} + E_x + Q \ . \tag{2.9}$$

Fixing E_c and taking the differential of E results in

$$dE = \frac{c^2 p_d dp_d}{E_d} + \frac{c^2(p_d - p_a cos\theta_a + p_c cos(\theta_c + \theta_d))dp_d}{E_c} \ . \tag{2.10}$$

Substituting Eq. (2.10) into Eq. (2.8), rewriting v, averaging over the initial spin states, and summing over the final spin states yields the unpolarized triple differential cross-section for proton knockout

$$\frac{d^3\sigma}{d\Omega_c d\Omega_d dE_c} = \frac{F_{kin}}{(2s_a+1)(2J_A+1)}\sum_{\mu_a\mu_c\mu_d M_A M_B}|T_{fi}|^2 \ , \tag{2.11}$$

where μ_i is the projection quantum number of the spin s_i for particle i $(i = a, c, d)$ and J_j denotes the total angular momentum quantum number of nucleus j $(j = A, B)$ with corresponding projection quantum number M_j. The kinematic factor F_{kin} is given by

$$F_{kin} = \frac{E_a E_c E_d}{(\hbar c)^7 (2\pi)^5}\frac{p_c p_d c}{p_a}\left[1 + \frac{E_d}{E_B}\left(1 - \frac{p_a}{p_d}cos\theta_a + \frac{p_c}{p_d}\cos(\theta_c + \theta_d)\right)\right]^{-1} \ . \tag{2.12}$$

The next step is to rewrite the transition amplitude, which contains most of the physics of the DWIA process. We start by writing

$$T_{fi} = \left\langle \Phi^{(-)}(B,c,d) \mid \widehat{V} \mid \Psi^{(+)}(A,a) \right\rangle \ , \tag{2.13}$$

where $\Psi^{(+)}(A,a)$ is the exact wave function describing the system, and $\Phi^{(-)}(B,c,d)$ represents the wave function of the exit channel in the absence of any interaction between protons c and d. V is the potential responsible for the knockout reaction. Introducing the wave function $\Phi^{(+)}(A,a)$ for the initial state in the absence of V and defining the transition operator $\widehat{t}$ as

$$\widehat{V} \mid \Psi^{(+)}(A,a)\rangle = \widehat{t} \mid \Phi^{(+)}(A,a)\rangle \ , \tag{2.14}$$

the transition amplitude can be written as

$$T_{fi} = \left\langle \Phi^{(-)}(B,c,d) \mid \widehat{t} \mid \Phi^{(+)}(A,a) \right\rangle \ . \tag{2.15}$$

It is then assumed that the wave functions $\Phi^{(+)}(A,a)$ and $\Phi^{(-)}(B,c,d)$ can be factorized in terms of separate wave functions for the dynamics of respectively $(a+A)$, $(c+B)$ and $(d+B)$ (refer to section 2.4) as well as the internal wave functions of all the particles. This yields

$$T_{fi} \approx \left\langle \psi(B)\eta^{(-)}_{cB}\eta^{(-)}_{dB}\psi(c)\psi(d) \mid \widehat{t} \mid \eta^{(+)}_{aA}\psi(a)\psi(A) \right\rangle \ , \tag{2.16}$$

where ψ is the internal wave function for the various particles (representing e.g. the structure of target A and residual target B, and the spin wave functions for a,c,d) and η describe the relative motion of the particles in the entrance and exit channels.

The impulse approximation assumes that the incident particle interacts with only one target nucleon, requiring the replacement of the general transition operator $\widehat{t}$ with a two-body transition operator for NN scattering $\widehat{t}_{NN}$. Since the knockout process under discussion involves identical spin $\frac{1}{2}$ particles, the antisymmetric properties of the wave functions of the two protons are taken into account by introducing the exchange operator $\widehat{P}_{ex}$, resulting in

$$T_{fi} \approx \left\langle \psi(B)\eta^{(-)}_{cB}\eta^{(-)}_{dB}\psi(c)\psi(d) \mid \widehat{t}_{NN}(1-\widehat{P}^{\dagger}_{ex}) \mid \eta^{(+)}_{aA}\psi(a)\psi(A) \right\rangle \ . \tag{2.17}$$

The wave function of the target nucleus $\psi(A) \equiv \psi_{J_A M_A}$ is now rewritten in terms of a single particle bound state wave function of nucleon b, $\phi^B_{LJM}(\overrightarrow{r})$, and the core B described by $\psi_{J_B M_B}$ [Sat83]. This yields

$$\psi_{J_A M_A} = n_A^{-1/2} \left\langle t_b \nu_b T_B N_B \mid T_A N_A \right\rangle \sum_{LJM} \theta_{LJ}\,(B,b \mid A) \left\langle J_B M_B JM \mid J_A M_A \right\rangle \phi^B_{LJM}\psi_{J_B M_B} \tag{2.18}$$

The quantum numbers LJM denote respectively the orbital angular momentum, the total angular momentum and the projection of the total angular momentum quantum numbers of the bound nucleon. The quantities T_j and N_j are the isospin and isospin projection quantum numbers of nucleus $j = A, B$. The corresponding quantities for the nucleons are t_i and ν_i (i = a,b,c,d), and $\langle t_b \nu_b T_B N_B \mid T_A N_A \rangle = C$ is a Clebsch Gordan coefficient for isospin. The quantity n_A is the mass number of nucleus A. The fractional parentage coefficient $\theta_{LJ}\,(B, b \mid A)$ is used in describing the decomposition of the target nucleus $A \rightarrow B + b$. It then follows that the transition amplitude in coordinate space is written as

$$T_{fi} = n_A^{-1/2} C \sum_{LJM} \theta_{LJ}\,(B, b \mid A)\, \langle J_B M_B JM \mid J_A M_A \rangle\, T_{LJM}\ , \tag{2.19}$$

with T_{LJM} given by [Ike95]

$$T_{LJM} = \int\int d^3r d^3r' \eta^{(-)*}_{\mu_c}(\vec{k}_{cB}, \vec{r}) \eta^{(-)*}_{\mu_d}(\vec{k}_{dB}, \vec{r}\,')(1 - \hat{P}^{\dagger}_{ex}) t_{NN}(|\vec{r} - \vec{r}\,'|) \\ \eta^{(+)}_{\mu_a}(\vec{k}_{aA}, \vec{r}) \phi^B_{LJM}(\vec{r}\,')\ . \tag{2.20}$$

The quantity $\eta^{(m)}_{\mu_i}(\vec{k}_{iI}, \vec{r}\,')$ represents the non-relativistic distorted wave function of particle i ($i = a, c, d$), moving relative to nucleus I ($I = A, B$) with momentum $\vec{k}_{iI}$ and situated at $\vec{r}\,'$ moving towards (away) from the nucleus for $m = +(-)$. The wave function $\eta^{(m)}_{\mu_i}$ includes spin by multiplying the spatial part of the distorted wave with the Pauli spinor $\chi^{1/2}_{\mu_i}$. The generation of these distorted waves are discussed in section 2.4. It can be shown [Cha77] that the unpolarized triple differential cross-section for proton knockout from nuclear state LJ is written as

$$\frac{d^3\sigma^{LJ}}{d\Omega_c d\Omega_d dE_c} = \frac{F_{kin} S_{LJ}}{(2s_a + 1)(2J + 1)} \sum_{\mu_a \mu_c \mu_d M} \left| \sum_{M_L} \langle L M_L s_d \mu_d \mid JM \rangle\, T'_{LJM} \right|^2\ , \tag{2.21}$$

with the new T'_{LJM} written as

$$T'_{LJM} = \int\int d^3r d^3r' \eta^{(-)*}_{\mu_c}(\vec{k}_{cB}, \vec{r}) \eta^{(-)*}_{\mu_d}(\vec{k}_{dB}, \vec{r}\,')(1 - \widehat{P^{\dagger}_{ex}}) t_{NN}(|\vec{r} - \vec{r}\,'|) \\ \eta^{(+)}_{\mu_a}(\vec{k}_{aA}, \vec{r}) \phi^B_{LJM_L}(\vec{r}\,') \chi^{s_d}_{\mu_d}\ . \tag{2.22}$$

The quantity $S_{LJ} = |C\theta_{LJ}|^2$ is the spectroscopic factor, which represents the probability to reach a single particle hole state LJ when a nucleon is removed from the target nucleus, and M_L is the projection quantum number of the orbital angular momentum quantum number L of the target proton in the nucleus.

The other observable relevent to this study, the analyzing power A_y, is defined by

$$A_y = \frac{1}{p} \cdot \frac{\sigma^{3\uparrow} - \sigma^{3\downarrow}}{\sigma^{3\uparrow} + \sigma^{3\downarrow}} , \tag{2.23}$$

where $\sigma^{3\uparrow(\downarrow)}$ denotes the triple differential cross-section for an incident beam of spin-up (spin-down) polarized protons, given by

$$\sigma^{3\uparrow(\downarrow)} = \frac{d^3\sigma^{LJ\uparrow(\downarrow)}}{d\Omega_c d\Omega_d dE_c} = \frac{F_{kin} S_{LJ}}{(2s_a+1)(2J+1)} \sum_{\mu_c \mu_d M} \left| \sum_{M_L} \left\langle LM_L \tfrac{1}{2}\mu_d \mid JM \right\rangle T^{\prime\uparrow(\downarrow)}_{LJM} \right|^2 , \tag{2.24}$$

and p is the degree of polarization of the projectile beam.

2.2.1 The Factorized DWIA

The general form of the DWIA triple differential cross-section, presented in Eqs. (2.21) and (2.20), can be recast in a factorized form for economy in the calculation and also to provide clearer insight as to the physical significance of the expression. The transition amplitude T_{fi} can be written in the *factorized* DWIA as

$$T_{fi} = n_A^{-1/2} C \sum_{LJM} \theta_{LJ}\,(B,b \mid A)\, \langle J_B M_B JM \mid J_A M_A \rangle \left\langle \vec{k_f} \mu_c \mu_d \mid \hat{t}_{NN} \mid \mu_a \mu_b \vec{k_i} \right\rangle T^{fac}_{LJM} , \tag{2.25}$$

where $\left\langle \vec{k_f} \mu_c \mu_d \mid \hat{t}_{NN} \mid \mu_a \mu_b \vec{k_i} \right\rangle$ is the antisymmetrized NN scattering amplitude and $\vec{k_i}$ and $\vec{k_f}$ are the initial and final relative momenta of the two interacting protons. The quantity T^{fac}_{LJM}, the so-called distorted momentum distribution, is given by

$$T^{fac}_{LJM} = \int d^3r\ \eta^{(-)*}_{\mu_c}(\vec{k}_{cB}, \vec{r}) \eta^{(-)*}_{\mu_d}(\vec{k}_{dB}, \vec{r}) \eta^{(+)}_{\mu_a}(\vec{k}_{aA}, \frac{B}{A}\vec{r}) \phi^B_{LJM}(\vec{r}) . \tag{2.26}$$

In order for the two-nucleon t-matrix element to be taken out of the integration of T_{LJM} it is required that the matrix element must vary little with momentum [Cha77], subsequently being replaced by a two-body t-matrix evaluated at asymptotic kinematics. This leads to a convenient zero-range approximation

$$t(\vec{r} - \vec{r}\,') \simeq t(q^2)\delta(\vec{r} - \vec{r}\,') , \tag{2.27}$$

with the momentum transfer $\vec{q}$ defined as [Ike95]

$$\vec{q} = \vec{k}_f - \vec{k}_i = (\vec{k}_{cB} + \vec{k}_{dB}) - (\vec{k}_{aA} - \vec{k}_B) , \tag{2.28}$$

which, together with Eq. (2.22), results in Eqs. (2.25) and (2.26). A more severe form of the factorization approximation results from the additional exclusion of the spin-orbit terms in the optical potentials used to generate the distorted waves. As a result, simplification of the spin summations leads to the convenient separation of the knockout cross-section into a reaction term, $(\frac{d\sigma}{d\Omega})_{NN}$, and a nuclear structure term, $\left|T^{fac}_{LJM}\right|^2$, so that

$$\frac{d^3\sigma^{LJ}}{d\Omega_c d\Omega_d dE_c} = F_{kin} S_{LJ} (\frac{d\sigma}{d\Omega})_{NN} \left|T^{fac}_{LJM}\right|^2 . \tag{2.29}$$

2.2.2 The Effective Polarization

The distortion of the scattering wave functions within the DWIA generally results in an effective initial spin polarization of the struck nucleon, as originally shown by Maris [Mar59]. This effective polarization causes pronounced asymmetries in cross-section results for incident beams of different polarization directions, and is sometimes referred to as the *Maris effect.*

A simple semi-classical picture can be used to illustrate the connection between asymmetries in cross-section results and the effective polarization of the struck nucleon [Jac73, Jac76]. Consider the two sets of asymmetrical kinematics for a co-planar quasi-free $(\overrightarrow{p}, 2p)$ process in nucleus A, shown in Fig. (2.2). From the figure it is clear that protons that originate from quasi-free events on the right-hand side of the nucleus traverses on the average less nuclear matter than protons originating from events on the left-hand side. Considering arguments about the size of the mean free path of medium energy protons through the nucleus it can be argued that the right-hand side of the nucleus contribute considerably more to the quasi-free cross-section than the left-hand side. For events with non-zero recoil momentum, as shown in Fig. (2.2), the dominant contribution of one side of the nucleus to the cross-section classically emphasize a definite orientation of the orbital angular momentum orthogonal to the scattering plane (clockwise according to the sketch). Through spin-orbit coupling this will favour a definite spin orientation of the nuclear proton. Considering the extreme single-particle model and knockout of protons from the $j = 3/2$ and $j = 1/2$ states this spin orientation will be, according to the sketch, clockwise for $j = 3/2$ and anti-clockwise for $j = 1/2$. Therefore, due to absorption and the spin-orbit interaction the nuclear proton in the quasi-free scattering process has an effective polarization orthogonal to the scattering plane. The considerable difference between spin-up spin-up and

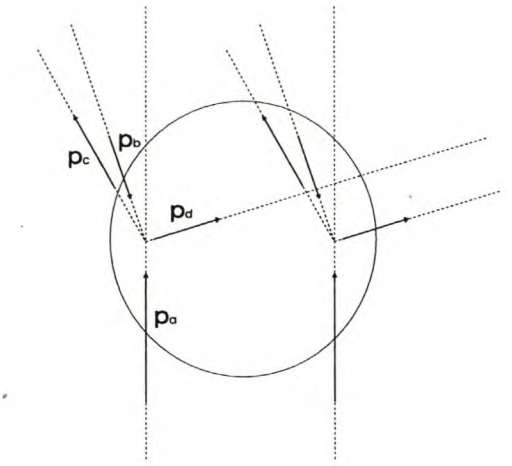

Figure 2.2: Two different quasi-free kinematics used to illustrate the Maris effect.

spin-up spin-down proton-proton interactions will then lead to large differences between cross-sections for different beam polarizations. Note that the absence of spin-orbit coupling, as is the case where $l = 0$, results in zero effective polarization.

Within the factorized DWIA the effective polarization is caused by the fact that the kinematical conditions of the experiment, through distortion, may destroy the isotropy of T^{fac}_{LJM} w.r.t. μ_b [Kit85]. The quasi-free knockout reaction is seen to involve a nuclear proton with momentum $-p_B$ and a spin wave function given by [Mar58]

$$\sum_{\mu_b=\uparrow,\downarrow} T^{fac,\mu_b}_{LJM} \cdot \chi^{1/2}_{\mu_b} \, . \tag{2.30}$$

The polarization expectation value of the spin of such an ensemble of protons, summed over the orientations of the final nuclei, is then given by

$$P_{eff} = \frac{\sum\limits_{M} \left[\left| T^{fac,\uparrow}_{LJM} \right|^2 - \left| T^{fac,\downarrow}_{LJM} \right|^2 \right]}{\sum\limits_{M,\mu_b} \left| T^{fac,\mu_b}_{LJM} \right|} \, . \tag{2.31}$$

Since the above equation was initially studied only within the fully factorized DWIA, the effective struck nucleon polarization is evaluated with spin-independent optical potentials. Kitching [Kit76] pointed out that the inclusion of a large spin-orbit distortion could have a profound effect on the $(\vec{p}, 2p)$ cross-section. It was however shown that in energy-sharing distributions the major features for the j-dependence of the predictions remains essentially unaffected by the inclusion of spin-orbit effects for all three particles [Kit76, Cha79, Cha83].

2.2.3 The PWIA

In the Plane Wave Impulse Approximation (PWIA) the wave functions describing protons a, c and d are not considered to be distorted by interaction with the target nucleus. In this context the evaluation of the term T_{LJM} simplifies considerably due to the presence of plane wave functions, and yields the following expression for the triple differential cross-section:

$$\frac{d^3\sigma^{LJ}}{d\Omega_c d\Omega_d dE_c} = F_{kin} S_{LJ} \cdot (\frac{d\sigma}{d\Omega})_{NN} \cdot |\phi(-\overrightarrow{p}_B)|^2 \ . \tag{2.32}$$

The wavefunction $\phi(-\overrightarrow{p}_B)$ represents the momentum distribution of the target proton in the nucleus, and is therefore the Fourier transform of the bound state wave function

$$\phi(-\overrightarrow{p}_B) = \frac{1}{(2\pi)^{1/2}} \int^{\infty} e^{i\overrightarrow{pB}\cdot\overrightarrow{r}} \phi^B_{LJM}(\overrightarrow{r}) d\overrightarrow{r} \ . \tag{2.33}$$

With the outline of the DWIA established we now proceed to discuss the calculation of the two-body t-matrix, the distorted waves and the bound state wave function.

2.3 The Two-Body t-matrix

At the heart of the impulse approximation is the two-body interaction, assuming the interaction between the projectile and struck nucleon to be somewhat similar to a free NN interaction. However, because the nuclear proton is interacting with the core, the initial state is off-shell (i.e. $E^2 \neq p^2 + m^2$). Since the two final state protons are both asymptotically free and therefore regarded as on-shell, the resulting t-matrix for quasi-free scattering is regarded to be half off the energy shell (half off-shell) [Red70]. In the case of the present study, with projectile energy of 200 MeV, a Q-value of 8.013 MeV and experimental conditions emphasizing minimum recoil, approximating the half off-shell t-matrix by an on-shell t-matrix is regarded as reasonable. This leads to ambiguities in the evaluation of the NN interaction regarding the assignment of the energy in the two-body scattering system.

The $(p, 2p)$ interaction involves a three-body final state. For $a + A = B + c + d$ conservation of four-momentum P requires

$$P_a + P_A = P_c + P_d + P_B \ . \tag{2.34}$$

T_a (MeV)	(θ_c,-θ_d)	p_{recoil} (MeV/c)	$T_{\text{Lab eff}}$ (MeV)	θ_{pp}^{com}
202	(22°,-62.3°)	0.81	184.53 (200.52)	47.19°
200.5	(28°,-54.6°)	8.04	177.25 (193.31)	60.96°
202	(33°,-49.7°)	8.476	178.40 (194.47)	71.84°

Table 2.2: Kinematic quantities for minimum recoil for knockout to the ground state in the $^{208}Pb(p,2p)^{207}Tl$ reaction in the final energy prescription (initial energy prescription).

This three-body problem is approximated by the two-body problem

$$P_a + P_b = P_c + P_d \ , \tag{2.35}$$

where P_b is defined as

$$P_b = P_A - P_B \ , \tag{2.36}$$

regarding $b = A - B$ as the struck nucleon and approximating the on-shell two-body interaction $a + \tilde{b} = c + d$ by $a + b = c + d$. A problem now arises: what are the kinematics at which the interaction occurs? The free NN interaction, and thus the on-shell t-matrix, is a function of the effective laboratory kinetic energy of two protons as well as the centre of mass scattering angle

$$\hat{t} = \hat{t}(T_{\text{Lab eff}}, \theta_{pp}^{com}) \ . \tag{2.37}$$

In order to substitute the half off-shell t-matrix with the t-matrix for the on-shell reaction $a + \tilde{b} = c + d$ two different energy prescriptions are routinely used.

In the final energy prescription (FEP) the effective laboratory kinetic energy for $a + \tilde{b} = c + d$ is calculated with the final state kinematics of protons c and d which results in

$$T_{\text{Lab eff}}^{FEP} = \frac{c^2 S_{FEP} - 4m_{proton}^4 c^4}{2m_{proton}c^2} \ , \tag{2.38}$$

where the Lorentz invariant Mandelstam variable S is given by

$$c^2 S_{FEP} = (E_c + E_d)c^2 - \hbar^2 c^2 (p_c^2 + p_d^2 + 2p_c p_d cos(\theta_d^{lab} + \theta_c^{lab})) \ , \tag{2.39}$$

and E_i represents the total energy of particle i. In the initial energy prescription (IEP) the kinematics of $a + b$ is used to calculate the effective kinetic energy, substituting S_{IEP}, given by

$$c^2 S_{IEP} = (E_a + m_{proton}c^2)^2 + c^2 p_a^2 \ , \tag{2.40}$$

for S_{FEP} in Eq. (2.38). For both the FEP and the IEP the centre of mass scattering angle for the NN interaction in the on-shell $a + \tilde{b} = c + d$ interaction is equated to the centre of mass scattering angle $cos(\theta_{ac}^{com})$ in the $a + b = c + d$ system, calculated by

$$cos(\theta_{ac}^{com}) = \frac{p_a p_c cos(\theta_c^{lab}) - E_a E_c + E_a^{com} E_c^{com}}{p_c^{com} p_a^{com}} \ . \tag{2.41}$$

Now that it is clear at which kinematical conditions the NN interaction is to be evaluated, we turn our attention to the specific representation of the non-relativistic two-body t-matrix. In a first attempt, experimentally determined free NN phase shifts, originating from the 1986 Arndt NN phase shift analysis [Arn86], are employed to write down the scattering amplitude [Hos68]. It would also be plausible to use, as done by Kudo *et al.* [Kud86], the Love & Franey t-matrix [Lov81, Fra85], which is a parameterization of the phenomenological free NN t-matrix, given here in the so-called KMT (Kerman, McManus and Thaler) form [Ker59]

$$\hat{t} = \frac{-4\pi(\hbar c)^2}{T_{com}} \left(A + B\vec{\sigma_1} \cdot \vec{\sigma_2} + C(\vec{\sigma_1} + \vec{\sigma_2}) \cdot \hat{n} + E\vec{\sigma_1} \cdot \hat{q}\vec{\sigma_q} \cdot \hat{q} + F\vec{\sigma_1} \cdot \hat{Q}\vec{\sigma_q} \cdot \hat{Q} \right) \ . \tag{2.42}$$

In this expression A, B, C, E and F are functions of the relative energy, the scattering angle in the centre-of-mass system and the total two-body isospin, and are obtained in a fitting procedure from free NN phase shift data. The unit vectors $[\hat{q}, \hat{n}, \hat{Q}]$ form a right-handed coordinate system with $\vec{q} = \vec{k_i} - \vec{k_f}$ denoting the direct momentum transfer, $\vec{Q} = \vec{k_i} + \vec{k_f}$ the exchange momentum transfer and $\hat{n}$ the unit vector normal to the scattering plane. $\vec{k_i}$ ($\vec{k_f}$) denote the initial (final) momentum of either proton in the centre-of-mass system.

Both these representations exclude effects of the nuclear medium on the NN interaction. However, it is known that for transitions that peak in the nuclear interior, the free NN interaction does not adequately account for experimental observations. Therefore a more sophisticated and correct way of representing the NN interaction in the DWIA model would be to include density dependent modifications of the t-matrix in the NN interaction.

Two types of density dependent NN interactions were investigated to complement the density independent free t-matrix calculations using the 1986 Arndt phase shifts. The first is the empirical effective interaction parameterized by Kelly *et al.* [Kel94], and in the second a modified t-matrix following the procedure proposed by Horowitz and Iqbal [Hor86] was used.

2.3.1 Empirical Effective Interactions

It is known that the NN effective interaction can be substantially modified by the presence of a nuclear medium [Kel80, Kel89a]. Although several theoretical calculations presently available agree on the general characteristics of the medium modifications, their detailed predictions vary considerably. In the absence of a reliable theoretical effective interaction, Kelly [Kel89b] argues the need to resort to empirical effective interactions guided by the results of nuclear theory. He proposed a simple fitting function, based on the results of nuclear matter calculations, with two to three parameters for each relevant term of the effective interaction, treating real and imaginary terms separately. The parameters are then fitted to a large body of elastic and inelastic scattering data, limiting the data set to relatively strong transitions for which multistep excitations are negligible.

The NN interaction in the nucleon-nucleus centre of mass frame can be represented in the form [Kel94]

$$\begin{aligned}\widehat{t} = t_{00}^{C} + t_{\tau}^{C}\vec{\tau}_1\cdot\vec{\tau}_2 + t_{\sigma}^{C}\vec{\sigma}_1\cdot\vec{\sigma}_2 + t_{\sigma\tau}^{C}(\vec{\sigma}_1\cdot\vec{\sigma}_2)(\vec{\tau}_1\cdot\vec{\tau}_2) + it_0^{LS}(\vec{\sigma}_1+\vec{\sigma_2})\cdot\hat{n} \\ +it_{\tau}^{LS}(\vec{\sigma}_1+\vec{\sigma}_2)\cdot\hat{n}\vec{\tau}_1\cdot\vec{\tau}_2 + t_0^{TND}S_{12}(\hat{q}) + t_{\tau}^{TND}S_{12}(\hat{q})\vec{\tau}_1\cdot\vec{\tau}_2 + t_0^{TNX}S_{12}(\widehat{Q}) \\ +t_{\tau}^{TNX}S_{12}(\widehat{Q})\vec{\tau}_1\cdot\vec{\tau}_2\ , \qquad (2.43)\end{aligned}$$

which is a slightly different and more elaborate representation of the t-matrix than given by Eq. (2.42). The quantities $\hat{q}$, $\widehat{Q}$ and $\hat{n}$ are defined as in the previous subsection and $S_{12}(\hat{q}) = 3(\sigma_1\cdot\hat{q})(\sigma_2\cdot\hat{q}) - \sigma_1\cdot\sigma_2$ is the two-body tensor operator. The quantity t_{ij}^{C} represents central interactions and t^m with $m = LS$ (TND, TNX) spin-orbit (tensor) interactions. Kelly [Kel94] showed that only the central and spin orbit terms in Eq. (2.43) are strongly affected by the medium. An empirical effective t-matrix t_{eff} therefore follows from Eq. (2.43) by replacing the terms $\mathrm{Re}(t_{00}^{C})$, $\mathrm{Im}(t_{00}^{C})$, $\mathrm{Re}(t_0^{LS})$ and $\mathrm{Im}(t_0^{LS})$ with the density dependent parameterization

$$t_i(q,\kappa_F) = (S_i - d_i\kappa_F^{\alpha_i})t_i^{f}(q,0) + \kappa_F^{\gamma_i}q^{\delta_i}\sum_{n=1}^{N} b_{in}\left[1+\left[\frac{q}{\mu_{in}}\right]^2\right]^{-\beta_i}\ . \qquad (2.44)$$

Medium modifications are thus included via the local Fermi momentum relative to its value at saturation density, represented by the quantity κ_F. The quantity $t_i^{f}(q,0)$ represents the free NN value at $\kappa_F = 0$, which for this study was calculated with the Love & Franey [Lov81, Fra85] interaction. Correlations among the parameters, however, generally necessitate the use of a

somewhat simpler parameterization, retaining only the most important features of the density dependence while minimizing correlations among the fitted parameters. This yields

$$\begin{aligned} Re[t_{00}^{C}(q,\kappa_F)] &= S_1 Re[t_{00}^{C}(q,0)] + \kappa_F^3 b_1 \left[1+\left[\frac{q}{\mu_1}\right]^2\right]^{-1} , \\ Im[t_{00}^{C}(q,\kappa_F)] &= (S_2 - d_2\kappa_F^2) Im[t_{00}^{C}(q,0)] , \\ \text{and} \quad Re[t_{0}^{LS}(q,\kappa_F)] &= S_3 Re[t_{0}^{LS}(q,0)] + \kappa_F^3 b_3 \left[1+\left[\frac{q}{\mu_3}\right]^2\right]^{-2} . \end{aligned} \tag{2.45}$$

The imaginary spin-orbit term is too weak to be fitted, and a suitable theoretical form is employed without parameter variation.

The parameters S_i, b_i, μ_i are obtained from fits to elastic and inelastic (p,p') cross-section and analyzing power data for ^{16}O, ^{40}Ca and ^{28}Si at incident energies ranging from 135 - 650 MeV [Kel94].

2.3.2 Density Dependent Interaction of Horowitz and Iqbal

In the relativistic framework of the DWIA (refer to section 2.6) the transition amplitude of the $(p,2p)$ reaction is written as

$$T_{fi} = \bar{\Phi}_B \bar{\Psi}_c \bar{\Psi}_d (1 - \hat{P}_{ex}) \hat{F} \Psi_a \Phi_A \ . \tag{2.46}$$

In their model Horowitz and Iqbal [Hor86] introduced the density dependence of the NN interaction by replacing the free nucleon mass M which appears in the four component Dirac spinor

$$\Psi = \sqrt{\frac{E+M}{2M}} \begin{bmatrix} 1 \\ \frac{\hat{\sigma}\cdot\hat{k}}{E+M} \end{bmatrix} \otimes \chi_s \ , \tag{2.47}$$

with an effective mass M^* due to the presence of large Lorentz scalar potential in the nuclear interior, as well as replacing the total energy E with an effective energy $E^* = \sqrt{k^2 + (M^*)^2}$. The value of M^* was obtained from the relationship between the average effective density of the nucleon inside the nucleus relative to the saturation density $\bar{\rho} = \frac{\rho}{\rho_0}$ as

$$M^* = M + S\bar{\rho} \ , \tag{2.48}$$

where the average scalar potential $S = -0.44$ is taken from mean field theory [Hor86]. The five relativistic amplitudes F_i can be written in terms of the non-relativistic two-body amplitudes

as in Eq. (2.42), through the relation

$$\begin{pmatrix} M_{ss} \\ M_{00} \\ M_{11} \\ M_{10} \\ M_{01} \end{pmatrix} = [O(k_c, M^*)] \begin{pmatrix} F_s \\ F_v \\ F_p \\ F_a \\ F_t \end{pmatrix} . \tag{2.49}$$

An explicit expression of the matrix $O(k_c, M^*)$ can be found in the article of Horowitz and Iqbal [Hor86]. Using the inverse of Eq. (2.49) and the free Arndt NN phase shifts, the Lorentz invariant scattering amplitudes are calculated, where $M^* = M$. Non-relativistic scattering amplitudes are then calculated with Eq. (2.49), for the unchanged F_i's with the new values for M^* and E^*, thus yielding a density dependent NN interaction that can be used in the non-relativistic DWIA.

However, it should be noted that recent studies by Van der Ventel *et al.* [Ven00] using a complete Lorentz invariant representation of the NN scattering matrix indicate that the treatment as described above severely overestimates the importance of the effective mass type of medium effect. It was nevertheless included as yet another independent calculation of the density dependent NN interaction.

2.4 Calculation of the Distorted Waves

The radial part of the distorted wave functions for the incident and outgoing particles are obtained by solving the Schrödinger equation with complex optical potentials.

The Hamiltonian for the entrance channel is given by [Jack65]:

$$\hat{H}_{entrance} = \hat{T}_a + \hat{T}_b + \hat{T}_A + \hat{V}_{bB} + \hat{V}_{ab} + \hat{V}_{aB} + \hat{H}_a + \hat{H}_A \ , \tag{2.50}$$

where

- $\hat{T}_i$ is the kinetic energy operator of particle i,
- $\hat{V}_{ij}$ is the potential describing the interaction between particles i and j,
- $\hat{H}_i$ is the internal Hamiltonian for particle i.

Similarly for the exit channel the Hamiltonian is given by

$$\widehat{H}_{exit} = \widehat{T}_c + \widehat{T}_d + \widehat{T}_B + \widehat{V}_{cd} + \widehat{V}_{Bd} + \widehat{V}_{Bc} + \widehat{H}_c + \widehat{H}_d + \widehat{H}_B \ , \tag{2.51}$$

Jackson [Jack65] furthermore shows that it is possible to express the kinetic energy operators in Eqs. (2.50) and (2.51) in terms of the overall centre of mass kinetic energy and a relative kinetic operator. By eliminating the centre of mass kinetic energy, which should have no effect on the distorted wave, the wave function for the initial state satisfies the equation

$$(\widehat{T}_{aA} + \widehat{T}_{bB} + \widehat{V}_{bB} + \widehat{V}_{aB} + \widehat{V}_{ab} + \widehat{H}_a + \widehat{H}_A)\widetilde{\Phi}^{(+)}(A,a) = E_i\widetilde{\Phi}^{(+)}(A,a) \ . \tag{2.52}$$

The $\widetilde{}$ serves as a reminder that $\widetilde{\Phi}^{(+)}(A,a)$ differs from $\Phi^{(+)}(A,a)$ due to the omission of the centre of mass kinetic energy term. The operator $\widehat{T}_{ij}$ is the relative kinetic energy operator between particles i and j. The wave function $\widetilde{\Phi}^{(+)}(A,a)$ has the form

$$\widetilde{\Phi}^{(+)}(A,a) = \eta^{(+)}_{\mu_a}\psi(A) \ , \tag{2.53}$$

where $\eta^{(+)}_{\mu_a} = \eta^{(+)}_{aA}\chi_{\mu_a}$ (with χ_{μ_a} the Pauli spinor) is the solution of

$$(\widehat{T}_{aA} + \widehat{V}_{aB})\eta^{(+)}_{\mu_a} = \varepsilon_{aA}\eta^{(+)}_{\mu_a} \ . \tag{2.54}$$

The potential term $\widehat{V}_{aB} \approx \widehat{V}_{aA} - \widehat{V}_{ab}$, in the above equation is taken to be the optical potential which describes $B + a$ scattering averaged over A at the relative kinetic energy $T^{rel}_{aA} = \frac{A}{A+a}T^{lab}_a$. The potential is expected to differ little from the optical potential for $a + A$ scattering [Cha77].

Similarly, for the exit channel it is found that by eliminating the centre of mass kinetic energy as well as the interaction between the outgoing particles (as required in section 2.2) Eq. (2.51) becomes

$$\widehat{H}_{exit} \Rightarrow \widehat{T}_{dB} + \widehat{T}_{cB} + \widehat{V}_{Bd} + \widehat{V}_{Bc} + \widehat{H}_c + \widehat{H}_d + \widehat{H}_B + \widehat{T}_{coup} \ . \tag{2.55}$$

The coupling term $\widehat{T}_{coup}$ is of the order of $1/A$ and is subsequently ignored for heavy nuclei, resulting in the factorization of the exit channel

$$\widetilde{\Phi}^{(-)}(Bcd) = \psi(B)\eta^{(-)}_{\mu_c}\eta^{(-)}_{\mu_d} \ , \tag{2.56}$$

where

$$(\widehat{T}_{dB} + \widehat{V}_{dB}) \cdot \eta^{(-)}_{\mu_d} = \varepsilon_{dB}\eta^{(-)}_{\mu_d} \ , \tag{2.57}$$

$$(\widehat{T}_{cB} + \widehat{V}_{cB}) \cdot \eta^{(-)}_{\mu_c} = \varepsilon_{cB}\eta^{(-)}_{\mu_c} \ . \tag{2.58}$$

The quantities $\widehat{V}_{dB}$ and $\widehat{V}_{cB}$ are the optical potentials that describe the d+B and c+B scattering interactions at relative kinetic energies T_{cB}^{rel} and T_{dB}^{rel}. These relative kinetic energies are defined as the kinetic energy of the exiting proton in the reference frame where the residual nucleus is at rest. Typically the relative kinetic energy between outgoing proton c and residual nucleus B is written as

$$T_{cB}^{rel} = \frac{S_{cB}c^2 - (m_c + m_B)^2c^4}{2m_Bc^2} \ . \tag{2.59}$$

The two different classes of phenomenological optical models that were utilized in this study are now discussed.

2.4.1 Schrödinger Equation Based Potentials

Complex optical model potentials for proton-nucleus scattering can be obtained by fitting experimental observables for elastic scattering, over a broad range of proton energy and target mass, to the solution of the Schrödinger equation. The global proton-nucleus optical model potentials resulting from these fits have parameters which are smooth functions of target A and Z and laboratory bombarding energy.

The radial dependence of the optical potential is parameterized with the standard Woods-Saxon form, which reflects the average density distribution of nucleons inside the nucleus. A surface absorptive term, which is taken to be proportional to the derivative of the Woods-Saxon potential, is also included. The full optical potential used contains a Coulomb potential term, a complex central, a complex spin-orbit and a complex exchange term. The central optical potential is given by:

$$-U(r)_{central} = \frac{V}{1+e^x} + \frac{iW}{1+e^{x'}} + \frac{4iW_d \cdot e^{x'}}{(1+e^{x'})^2} - U_{coul}(r) \ , \tag{2.60}$$

with $x = \frac{r - r_0 \cdot A^{1/3}}{a}$ and $x' = \frac{r - r_0' \cdot A^{1/3}}{a'}$. V, W and W_d are the potential strengths of the real, imaginary and surface absorptive parts of the central potential. r_0 and r_0' are radius parameters for the real and imaginary parts of the central potential, with a and a' the real and imaginary central diffuseness parameters. A is the atomic mass of the recoil nucleus. $U_{coul}(r)$ denotes the Coulomb potential due to a sphere of radius $R_{coul} = 1.25$ fm$\cdot A^{1/3}$

$$U_{coul}(r) \ = \ +\frac{Ze^2}{r} \qquad r \geq R_{coul}$$

$$= +\frac{Ze^2}{2R_{coul}}(3 - \frac{r^2}{R_{coul}^2}) \qquad r \leq R_{coul} \ , \tag{2.61}$$

The total optical potential is obtained by adding spin orbit and exchange terms, with the potential strength, radius and diffuseness parameters defined in an equivalent manner as above

$$-U(r) = -U(r)_{central} + g \cdot (\vec{l} \cdot \vec{\sigma}) \cdot \frac{1}{r \cdot a_{so}} \cdot \frac{(V_{so} + iW_{so}) \cdot e^{xs}}{(1 + e^{xs})^2} + (-1)^l \cdot \frac{V_{ex}}{1 + e^{xex}} \ . \tag{2.62}$$

Furthermore

$$\begin{aligned} \vec{l} \cdot \vec{\sigma} &= l \text{ for } j = l + s \\ &= -l - 1 \text{ for } j = l - s \ , \end{aligned} \tag{2.63}$$

where $\vec{\sigma}$ is the intrinsic spin of the nucleon and $\vec{l}$ represents the orbital angular momentum of the nucleon, and the quantity $g = 2$ fm^2. Values for the various parameters as used in this study are provided by the global optical model parameterizations of Nadasen [Nad81], Schwandt [Sch82] and Madland [Mad87].

Nadasen

Nadasen *et al.* [Nad81] analyzed differential cross-section data for the elastic scattering of protons from ^{40}Ca, ^{90}Zr, and ^{208}Pb targets over the energy range of 60-180 MeV. Due to the lack of analyzing power data of sufficient quality at the time, the primary emphasis of his study was a systematic description of cross-section data in terms of a phenomenological optical model. This resulted in a 10-parameter optical-model potential using relativistic kinematics and a relativistic extension of the Schrödinger equation.

Madland and Schwandt

The optical model of Nadasen has in the past been used very successfully to generate the distorted waves within the quasi-free knockout framework, producing theoretical cross-sections that are in good agreement with experimental data [Cow91, Bla93, Cow95].

However, since Nadasen did not rigorously include analyzing power results in his analysis one would expect the spin orbit part of the potential to be somewhat unreliable, resulting in

doubts about the validity of the use of the potential when considering a description of $(p, 2p)$ analyzing power results. Correcting this shortcoming, Schwandt *et al.* [Sch82] and Madland *et al.* [Mad87] generated potentials using analyzing power as well as cross-section data from a more extensive range of target nuclei than Nadasen.

Schwandt used measurements of the differential cross-sections and analyzing powers for elastic scattering of protons from ^{24}Mg, ^{28}Si, ^{40}Ca, ^{90}Zr, ^{92}Zr, ^{120}Sn and ^{208}Pb targets over the energy range of 80-180 MeV to generate the conventional optical model parameters Only quantitative differences between Nadasen and Schwandt exist, while the qualitative aspects of the potentials remain the same.

Madland, on the other hand, extended the phenomenological optical-model potential to the energy range of 50-400 MeV, using the potential of Schwandt and modifying it optimally to reproduce experimental proton reaction cross-sections for ^{27}Al, ^{56}Fe and ^{208}Pb, while allowing only minimal deterioration in the fits to the elastic cross-sections and analyzing powers.

Corrections for Non-locality

In order to give a more realistic representation of nucleon-nucleus scattering, mean field potentials (such as the phenomenological optical model potential under discussion) should incorporate non-localities. Perey and Buck [Per62] showed that it is plausible that the results predicted by a non-local optical model could be reproduced using an equivalent local optical model. They developed a simple parameterization of the non-local potential $V_{non-local}$ in terms of the local potential V_{local}

$$V_{non-local} = V_{local} \exp[\frac{\mu\beta^2}{2\hbar^2}(E - V_{local})] \ , \tag{2.64}$$

where β represents the range of non-locality and μ the reduced mass of the nucleon-nucleus system. This results in multiplying the wave function for the distorted waves, generated with the local potential, with the damping factor

$$\exp[\beta^2\mu\frac{V_{local}}{4\hbar^2}] \ , \tag{2.65}$$

to yield results that incorporate non-locality.

2.4.2 Potentials Based on the Dirac Equation

The Dirac Equation Based (DEB) optical potential is obtained from the relativistic optical potential when the Dirac equation is transformed into a Schrödinger-like equation for the upper component of the Dirac spinor. Though derived in this way, the DEB potential can be used in the non-relativistic formalism as another phenomenological optical potential, with the advantage that solving the Schrödinger equation with this potential produces the same elastic scattering results as the Dirac equation [Udi95]. Another advantage of the Dirac phenomenology is that it naturally gives rise to important characteristics of the non-relativistic nuclear optical potential, for example the central and spin-orbit terms [Coo93].

The DEB potential is obtained by rewriting the Dirac equation, which contains a scalar S and a vector V potential, as well as a Coulomb potential U_{coul}, as

$$\left(i\vec{\alpha}\cdot\vec{\nabla}-\beta(M+S)+E-V-U_{coul}\right)\Psi=0\ , \tag{2.66}$$

where $\Psi\equiv(\Psi_{up},\Psi_{down})$ is a Dirac four spinor. This results is a second order differential equation for the upper component. This then provides the equivalent Schrödinger equation [Udi95]

$$\left[\nabla^2+(E-U_c)^2-m^2-2E\left(U_{cent}+U_{S.O.}\vec{\sigma}\cdot\vec{L}\right)\right]\psi=0\ , \tag{2.67}$$

with ψ a bi-spinor and where the effective local central potential is given by

$$U_{cent}=\frac{1}{2E}\left(2EV+2mS-V^2+S^2-2U_cV+2EU_D\right)\ , \tag{2.68}$$

with

$$U_D=\frac{1}{2E}\left[-\frac{1}{2r^2A}\frac{d}{dr}\left[r^2\frac{dA}{dr}\right]+\frac{3}{4A^2}\left[\frac{dA}{dr}\right]^2\right]\ , \tag{2.69}$$

and

$$A(r)=\frac{(m+S+E-V-U_c)}{(m+E)}\ . \tag{2.70}$$

The effective local spin-orbit potential is given by

$$U_{S.O.}=\frac{1}{2E}-\frac{1}{rA}\left[\frac{dA}{dr}\right]\ . \tag{2.71}$$

Note that, in contrast with the non-relativistic approach, the real and imaginary spin-orbit terms appear as a natural consequence of the Dirac equation.

This standard Lorentz scalar Lorentz vector model of the Dirac phenomenology has been shown to be remarkably successful in reproducing a large body of nucleon-nucleus elastic and inelastic scattering data over a wide range of projectile energies and target mass numbers ([Ham90] and references therein), prompting its use as a distorting potential in the DWIA. Parameterizations for the scalar and vector potentials as provided by Hama [Ham90] and Cooper [Coo93] were utilized.

Hama

The global Dirac optical model fit of Hama *et al.* [Ham90] was obtained using elastic proton scattering data from heavy nuclei (^{40}Ca, ^{48}Ca, ^{56}Fe, ^{60}Ni, ^{90}Zr and ^{208}Pb) in the energy range 65 to 1040 MeV. Where the Nadasen potential was obtained from only cross-section data compared to the Schwandt and Madland potentials with cross-section and analyzing power data, Hama went a step further and also used the limited available data for the spin rotation function Q.

In general, the scalar and vector potentials are written as [Ham90]

$$V(r,E,A) = V_v(E,A)f_v(r,E,A) + i\left[W_v(E,A)g_v(r,E,A) + W_{vsp}(E,A)h_v(r,E,A)\right] \ , \quad (2.72)$$

and

$$S(r,E,A) = V_s(E,A)f_s(r,E,A) + i\left[W_s(E,A)g_s(r,E,A) + W_{ssp}(E,A)h_s(r,E,A)\right] \ , \quad (2.73)$$

where the quantity E denotes the total energy of the incident proton in the centre of mass frame, A is the target mass number and r a radius parameter. The real $f(r,E,A)$ and imaginary $g(r,E,A)$ volume form factors have been taken to be symmetrized Woods-Saxons given by

$$f(r,R,Z) = \left\{1 + \exp\left[\frac{(r-R)}{z}\right]\right\}^{-1} \times \left\{1 + \exp\left[-\frac{(r-R)}{z}\right]\right\}^{-1} \ , \quad (2.74)$$

where R and z are parameterized in terms of the centre-of-mass energy of the nucleon-nucleus system E and target mass number A. The surface form factors $h(r,E,A)$ are taken as the derivative of a symmetrized Woods-Saxon.

The real and imaginary terms of the vector potential are parameterized as follows:

$$Re[V(r,E,A)] = R_v\left(V_0 + \frac{V_1}{E} + \frac{V_2}{E^2} + \frac{V_3}{E^3}\right) \times f(r,R_1,z_1) \quad , \quad (2.75)$$

and

$$Im[V(r,E,A)] = R_v\left(W_0 + \frac{W_1}{E} + \frac{W_2}{E^2} + \frac{W_3}{E^3}\right) \times f(r,R_2,z_2)$$
$$+R_v\left(W_{0sp} + \frac{W_{1sp}}{E} + \frac{W_{2sp}}{E^2} + \frac{W_{3sp}}{E^3}\right) z_3 \frac{d}{dR_3} f(r,R_3,z_3)\ , \tag{2.76}$$

where the geometry parameters R_i and z_i are given by

$$\begin{aligned} R_i &= A^{1/3}\left(r_{0i} + r_{1i}A^{-2/3} + r_{2i}A^{1/3} + r_{3i}/E + r_{4i}/E^2 + r_{5i}/E^3\right) \\ z_i &= a_{0i} + a_{1i}A + a_{2i}A^2 + a_{3i}/E + a_{4i}/E^2 + a_{4i}/E^3\ , \end{aligned} \tag{2.77}$$

with $i = 1,2,3$. R_3 and z_3 are assumed to be independent of E. The scalar potential has the same form, with vector parameters replaced by their scalar counterparts.

There are two different parameterizations under discussion in [Ham90], with the above representing the first and referred to as the DHD parameterization. The second parameterization (DH2D) differ only in the treatment of the surface term. Both these parameterizations were used in the DWIA calculations which will be presented in Chapter 5.

Cooper

Cooper *et al.* [Coo93] presents an energy dependent, but A-independent, potential which reproduce proton scattering observables for proton energies from 20 to 1040 MeV for the targets ^{12}C, ^{16}O, ^{40}Ca, ^{90}Zr and ^{208}Pb. This parameterization will be referred to as the EDAI potential of Cooper. In addition they also provide an energy and A-dependent global optical potential which extends the potential of [Ham90] to lower energies (20 MeV) and for lighter targets (^{12}C, ^{16}O).

The general form of the scalar and vector potentials as presented in Eqs. (2.72) and (2.73) were extended by [Coo93] by adding a surface peaked term in the real part of the potential. Furthermore the geometries of the form factors were chosen to be of the cosh form[1], compared to the symmetrized Woods-Saxons of [Ham90]. For the energy and A-dependent potential each of the 8 strengths are parameterized in terms of the E and A. The resulting parameterizations (referred to as EDAD1, EDAD2, EDAD3) are more extensive than that of [Ham90], resulting in between 106 and 176 parameters, depending on the choice of 3 different parameterizations.

[1] e.g. the vector potential form factor is written as $f(r,E,A) = \frac{cosh(R/a)-1}{cosh(R/a)+cosh(r/a)-2}$.

Non-locality Corrections

It is generally accepted that the full relativistic approach to nucleon-nucleus scattering may already include the bulk of non-local effects as observed in the non-relativistic approach [Udi95].

It can be shown that the solution of the equivalent Schrödinger equation Eq. (2.67) is related to the solution of the upper component of the Dirac equation by

$$\begin{aligned} \Psi_{up} &= K(r)\psi(r) \\ K(r) &= A^{1/2}(r) \end{aligned} \tag{2.78}$$

with $K(r)$ referred to as the Darwin factor [Udi95] and $A(r)$ defined as in Eq. (2.70). Consequently any solution of the Schrödinger equation with the DEB optical potential incorporates non-locality to the same degree as the full Dirac solution when the wave function is multiplied with the Darwin factor.

The effect of non-locality obtained by including the Darwin factor in the wave function was shown by Udias *et al.* [Udi95] to be equivalent to the Perey damping-factor approach with a range of non-locality of $\beta = 1$.

2.5 Bound State Wave Functions

The radial part of the single particle bound state wave function is generated as a solution of the Schrödinger equation with a potential that consists of a Woods-Saxon central potential term, a Woods-Saxon derivative spin-orbit term and a Coulomb potential term

$$-U(r) = \frac{V_c}{1+e^{x_c}} + g \cdot (\vec{l} \cdot \vec{\sigma}) \cdot \frac{1}{r \cdot a_{so}} \cdot \frac{V_{so} \cdot e^{x_{so}}}{(1+e^{x_{so}})^2} - U_{coul}(r) \ , \tag{2.79}$$

where $x_i = \frac{r - R_i \cdot A^{1/3}}{a_i}$, V_i is the strength of the potential, R_i is the radius parameter and a_i is the diffuseness parameter ($i \equiv so, c$). The various parameter sets [Cha83, Mah88, Qui88, Ma91, Are97] utilized in the calculations in Chapter 5 are listed in table 2.3. The quantity $\mathbf{V}_c$ in the table indicates that the strength of the potential was adjusted in order to reproduce the specific binding energy of the bound proton. Non-locality of the bound state wave functions is treated, similar to the treatment of non-locality in the distorted waves, by introducing the Perey damping factor (refer to section 2.4.1).

	[Cha83]	[Mah88]	[Ma91]	[Are97]	[Qui88]
R_{coul} (fm)	1.25	1.18	1.23	1.250	1.25
R_c (fm)	1.25	1.198	1.27	1.198	1.15
R_{so} (fm)	1.25	1.064	1.23	1.198	1.15
-V_c (MeV) (for $3s_{1/2}$)	$\mathbf{V}_c$	65	59.33	$\mathbf{V}_c$	$\mathbf{V}_c$
V_{so} (MeV)	5.00	12.08	7.78	5.00	6.00
a_c (fm)	0.63	0.700	0.67	0.7	0.65
a_{so} (fm)	0.63	0.738	0.67	0.7	0.65

Table 2.3: The bound state potential parameter sets.

Relativistic bound state proton wave functions are obtained as a solution of the Dirac equation in potential wells derived from relativistical mean-field Hartree calculations [Hor81]. Similar to the procedure outlined in section 2.4.2, it can be shown that the upper component of the relativistic bound state wave function can be used to solve a Schrödinger-like equation, thus providing yet another bound state wave in the non-relativistic DWIA calculation.

2.6 The Relativistic DWIA

The inability of the DWIA to predict experimental $^{40}Ca(p,2p)$ results at 300 MeV, especially the analyzing power, prompted the development of the Relativistic Distorted Wave Impulse Approximation (RDWIA) for $(p,2p)$ reactions [Kan90] by Cooper and Maxwell [Coo89, Max90, Max93], with later contributions by Ikebata [Ike95] and Mano and Kudo [Man98].

In the Dirac impulse approximation the $(p,2p)$ reaction is viewed, as in the non-relativistic case, as a single nucleon knockout process. Analogous to a non-relativistic DWIA formalism the matrix element describing the process consists of a NN t-matrix sandwiched between a relativistic bound state and distorted wave in the initial state, and two distorted waves in the final state. In position space the direct part of this matrix element has the form [Coo89]

$$T_{fi}^{D} \propto \int\int d^4x\, d^4x'\; \bar{\Psi}_{\mu_c} \bar{\Psi}_{\mu_d} \hat{F} \Psi_{\mu_a} \Phi^{B}_{LJM} \;, \tag{2.80}$$

where Ψ_i is the distorted four-component wave function of proton i and Φ^{B}_{LJM} is the four-component wave function of the bound nucleon. The quantity $\hat{F}$ is the Lorentz invariant NN

amplitude, typically parameterized as

$$\hat{F} = \sum_{i}^{5} F^i(\lambda_1^i \otimes \lambda_2^i), \quad \text{with} \quad \lambda^i \equiv \{I, \gamma^\mu, \gamma^5, \gamma^5\gamma^\mu, \sigma^{\mu\nu}\} \ , \tag{2.81}$$

the so-called SPVAT parameterization of the relativistic scattering amplitude [Hor86]. The quantities γ_i represent the Dirac matrices.

The distorted waves are obtained by solving the Dirac equation using appropriate scalar, vector and Coulomb potentials. The scalar and vector optical potentials may be obtained from either a microscopic calculation or from global optical potential sets such as the one by Hama *et al.* [Ham90]. Bound state waves are calculated in a similar fashion.

2.7 Numerical Calculations

Theoretical results for the non-relativistic DWIA were obtained with the latest (1998) version of the computor code *THREEDEE* [Cha98]. The code employs the non-relativistic factorized DWIA (refer to Eqs. (2.11) and (2.25)) in which the bound state and distorted wave functions are two-component spinors. Radial density dependence of the two-body amplitudes for the density dependent calculations was taken into account by including the the NN scattering amplitude $\left\langle \vec{k_f}\mu_c\mu_d \mid \hat{t}_{NN} \mid \mu_a\mu_b\vec{k_i} \right\rangle$ from Eq. (2.25) in the integration of Eq. (2.26).

Relativistic kinematics is used in the calculation of the relative kinetic energies needed for the generation of the distorted waves, and also in establishing the kinematics at which the two-body t-matrix is to be evaluated. Except where otherwise noted, all *THREEDEE* calculations were performed employing the Final Energy Prescription and with the standard bound state parameter set of [Mah88]. In the interest of consistency non-locality corrections for the real and imaginary central potential terms for $(a + B)$, $(B + c)$ and $(B + d)$ scattering, for both the Schrödinger and the DEB optical potential, as well as the bound state wave was achieved through the Perey damping factor with non-locality range $\beta = 0.85$ fm.

Relativistic DWIA calculations were performed with the code *RELP2P* [Man00], which employs the finite-range RDWIA model of Mano *et al.* [Man98]. In this model the single particle bound state wave functions are calculated from relativistic mean fields produced by the Dirac Hartree model. Distorted wave functions are calculated from optical potentials obtained

by folding nuclear densities with the nucleon nucleon interaction of Horowitz [Hor85]. The NN amplitude is written in terms of the relativistic Love & Franey model [Hor85].

In all the calculations it is assumed that the ground state and first three excited states of ^{208}Pb are unfragmented, which is a reasonable assumption for the $3s_{1/2}$ and $2d_{3/2}$ states [Qui86, Qui88]. However, it should be noted that the $2d_{5/2}$ and $1h_{11/2}$ states are fragmented to a larger extent than the ground and first excited states [Qui88].

Chapter 3

Experimental Method

This chapter provides an outline of the experimental setup and procedures used in the measurement of the triple differential cross-section and analyzing power of the proton knockout reaction $^{208}Pb(\overrightarrow{p},2p)^{207}Tl$. Measurement of the quasi-free knockout of protons to the ground state in ^{207}Tl requires an experimental arrangement capable of yielding a missing mass resolution of less than 351 keV. Such is the energy resolution needed to distinguish between the knockout to the ground state and the first excited state of ^{207}Tl, as is evident from Fig. (3.1). This high resolution requirement was a central theme of the experimental preparations.

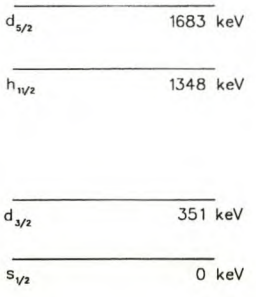

Figure 3.1: Energy levels of ^{207}Tl according to [Mar93].

The experimental work was conducted at the National Accelerator Centre (NAC)[1], Faure, South Africa, utilizing the particle beam delivered by the Separated Sector Cyclotron (SSC), the large accelerator of charged particles at NAC.

The $(\overrightarrow{p},2p)$ reaction is characterized by a three-body final state, which can be determined (for a known incident energy) through momentum and energy conservation by measuring the kinetic energies of the two outgoing protons at pre-defined detection angles. For this study a polarized proton beam of nominally 200 MeV was delivered to the magnetic spectrometer

[1]The facility has since been renamed, and is now known as *iTHEMBA LABS*.

experimental area at NAC, where the protons were detected in coincidence with a magnetic spectrometer and a detector telescope consisting of a 1000 μm Si surface barrier detector and a 15 mm N-type high purity planar Ge-detector.

3.1 General Considerations

Experimental cross-section and analyzing power measurements were performed for three angle pairs. The choice of these angle pairs was guided by the following physics requirements and practical restrictions:

1. The angle pair must be quasi-free, referring to a geometry where zero momentum of the recoiling residual nucleus, i.e. the quasi-free point, is kinematically accessible. The choice of such a geometry is advantageous because the reaction mechanism is expected to be simple and to lend itself more readily to a direct comparison with free (p,p) scattering at zero recoil than at other kinematic conditions. Furthermore, the triple differential cross-section of the s-state knockout is at a maximum near zero-recoil.

2. The finite thickness of the available Ge-detector's crystal restricts observation of protons in the detector telescope to protons with kinetic energy of less than 78 MeV. This imposes a lower limit on the angular placement of the detector telescope, since moving it to smaller forward angles would exclude data at the top of the s-state cross-section distribution.

3. The design of the scattering chamber imposed a lower limit on the angular placement of the magnetic spectrometer.

Within the above-mentioned limits the angle pairs $(\theta_{K600};\theta_{telescope}) \equiv (22°, -62.3°)$, $(30°, -54.6°)$ and $(35°, -49.7°)$ are representative of the range of measurable geometries. The minus sign for $\theta_{telescope}$ indicate an angle on the opposite side of the proton beam from θ_{K600}. Due to hydrogen contamination of the ^{208}Pb targets (a natural consequence of the manufacturing procedure of the Pb-target) modifications to the above-mentioned angle pairs were however required. Hydrogen contamination of the target is problematic since the comparable kinematics of the $^{208}Pb(p,2p)$ quasi-free knockout events and elastic scattered $H(p,p)$ events, coupled with the finite angular resolution of the detector, cause their coincidence geometries to overlap to a

large extent. Combined with the cross-section of elastic scattering, which is orders of magnitude higher than that of quasi-free knockout, the reaction tails caused by detecting $H(p,p)$ events in the Ge-detector totally obscures the $(p,2p)$ events in a limited energy range. For two of the angle pairs the problem was minimized by slightly decreasing θ_{K600}, and hence also the solid angle overlap. The third angle pair was arbitrarily kept as purely quasi-free. Measurements were thus performed for the following angle pairs: $(22°, -62.3°)$, $(28°, -54.6°)$ and $(33°, -49.7°)$.

The experimental results were obtained in two different experiments (PR15c and PR15d) conducted at NAC. Because of the multi-disciplinary nature of NAC, nuclear physics research is conducted over weekends, with proton and neutron therapy as well as isotope production performed during the week. The first measurement, yielding results for the angle pair (28°,-54.6°) [Cow97], was therefore performed over a period of four weekends in April 1998. In the second and third quarter of 2000 a more ambitious project [Nev99], conducted over 9 weekends using a different scattering chamber and also a thinner ^{208}Pb target, led to the measurement of the remaining two angle pairs. Where not otherwise noted, experimental details and methods apply to both the 1998 and 2000 experiments.

3.2 Polarized Proton Beam

A layout of the experimental facilities at the NAC is presented in Fig. (3.2). The polarized proton beam from the polarized ion source (PIS) was injected into the SPC2[2] and accelerated to an energy of 8.3 MeV. The beam was then transferred to the Separated Sector Cyclotron (SSC) where it was accelerated to an energy of 200.5±0.5 MeV for the 1998 study and 202±0.5 MeV in the 2000 study. By transferring the beam via the X, P and S beam-lines the polarized proton beam was delivered to the spectrometer experimental area.

Due to the high energy resolution requirements of this experiment, a very small energy spread in the proton beam was required. Without taking any specific precautions the energy spread in the 200 MeV proton beam is estimated to be ~380 keV. Ion-optics calculations of the beam transport system indicate that closing two emittance limiting slits in the X and P-lines (namely 9X and 1P), coupled with appropriate energy settings of quadrupole magnets in front of these

[2]One of two Solid Pole injector Cyclotrons (SPC) at NAC.

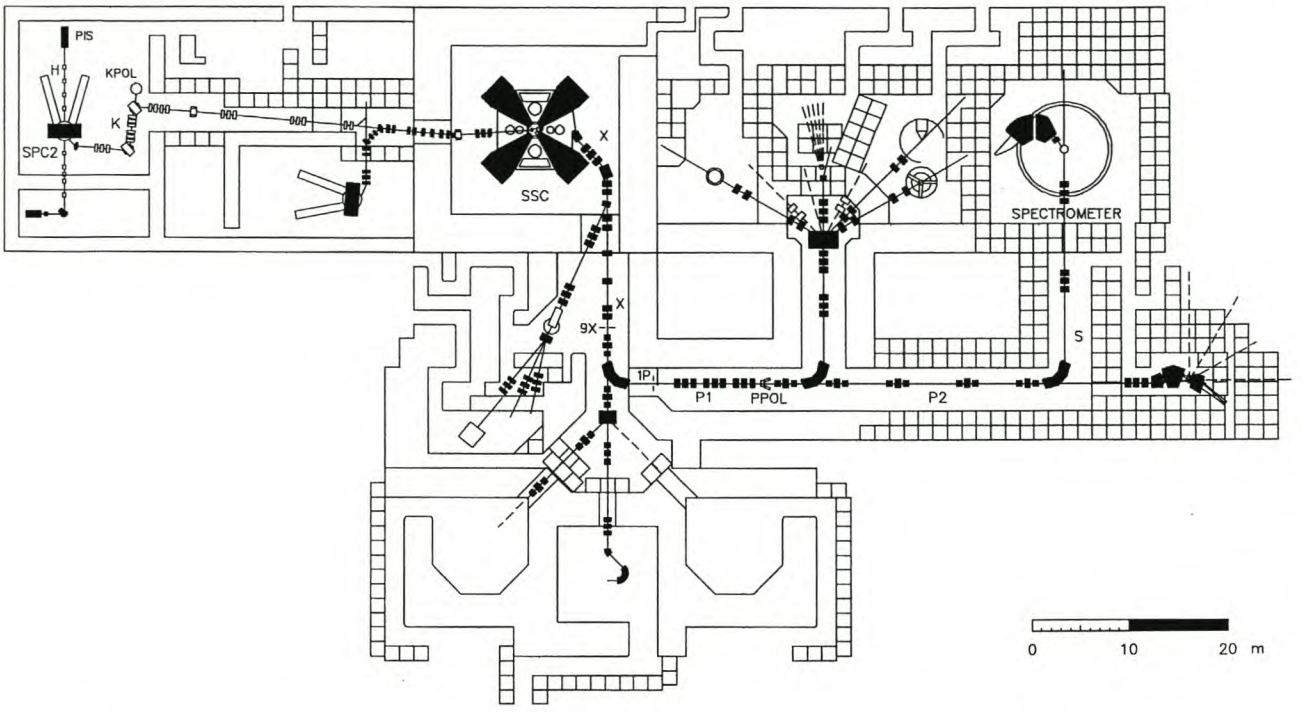

Figure 3.2: A layout of the experimental facilities at the National Accelerator Centre.

slits, would minimize the energy spread in the beam [Fou00]. The actual size of the openings, on average 2.5 mm, was in the end dictated by balancing gain in beam energy resolution with the inevitable loss in beam current on closing the slits. This resulted in a maximum beam intensity of ~30 nA with a corresponding energy spread estimated to be 125 keV.

The proton beam was polarized in a plane normal to the scattering plane, with the polarization direction flipped every 10 seconds. Due to various improvements made to the polarized ion source the absolute value of the polarization degree obtained in the 2000 experiment was higher than the 1998 experiment, although differences between the up and down polarization degrees and variation of this difference with time still proved to be problematic. These results will be presented in the following section.

3.3 Beam Polarization Measurement

Beam polarization was measured utilizing scattering from targets with known values for the analyzing power A_y. At the National Accelerator Centre beam polarization can be determined in either the low energy polarimeter (KPOL) between the SPC2 and the SSC, or the high

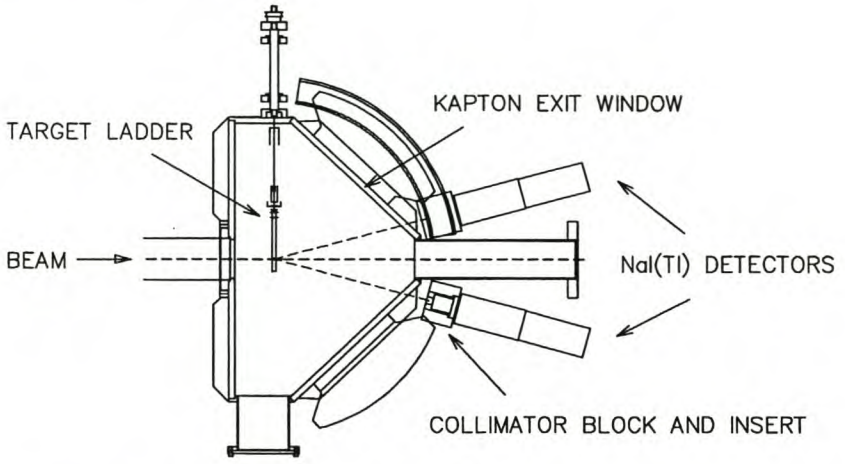

Figure 3.3: Experimental layout of the P-line polarimeter.

energy polarimeter (PPOL) in the P-line, the high energy beam-line leading from the SSC to the various experimental halls (refer to Fig. (3.2)). The P-line polarimeter was routinely used during experimental runs to determine beam polarization, while the K-line polarimeter was used by the beam operators to optimize the degree of polarization prior to the experimental runs of each weekend. Deterioration of beam quality precluded continuous monitoring of beam polarization, resulting in periodic measurements as described in section 3.7.

The K-line polarimeter consists of a gas cell containing high purity helium gas with entrance and exit windows of Havar. Two 150 μm Si-detectors are positioned at $\theta_{lab} = 110°$. The energy loss in the 6 micron Havar of the 8.3 MeV proton beam incident on the He-target results in 8.14 MeV effective proton incident energy. The analyzing power for the scattering of 8.14 MeV protons from He at $\theta_{com} = 123.7°(\equiv \theta_{lab} = 110°)$ is known to be 0.95 [Sch71]. For further detail refer to the thesis of Steyn [Ste97].

The P-line polarimeter-setup, shown in Fig. (3.3), consists of a 75 μm thick $(CH_2)_n$ foil mounted on a target ladder situated in a dedicated scattering chamber in the P-line. Two NaI(Tl) detectors, collimated with 5 cm thick brass collimator blocks and appropriate inserts, are positioned at θ_{lab} =18°, separated from the scattering chamber vacuum by 75 μm thick $(CH_2)_n$ exit windows. The $^{12}C(p,p)$ elastic scattering reaction at 200 MeV with A_y=0.98 [Mey82] is used to determine the beam polarization.

The same electronic setup and data acquisition system, easily interchangeable, was used for both polarimeters (since the location of the K-line polarimeter makes simultaneous mea-

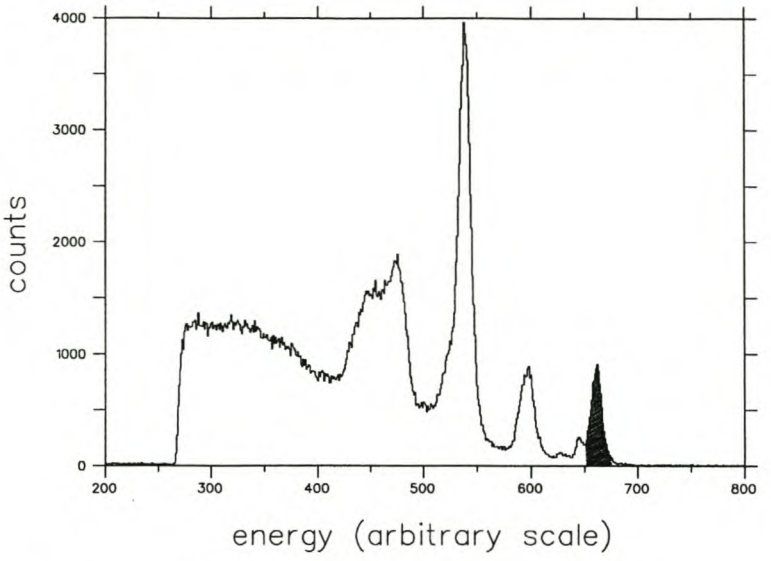

Figure 3.4: A typical energy spectrum for the P-line polarimeter detectors. The selected region indicate the events used for beam polarization measurements.

surements impossible). The resulting energy spectrum for the P-line polarimeter is shown in Fig. (3.4), displaying the ground state and 4.4 MeV and 9.64 MeV excited states of ^{12}C. The broad peak to the left of these states originates from elastic scattering from hydrogen, and the small peak at the low-energy shoulder of the elastic ^{12}C peak is attributed to scattering off the collimators in the polarimeter setup.

In the idealized scenario where $p_\uparrow = p_\downarrow = p$ the beam polarization normal to the scattering plane can be established from the known analyzing power A_y via the following equations [Hae74]:

$$\begin{aligned} p &= \frac{\epsilon}{A_y}\,, \\ \text{where} \quad \epsilon &= \frac{r-1}{r+1}\,, \\ \text{and} \quad r &= \left(\frac{L_\uparrow R_\downarrow}{L_\downarrow R_\uparrow}\right)^{1/2}. \end{aligned} \tag{3.1}$$

Typically $L_{\uparrow(\downarrow)}$ denotes the number of events registered in the left detector associated with incoming particles with upward (downward) beam polarization. The use of this so-called cross-ratio formalism is preferred since it cancels the influence of instrumental asymmetries. However, for the more realistic case where $p_\uparrow \neq p_\downarrow$ the polarization of the spin-up and spin-down beams are determined independently, taking first order instrumental asymmetries into account as follows:

$$p_{\uparrow(\downarrow)} = \frac{1}{A_y}\left(\frac{L_{\uparrow(\downarrow)} \cdot unpol - R_{\uparrow(\downarrow)}}{L_{\uparrow(\downarrow)} \cdot unpol + R_{\uparrow(\downarrow)}}\right). \tag{3.2}$$

The parameter $unpol = \frac{R_{unpol}}{L_{unpol}}$, where $R(L)_{unpol}$ is the amount of events in the right (left) detector for an unpolarized beam, provides a measure of the asymmetry of the polarimeter setup, mainly due to an off-centre beam-spot. The error in the average beam polarization as defined in Eq. (3.1), neglecting uncertainty of A_y, is given by

$$\frac{\Delta p}{p} = \frac{1}{A_y} \cdot \frac{r}{r^2 - 1} \cdot \left[\frac{1}{L_\uparrow} + \frac{1}{R_\uparrow} + \frac{1}{L_\downarrow} + \frac{1}{R_\downarrow} \right]^{1/2} . \tag{3.3}$$

This value was taken to approximate the polarization error in $p_\uparrow$ and $p_\downarrow$, and ranged between 0.5 and 1 %. Beam polarization averaged $\sim$ 70% in 1998, and was improved to an average of $\sim$ 80% for the 2000 experiment. The results of the periodical measurements for both experiments are summarized in Fig. (3.5).

3.4 Targets and Scattering Chamber

As noted earlier, the main differences between the experimental setups of the 1998 and the 2000 experiments concerns the use of different scattering chambers and target thicknesses.

The original scattering chamber used in 1998, of relatively simple design with a diameter of 302 mm, was previously used in spectrometer singles measurements and provided for only minimal angular movement of the spectrometer arm. The size of the *Ge*-detector and associated cryostat as well as the requirement that the *Si*-detector should not be positioned too close to the target necessitated the installation of the whole detector telescope on the outside of the scattering chamber. A fixed exit port at 58°, with an exit window of 75 μm kapton foil, was therefore added. The fixed telescope position severely limited the ability to calibrate the *Ge*-detector, as will be discussed in section 4.3.2.

In 1999 NAC acquired a 524 mm diameter scattering chamber from the decomissioned electron accelerator facility at NIKHEF, where it was used in a dual magnetic spectrometer system. After appropriate modifications it replaced the 302 mm scattering chamber in the spectrometer vault. Among its advantages over the old chamber are the smaller forward-angle limit for positioning of the magnetic spectrometer (22° compared to 26° with the previous scattering chamber), movable exit ports on both sides of the beam as well as its larger diameter. This much bigger scattering chamber enabled the placement of the *Si*-detector inside the scattering

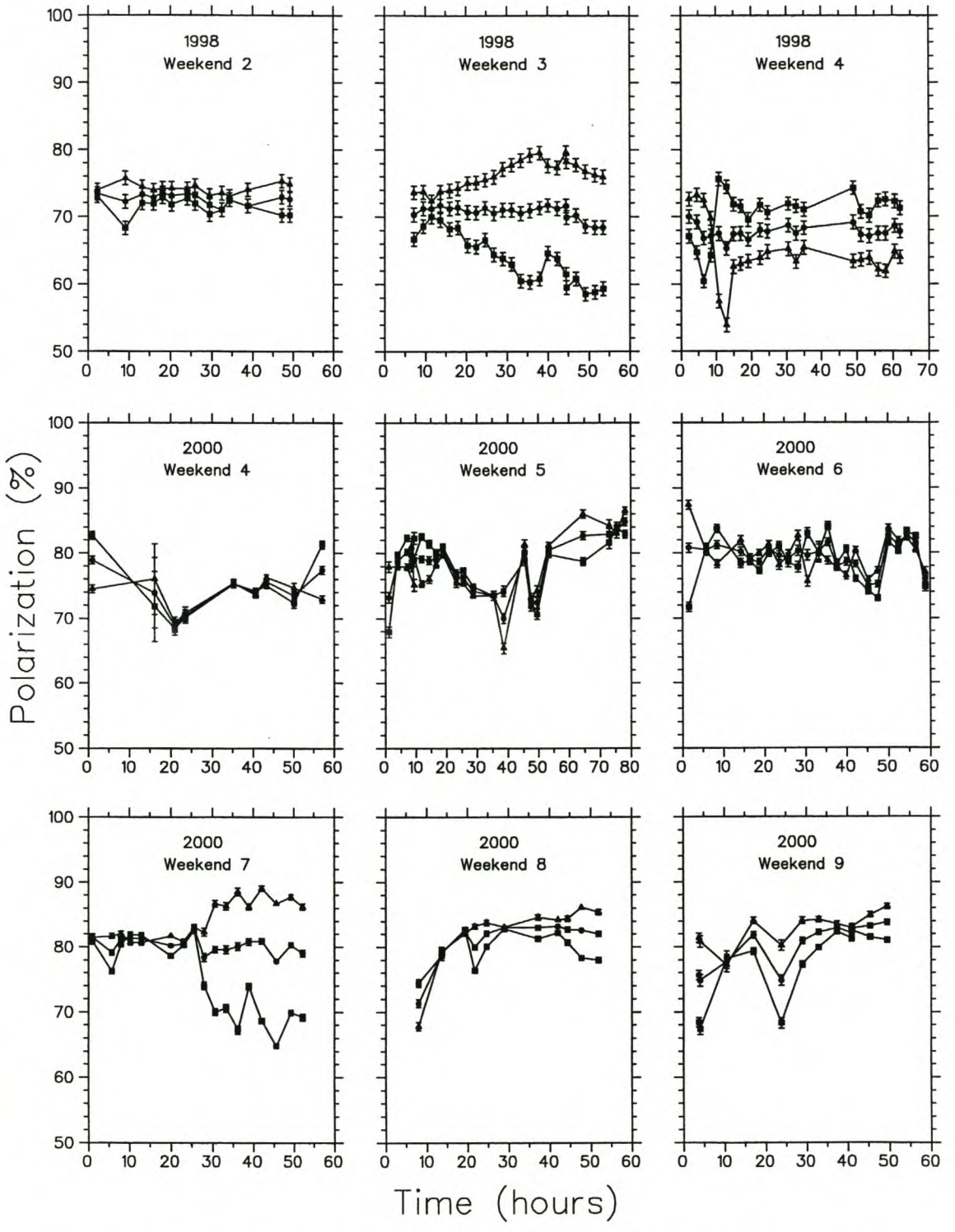

Figure 3.5: Polarization statistics for the 1998 and 2000 experiments, showing the average (circle) beam polarization as well as the upward (triangle) and downward (square) beam polarizations.

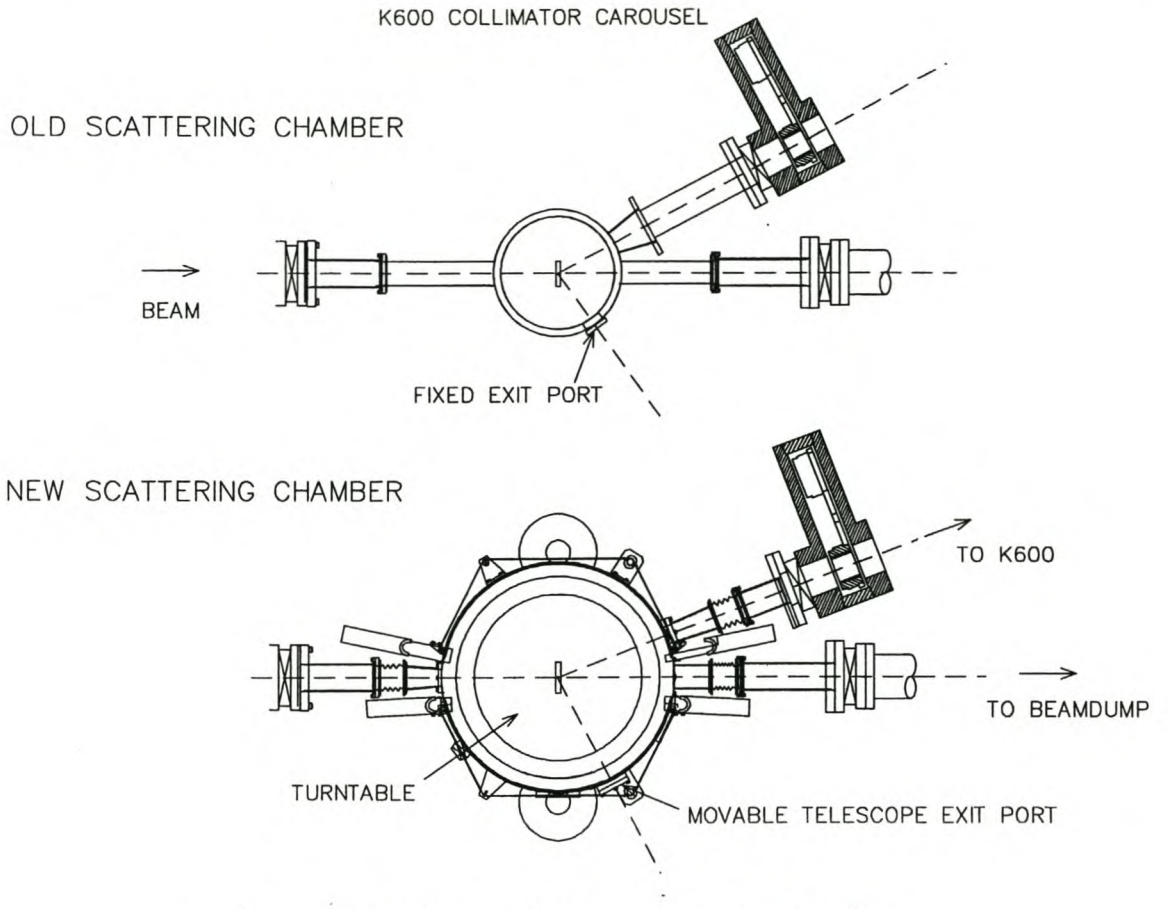

Figure 3.6: A layout of the two scattering chambers

chamber, resulting in thinner dead layers (refer to section 4.4.1), and was also instrumental in the proper calibration procedure for the *Ge*-detector. Fig. (3.6) illustrates some of the differences between the scattering chambers.

Two self-supporting isotopically enriched ^{208}Pb target foils of different thicknesses were used in this study. The thick ^{208}Pb target, used in both the 1998 and 2000 experiments, was 98% isotopically enriched with a thickness of 7.7 ± 0.54 mg·cm^{-2}. The thinner 99% isotopically enriched ^{208}Pb target, used exclusively in the 2000 experiment, had a thickness of 0.74 ± 0.04 mg·cm^{-2}. The thinner target was acquired after it became apparent from the results of the 1998 experiment that the target thickness negatively affects the experimental energy resolution. These effects are discussed in more detail in Appendix B.

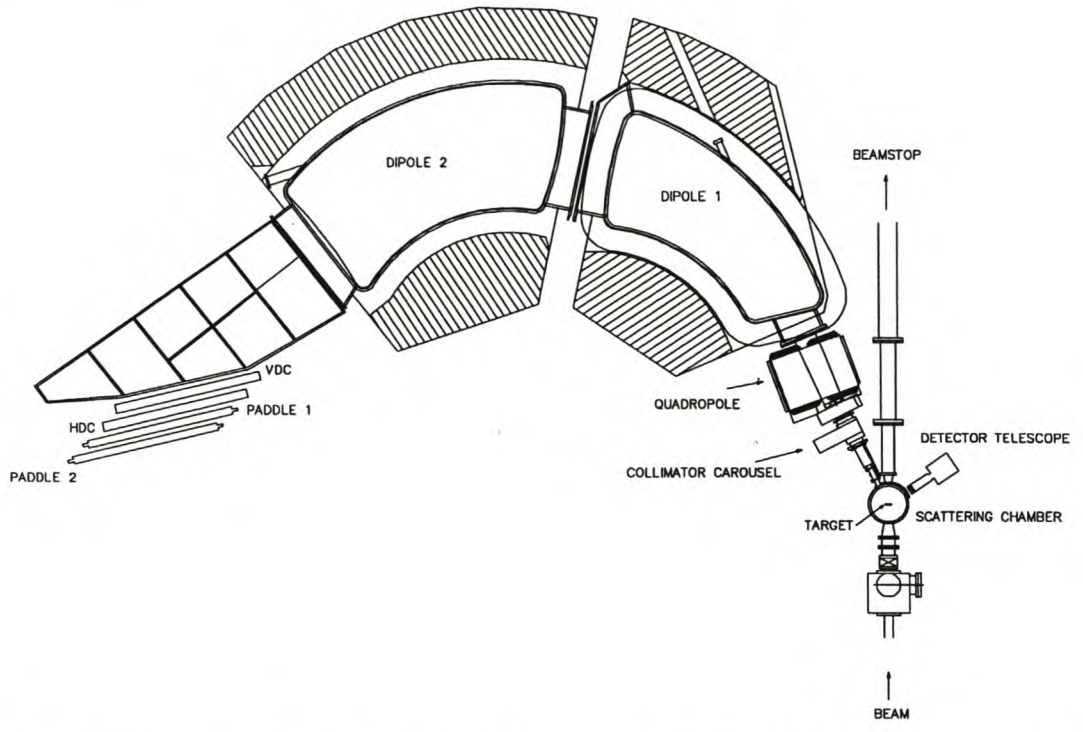

Figure 3.7: An overview of the detector configuration, displaying the K600 with its associated focal-plane detectors and the detector telescope.

3.5 The Detector Setup

In a previous study of proton knockout from ^{208}Pb, coincidence measurements were performed with NaI(Tl) detectors [Cow95], resulting in missing-mass resolution of approximately 2 MeV. The high energy resolution requirements of this study led to the utilization of the K=600 magnetic spectrometer in coincidence with a high purity Ge-detector, the stopping E detector in the $\Delta E - E$ detector telescope. A layout of the experimental setup is displayed in Fig. (3.7).

3.5.1 The K=600 Magnetic Spectrometer

The K=600 QDD magnetic spectrometer[3], from here on referred to as the K600, served to momentum analyze the high energy protons on the beam-left side of the coincidence setup. The magnetic components of the K600 used to achieve dispersion of the incident flux of charged

[3]The energy constant K, defined as $K = \frac{mE}{q^2}$, provides a measure of the maximum value for the combined quantities of mass m (units of proton mass), charge q (units of proton charge) and kinetic energy E (MeV) a magnetic device is designed for.

particles are the two dipole magnets, with the quadrupole used for vertical focusing. Two trim coils, located inside the dipoles, are used to achieve the final focusing at the focal-plane. The so-called K-coil, a quadrupole focusing element, is used to adjust for first-order kinematic variations of momentum with angle $(x \mid \theta)$ (notation as used in [Eng81]). The H-coil, a hexapole focusing element, is used to correct for $(x \mid \theta^2)$ abberations.

The solid angle acceptance of the K600 of 5.76 msr was defined by a collimator of radius $r = \frac{63}{2}$ mm, situated in front of the quadrupole magnet in a collimator carousel, at a distance of 735.5 mm from the target centre. The maximum uncertainty for the solid angle subtended by the spectrometer, due to uncertainties in the collimator radius and distance from the target, is estimated to be 0.3% [New96]. The finite size of the beam-spot on the target (a circle of radius $\sim$ 1 mm) had a negligible effect on the solid angle error.

The region of measurable proton energies in the detector telescope defined the momentum range over which the K600 was used to detect the coincident protons. The limited size of the momentum bite covered by the K600, translated to an energy range of typically 20-25 MeV, required measurements for up to three different field settings in order to cover the whole energy range of interest. The size of the momentum bite follows from $\Delta p = p_0 \cdot \frac{x}{D}$, with x the length of the focal-plane, D the dispersion and p_0 the reference momentum for a specific spectrometer setting. Since the detector was operated in the medium dispersion mode, where x=78 cm and D=8.4 m, it follows that $\frac{p_{max}}{p_{min}} = 1.09$. The field-sets as used in the $(p, 2p)$ measurements are listed in table 3.1. Calculations of these field-sets were based on previous K600 calibration parameters, with the listed values for $p_{min/max}$ and $E_{min/max}$ representing the boundaries of the central 80% of the focal-plane sensitive area. The calculation of the current-settings for the dipole magnets for a specific reference momentum is done by means of a simple parameterization modeling of the two-dimensional median plane field maps of the spectrometer magnets [New96].

Position sensitive detectors in the focal-plane consisted of two multi-wire drift chambers and a pair of plastic scintillation detectors. Drift chambers are excellent counters for providing position sensitive information for detection systems such as magnetic spectrometers, because of its good position resolution, high counting-rate capability and uniformity over the sensitive area. Since the anode plane of the chamber is placed such that it coincides with the focal-plane of the magnetic spectrometer (to first order, keeping in mind that the real focal-plane is not a

Angle Pair	p_0 (MeV/c)	p_{min} (MeV/c)	p_{max} (MeV/c)	E_0 (MeV)	E_{min} (MeV)	E_{max} (MeV)
(22°,-62.3°)	543.41	516.57	556.95	146.00	132.80	152.85
	595.46	558.23	603.46	173.00	153.50	177.30
(28°,-54.6°)	504.43	472.89	511.21	127.00	112.43	130.22
	539.41	505.68	546.65	144.00	127.59	147.63
	576.58	540.53	584.33	163.00	144.56	167.07
(33°,-49.7°)	510.74	478.80	517.60	130.00	115.11	133.29
	551.35	516.87	558.75	150.00	132.95	153.77

Table 3.1: Calculated K600 field-sets for the various angle pairs.

flat surface), it can be established by interpolation to a high degree of accuracy where a particle traversed the focal-plane, thus providing accurate momentum information.

Drift chambers of two different geometric configurations were utilized. The Vertical Drift Chamber (VDC) was used to determine position information along the length of the focal-plane, and the Horizontal Drift Chamber (HDC) was used to measure particle position in the vertical of the focal-plane. This served as an indication of the quality of the incident beam.

The VDC and HDC, both developed and built at NAC, consist each mainly of two high-voltage cathode planes with a signal-wire anode plane midway between them. A cross-sectional view of the VDC is shown in Fig. (3.8). Two 25 μm thick mylar planes are used to isolate the interior of the VDC from atmosphere. The volume between the two cathode planes is filled with gas mixture of 90% Ar and 10% CO_2. The cathode planes are made of 27 μm thick aluminum foil separated by a distance of 16 mm. A negative high voltage of 3800 V was applied to these planes. The signal-wire plane of the VDC consists of 198 signal wires, 25 μm thick, spaced 4 mm apart and made from gold-plated tungsten. These signal wires are kept at 0 V potential. Interspersed between these wires are 199 so-called guard wires, which provide field shaping [Ber77] and define cells, associated with each signal wire, of about 4 mm. These wires are made of 50 μm thick gold-plated tungsten, also spaced 4 mm apart. A negative voltage of 500 V was applied to the guard wires. The HDC is of a similar make-up, with 16 signal wires and 17 guard wires in horizontal planes opposed to the 198 and 199 vertical wires of the VDC.

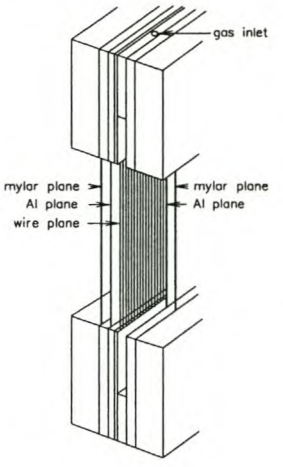

Figure 3.8: The main components of the VDC.

Two 122 cm × 10.2 cm plastic scintillator detectors (also referred to as *paddle* detectors because of their geometry) with a photo multiplier (PM) tube on each end, the first 3.18 mm and the second one 12.7 mm thick, were positioned close to the focal-plane just downstream from the drift chambers. The main purpose of these detectors were to provide event trigger signals and also to aid in particle identification through $\Delta E - \Delta E$ particle identification spectra.

3.5.2 Detector Telescope

The $\Delta E - E$ detector telescope consisted of a Ge stopping E detector and a Si ΔE detector. The high purity n-type planar Ge-detector (Eurisys Mesures *EGP 800-15-R*) consists of a 15 mm thick cylindrical Ge crystal with a 16 mm radius, separated from atmosphere by a 0.125 mm Be entrance window. The finite thickness of the crystal limits the Ge-detector's ability to detect protons to a maximum energy of $\sim$ 78 MeV, thus restricting the detector telescope to the measurement of the low energy protons in the coincidence setup.

For the ΔE detector a 1000 μm thick Si surface barrier detector (Ortec *TB-020-300-1000*) with an effective area of $\sim$ 300 mm^2 was used. The choice of the thickness of the Si-detector was guided by the need to cleanly separate the proton locus from the adjacent deuteron locus in the ΔE-E particle identification spectrum. Three different Si-detectors were utilized during the course of the measurements.

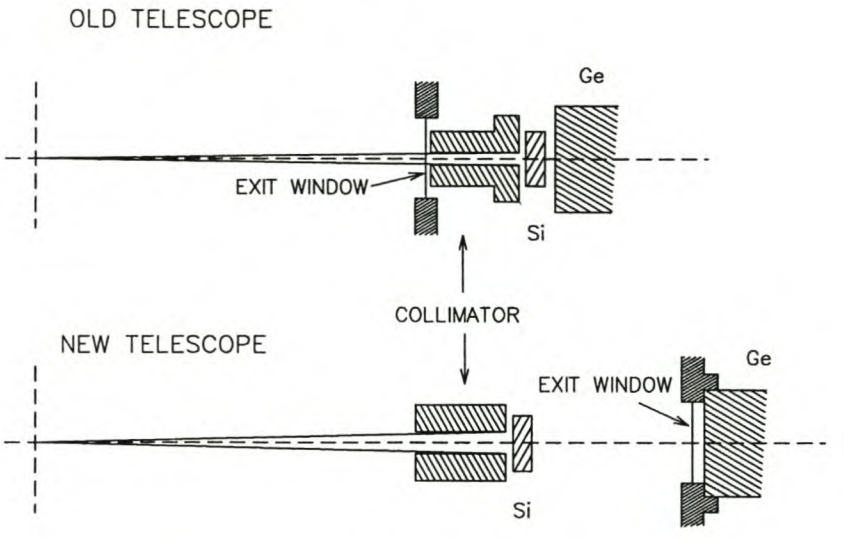

Figure 3.9: A graphic representation highlighting the differences between the old (1998) and new (2000) telescope setups.

As was mentioned before, for the 1998 experiment the telescope as a whole was mounted on the outside of the scattering chamber against the kapton exit window. A schematic of the mounting is showed in Fig. (3.9). The solid angle of 2.5 msr was defined by a 10.95 mm diameter brass collimator with a thickness of 42.2 mm, the back plane of which was situated at 194.2 mm from the centre of the target ladder. Helium gas was trickled through the region between the kapton exit window and the Si-detector in order to minimize energy loss of the protons on the outside of the scattering chamber. Uncertainty in the detector telescope solid angle was estimated to be 1.5%. Again it was found that the finite size of the beam-spot did not have any significant effect on the solid angle error.

As part of the improvements to the experimental setup in the 2000 experiment, the Si-detector was mounted on the turntable inside the new bigger scattering chamber, with the Ge-detector mounted on the outside of a kapton exit window, again with a flow of helium gas through the region between the Be entrance window of the Ge and the scattering chamber exit window. The solid angle of 5.59 msr, within an uncertainty of 1.2%, was defined by a 48.1 mm thick brass collimator block with radius 16 mm situated in front of the Si-detector as showed in Fig. (3.9), the backplane of which was 189.6 mm from the target centre.

Semiconductor detectors such as the *Ge*-detector are susceptible to performance degradation caused by radiation damage to the crystal structure of the detector crystal, mainly attributable to the presence of fast neutrons in the radiation flux [Kno89]. For this reason the *Ge*-detector was annealed on occasions during the experiment. Frequent testing with a ^{152}Eu γ-source indicated that the detector performed consistently throughout both experiments. Radiation damage to the *Si*-detector required replacement on occasion.

3.6 Electronics and Data Acquisition

Standard NIM and CAMAC fast electronics hardware were used to process the timing and energy signals from the detectors. A VME front-end [Yo94] served as the interface between the CAMAC system and a dedicated VAX data acquisition computer. A VAXstation 4000 workstation was used for online data acquisition using the XSYS analysis software [Pil89].

Two event streams were acquired; event 0 denoting a valid K600 event (singles *or* coincidence), and event 1 denoting a telescope singles event. Details on the event-trigger and timing electronics are given below. Standard techniques were employed in the electronic setups of the current integration, pulsers, clock and for the linear electronics of the telescope and scintillators. Further details on these techniques can be found in the thesis of Förtsch [For92].

An event-trigger for event 0 was generated by the electronics in the spectrometer vault as shown in Fig. (3.10). Coincidence was established between the two scintillator detectors in the focal-plane, where the mean-timer ensured independence of the timing of the paddle signal with position along the focal-plane. This paddle coincidence signal was sent to the data-room coincidence electronics (as P1·P2 in Fig. (3.11)) to establish whether the spectrometer event was in coincidence with a detector telescope event. Coincidence between the ΔE and E detectors, a prerequisite for a valid telescope event, was established from the timing output signals from the pre-amplifiers of the telescope detectors. An event 0 event-trigger was then generated by the spectrometer timing electronics in the absence of a fast-clear signal. The fast-clear signal, generated by the data-room electronics, denoted either a non-coincidence or a non-prescaled (prescaling by a factor of 100) K600 singles event.

An event-trigger for event 1 was generated for telescope singles as shown in Fig. (3.11). As for

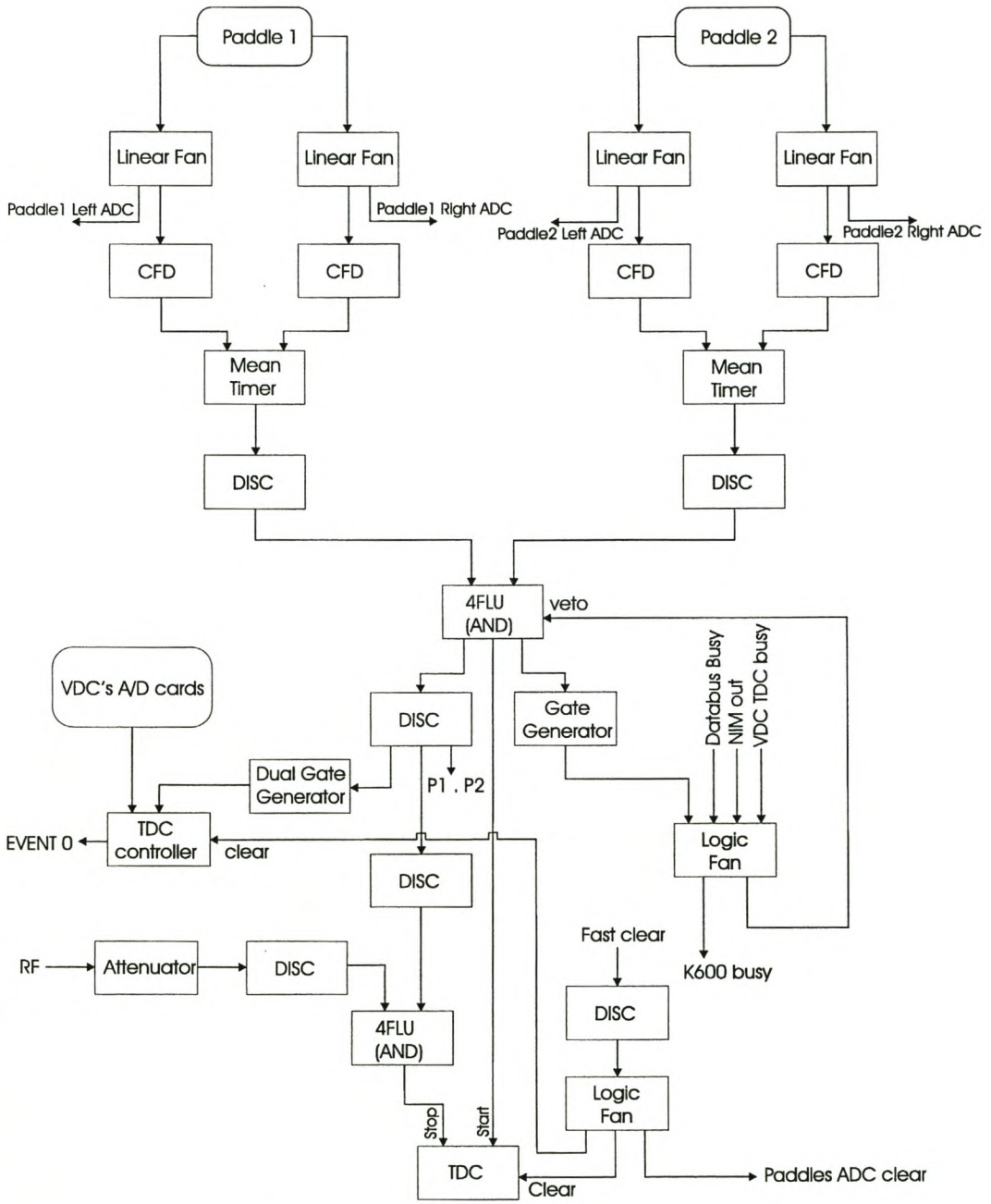

Figure 3.10: Event-trigger and timing electronics for the magnetic spectrometer.

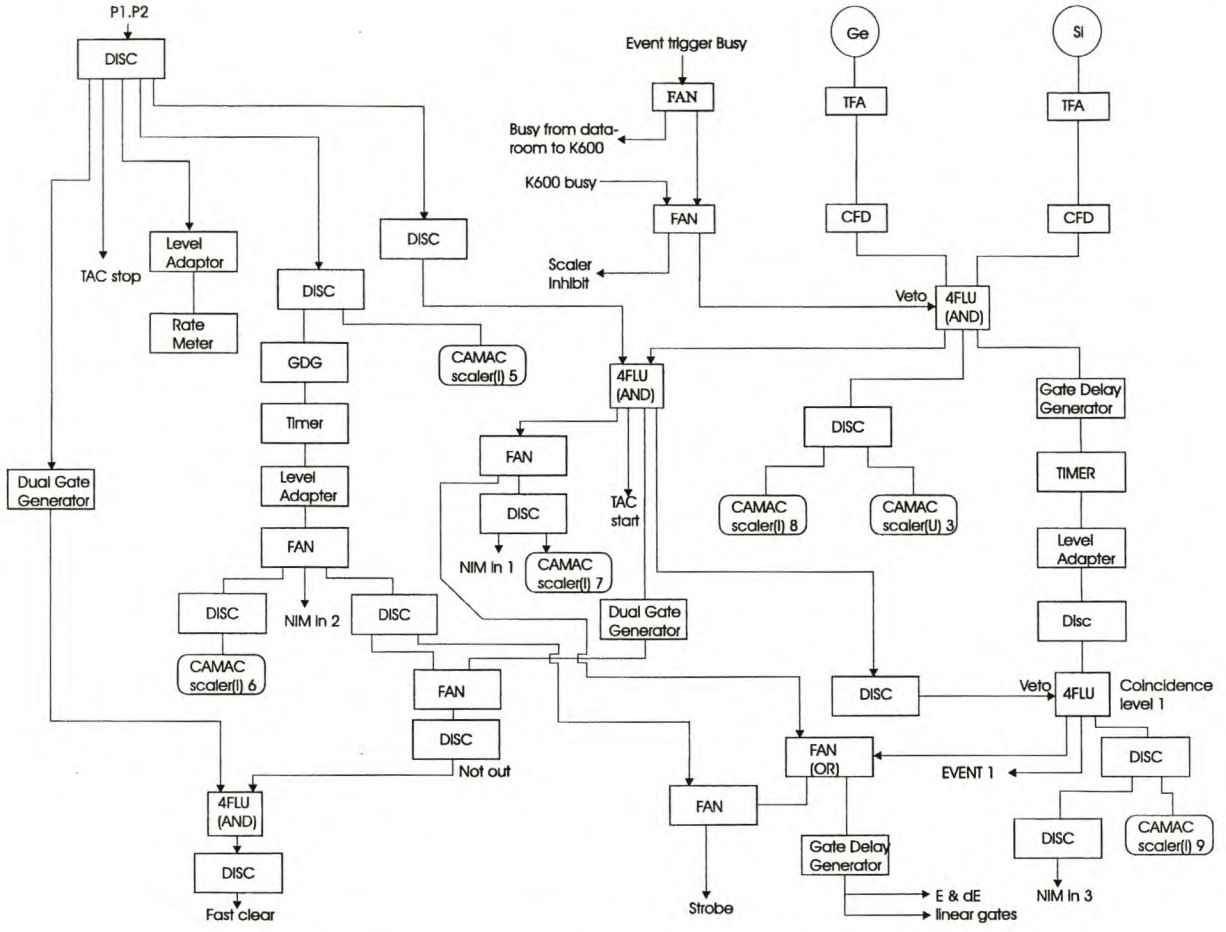

Figure 3.11: Coincidence electronics in the data-room.

the spectrometer singles only a fraction (5%) of the telescope singles events were accumulated.

Beam packets of the 200 MeV proton beam at NAC are separated by 38.5 ns. In order to establish coincidence between the spectrometer and the telescope events the narrow logic pulse from a telescope event should arrive at the logic unit during the time that the wide logic pulse from a paddles event is present. The spectrometer and telescope event signals were used respectively as the stop and start signals of a time-to-analog (TAC) converter module in order to generate a coincidence timing spectrum. Different types of coincidences, i.e. prompt and delayed coincidences, manifested as different peaks in the timing spectrum. Prompt coincidences contain true plus accidental events, whereas delayed coincidences are purely accidental events.

A relative time-of-flight (TOF) measurement used for particle identification (refer to section 4.1) was generated with the electronic setup of Fig. (3.10). A TDC was used to digitize the interval between a paddle coincidence signal and a SSC RF signal.

Signals from the drift chambers were processed with a dedicated CAMAC data acquisition system. Each signal wire was connected to a pre-amplifier, a discriminator and a TDC (time-to-digital converter) via 16-channel drift-chamber-mounted pre-amplifier/discriminator (A/D) cards and 32-channel time digitizer modules (TDM). Drift-times for each of the signal wires were determined with the TDM's, where each channel represented a different signal wire. Time measurement was started when a signal was registered on a signal wire, and stopped on the receipt of an experimental common signal, obtained by delaying the output pulse from the logic unit that established paddle coincidence.

Accurate measurement of relative drift-times in the VDC necessitate that all the TDC channels on the TDM's respond identically to a fixed time interval. To insure the alignment of the TDC values an internal and external *auto-trimming* procedure was required. For internal auto-trimming the pedestals and gains of all the TDC channels are trimmed to the same value. In external auto-trimming all variations in times due to differences in the VDC-mounted A/D cards and differences in the cable lengths connecting these cards with the TDM's are calibrated out. Problems were experienced with the auto-trimming for weekend 4 of the 2000 experiment, where due to bad TDC cards, four wires yielded bad drift-times. This resulted in lower than usual efficiencies for the focal-plane detector system. For the rest of the weekends of the 2000 measurement problems were experienced with the auto-trimming of the TDC channel of wire no. 179. This was corrected for in the data acquisition software by artificially aligning the drift-time measurement of wire no. 179 with that of the rest of the wires.

3.7 Experimental Procedure

With the Si-detector and the spectrometer setup as described in the previous sections and the necessary electronic circuits put in place, the scattering chamber was pumped down to the required vacuum ($\sim 10^{-5}$ mbar). Inside the scattering chamber was the target ladder containing the following targets: a ^{208}Pb target used for the quasi-free data acquisition, a $(CH_2)_n$ target used for the setup procedures of the electronics, an empty target frame used for beam halo tuning, an Al_2O_3 scintillation target used for beam positioning and a ^{12}C target for calibration purposes.

The 200 MeV proton beam was positioned in the centre of the target with the help of the scintillating properties of the Al_2O_3 target. This process was monitored by viewing the scintillation target with a closed circuit video camera positioned at one of the ports of the scattering chamber. Beam positioning was considered successful when the beam passed cleanly through the 3 mm diameter hole of the target. Beam halo, secondary particles originating from scattering events in the beam-pipe elements upstream from the target, was minimized with the help of the empty frame by tuning the proton beam until the count rate of the paddles reached a minimum. This was done with the field-setting of the K600 tuned for measurement of protons in the continuum region. It was considered adequate if the count rate with the empty target amounted to less than 5-7% of the value obtained when the ^{208}Pb-target was put in the in-beam position. Although high, considering the small momentum bite viewed by the K600, this was considered adequate since halo contribution to the background of an exclusive measurement is highly unlikely to be problematic.

At this point a look-up table for the calculation of focal-plane co-ordinates was generated from the average drift-time spectrum associated with inelastically scattered protons from the $^{12}C(p,p')$ reaction at 200 MeV (see section 4.2.1 for a more detailed discussion).

Using the elastic scattered protons off the ^{208}Pb target the spectrometer resolution was optimized by remotely adjusting the currents of the H and K-coils. This was done by examining the two dimensional spectrum of the time-of-flight (TOF) of the scattered protons plotted as a function of focal-plane position. With the resolution of the spectrometer properly optimized the focal-plane position of events associated with the elastic peak in the $^{208}Pb(p,p')$ spectrum should not be dependent on the time-of-flight of the particle, or equivalently the corresponding track through the spectrometer.

Finally the K600 was calibrated by means of $p+^{12}C$ elastic and inelastic scattering. Because of the relatively low mass of the ^{12}C target a slit collimator was used in order to minimize kinematic spread and thus peak position uncertainty in the focal-plane.

Only after the initial beam tuning procedure and calibration and optimization of the spectrometer were completed was the Ge-detector added to the experimental setup. This precaution was deemed necessary in order to minimize the neutron damage sustained by the Ge-detector, especially during the process of centering the beam-spot on target. With the Ge-detector posi-

tioned at free (p,p) kinematics, the energy resolution of the coincident setup was checked with the $H(p,p)$ reaction using the $(CH_2)_n$ target. After it was clear that the resolution was adequate, the Ge-detector was placed in the quasi-free position and the coincidence data acquisition with the ^{208}Pb target could commence.

Typical experimental runs lasted two to three hours, interrupted by P-line polarization measurement runs. The accuracy of the P-line polarimeter measurements were very sensitive to excessive background events caused by the beam colliding with beam-line components downstream from the polarimeter scattering chamber. Such events could completely obscure the elastic $^{12}C(p,p)$ events. Therefore a very small beam ($\sim$ 2 nA) was utilized, and care had to be taken to stop the beam well away from the polarimeter. Only 10 nA of the available 30 nA was used for measurements conducted with the thick target, a necessary requirement in order to limit electronic dead time and also to keep the event-rate in the Ge-detector below the recommended level. The full 30 nA was used for the thin ^{208}Pb target measurements. The stability of the magnetic fields of the dipoles of the K600 was monitored throughout the experiment by means of NMR probes, and was found to be satisfactory.

Due to a threshold error (which was only discovered in replay) in the electronics of the Si-detector setup for the experiment with the thin ^{208}Pb-target, cross-sections for the separated $3s_{1/2}$ and $2d_{3/2}$ states could not be extracted for the thin target measurements for the angle pair $(22°, -62.3°)$. As was confirmed, the wrong threshold did not affect measurement of the analyzing power. Subsequent to discovering the error, some measurements were performed utilizing the thick target, resulting in cross-sections for this angle pair to be available only for the thick ^{208}Pb target. Beam-time restrictions limited measurements for the angle pair $(33°, -49.7°)$ to the use of the thick ^{208}Pb target only.

Chapter 4

Data Analysis

Off-line data analysis was performed with a VAXstation 4000 workstation using the XSYS analysis software. An outline of the event sorting algorithm used in XSYS is given in Fig. (4.1), and can be summarized as follows: for the event trigger generated by the focal-plane paddles (event 0) the first step is to distinguish between protons and other charged particles detected with the spectrometer. The two different particle identification techniques used for this purpose are outlined in section 4.1. Position and angle coordinates associated with protons passing through the focal-plane are then determined for valid VDC events (refer to section 4.2), with the position information used to establish proton momentum. Details on the calibration procedure are given in section 4.3.3. At this point it is established whether event 0 is a K600 pre-scaled singles or a coincidence event. For coincidence events telescope raw data are acquired, and protons are identified by means of standard E-ΔE methods as outlined in section 4.1. From the calibration parameters found in section 4.3.2 energies of detected protons in the telescope can be established. For true coincidences (refer to section 4.6.1) a binding energy spectrum is generated. In the binding energy spectrum (also referred to as the missing mass spectrum) coincident events are histogrammed according to the kinetic energy of the 3-body final state. Events that correspond to proton-knockout to the $3s_{1/2}$, $2d_{3/2}$, $2d_{5/2}$ and $1h_{11/2}$ states in the residual ^{207}Tl nucleus are then identified. Gates are set over the ground state and first 3 excited states, and energy-sharing distributions, i.e. the number of knockout events as a function of the energy of the protons detected in one of the detectors, are generated for these states.

The online energy resolution achieved was insufficient to fully separate the ground state of ^{207}Tl from the first excited state. An off-line peak-fitting procedure, reported on in section 4.5, was therefore engaged in to yield results for the $3s_{1/2}$ and $2d_{3/2}$ states. In section 4.6 it is shown how information about the cross-section and analyzing power for the $(p, 2p)$ reaction can be extracted from the raw energy-sharing data.

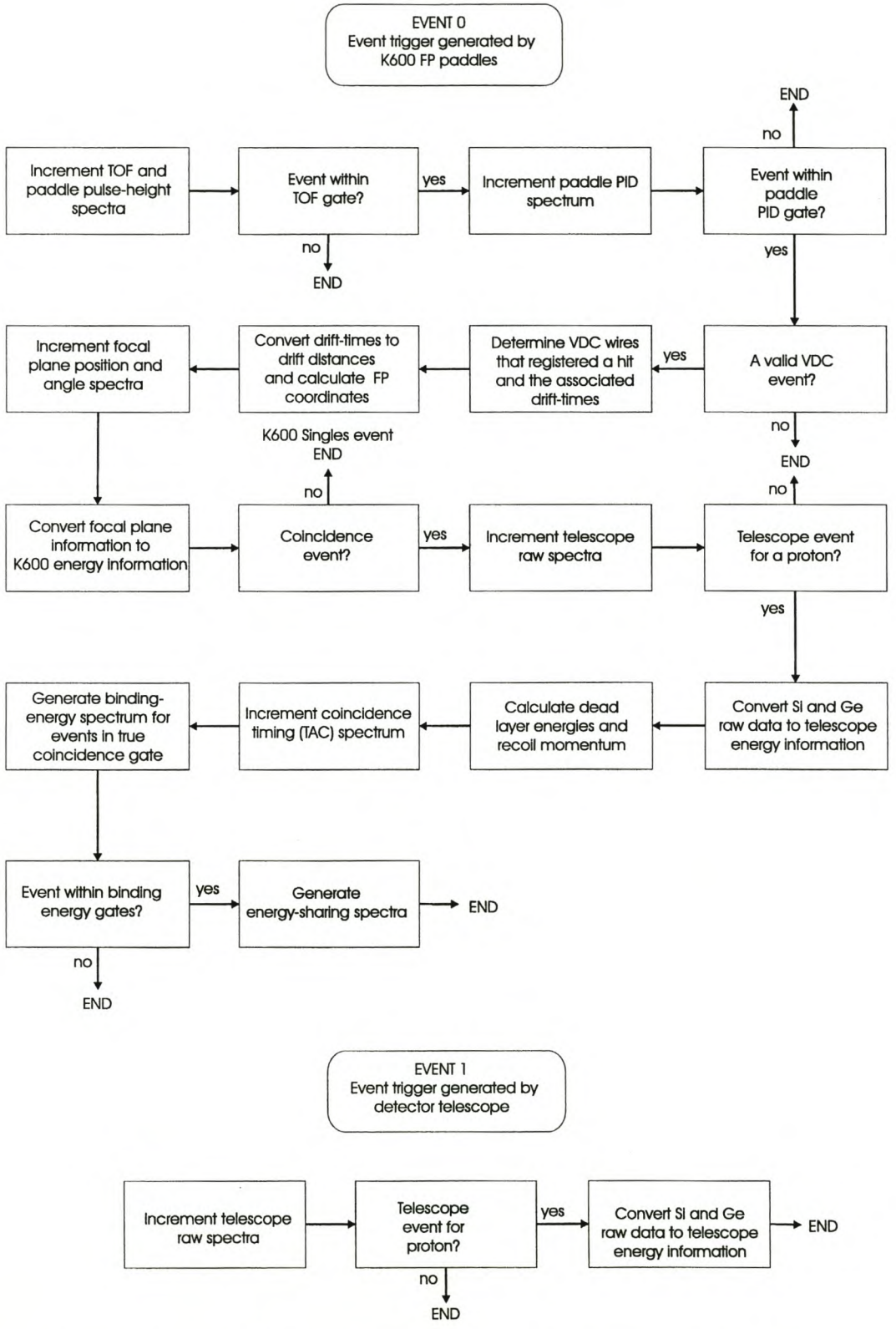

Figure 4.1: A simplified flow diagram illustrating the event sorting algorithm.

4.1 Particle Identification

Particle identification (PID) in the magnetic spectrometer can be achieved through time-of-flight (TOF) selection and a ΔE-ΔE particle identification technique. For TOF selection we consider a charged particle with mass m and charge q, moving at a velocity v through a constant magnetic field B. The radius of curvature r, and therefore the length of the flight-path of the particle through the magnetic field, is related to the rigidity of the particle ($R = \frac{p}{q}$) as follows

$$qvB = \frac{mv^2}{r} \qquad \rightarrow \qquad rB = \frac{p}{q} = R \,, \tag{4.1}$$

where p denotes the particle momentum. The minimum and maximum flight-paths associated with the angular acceptance of the spectrometer can be calculated by means of ion optical simulations [New96]. Different particles of similar rigidity therefore follow the same minimum and maximum trajectories, but due to the difference in momentum will have a different associated minimum and maximum time-of-flight (TOF), i.e. the time elapsed from the moment the particle struck the target until it is detected in the focal-plane. For a given momentum setting of the spectrometer such a TOF spectrum can be calculated, and it has been shown [New96] that clear separation between protons, helions, tritons and alphas can be achieved. In practice the TOF is measured as the relative time elapsed between a coincident paddle signal and the radio-frequency (RF) signal from the SSC. Protons can then be selected by setting a software gate on the appropriate peak in the TOF spectrum, as shown in Fig. (4.2c).

The scintillation counters in the focal-plane of the K600 can also be used for particle identification through a ΔE-ΔE spectrum. Energy-loss of particles passing through the scintillation detectors depends on the type of particle and the kinetic energy of the particle. Taking the geometrical average of the signals from the two PM tubes on the ends of each scintillator eliminates the dependence of the pulse height on the position of the event along the length of the scintillator. A clear locus, seen in Fig. (4.2a), identifies protons in the paddle PID spectrum. Both this and the TOF selection technique was employed for particle identification in the K600. Particle identification in the telescope was achieved by a standard ΔE-E PID technique, plotting the telescope events in the two-dimensional spectrum as shown in Fig. (4.2b).

The possibility exists that some protons of interest may be located outside the gates set over the proton loci. By analyzing the yield for coincident events for various gate settings this was

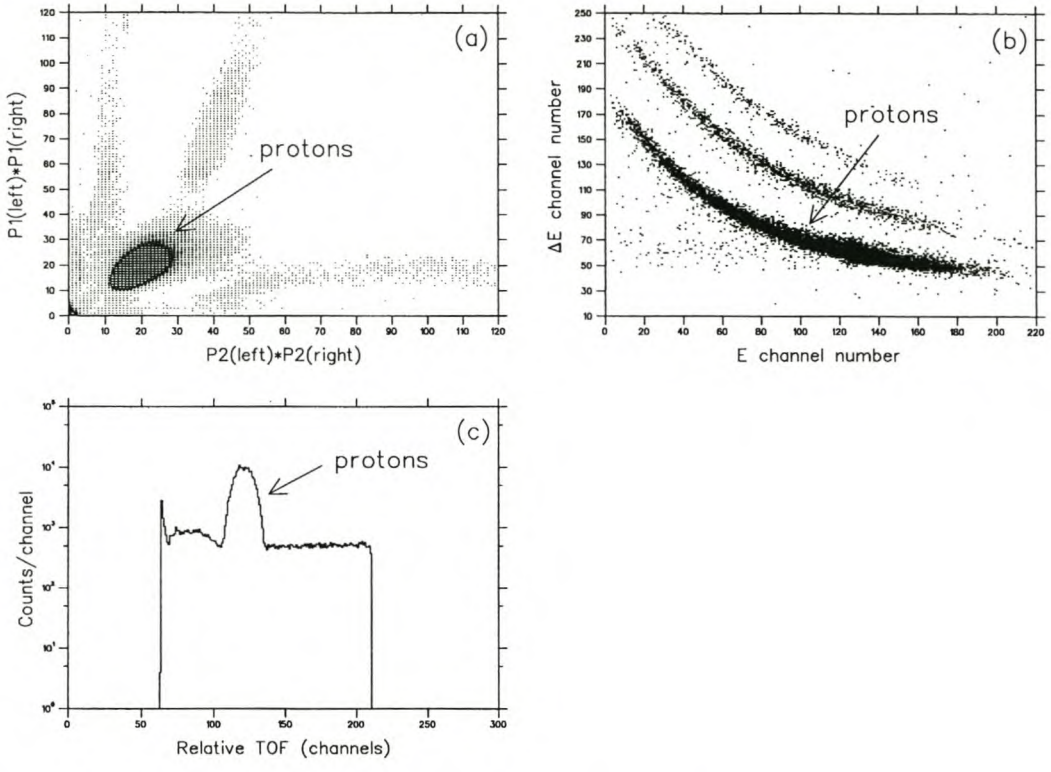

Figure 4.2: Particle identification in the magnetic spectrometer was achieved through (a) the focal-plane ΔE-ΔE spectrum and (c) TOF selection. A ΔE-E PID technique (b) was used in the detector telescope.

found to contribute <1% to the uncertainty in the yield for quasi-free events.

4.2 VDC Operation

Focal-plane position information was determined for all valid VDC events. A valid VDC event is defined as an event where at least 3 and less than 9 VDC signal wires registered a hit. The drift-times associated with these events must be within the range specified by a software gate on the average drift-time spectrum, as shown in Fig. (4.3). Focal-plane position is then determined using the drift-times and wire-position coordinates of the three wires situated around the wire associated with minimum drift-time. A further condition determining a valid VDC event is that this three-wire group should either consist of three consecutive wires or should be found in a group of four consecutive wires.

In the following sections a short summary of the techniques used to obtain accurate focal-

plane positions and spatial resolution is provided.

4.2.1 Determining Focal-Plane Position

Accurate information on the position of the particles passing through the focal plane can be obtained once the drift-time characteristics of the detector is established. Knowing the drift-time distribution $\frac{dN}{dt}$, the distance y from the signal wire to the position where the particle passed through a specific drift-cell in the VDC can in principle be obtained from

$$y(t) = (\frac{dN}{dy})^{-1} \int_{t_0}^{t} \left(\frac{dN}{dt'}\right) dt' \ , \tag{4.2}$$

where t_0 is the arrival time of the particle in the drift-cell, and t is the time at which the pulse appears at the anode [Ber77]. The quantity $\frac{dN}{dy}$ is a measure of the spatial distributions of events in the drift-cell.

A characteristic drift-time distribution is obtained by uniformly 'illuminating' the focal-plane with particles and measuring the average timing response of all the signal wires. This uniform distribution of events in the focal-plane, a situation experimentally obtained utilizing inelastically scattered protons from a ^{12}C target at a K600 energy of ~120 MeV, ensures a constant value for $\frac{dN}{dy}$. For such a 'white spectrum' the drift-time distribution $\frac{dN}{dt}$ is thus proportional to the drift velocity ω(t), and it follows that

$$y(t) = \int_{t_0}^{t} \omega(t')dt' \quad \propto \quad \int_{t_0}^{t} \left(\frac{dN}{dt'}\right) dt' \ . \tag{4.3}$$

With Eq. (4.3) and the drift-time distribution acquired through the above 'white spectrum' a lookup-table is generated, where drift-distances are correlated with drift-times. From the three sets of coordinates consisting of signal wire positions $(i-1)$, (i) and $(i+1)$ and their associated drift distances d_{i-1}, d_i and d_{i+1}, depicted in Fig. (4.4), the path of the particle through the VDC can be reconstructed. Intersection of this path with the focal-plane as well as the angle of the particle trajectory relative to the focal-plane is then determined by linear regression.

4.2.2 VDC Spatial Resolution

Position resolution of the VDC can be estimated from the drift distances d_{i-1}, d_i and d_{i+1} of the selected three signal wires. In an ideal measurement, with a straight line passing through all

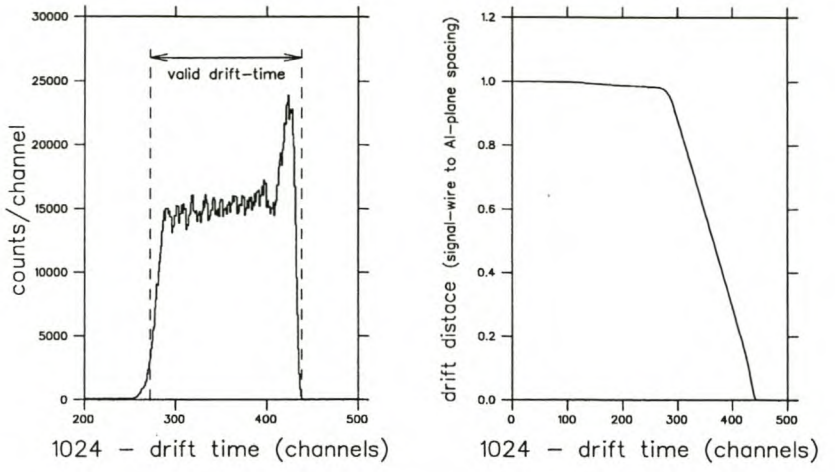

Figure 4.3: The average drift-time spectrum and associated lookup-table.

three drift-distance versus wire number coordinates, the intrinsic resolution of the VDC given by the quantity

$$\Delta = |d_{i+1} - d_{i-1}|/2 - d_i \ , \tag{4.4}$$

is zero. Non-zero values of Δ are caused by uncertainties in the drift-length measurements. If one associates an uncertainty value of δ_i with each drift-length d_i of the i'th drift cell, the uncertainty in the value of Δ can be calculated, from error propagation equations, to be

$$\delta_\Delta = \sqrt{(\frac{1}{2}\delta_{i-1})^2 + (\frac{1}{2}\delta_{i+1})^2 + {\delta_i}^2} \ . \tag{4.5}$$

If it is assumed that $\delta_{i-1} \approx \delta_i \approx \delta_{i+1} \approx \delta$ it follows that $\delta_\Delta \approx \sqrt{\frac{3}{2}}\delta$. A plot of the experimental values of Δ is given in Fig. (4.5), yielding a typical value of $\delta_\Delta = 0.3$ mm.

This value for the uncertainty in the drift-length can also be related to the uncertainty in the wire-plane intersection of the particle track, if it can be assumed that

$$\frac{d_{i+1}}{x_{i+1}} = \frac{d_i}{x_i} = \frac{d_{i-1}}{x_{i-1}} = k \ , \tag{4.6}$$

with k the gradient of the particle's trajectory. It would then follow that

$$\Delta = k \times (|x_{i+1} - x_{i-1}|/2 - x_i) \tag{4.7}$$

and that the position resolution of the VDC can be calculated if the angle of the particle's path through the VDC relative to the focal plane is known. In the analysis of the position resolution

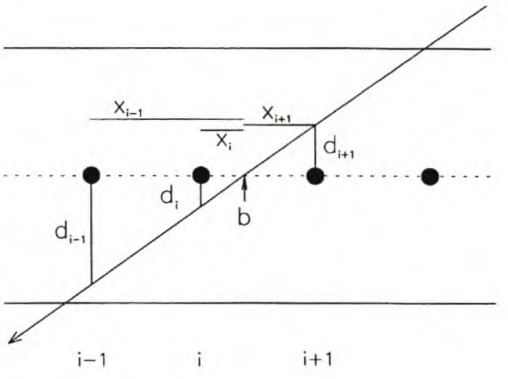

Figure 4.4: Wire-numbers and drift-distances used to calculate the focal-plane position.

in this experiment the angle factor k was ignored (note that only for an incident angle of 45°, $k = 1$ and the values of Δ are strictly correct). Nevertheless, this method gives the values of position resolution to within 25%. Higher accuracy is not needed, since the energy resolution of the K600 spectrometer is typically 50 keV (FWHM) [New96]. With a position resolution of about 0.3 mm the VDC has an energy resolution of ~8 keV. The only criteria for the resolution of the VDC is that it must not add significantly to the resolution of the spectrometer itself.

4.2.3 The Lookup-table Shift

It is physically impossible for the TDM modules associated with the signal wires (refer to section 3.6) to measure a zero drift-time. This results in a non-zero offset in the lookup-table, where for example a zero value for the drift-time does not necessarily imply a zero drift distance. To remedy this situation a two-dimensional resolution spectrum of Δ versus $(b - integer(b))$ can be used as a tool to indicate whether it is necessary to correct for the offset in the lookup-table. The symbol b denotes the calculated position in the focal-plane where the trajectory of a particle crossed the focal-plane, and is measured in units of the signal wire separation. The quantity $integer(b)$ denotes the position of the closest signal wire.

Let us assume by way of illustration that the TDM-modules supplies drift-times that are fractionally smaller than what it should be. The lookup-table is therefore, in terms of Fig. (4.3), shifted towards the right. The error in the drift distances for signal wire i due to this shift is denoted by ζ_i. Consider the particle trajectory illustrated in Fig. (4.4), where it crosses the focal-plane below the halfway mark between two signal wires, so that $b - integer(b) > 0$. It

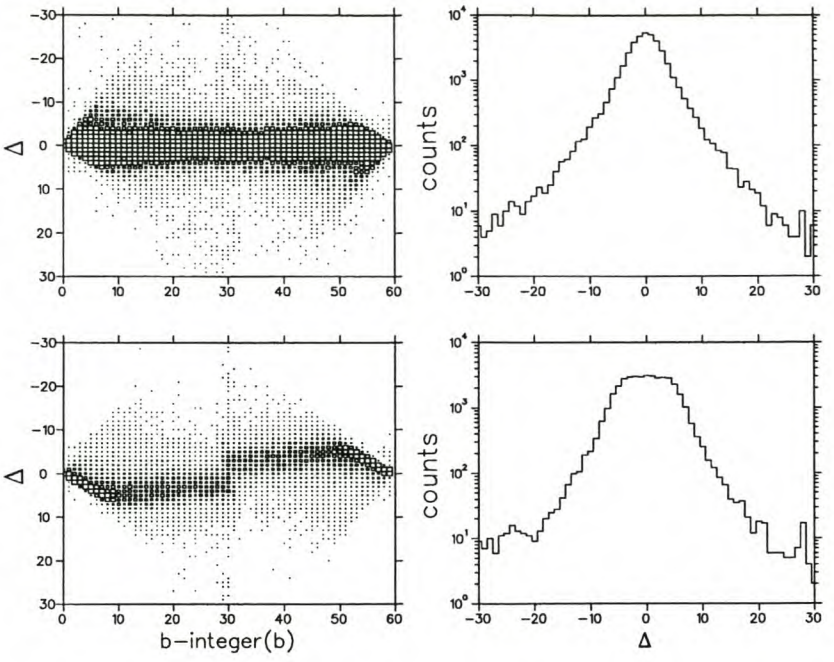

Figure 4.5: Spatial resolution spectra before (bottom) and after (top) the lookup-table-shift.

follows from Eq. (4.4) that the new value of intrinsic resolution, Δ', is given by

$$\begin{aligned}\Delta' &= \frac{(d_{i+1}+\zeta_{i+1})-(d_{i-1}+\zeta_{i-1})}{2}-(d_i+\zeta_i)\\ &= (\frac{d_{i+1}-d_{i-1}}{2}-d_i)+(\frac{\zeta_{i+1}-\zeta_{i-1}}{2}-\zeta_i)\\ &= \Delta+(\frac{\zeta_{i+1}-\zeta_{i-1}}{2}-\zeta_i) \quad . \end{aligned} \tag{4.8}$$

From the general shape of the lookup-table it can be assumed that for larger drift-times the corresponding error due to the lookup-table shift is smaller, and therefore that

$$(\frac{\zeta_{i+1}-\zeta_{i-1}}{2}-\zeta_i)<0 \quad . \tag{4.9}$$

The intrinsic resolution spectrum is therefore shifted to the right. Similarly it can be shown that for a trajectory which crosses the focal-plane above the halfway mark between signal wires, the peak in the intrinsic resolution spectrum will be positioned around a point to the left of zero. These shifts are evident in the double peak structure of the intrinsic resolution spectrum, as well as in the discontinuity in the spectrum of Δ against $(b-integer(b))$ as shown in Fig. (4.5). In this spectrum all events above the halfway mark between two signal wires are represented in the straight locus above the resolution zero point, and all events below the halfway mark between two signal wires are represented by the straight locus below the resolution zero point. The

discontinuity in the locus on the two dimensional resolution spectrum can be removed through an appropriate shift of the lookup-table. The spectrum becomes a straight line as in the top of Fig. (4.5), thereby optimizing the VDC resolution.

4.3 Detector Calibration

4.3.1 *Si*-detector

The *Si*-detectors were calibrated with a ^{228}Th α-source. A least squares fit method was used to obtain the calibration parameters, listed in table (4.1), for a straight line passing through the calibration points. It is assumed that the response of the detector to alphas and protons are equivalent. Energy resolution (FWHM) of 50-70 keV was achieved for the calibrated *Si*-detectors.

Detector	slope (MeV/bin)	offset (MeV)
Si (1998)	0.0111049	0.0101245
Si-1 (2000)	0.0125693	-0.0413401
Si-2 (2000)	0.0124611	0.0704400

Table 4.1: *Si* calibration parameters.

4.3.2 *Ge*-detector

Calibration of the *Ge*-detector in the 1998 experiment was achieved by making a coincident measurement of the $H(p,p)$ reaction at 200 MeV for the elastic scattering angle pair $(32.7°, -54.6°)$. With knowledge of the solid angles of both detectors a rough estimation was made of the central energy of the protons observed in the detector telescope. Assuming a linear relationship as well as a zero offset, a reasonable assumption when regarding the results from the improved 2000 calibration procedure, lead to the rough calibration

$$E_{Ge} = 0.0124 \times \text{bin} \; . \tag{4.10}$$

This calibration was then optimized in the off-line analysis as outlined in section 4.3.4.

Reaction	θ	E (MeV)	θ	E (MeV)	θ	E (MeV)
$^{197}Au(p,p)^{197}Au_{gs}$	31.5°	64.122	-	-	-	-
$^{12}C(p,p)^{12}C_{gs}$	31.5°	62.504	40.0°	61.510	65.0°	57.578
$^{12}C(p,p)^{12}C_{4.4\ \mathrm{MeV}}$	31.5°	58.093	40.0°	57.066	65.0°	53.377
$^{12}C(p,p)^{12}C_{9.64\ \mathrm{MeV}}$	31.5°	52.665	40.0°	51.736	65.0°	48.195
$H(p,p)$	31.5°	44.999	40.0°	35.054	-	-

Table 4.2: Reactions and associated kinematics for Ge-calibration runs with a 66.5 MeV proton beam.

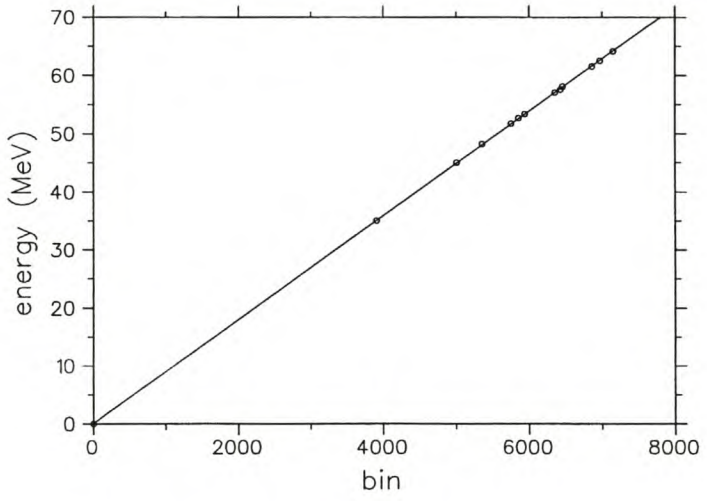

Figure 4.6: The calibration curve of the Ge-detector.

For the experiment conducted in 2000 the calibration procedure was vastly improved. Various calibration points at different angles were obtained utilizing a 66.5 MeV proton beam and the reactions listed in table (4.2). The listed proton energies are what would be observed by the Ge-detector, taking the relevant dead-layers as explained in section 4.4.1 into account. To minimize kinematic energy spread the calibration measurements (with the exception of the ^{197}Au(p,p) measurement) were performed with a much smaller solid angle; 0.26 msr compared to the solid angle of 5.59 msr for the coincidence experiment. A first order polynomial fit of the data, including the point of origin (see Fig. 4.6), resulted in the calibration equation

$$E_{Ge} = 0.0089682 \times \mathrm{bin} + 0.056154\ . \tag{4.11}$$

An effective proton energy resolution (FWHM) of 215 keV was attained for the ^{197}Au(p,p) elastic scattering reaction.

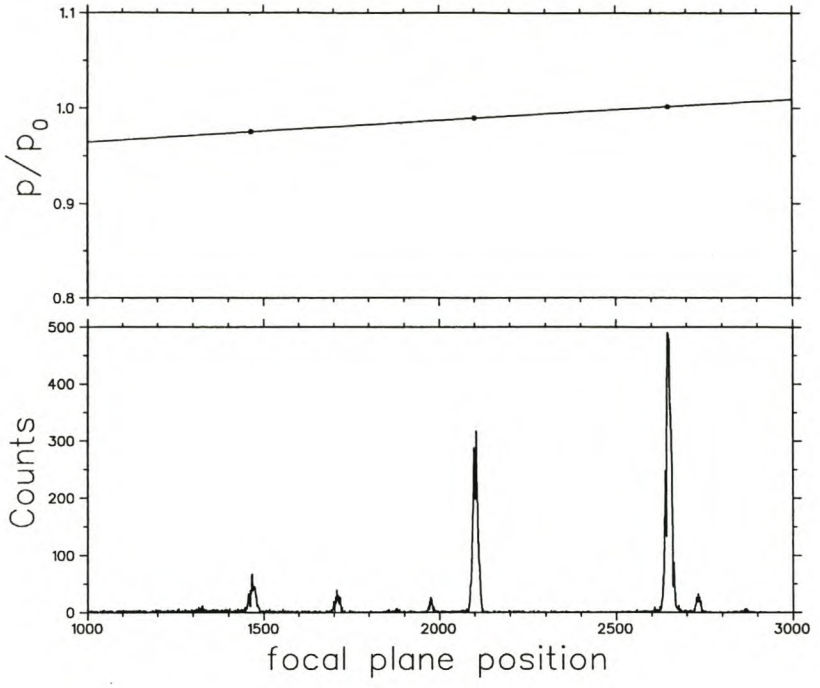

Figure 4.7: The focal-plane position spectrum of $^{12}C(p,p)$ scattering and the calibration curve of the K600-detector. The small peak to the right of the $^{12}C(p,p)^{12}C_{gs}$ peak is due to elastic scattering from ^{16}O.

4.3.3 The K600

Calibration of the K600 was achieved through $p +^{12} C$ elastic and inelastic scattering with a 200 MeV proton beam. In order to minimize kinematic broadening of the observed peaks a vertical slit collimator (41 × 14 mm) replaced the circular $r = 31.5$ mm collimator for the calibration measurements. Fig. (4.7) displays the resulting $^{12}C(p,p')$ focal-plane position spectrum.

For a specific field-setting of the magnetic spectrometer the relationship between particle momentum p and focal-plane position x_{FP} can be written to first order as [Hen74]

$$x_{FP} = M_x x_1 + D\frac{\Delta p}{p_0} , \tag{4.12}$$

where x_1 is the horizontal position coordinate of the particle on entering the spectrometer and $\frac{\Delta p}{p_0}$ is used as a measure of momentum spread. The quantity Δp can be rewritten as $\Delta p = p - p_0$, where p_0 is a reference momentum associated with the chosen field-set[1]. M_x denotes

[1] A typical definition of the reference momentum is the momentum required to pass through the centre of the magnetic system for that specific field-set.

	$\frac{1}{D}$	$-\frac{M_x}{D}x_1 + 1$
2^{nd} weekend	2.3016×10^{-5}	0.93796
3^{rd} weekend	2.3068×10^{-5}	0.93632
4^{th} weekend	2.2650×10^{-5}	0.93707

Table 4.3: Calibration parameters of the K600 for the 1998 experiment.

the horizontal linear magnification and D the dispersion of the spectrometer. By rewriting Δp Eq. (4.12) yields the calibration equation

$$\frac{p}{p_0} = \frac{1}{D}x_{FP} - \frac{M_x}{D}x_1 + 1 \ . \tag{4.13}$$

Since x_1 is taken to be a constant (because of the relatively small size of the beam-spot on target) and D, M_x and p_0 are constants , Eq. (4.13) represents a linear calibration relationship between p and x_{FP}, associated with a certain p_0.

The actual focal-plane of the K600 is a bowed surface, and does not coincide with the flat surface of the signal-wire array of the VDC. The particle momentum would then be best represented by a quadratic function of x_{FP}, and from Li [Li94] it follows that

$$p = 0.3B_{D1}\rho\left[1 + \frac{(x_{FP} - x_0)}{D} + \frac{(x_{FP} - x_0)^2}{Q}\right] \ , \tag{4.14}$$

where B_{D1} is the field in the first spectrometer dipole D1 (measured in kGauss). The quantity Q reflects the non-linearity of the transformation. The quantity x_0 is the focal-plane position of particles with corresponding reference momentum p_0, and the term $(0.3B_{D1}\rho)$ can be interpreted as the reference momentum p_0 [Li94]. Therefore the momentum calibration equation of the K600 can be written as

$$\begin{aligned} \frac{p}{p_0} &= 1 + \frac{(x_{FP} - x_0)}{D} + \frac{(x_{FP} - x_0)^2}{Q} \ , \\ &= \frac{1}{Q}x_{FP}^2 + \frac{(Q - 2Dx_0)}{QD}x_{FP} + \left(1 - \frac{x_0}{D} + \frac{x_0^2}{Q}\right) \ , \\ &\equiv ax_{FP}^2 + bx_{FP} + c \ , \end{aligned} \tag{4.15}$$

resulting in a simple quadratic parameterization.

Calibration of the spectrometer was performed for each weekend. Although calibration was done only for one specific field setting (covering a proton energy range of ~178-205 MeV) it was

	$\frac{1}{Q}$	$\frac{(Q-2Dx_0)}{QD}$	$\left(1-\frac{x_0}{D}+\frac{x_0^2}{Q}\right)$
4^{th} weekend	-5.6000×10^{-10}	2.5600×10^{-5}	0.93136
5^{th} weekend	-5.3669×10^{-10}	2.5311×10^{-5}	0.93704
6^{th} weekend	-4.9203×10^{-10}	2.5237×10^{-5}	0.93962
7^{th} weekend	-5.1694×10^{-10}	2.5346×10^{-5}	0.93703
8^{th} weekend	-5.3468×10^{-10}	2.5236×10^{-5}	0.93654
9^{th} weekend	-4.4031×10^{-10}	2.4818×10^{-5}	0.93877

Table 4.4: Calibration parameters of the K600 for the 2000 experiment.

assumed that it would also be valid for each of the other field settings used during that weekend. Analysis of the 1998 experiment was conducted with the calibration of the K600 according to Eq. (4.13). As part of improvements made to the new experiment the second-order calibration of Eq. (4.15) was used in the 2000 study. The calibration parameters are listed in tables 4.3 and 4.4.

Typical effective energy resolution of $\sim$ 100 keV (FWHM) was obtained in the 1998 study for the $^{208}Pb(p,p)$ elastic reaction at 200.6 MeV. For the 2000 study effective energy resolution of $\sim$ 60 keV (FWHM) was obtained with the elastic $^{208}Pb(p,p)$ reaction for the thin target with 201.5 MeV protons, measured at 22°. The corresponding momentum resolutions are roughly 200 keV/c and 100 keV/c for respectively the 1998 and 2000 (thin target) experiments.

4.3.4 Optimizing Binding Energy Resolution

The high energy resolution requirement of the experiment was aimed at attaining a high resolution binding energy spectrum in order to distinguish between the different final states in ^{207}Tl. The binding energy represents the total kinetic energy of the 3-body final state, and is calculated as

$$E_{BE} = E_{K600} + E_{Ge} + E_{Si} + E_{deadlayer} + E_{recoil} \ , \tag{4.16}$$

where $E_{deadlayer}$ corrects for proton energy losses in dead layers in the detector setup (refer to the next section), and E_{recoil} corrects for the recoil momentum of the residual target. Inadequate calibration procedures, e.g. for the Ge calibration procedure in the 1998 experiment, resulted in inadequate energy resolution and prompted the use of a software resolution optimization

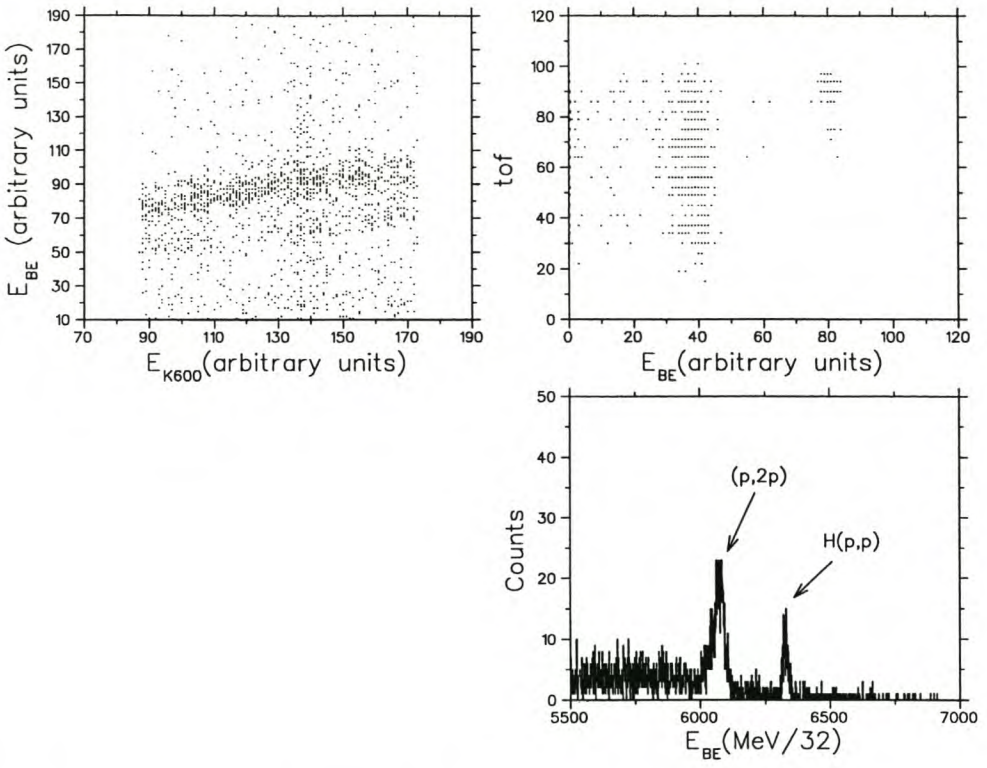

Figure 4.8: Bad energy resolution manifests as oblique lines in the two-dimensional plots of E_{BE} vs. E_{K600} and TOF vs. E_{BE}. This results in a binding energy spectrum where different states cannot be easily selected.

procedure. This software optimization also compensates for various other potential errors in the calibration procedures which might have a negative influence on the energy resolution, such as possible beam-offset[2], uncertainty in the beam energy and the uncertainty in the angle measurement of the detectors.

The inadequacy of the calibration values obtained from the previous sections is quite clear from Fig. (4.8). In the two-dimensional plot of the binding energy versus the K600 energy the $(p, 2p)$ loci rising with spectrometer energy prevents clear separation of states in the projection binding energy spectrum. Bad calibration is also evident from the two-dimensional plot of the TOF versus the binding energy.

In the 1998 experiment the calibration of the *Ge*-detector was regarded as the weakpoint, with the K600 calibration regarded as correct. Starting with the rough *Ge* calibration parameter

[2]Care was taken to centre the beam on target, but it was impossible to ensure that the angle of incidence was precisely 0°.

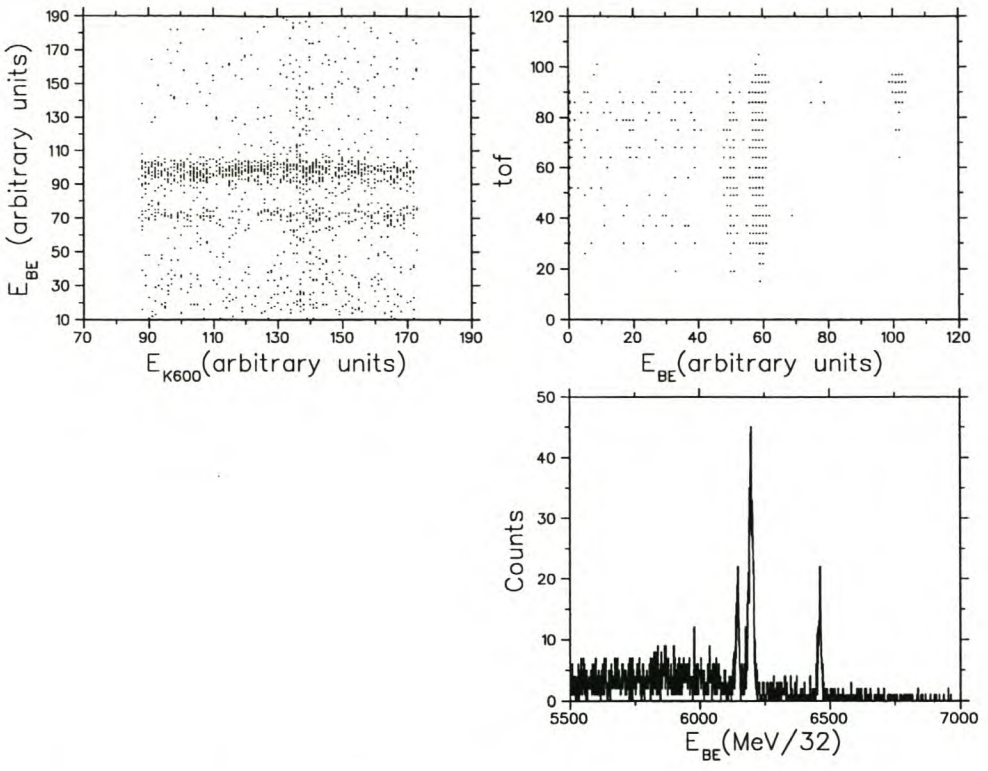

Figure 4.9: The good energy resolution counterpart of Fig. (4.8). In the resulting binding energy spectrum different states are clearly identifiable.

and searching a reasonable area around this with appropriate step-sizes an optimum value of the slope of the *Ge* calibration for each weekend was obtained. This led to the value of the slope parameters for the 3 weekends to be respectively 0.01215, 0.01187 and 0.01155. In the experiment conducted in 2000 the initial *Ge* calibration was taken to be correct, and the new quadratic term of the K600 calibration was optimized. Calibration optimization was deemed good when both the two-dimensional plots of binding energy versus the K600 energy and the TOF versus the binding energy yielded straight loci, as shown in Fig. (4.9).

Although this off-line calibration optimization procedure might seem rather arbitrary, all that is required in the end is to achieve as small as possible width of the peaks in the binding energy spectrum. For the 1998 experiment quasi-free events from the thick ^{208}Pb target yielded peaks with FWHM of $\sim$ 480 keV. Improved experimental energy resolution was obtained in the second experiment utilizing a much thinner ^{208}Pb target, with FWHM in the binding energy spectrum of around 310 keV.

4.4 Corrections

4.4.1 Dead-layers

The energy measured for protons detected in the detector telescope was corrected for the energy-loss in the 75 μm Kapton scattering chamber exit window, the He-filled volume between the exit window and the *Ge*-detector, and the 0.125 mm Be entrance window of the *Ge*-detector. For the 2000 study energy-loss in the dead-layers (in MeV) is related to the energy measured in the *Ge*-detector (in MeV) by the equation

$$E_{deadlayer} = \frac{a_1 b_1 + c_1 (E_{Ge})^{d_1}}{b_1 + (E_{Ge})^{d_1}} \ . \tag{4.17}$$

Because the *Si*-detector was placed between the Kapton window and the *Ge*-detector for the 1998 experiment the dead-layer parameterization was split in two. In a first calculation the energy-loss in the Kapton and 4.2 cm He was related to the energy detected in the *Si*-detector,

$$E_{deadlayer-1} = \frac{a_2 b_2 + c_2 (E_{Si})^{d_2}}{b_2 + (E_{Si})^{d_2}} \ . \tag{4.18}$$

Secondly the energy-loss in the Be entrance window was related to energy measured in the *Ge*-detector by

$$E_{deadlayer-2} = a_3 + b_3 (1 + (\frac{E_{Ge}}{c_3})^{d_3})^{-1} \ . \tag{4.19}$$

The various parameters for these dead layer parameterizations are given in table (4.5).

	$i = 1$	$i = 2$	$i = 3$
a_i	4.88019×10^{-2}	-3.26918×10^{-4}	2.70353×10^{-2}
b_i	0.297377	14.0410	4.23944
c_i	4.76740	0.783814	2.18161
d_i	-0.995099	1.19116	0.953573

Table 4.5: Parameters for the dead-layer parameterizations.

4.4.2 Hydrogen Contamination Correction

For sufficient overlap between the solid angles of free elastic scattering and quasi-free knockout, the overwhelming amount of elastic scattered $H(p,p)$ events, due to hydrogen contamination

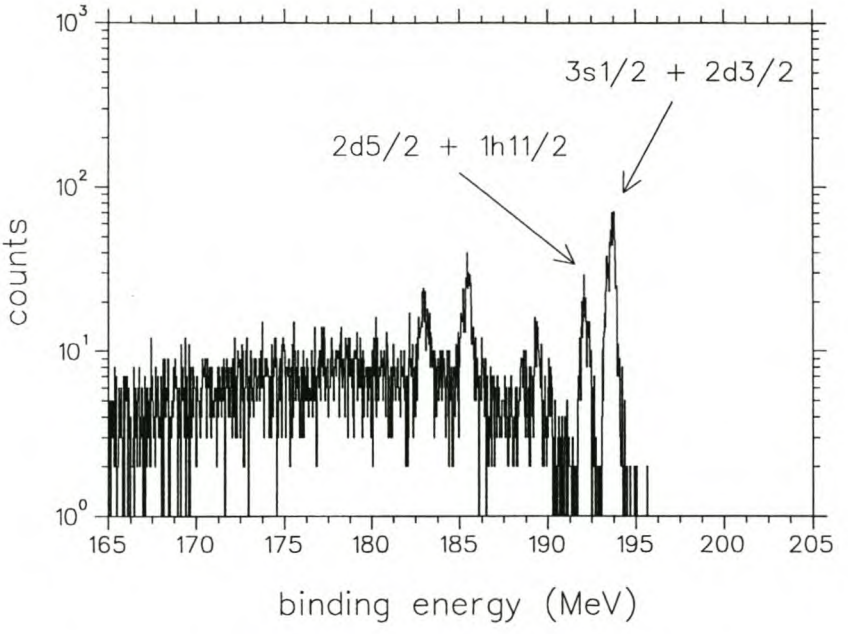

Figure 4.10: A typical binding-energy spectrum for an incident beam of 202 MeV protons.

of the Pb targets as discussed in section 3.1, can lead to the pollution of the quasi-free locus with the reaction tail of the Ge-detector. The problem was negligible for the $(28°, -54.6°)$ and $(33°, -49.7°)$ measurements, since the solid angle overlap was minimized by positioning the K600 at a slightly smaller angle than the required quasi-free angle. A typical binding energy spectrum for these angle pairs is shown in Fig. (4.10). The states relevant to this study are indicated in the figure, and some deeper-lying states are also discernible.

Data for the pure quasi-free angle-pair $(22°, -62.3°)$ was however affected by the hydrogen contamination, and in Fig. (4.11) it is seen how the reaction tail obscures part of the quasi-free locus. This results in an uncomfortably high background in the associated binding energy spectrum.

In the two-dimensional plot of the TOF versus the focal-plane position for spectrometer singles, shown in Fig. (4.12a), free scattering events manifest as an easily discernible locus above a structure-free background. All the free scattering events were then vetoed in the analysis by placing a gate over the $H(p,p)$ locus. Analysis was then performed as usual, leading to the reaction tail corrected binding energy spectrum as in Fig. (4.13). In this way it was possible to reduce the occurrence of $H(p,p)$ events in the binding energy spectrum from typically 20 times larger than the quasi-free peaks to a size smaller than that of the $(3s_{1/2} + 2d_{3/2})$ peak. The

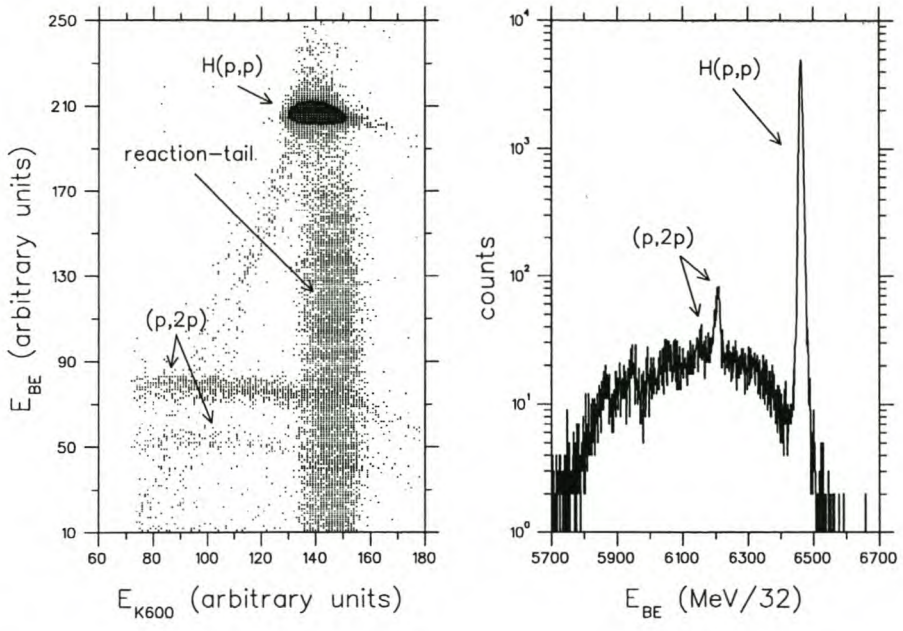

Figure 4.11: In the two-dimensional plot of E_{BE} vs. E_{K600} the reaction tail of the Ge obscures part of the quasi-free locus. This results in a binding energy figure with a large number of background events in the quasi-free region.

remaining contamination of the quasi-free locus was found to be negligible.

Of course not only were $H(p,p)$ events eliminated, but some valid $(p,2p)$ events were also thrown away in the above process. This situation was remedied in the final energy-sharing distributions with a procedure to replace the lost 'focal-plane flux'. In order to correct for valid events lost, the result of which is shown in the singles spectrum Fig. (4.12c), the gate used to select the free scattering events was shifted appropriately in order to cover a similar region, but free of $H(p,p)$ events. Using the events from this gate as an indication of the non-$H(p,p)$ events lost, correction factors were determined for the singles spectrum, resulting in Fig. (4.12d). Since $(p,2p)$ events are found evenly distributed in the broad band in Fig. (4.12a), it was assumed that equal percentages of singles and coincidence events were lost. The same correction factors were therefore used to correct the energy sharing distributions.

4.5 Separation of States

Sufficient energy resolution to achieve complete online separation of the different states was not attained. Straggling and other effects due to the finite thickness of the target, as discussed in

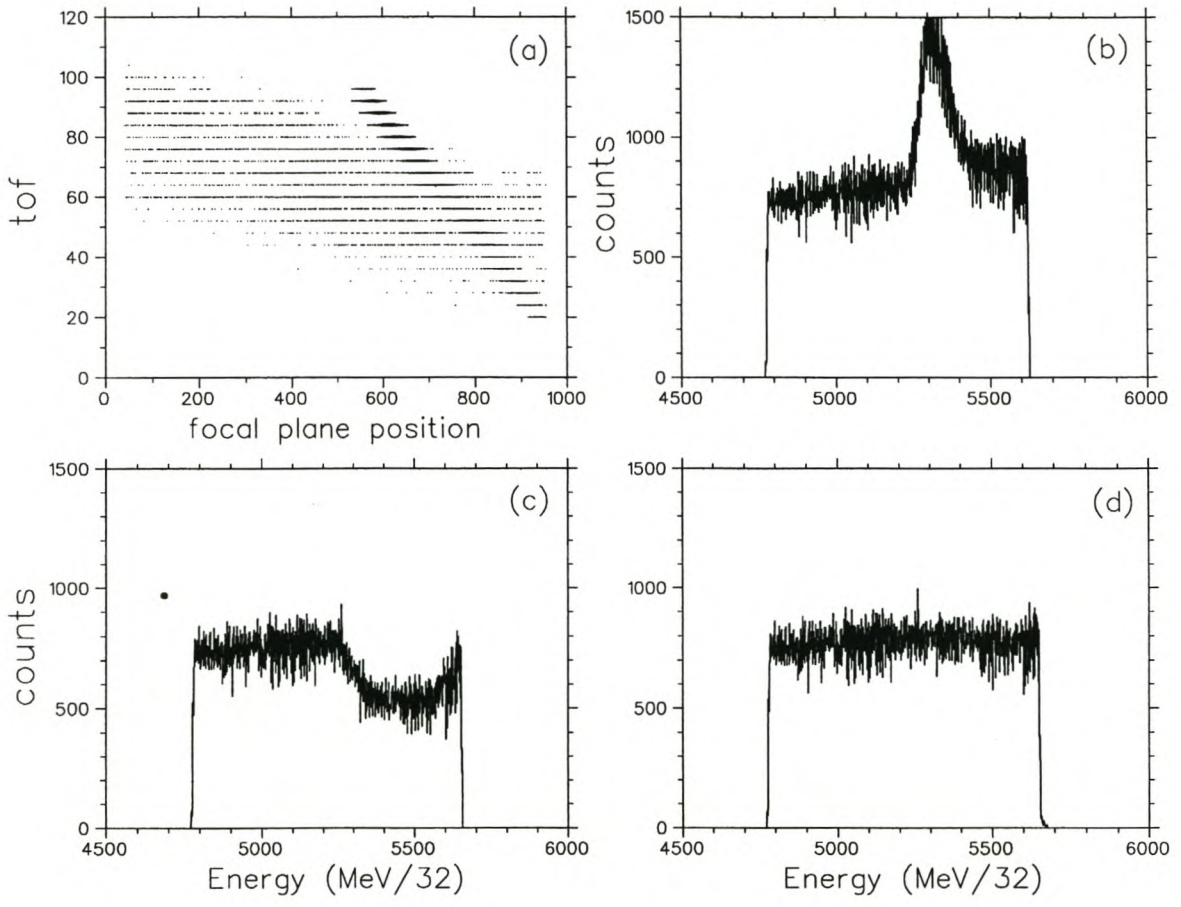

Figure 4.12: The reaction tail problem: The $H(p,p)$ locus is easily discernible in the TOF vs. focal-plane position spectrum (a). In (b) the projection of (a) to the focal-plane axis is shown, with the $H(p,p)$ events visible as the peak above the constant background. By setting a gate over the $H(p,p)$ locus in (a) to veto the free scattering events, some valid events are also discarded, resulting in the hole in (c). Figure (d) depicts the focal plane singles spectrum after appropriate corrections (see text).

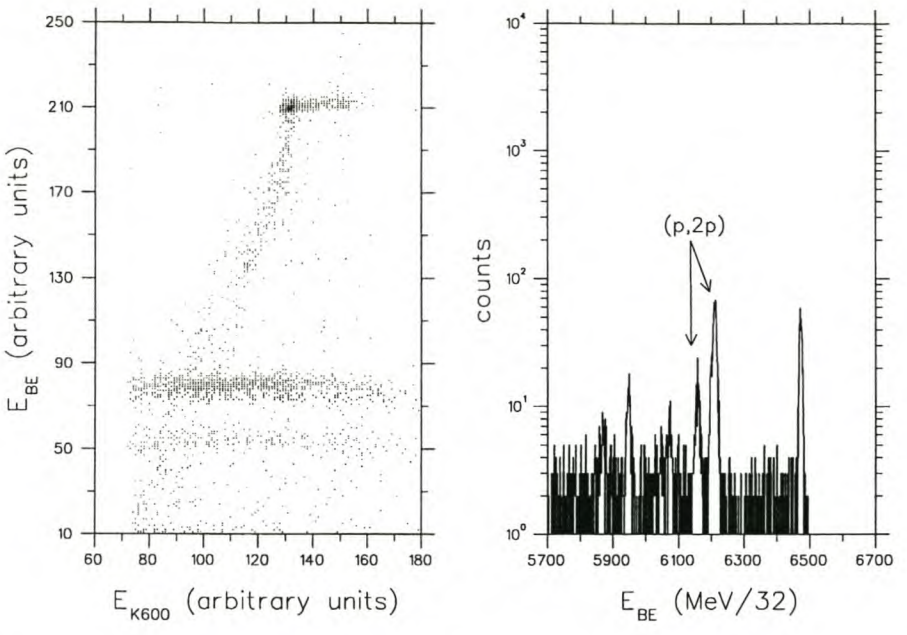

Figure 4.13: The binding energy spectrum after corrections for the hydrogen contamination of the target.

Appendix B, ultimately limited the energy resolution. The data was however still of sufficient quality to allow the extraction of data for the $3s_{1/2}$ and $2d_{3/2}$ states by means of a peak-fitting procedure. The much lower statistics for the $2d_{5/2}$ and $1h_{11/2}$ states together with the fact that the contribution of the $1h_{11/2}$ state to the sum of states is negligible over most of the observed energy range (refer to Chapter 5) precluded any efforts to obtain results for each of these states separately.

Due to beamtime restrictions sufficient data required to perform peak deconvolution was acquired only for the (28°;-54.6°) and (22°;-62.3°) angle pairs. Data for spin-up and spin-down incident beam polarization for each of these angle pairs were subjected to the following fitting procedure. For a selected energy bite in the energy-sharing distribution (varying between 6 and 13 MeV, depending on statistics) the binding energy spectrum was reconstructed. Peakfitting was then performed on this 'restricted-origin' binding energy spectrum, constrained by the known separation energies of the proton bound states. As noted earlier in section 2.7 it is assumed that the states are unfragmented. It is further also assumed that the width of the states are entirely due to experimental resolution, and are therefore the same for both states. The FWHM of the peaks were established from the $(3s_{1/2} + 2d_{3/2})$ peak in the binding energy spectrum for a region in the energy-sharing distribution where the $3s_{1/2}$ state is dominant.

Least-squares peak-fitting was done with the logistic peak function[3]. The choice of peak function was based on the best fit to the elastic $H(p,p)$ peak in the binding energy spectrum obtained from various peak functions. A representative subset of the fits is displayed in Fig. (4.14). It should however be mentioned that results obtained for Gaussian peak functions yielded practically the same results. The total number of counts in the binding energy spectrum was divided according to the areas of the fitted peaks to yield results for only the s and d states for each of the energy bites. These counts were then converted to cross-section and analyzing powers with the same procedure as used for the unresolved results as outlined in the following section.

4.6 Experimental Cross-sections and Analyzing Powers

Events representing proton knockout to a combination of states ($(3s_{1/2}+2d_{3/2})$, $(2d_{5/2}+1h_{11/2})$ and the combination of all four states) were selected by setting a gate over the relevant peaks in the binding energy spectrum. For all the events in such a gate an energy-sharing distribution was created, displaying the number of quasi-free events as a function of the energy of the protons detected in the K600. For the separated results the counts per energy bin for the $3s_{1/2}$ and $2d_{3/2}$ states were acquired as set out in the previous section.

Experimentally the triple differential cross-section for e.g. upward polarized incident protons in the laboratory reference frame is written as

$$\frac{d^3\sigma^{\uparrow}}{d\Omega_1 d\Omega_2 dE} = \frac{10^{27}\cdot C^{\uparrow}}{N^{\uparrow}\cdot\rho\cdot D\cdot\varepsilon\cdot\Delta\Omega_1\cdot\Delta\Omega_2\cdot\Delta E}\,, \tag{4.20}$$

in units of $mb\ sr^{-2}MeV^{-1}$. In the above equation

- $C^{\uparrow}$ is the number of quasi-free events in an energy bin ΔE,
- $N^{\uparrow}$ is the number of incident upward polarized protons,
- ρ is the number of target nuclei per unit area,
- D is an electronic dead time correction factor,
- ε is the K600 VDC efficiency (the plastic scintillators were assumed to be 100% efficient),
- $\Delta\Omega_1$ is the solid angle of the Ge in sr,

[3] $y = \frac{exp\left[-\left(\frac{x-b}{c}\right)\right]}{\left[1+exp\left[-\left(\frac{x-b}{c}\right)\right]\right]^2}$

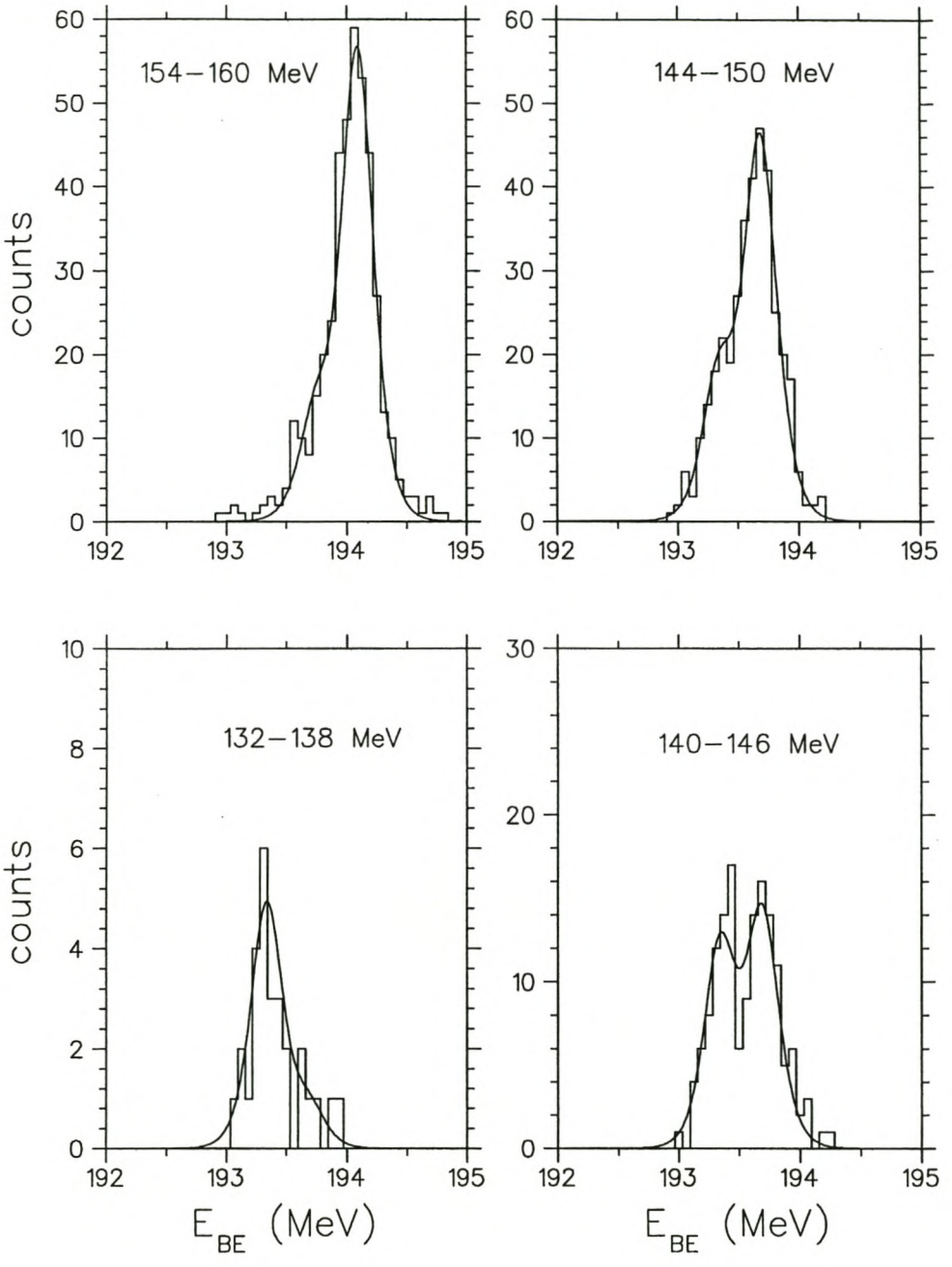

Figure 4.14: Typical peakfits in the binding energy spectrum, representing different energy-bites in the energy sharing spectrum, ranging from the worst to the best fitting scenarios.

- $\Delta\Omega_2$ is the solid angle of the K600 in sr, and
- ΔE is energy bin size in MeV (4 MeV for the unseparated results). Note that the separated data represent quite large overlapping energy bins.

The unpolarized triple differential cross-section ($\frac{d^3\sigma}{d\Omega_1 d\Omega_2 dE} \equiv d^3\sigma$) is then written in terms of the upward ($d^3\sigma^{\uparrow}$) and downward ($d^3\sigma^{\downarrow}$) polarized triple differential cross sections as

$$d^3\sigma = \frac{d^3\sigma^{\uparrow} + d^3\sigma^{\downarrow}}{2 + A_y \cdot (p^{\uparrow} - p^{\downarrow})} , \tag{4.21}$$

which follows from

$$\begin{aligned} d^3\sigma^{\uparrow} &= d^3\sigma(1 + A_y \cdot p^{\uparrow}) , \\ d^3\sigma^{\downarrow} &= d^3\sigma(1 - A_y \cdot p^{\downarrow}) . \end{aligned} \tag{4.22}$$

The experimental analyzing power for the general case where $p^{\uparrow} \neq p^{\downarrow}$ is obtained from the above

$$A_y = \frac{C^{\uparrow} - C^{\downarrow}}{C^{\uparrow}p^{\downarrow} + C^{\downarrow}p^{\uparrow}} . \tag{4.23}$$

4.6.1 Experimental Yields

Energy-sharing distribution yields were obtained for the different field-sets of the K600 for subgroups of experimental runs associated with the same degree of upward and downward polarization. Corrections of these yields for accidental coincidences were obtained by generating a relative timing spectrum of the left and right detectors for coincidence events. Accidental coincidence results were sorted separately in order to subtract their contribution from the true events. The fraction of accidental to true+accidental coincidences varied between different field-sets from a minimum of 1% to a maximum of 30% . Although 30% is quite a substantial figure it should be noted that the quoted figure is relevant for *all* coincidence events, and that the effective contribution to the quasi-free region in the binding energy spectrum is much lower. Background subtraction was only done for measurements at such a field-set where $H(p,p)$-overlap caused the quasi-free events in the binding energy spectrum to sit on top of a background. Otherwise no such correction was deemed necessary.

Cross-section and analyzing power results were generated for each of the above-mentioned subgroups of energy-sharing distributions results. The final results for the different field-sets

were composed of the different polarization-bound data-sets combined according to the method of weighted mean [Leo87], where the final value for the observable x_i is calculated by

$$\overline{x} = \frac{\sum_i \frac{x_i}{(\delta x_i)^2}}{\sum_j \frac{1}{(\delta x_j)^2}} , \tag{4.24}$$

and the associated error δx_i is given by

$$\overline{\delta x_i}^2 = \frac{1}{\sum_j \frac{1}{(\delta x_j)^2}} . \tag{4.25}$$

For the separated results insufficient statistics prevented the use of the peakfitting procedure for each of the different polarization-bound subgroups of data. The total energy-sharing distribution yield of a specific weekend was acquired, and then analyzed using an average value for the upward and downward polarization. This averaged value was calculated by weighting the different polarizations p_i for each polarization subgroup i, with the associated contribution of incident protons N_i to the total amount of incident protons N_{total}, e.g.

$$p_w^{\uparrow} = \frac{1}{N_{total}^{\uparrow}} \sum_i p_i \cdot N_i^{\uparrow} . \tag{4.26}$$

Data from different weekends could then be combined with the method of weighted mean. It was confirmed with the unseparated results that within the experimental uncertainty there exist a negligible difference between results obtained from the proper data combination method, and the mean polarization method.

4.6.2 Incident Flux

The number of incident protons is calculated by

$$N = \frac{N_{CI} \cdot R \cdot 10^{-12}}{e} , \tag{4.27}$$

where

- N_{CI} is the current-integrator scaler reading, representing the number of digital pulses generated by the current integrator. The dead time of the data acquisition system was automatically taken into account by inhibiting the current-integrator scaler reading with a data-acquisition busy signal. Typical computer dead time was quite low and ranged between 1% and 2%.
- The quantity R represents the selected range (in nA) of the current integrator module, which

represents $R\cdot$ 1000 counts per second for a full-scale current read-out, and

- e is the proton electric charge (in coulomb).

Uncertainty from the beam current integrator is estimated to be be 0.5% [New96].

4.6.3 Target Nuclear Density

The number of nuclei per unit area of the ^{208}Pb target is calculated from

$$\rho = \frac{\lambda \cdot N_A}{A} , \tag{4.28}$$

where

- λ is the target thickness (g·cm^{-2}),
- N_A is Avogadro's number, and
- A is mass number.

4.6.4 Electronic Dead Time

A pulser signal, triggered at a rate proportional to the beam current, was supplied to the *Ge*-detector. The electronic dead time was then determined by comparing the number of pulser events for the *Ge*-detector as processed by the timing electronic setup, to the value of a pulser scaler that bypassed the electronics. Typical values for the electronic dead time were less than 2%, and never exceeded 10%.

4.6.5 VDC Efficiency

The efficiency, ε, of the VDC is an indication of its ability to detect charged particles in the focal-plane. It is given by the product of the geometric efficiency (ε_g) and the intrinsic efficiency (ε_i) parameters [Leo87]:

$$\varepsilon = \varepsilon_g \cdot \varepsilon_i . \tag{4.29}$$

For the K600 spectrometer at NAC it was determined with a horizontal drift chamber (HDC) that the particles of a selected rigidity were well-focused in the vertical direction in the focal plane position. It was found that the central wire of the HDC registered by a large margin

the most hits. In view of this, the geometric efficiency was taken to be 100%. The intrinsic efficiency on the other hand is defined as

$$\varepsilon_i = \frac{N_{accepted}}{N_{tot}} , \tag{4.30}$$

where N_{tot} denotes the total number of events of a selected rigidity recorded in the focal-plane of the spectrometer. The quantity $N_{accepted}$ denotes the number of *valid* events recorded, which means that these events adhere to the criteria described earlier. Therefore

$$N_{accepted} = N_{tot} - (N_{\geq \max} + N_{\leq \min} + N_{idt} + N_{nogroup}) , \tag{4.31}$$

where

- $N_{\geq \max}$ is the number of events for which more than 8 wires fired,
- $N_{\leq \min}$ is the number of events for which less than 3 wires fired,
- N_{idt} is the number of events for which the drift-time is outside the valid drift-time range,
- $N_{nogroup}$ is the number of events where a valid three-wire group could not be found in an otherwise valid event.

VDC efficiency is an excellent monitor for gas quality and functioning of the TDC-cards. The average intrinsic efficiency obtained typically varied between 93% and 95%.

4.7 Error Analysis

4.7.1 Statistical Errors

The statistical error for the triple differential cross-section for upward (downward) polarized beams is given by

$$\delta(d^3\sigma^{\uparrow(\downarrow)}) = \frac{10^{27}}{D \cdot \varepsilon \cdot \rho \cdot N \cdot \Delta\Omega_1 \cdot \Delta\Omega_2 \cdot \Delta E} \cdot \sqrt{C^{\uparrow(\downarrow)}} . \tag{4.32}$$

From the error propagation equation it follows that the error for the unpolarized triple differential cross-section is given by

$$\begin{aligned} \delta^2\left(\frac{d^3\sigma^{\uparrow} + d^3\sigma^{\downarrow}}{2 + A_y \cdot (p^{\uparrow} - p^{\downarrow})}\right) = & \left(\frac{1}{2 + A_y \cdot (p^{\uparrow} - p^{\downarrow})}\right)^2 \left[\delta^2(d^3\sigma^{\uparrow}) + \delta^2(d^3\sigma^{\downarrow})^2\right] \\ & + \frac{\left(d^3\sigma^{\uparrow} + d^3\sigma^{\downarrow}\right)^2}{(2 + A_y \cdot (p^{\uparrow} - p^{\downarrow}))^4} \left[\left(p^{\uparrow} - p^{\downarrow}\right) \delta(A_y)\right]^2 , \end{aligned} \tag{4.33}$$

Error Source	Error % 1998	Error % 2000
Thick target thickness	7	7
Particle identification	1	1
K600 solid angle	0.3	0.3
Telescope solid angle	1.5	1.2
Current integrator	0.5	0.5
Ge efficiency	3	3

Table 4.6: Summary of the systematic errors.

where it is assumed that the error in polarization is negligible.

The statistical error for the analyzing power, expressed as in Eq. (4.23), was calculated as

$$\delta A_y = \left[\frac{\left(C^{\uparrow} + C^{\downarrow}\right)}{\left(C^{\uparrow}p^{\downarrow} + C^{\downarrow}p^{\uparrow}\right)^2} + \frac{\left(C^{\uparrow} - C^{\downarrow}\right)^2}{\left(C^{\uparrow}p^{\downarrow} + C^{\downarrow}p^{\uparrow}\right)^4} \cdot \left(C^{\uparrow}p^{\downarrow 2} + C^{\downarrow}p^{\uparrow 2}\right) \right]^{\frac{1}{2}} . \tag{4.34}$$

4.7.2 Systematic Errors

The various systematic errors considered for the cross-section results are listed in table 4.6. Until now nothing has been said about the efficiency of the *Ge*-detector. Loss of the full energy of protons in the *Ge*-detector due to inelastic interactions will cause loss of coincident events. It is known [Mea69] that the percentage interaction loss in *Ge* ranges from 1.3% at 30 MeV to 6% at 75 MeV. On average this effect is expected to contribute 3% to the cross-section systematical error. Since it is assumed that the errors listed in table 4.6 are uncorrelated they are added in quadrature, giving an overall systematic error of ~7.8% for both the 1998 and 2000 thick-target results.

As the analyzing power is defined in terms of ratios of spin-up and spin-down cross-sections, the systematic errors as listed in table 4.6 will cancel in first order. However, an uncertainty in the determination of the analyzing power arises from the uncertainty in the degree of polarization of the incident beam. This can be estimated from the equation [Car99]

$$\delta A_y = A_y \frac{\Delta p}{p} . \tag{4.35}$$

Since the uncertainty in polarization was in the range of $1.5 - 2\%$ the resulting errors are negligible when compared to the statistical uncertainties of A_y. Due to possible drift in the degree of polarization during the data-taking runs a further uncertainty of 1% is associated with the analyzing power results.

Chapter 5

Results

In this chapter the experimental triple differential cross-section and analyzing power results for the $^{208}Pb(\overrightarrow{p}, 2p)^{207}Tl$ knockout reaction near the quasi-free point, at the proton bombarding energy of 200 MeV, are presented and compared to theoretical calculations. The sensitivity of the non-relativistic DWIA calculations to various parameters are investigated. Among these are the effect of the choice of optical potential, different representations of the NN interaction contained in the t-matrix, the effect of non-locality corrections, the choice of bound state parameter sets and the choice of the energy prescription for the NN interaction. Relativistic DWIA calculations are also briefly discussed for comparison with the non-relativistic model.

The data is presented as a function of the energy of the most energetic proton in the final state, which for this experiment represents the proton detected in the magnetic spectrometer. This type of presentation is illuminating because the dependence of the two-body NN kinematics on the energy-sharing in the 3-body final state is such that the NN analyzing power is only weakly dependent on this variable. Consequently any strong variation of the $(p, 2p)$ analyzing power with energy-sharing can be attributed to aspects of quasi-free knockout [Mil98].

Experimental data for the unseparated $(3s_{1/2} + 2d_{3/2} + 2d_{5/2} + 1h_{11/2})$, $(3s_{1/2} + 2d_{3/2})$ and $(2d_{5/2} + 1h_{11/2})$ states are presented for all three angle pairs. For reasons mentioned previously (refer to sections 3.7 and 4.5) analyzing power data for the $3s_{1/2}$ and $2d_{3/2}$ single state knockout exists only for the two angle pairs (22°;-62.3°) and (28°;-54.6°), and the corresponding cross-section data only for the latter angle pair. The numerical experimental results are listed in Appendix A. All the figures presenting experimental data and theoretical calculations are to be found at the end of this chapter.

5.1 Experimental Results

Experimental triple differential cross-section and analyzing power results for the unseparated valence states are displayed and compared to theoretical calculations in Figs. (5.1) and (5.2). As for most of the figures shown in this chapter, panels in different rows represents results for different angle pairs, and knockout to different combinations of states for these various angle pairs are found in panels in the different columns. The error bars shown represent the statistical uncertainty. The theoretical results for the combined knockout to the various states, added in a suitable manner in order to compare it to experimental results of unresolved states, represent standard[1] non-relativistic DWIA calculations performed with the Nadasen [Nad81] optical potential to generate distorted waves, and the bound state parameter set of Mahaux [Mah88]. The Perey damping term [Per62] with non-locality range of $\beta = 0.85$ fm was used to take non-locality effects for the distorted and bound-state waves into account. The free (Arndt [Arn86] phase-shift based) NN interaction in the final energy prescription was employed to evaluate the NN scattering amplitude. These effective theoretical cross-sections and analyzing powers were calculated by weighting contributions from the different states with relative spectroscopic factors (RSF), obtained by Royer *et al.* [Roy70] in a $^{208}Pb(d,^3He)^{207}Tl$ study. For the combined knockout from n states the effective theoretical analyzing power is thus given by

$$A_{eff} = \frac{\sum_i^n d^3\sigma^i \cdot A_y^i \cdot RSF^i}{\sum_j^n d^3\sigma^j \cdot RSF^j} , \tag{5.1}$$

and the effective triple differential cross-section by

$$d^3\sigma_{eff} = \sum_i^n d^3\sigma^i \cdot RSF^i , \tag{5.2}$$

where $d^3\sigma^i$, A_y^i and RSF^i respectively represents the triple differential cross-section, analyzing power and relative spectroscopic factors for knockout to state i (normalized to $RSF^{3s_{1/2}}$).

As in the previous study of the $^{208}Pb(p,2p)$ reaction [Cow95, Are97], the spectroscopic factors calculated from the combination of states are obtained by normalizing the combined theoretical calculations to the experimental values, assuming that the main contribution to the

[1] Similar calculations have been employed successfully in the past to predict energy-sharing cross-section distributions [Sam86, Cow91, Bla93, Cow95].

Angle pair	all states	$3s_{1/2} + 2d_{3/2}$	$3s_{1/2}$	$2d_{3/2}$	$2d_{5/2} + 1h_{11/2}$	$2d_{5/2}$
(22°,-62.3°)	0.56 ± 0.05	0.49 ± 0.04	-	-	0.45 ± 0.04	0.53 ± 0.04
(28°,-54.6°)	0.73 ± 0.06	0.65 ± 0.05	0.61 ± 0.05	0.73 ± 0.06	0.53 ± 0.04	0.58 ± 0.05
(33°,-49.7°)	0.42 ± 0.04	0.35 ± 0.03	-	-	0.43 ± 0.03	0.46 ± 0.04

Table 5.1: Experimental spectroscopic factors extracted using the standard DWIA calculation. The error indicates experimental systematic errors.

combined cross-section is either from the s-state, as in the case of all states combined and for the combination of states $(3s_{1/2} + 2d_{3/2})$, or from the d-state for the combination of states $(2d_{5/2} + 1h_{11/2})$. The spectroscopic factors[2] are listed in table 5.1.

The experimental results and theoretical calculations for the separated ground and first excited states are displayed in Fig. (5.3), along with the results for the pair of states $(2d_{5/2}+1h_{11/2})$. Note that whereas in Figs. (5.1) and (5.2) the experimental results of the $(2d_{5/2}+1h_{11/2})$ states were compared to theoretical values for the combination of the two states, the theoretical values presented in Fig. (5.3) are for the $2d_{5/2}$ state only. By comparing DWIA calculations for only the $2d_{5/2}$ state with the result of the combination of the two states, shown in Fig. (5.4), it is evident that the contribution of the $1h_{11/2}$ state is negligibly small over most of the energy range covered in this experiment, and can subsequently be ignored. Only for the (22°;-62.3°) results below 135 MeV does the difference become substantial.

From Figs. (5.1) and (5.3) it is clear that the cross-sections are adequately predicted by the DWIA calculation. Good shape agreement is found between experiment and theory for the mixed state results of all the angle pairs, as well as the $3s_{1/2}$ and $2d_{3/2}$ results for the angle pair (28°;-54.6°). Only for the $2d_{5/2}$ results, and only in the region of minimum cross-section, does the theory consistently over-predict the cross-section. The experimental spectroscopic factors from table 5.1 compare favorably with those from the literature, listed in table 5.2. Despite the fact that the spread in spectroscopic factors is bigger than the expected systematic error of the experiment, reasonable agreement with previous studies is attained.

Serious discrepancies for the analyzing powers results are evident from Figs. (5.2) and (5.3). For results involving the $3s_{1/2}$ state the experimental analyzing power is noticeably lower than

[2]The listed spectroscopic values are normalized to the $2j + 1$ shell-model limit.

Reference	Study	Spectroscopic Factor
[Are97, Cow95]	$(p, 2p)$	$0.7 - 0.8$
[McD90]	$(e, e'p)$	0.65
[Jin92]	$(e, e'p)$	0.71
[Udi93]	$(e, e'p)$	0.70
[Pan84]	theory	0.71 ± 0.1
[Mah91]	theory	0.69

Table 5.2: Existing spectroscopic factors for the $3s_{1/2}$ state.

the theoretical values. Results for the separated $3s_{1/2}$ and $2d_{3/2}$ states reveal similar trends of reduced experimental A_y compared to the theoretical prediction. Only theoretical results for the $2d_{5/2}$ state display reasonable agreement with the experimental values. Note also that discrepancies between theory and experiment for especially the $(3s_{1/2} + 2d_{3/2} + 2d_{5/2} + 1h_{11/2})$ and $(3s_{1/2} + 2d_{3/2})$ results increase as the primary scattering angle θ_{K600} decrease. A similar observation was made by Li [Li94] in a study of the $^{3,4}He(p, 2p)$ reaction at 200 MeV. In a representation of the data as a function of the recoil momentum of the residual nucleus (p_B), shown in Fig. (5.5), this is seen to form a clear trend at the quasi-free point.

From the results we conclude that the theoretical model as applied above can successfully predict the cross-section, but that it generally fails for the analyzing power. In a naive picture of quasi-free scattering, the A_y is expected to agree with free scattering values. This simple picture is modified by, among other, the target-nucleon momentum distribution and distortion effects on the incoming and final state protons. Therefore, the observed A_y for the exclusive $(p, 2p)$ measurement has contributions from both the quasi-free reaction, as well as the underlying spin correlation coefficient of the pp interaction. The sensitivity of the non-relativistic theoretical calculations to these different contributions are investigated in the following sections.

5.2 Distortion Effects

Proton distortion effects for a heavy target such as ^{208}Pb are quite severe; triple differential cross-sections are typically diminished to less than 5% of the plane wave value [Cow95]. Despite

this massive reduction the previous section illustrated the same excellent shape agreement between experimental and theoretical triple differential cross-sections, as well as the encouraging spectroscopic factor results, as obtained from the low energy-resolution study of the $^{208}Pb(p,2p)$ reaction by Cowley and Arendse [Cow95, Are97]. This implies that, at least as far as the cross-section is concerned, distortions are introduced reliably. However, the reduction effect observed for the A_y clearly indicates that something is amiss, and merits an investigation into the effect of distortions on the analyzing power. The aspects of the distortions expected to prominently contribute to the analyzing power are the spin-orbit interactions as contained in the optical potentials, and the effective initial spin polarization (Maris effect) of the struck nucleon [Cha79]. Before these aspects will be studied in more detail, we first regard PWIA calculations to illustrate the prominent contribution of distortions to the analyzing power.

5.2.1 PWIA Calculations

PWIA results are obtained by setting all the distorting nuclear potentials, as well as the proton-nucleus Coulomb potential, to zero. In the absence of any distortions the analyzing power is representative of the free scattering value. This follows from the factorized form of the PWIA triple differential cross-section, shown in Eq. (2.32), where the term $F_{kin} \cdot S_{LJ} \cdot |\phi(-\overrightarrow{p}_B)|^2$ is eliminated in the ratio of cross-sections that forms the A_y, resulting in an expression of free-scattering cross-sections. Because the total energy and relative scattering angle at which the pp interaction occurs remains approximately constant over the energy-sharing range, the analyzing power will not vary appreciably as a function of energy of the outgoing proton, or between different states. This is illustrated by the straight line PWIA calculations for the analyzing power for the free NN interaction, evaluated in the final energy prescription, as shown in Fig. (5.6). The arrows indicate the position of minimum recoil. On the other hand, the PWIA cross-section results, shown in Fig. (5.7), are modified from the free NN cross-section by the momentum distribution of the bound protons.

The disparity between the PWIA and DWIA calculated A_y is evident from Fig. (5.6). Introducing distortions dramatically modifies the analyzing power from the free-scattering analyzing power benchmark. Both the spin-orbit term of the optical potential as well as the effective polarization of the knocked-out target nucleon, generated through the absorptive (imaginary)

central terms of the optical potentials, introduces reaction dependence on the spin orientation of the incoming protons. Because of the energy dependence of the distorting optical potentials, asymmetries between cross-sections for polarized incoming protons occur that vary with outgoing proton energy, giving rise to the fluctuation of A_y with energy.

5.2.2 Different Optical Model Potential Sets

Now that the major role played by the distorting optical potential in generating the shape of the analyzing power has been illustrated, we investigate the sensitivity of the non-relativistic DWIA calculation to the choice of different optical model potential (OMP) sets. The various OMP sets used are those mentioned in section 2.4. The calculated cross-sections and A_y shown in Figs. (5.8), (5.9), and (5.10) were obtained using the three Schrödinger-type optical potentials and the free NN interaction. Details of the calculations are as in section 5.1. Shown in Figs. (5.11), (5.12) and (5.13) are results for similar calculations using the six Dirac Equation Based (DEB) OMP parameter sets. Note that the cross-section results for the above-mentioned calculations are plotted with arbitrary spectroscopic factors. Although these latter potentials inherently contains non-locality through the Darwin term, this was neglected in favor of the non-locality correction using the Perey factor in order to be consistent with the non-relativistic optical potential calculations. These calculations are contrasted with calculations that employs the Darwin term in a brief examination of the prominence of non-locality effects in section 5.6.

For both the Schrödinger and the Dirac equation based optical potentials the overall shape of the cross-sections agrees very well with the experimental values. The variation in the spectroscopic factors, as presented in Appendix A, is due to the differences in the size of the imaginary part of the central potential, illustrated in Fig. (5.14). The analyzing powers calculated with the DEB optical potentials reveal an insensitivity with respect to different potential sets, all overestimating the analyzing power. And although differences are observed between calculations for the Nadasen [Nad81] potential and the virtually overlapping Madland [Mad87] and Schwandt [Sch82] potentials, calculations using the Schrödinger equation based potential sets are similarly inadequate. As remarked earlier, the calculation of spin-observables with the Nadasen [Nad81] potential could be somewhat unreliable due to the exclusion of analyzing power results in the extraction of the potential from elastic scattering experiments. For this reason the Schwandt

[Sch82] OMP is chosen arbitrarily as representative of the Schrödinger equation based optical potentials. Based on reaction cross-section arguments [Are97] the second parameterization of the DEB potential by Hama *et al.* [Ham90] (from here on referred to as the DH2D potential set) is considered the most appropriate phenomenological DEB optical potential. The small differences between calculations for these two representative optical potentials are evident from Figs. (5.15), (5.16) and (5.17). All further investigations will be done in terms of only these two optical potential sets.

The applicability of the different potential sets originate from the energy and target ranges of the data from which they were generated. All of the potential sets used above, except for those of Cooper *et al.* [Coo93], are strictly applicable only for proton-nucleus interactions $\geq$ 60 MeV. For the proton energy range probed by the knockout data of this investigation the potentials must be extrapolated to as low as 20 MeV, which raises questions about the applicability of these potentials, since the extrapolations may not be well behaved at the lowest energies. However, if this was the major source of the analyzing power discrepancy one would expect the problems to be localized at the high energy end of the energy-sharing distribution, i.e. where proton nucleus distortions at low energies of the associated proton are calculated. Since this is not the case, and since calculations with the potential sets of Cooper *et al.* [Coo93] yields results that does not differ significantly from results obtained with the more energy-restricted potentials of Hama *et al.* [Ham90], it is concluded that the reduction effect in the analyzing power in unlikely to be due to insufficiencies caused by the extrapolation of the OMP.

5.2.3 Modifications to the Optical Potential

From comparison between DWIA and PWIA results it is evident that the variation in the analyzing power as a function of the energy of the scattered proton originates from the distorted waves, as embedded in the term T_{LJM} in Eq. (2.20). Although different optical potentials yield distinctly different analyzing power results, none of those tested are capable of reproducing the measured A_y. In order to rule out the possibility that this state of affairs is brought about by deficiencies common to all potential sets used, the contribution of the various potential terms are investigated.

Figs. (5.18) and (5.19) illustrates the effect on the A_y when the real and imaginary spin-

orbit potentials are neglected. It is observed that, as expected due to the Maris effect, the A_y for the $3s_{1/2}$ state approaches the plane-wave limit, and no longer varies appreciably as a function of energy of the outgoing proton. On the other hand, the qualitative features of the analyzing power of the d-states remain the same, irrespective of whether the spin-orbit interaction is included in the generation of the distorted waves or not. Similar trends have been illustrated for the $^{208}Pb(p,2p)$ reaction at 150 MeV [Cha83]. It is also instructive to compare the effect of the exclusion of the spin-orbit interaction in either the entrance or exit channels. Figs. (5.20) and (5.21) represent calculations for different optical potentials where the spin-orbit interaction for respectively the incident and outgoing protons were neglected. It is seen that the main contribution to the shape of the A_y, for especially the $3s_{1/2}$ state, originates from the spin-orbit interaction between the projectile and initial nucleus, and not so much on the spin-orbit interaction between the outgoing protons and the residual nucleus. This follows from the fact that the contribution of the (real) spin-orbit potential relative to the central potential is more prominent at higher energies, as seen from a comparison of Figs. (5.14) and (5.22). This serves as another counter against objections regarding the use of the optical potential sets at low energies, at least concerning the spin-orbit terms, because the main contribution to the analyzing power originates from the spin-orbit interaction at energies well within the valid optical potential energy range. As was seen before, the d-states are much less sensitive to the presence of the spin-orbit interaction.

The contribution of the real and imaginary central potentials (excluding the Coulomb potential) are shown in Figs. (5.23) and (5.24). The central potential is seen to have only a damping effect on the (spin-orbit generated) analyzing power of the $3s_{1/2}$ state. It can thus be said that the presence of the spin-orbit potential supplies the central potential with a 'handle' with which it can influence the analyzing power. The effect on the d-states are more pronounced, where for especially the $2d_{3/2}$ state the absence of the central potential results in shifted analyzing power distributions. This shift decreases with an increase in the primary scattering angle, θ_{K600}. The resulting analyzing power is now mostly due to the spin-orbit interaction, the effects of which are no longer suppressed by the central potentials. Further calculations were also performed to separately study the effect of the real and imaginary parts of the central potential. This is shown in Fig. (5.25) and (5.26). It is seen that for the $2d_{5/2}$ state the imaginary central potential plays a more prominent role than the real potential, and vice versa for the $2d_{3/2}$ state.

Cross-section results for calculations where the central, Coulomb and spin-orbit terms in the Schwandt [Sch82] OMP are successively excluded in the calculation are shown in Fig. (5.27). Calculations for the DH2D potential (not shown here) yield similar results. The relatively small contribution of the spin-orbit term to the cross-section compared to that of the central terms is clearly seen.

It is concluded that for the $3s_{1/2}$ state the A_y is mainly shaped by the spin-orbit part of the OMP, whereas for the other $l \neq 0$ states both the spin-orbit term and the Maris effect contribute. For the $2d_{3/2}$ state severe distortions due to the heavy ^{208}Pb target causes asymetries in cross-section, due to the Maris effect, to dominate over the contribution of the spin-orbit part of the OMP to A_y, whereas for the $2d_{5/2}$ state the sources of asymmetry are divided between the spin-orbit potential of the OMP and the Maris effect.

A Closer Look at the Spin-Orbit Potential

Because the spin-orbit potential plays such a big role in determining the A_y of the s-state, modifications to the spin-orbit interaction and its effect on the analyzing power results requires further investigation. The physical significance of the real spin-orbit term is well-established within the non-relativistic framework. On the other hand, the imaginary spin-orbit term has a dubious physical meaning, and is said to merely represent a spin-dependent modification of the central imaginary potential, reducing absorption in the surface area [Nad81, Sch82]. Positive values for the imaginary W_{so} does therefore not imply flux creation. This is in contrast with the Dirac equation based OMP, where the imaginary spin-orbit potential appears as a natural consequence of the Dirac framework, and is shown to be critical to the fit of OMP calculations to proton nucleus scattering data, even at low energies [Coo93].

We investigate the effects on A_y for arbitrary changes to the real and imaginary spin-orbit potentials. In Figs. (5.28) and (5.29) calculations for $W'_{so} = a \times W_{so}$, with $a = (-2, -1, 0, 1, 2)$, are presented. Changing the sign of W_{so}, making it repulsive as in the case of the real spin-orbit term, clearly improves agreement of experiment with theoretical results: for the Schwandt [Sch82] potential this results in reflection of the calculation around the axis defined by the PWIA calculation. It is noticed that the differences between calculations for W_{so} and $-W_{so}$ for a 'standard' OMP are much more pronounced than for a DEB OMP. This is due to a bigger

contribution of W_{so} to the total imaginary part of the OMP in the case of the Schwandt [Sch82] OMP as opposed to the DH2D potential at 200 MeV, illustrated in Fig. (5.22). The drastic effects that changes to the real spin-orbit potential has on the analyzing power are shown in Figs. (5.30) and (5.31), for $V'_{so} = a \times V_{so}$ with $a = (-2, -1, 0, 1, 2)$.

Although better agreement between theory and experimental data can be achieved by appropriately changing the various potential parameters, the physical significance of this is of dubious value. Any arbitrary change in the various terms of the OMP seriously compromise the ability to predict proton-nucleus elastic scattering observables. A peculiar feature of the calculated analyzing powers of the s-state for *all* the calculations featuring modified spin-orbit potentials is that variation in the spin-orbit potential has a negligible influence on the analyzing power at the point of minimum recoil. We learn from this, as also stated by Miller [Mil98], that the consistent failure of the analyzing power prediction at the quasi-free point indicates that deficiencies of the OMP alone cannot be blamed for the failure of the model. If we believe in the validity of the non-relativistic DWIA model, this indicates the need for a refinement of other aspects of the model, such as the description of the NN interaction.

5.3 Density Dependence of the NN Interaction

In a study of proton knockout from the $s_{1/2}$ states of ^6Li, ^{12}C and ^{40}Ca at 392 MeV [Hat97] at the quasi-free point, it was shown that the experimental A_y exhibited a reduction as a function of averaged density, which suggests the existence of a nuclear medium effect on the NN interaction. It is also known that utilizing a density dependent t-matrix results in the reduction of the calculated analyzing power for exclusive quasi-free scattering at 400 and 500 MeV [Nor98, Mil98, Nor99]. In this section calculations for the standard free NN interaction are contrasted with two different methods of incorporating density dependence in the NN interactions; the Kelly empirical effective interaction [Kel94], and the effective mass type density dependent interaction of Horowitz and Iqbal [Hor86].

The effect of introducing density dependent NN interactions are highlighted in the PWIA calculations shown in Fig. (5.32), where complications due to distortions are ignored. Different types of interactions yield, as expected, different A_y, albeit still constant with energy-sharing,

and density dependence has the effect of reducing the free analyzing power. We find that this reduction is decreasing with increase of θ_{K600}. This suggests that at bigger primary scattering angles the quasi-free reaction samples the NN interaction closer to the nuclear surface, where the nuclear density is lower. Confirmation of this is given in section 5.4.

Density dependent calculations where distortions are generated through the Schwandt [Sch82] OMP are presented in Figs. (5.33), (5.34) and (5.35). Except for the different NN interactions involved, the detail of the calculations are the same as in section 5.1. Similar calculations using the DH2D potential are presented in Figs. (5.36), (5.37) and (5.38). The reduction in analyzing power due to medium modified NN interactions results in acceptable agreement for the $2d_{5/2}$ state, and less satisfactory agreement for the $2d_{3/2}$ state. For the $3s_{1/2}$ state the disagreement remains significant. No meaningful difference between the two different types of density dependent calculations are observed. Although the reduction in analyzing power is a move in the right direction, it is insufficient to give a satisfactory prediction of the experimental values over the whole energy-sharing range. This is especially true for the $3s_{1/2}$ state. It is also observed that the discrepance tends to be at a minimum at the point of minimum recoil.

As an indication of the insensitivity of the cross-section to subtle effects such as density dependence, we observe that the cross-section results are satisfactory in all instances, and are not visibly affected by different density dependent interactions. Spectroscopic values, summarized in Appendix A, largely remain unaffected.

5.4 Radial Localization of the DWIA Cross-section

At a first glance the limited effect of the inclusion of density dependence on the analyzing power might seem to be unexpectedly small for such a heavy target as ^{208}Pb. However, the significant contribution of the spin-orbit potential terms (surface terms for both the Schrödinger and the Dirac equation based optical potentials) to analyzing power calculations is a possible indication that the interaction under investigation is surface peaked. Effects due to the medium modification of the NN interaction may therefore not significantly influence the results.

Confirmation of the surface localization of the quasi-free knockout reaction under investigation is provided by calculating the contribution of the triple differential cross-section as a

function of the nuclear radial distance. The calculation was performed for the fully factorized DWIA, as modeled by an earlier version of the code *THREEDEE*. This technique requires the integration of T_{LJM}^{fac} (refer to Eq. (2.26)) from a lower cutoff radius $r \neq 0$ to a suitable maximum radius, in order to obtain a value for the triple differential cross-section, $d^3\sigma(r)$, which provides a measure of the contribution to the reaction in the range $r \to \infty$. By varying the lower cutoff radius the difference $\Delta d^3\sigma = d^3\sigma(r) - d^3\sigma(r + \Delta r)$ serves as a measure of the contribution to the reaction in the range from $r \to r + \Delta r$ [Sam81] .

The histograms shown in Fig. (5.39) represents the radial distribution of contributions to the DWIA cross-section at the point of minimum recoil. These results are arbitrarily normalized to comparable magnitudes for comparison purposes. Negative values for the radial contribution are attributed to interference between the distorted waves. The smooth solid curves represent the bound state radial wave functions, shown for radial reference. It is clear that the reaction is localized mainly on the nuclear surface at a radius $\sim r_c \times A^{1/3} = 7.1$ fm (for $r_c = 1.2$ fm). After closer inspection it is seen that only by looking at the smaller contributions toward the nuclear centre does differences between different states and angle pairs become noticeable. For all the measured angle pairs the cross-section of the s-state displays a bigger contribution from the nuclear interior than the d-states. A definite trend is also observed for the s-state, where the contribution to the reaction from the nuclear interior is decreasing with increasing θ_{K600}.

The fact that the s-state has a bigger contribution from the nuclear interior suggest that it should be more susceptible to medium effects of the NN interaction. This sensitivity will decrease for increase in primary scattering angle, since the contributions in the nuclear interior is shown to decrease. These conclusions are however valid only at, or near, the quasi-free point. Further calculations were performed at arbitrary points ($p_{recoil} \geq 80$ MeV/c) away from the point of minimum recoil. An increase in the contribution to the reaction at smaller radii, compared to the quasi-free point calculations, is observed in Fig. (5.40). If it is assumed that the problem with the model is mainly due to an inadequate description of the density dependent t-matrix, then the better agreement at the quasi-free point for calculations that include medium effects is reasonable since away from the quasi-free points medium effects plays a bigger role, and thus results in bigger differences between data and theory.

5.5 Bound State Wave Function

It is well known that for the non-relativistic DWIA the cross-section is sensitive to the choice of bound state potential set [Kit80, Are97]. The shape and especially the magnitude of the triple differential cross-sections are sensitive to the *rms* radius of the single particle wave function. On the other hand, studies of the $^{16}O(p, 2p)$ reaction at 200 MeV [Kit80] revealed that the analyzing power is insensitive to the *rms* radius. Within the framework of the relativistic DWIA it was also shown that modification to the bound state results in substantial changes in the cross-section [Coo89, Max90, Max94, Ike95]. Ikebata [Ike95] illustrated that the A_y results, similar to the cross-section results, shifts toward the data as the *rms* radius increases. The difference between the different calculations is however much less pronounced than in the case of the cross-section.

The bound state wave used in the calculation is constrained by electron scattering data, and is therefore not likely to be problematic. Nevertheless, the sensitivity of the analyzing power was investigated by comparing the results of calculations using six different single particle bound state waves. Five of these were generated from parameter sets [Cha83, Mah88, Qui88, Ma91, Are97] for the standard bound state wave functions as a solution of the Schrödinger equation, while the remaining one was obtained as a solution of the Dirac equation in potential wells derived from relativistically mean-field Hartree calculations. Calculations for the free NN interaction and the Schwandt [Sch82] OMP for the six different bound state potentials are shown in Figs. (5.41) and (5.42). All bound state parameter sets yield reasonable *rms* values, ranging between 5.06 fm and 5.32 fm for the $3s_{1/2}$ state, and compares favourably with $(e, e'p)$ [Qui88] and sub-Coulomb (t, α) [Woo82] studies. All the calculations for the standard Woods-Saxon-type bound state waves were performed by including non-locality effects on the proton bound state wave function through the Perey damping factor with non-locality range of $\beta = 0.85$. For the relativistically calculated bound state non-locality is automatically taken into account [Hor81].

From the calculations it is clear that the analyzing power is not very sensitive to the bound state wave function. The discrepancies in the cross-sections are much more pronounced, as expected from previous studies. For example, Arendse [Are97] showed that the choice of different bound state parameter sets results in an uncertainty of the spectroscopic value of typically 15%.

5.6 Non-locality Effects on the Distortions

The insensitivity of the analyzing power to the influence of non-locality effects of the potentials used to generate the distorted waves are demonstrated in this section. The calculations represented in Figs. (5.43), (5.44) and (5.45) contrast DWIA predictions (for different NN interaction types evaluated in the FEP, different OMP, and the standard bound state wave-function) with and without non-locality taken into account for the distorted waves. Non-locality corrections were achieved through the damping factor of Perey and Buck [Per62], with the range of non-locality $\beta = 0.85$ fm. From the results it is clear that the effect is small for the analyzing power. As found previously [Ant81, Kan90, Are97], the spectroscopic factors reduce when non-locality is ignored, without significantly changing the shape of the cross-section distribution.

Calculations for the DEB optical potential were also performed where non-locality is introduced through the Darwin term. From Figs. (5.46) and (5.47) it follows that results for the Dirac equation based OMP for the Kelly NN interactions and the DH2D OMP with non-locality calculated by using the Perey factor compares favorably with relativistic calculations with the Darwin factor. Udias *et al.* [Udi95] mentions that the effect of the Darwin factor is the same as the effect when using the Perey factor with $\beta = 1$. For the present experimental conditions this is shown to be closer to $\beta = 0.85$ (refer to Fig. (5.48)).

5.7 Energy Prescription

Approximating the half off-shell t-matrix with an on-shell t-matrix could in principle have a big influence on the DWIA calculations. However, off-shell effects for this study, with a projectile energy of 200 MeV, a Q-value of 8.013 MeV and kinematics emphasizing minimum recoil, are assumed to be negligible. Furthermore, since the half-off shell results are expected to yield results between the initial and final energy prescriptions of the on-shell interaction, this section is only concerned with the determination of the sensitivity of the calculation to the choice of energy prescription of the on-shell t-matrix. It was shown in the previous low resolution study of the $^{208}Pb(p,2p)$ reaction at 200 MeV [Are97] that the cross-section is insensitive to the choice of energy prescription, as was found for the cross-section studies of the $^{16}O(p,2p)$ reaction at 151 MeV [Cow91], and $^{4}He(p,2p)$ reaction at 100 MeV [Whi90]. Nothing is as yet known about

the sensitivity of the analyzing power.

Shown in Figs. (5.49), (5.50) and (5.51) are IEP and FEP calculations made for the DH2D optical model of Hama [Ham90] and the different NN interaction types. Equivalent cross-section results are depicted in Fig. (5.52). Different BSWF parameter sets were earlier shown not play a role, and therefore the standard set of [Cow95] was used in the calculations shown in the figures. Hardly any difference between the two energy prescriptions are noticed for calculations using either the free or the Horowitz Iqbal NN interaction. Only the Kelly interaction is shown to be somewhat sensitive to the choice of energy prescription. The FEP cross-section is higher than the IEP, and the inverse is true for analyzing power results. This sensitivity to the energy prescriptions is however not sufficient to explain the analyzing power reduction.

5.8 Calculations with the RDWIA

The initial failure of the DWIA to predict analyzing powers at 200 MeV [Kit80, Ant81] was solved by the relativistic finite-range DWIA calculations of Maxwell *et al.* [Max90, Max93] and Mano *et al.* [Man98]. This success at 200 MeV is in contrast with the failure of these calculations to achieve similar success at 500 MeV [Max96, Mil98]. In a first test of the predicative powers of the RDWIA for proton knockout from a heavy target at the projectile energy of 200 MeV, the relativistic finite-range DWIA calculation as modeled by Mano *et al.* [Man98] is compared to a non-relativistic DWIA calculation.

In Fig. (5.53) calculations performed with the relativistic DWIA code of Mano [Man00] are compared to a representative density dependent non-relativistic DWIA calculation, using the DH2D OMP and the Kelly NN interaction. Experimental results are compared to the RDWIA calculations in Figs. (5.54), (5.55) and (5.56). The marked reduction observed for the s-state analyzing power in the region of recoil momentum $\geq$ 70 MeV/c, found to increase with decrease of θ_{K600}, is responsible for the improvement in overall agreement with all the experimental results involving the $3s_{1/2}$ state. However, near the quasi-free point it is found that the relativistic calculations suffer from similar discrepancies with the experimental data as the non-relativistic calculations. The results for the $2d_{3/2}$ state appears to be an 'attenuated' version of the non-relativistic calculation, which leads to a better agreement for the $2d_{3/2}$ results

for the angle pair (22°;-62.3°), while resulting in worse agreement for the angle pair (28°;-54.6°). The relativistic calculation also fails to give good predictions of the experimental data for the $2d_{5/2}$ state, faring even worse than the non-relativistic calculations. Both the relativistic and non-relativistic calculations for the cross-sections yield similar agreement with the experimental values.

Although the failure of the relativistic DWIA calculation is not as spectacular as found for the $^{16}O(p,2p)$ reaction at 500 MeV [Mil98], it is nevertheless an effect not seen for the quasi-free scattering experiments at 200 MeV for the lighter targets (^{16}O,^{40}Ca). It should however be remembered that these calculations are only for the free NN interaction, and that density dependent calculations should be performed before the relativistic DWIA can be discarded.

5.9 Comment on a Possible Poor Understanding of the NN Interaction

If one assumes that the DWIA is a valid representation of the physical process under investigation, then the inability to reproduce the analyzing power could possibly imply an inadequate description of the NN interaction, which yields a too high benchmark analyzing power. This is illustrated in Fig. (5.57) by a relative shift of 0.15 between the experimental and theoretical A_y of the mixed $(3s_{1/2} + 2d_{3/2} + 2d_{5/2} + 1h_{11/2})$ and $(3s_{1/2} + 2d_{3/2})$ states, which leads to much improved agreement between theory and experiment.

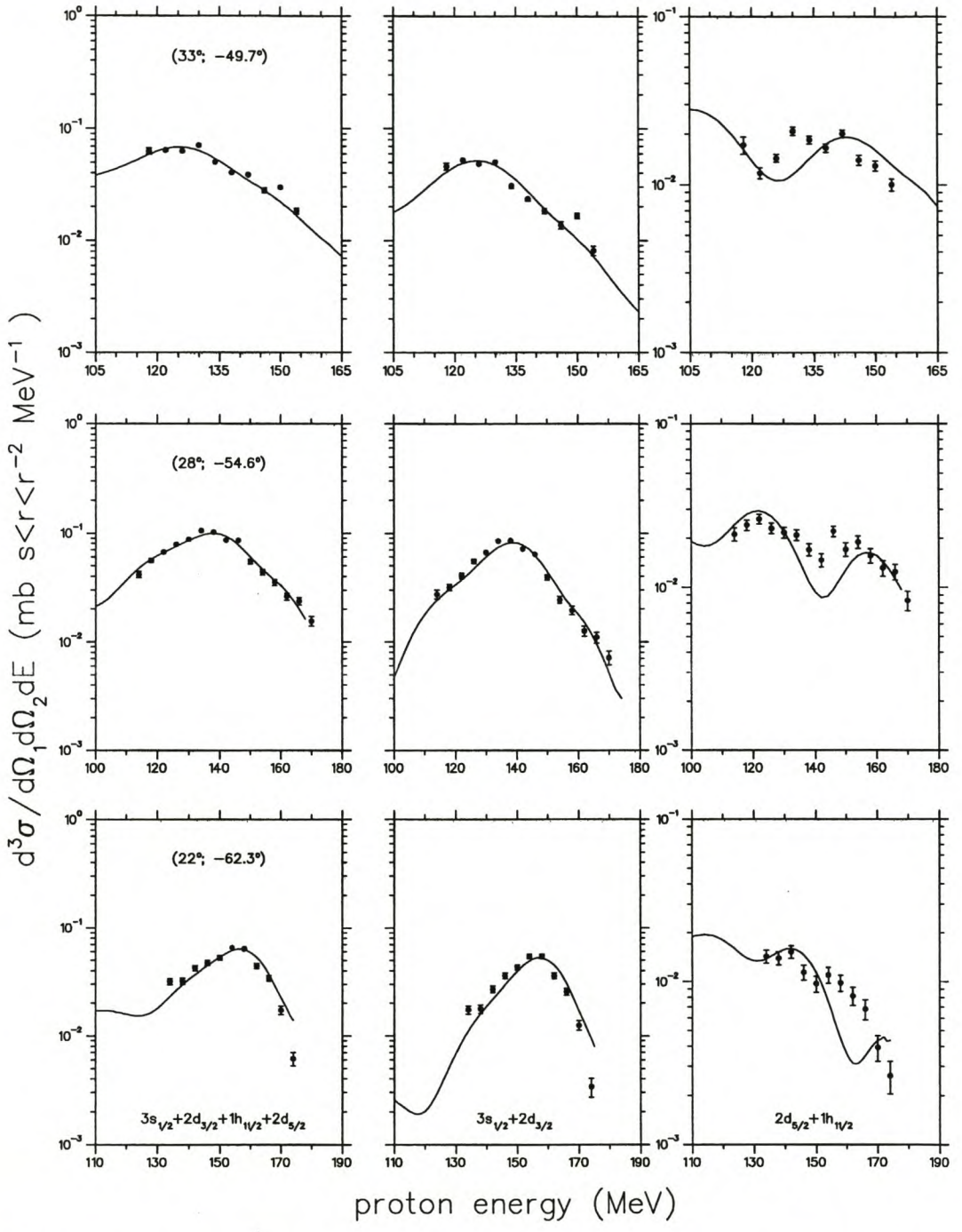

Figure 5.1: Energy-sharing cross-sections for the $^{208}Pb(p,2p)^{207}Tl$ reaction at 200 MeV for the unresolved valence states. The solid curves represents standard DWIA calculations which employs the free NN interaction and the Nadasen [Nad81] optical potential. The DWIA calculations shown are plotted with the spectroscopic factors from table 5.1, multiplied by the shell model value of $2j+1$.

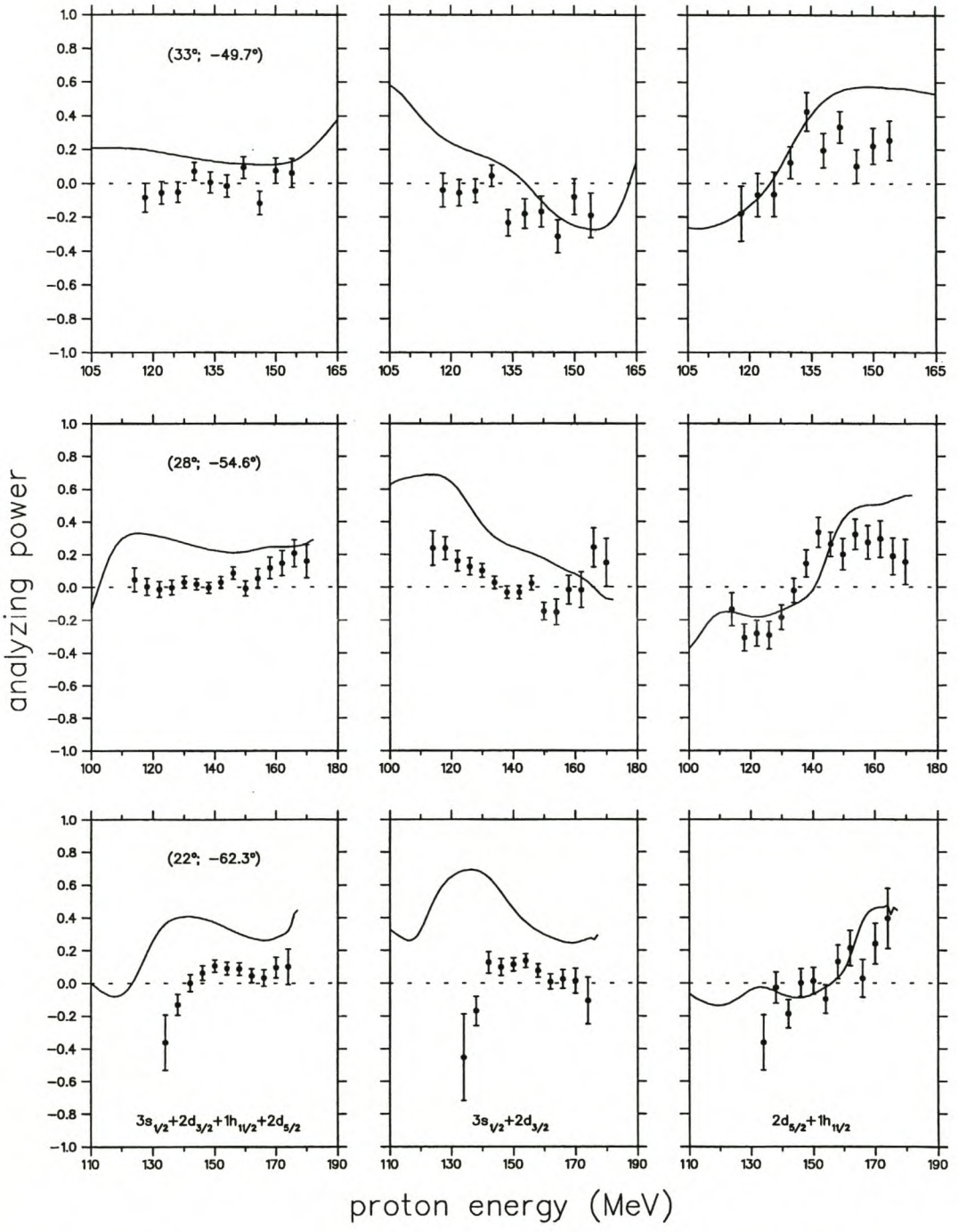

Figure 5.2: Energy-sharing analyzing powers for the $^{208}Pb(p,2p)^{207}Tl$ reaction at 200 MeV for the unresolved valence states. The details of the calculations are the same as in Fig. (5.1).

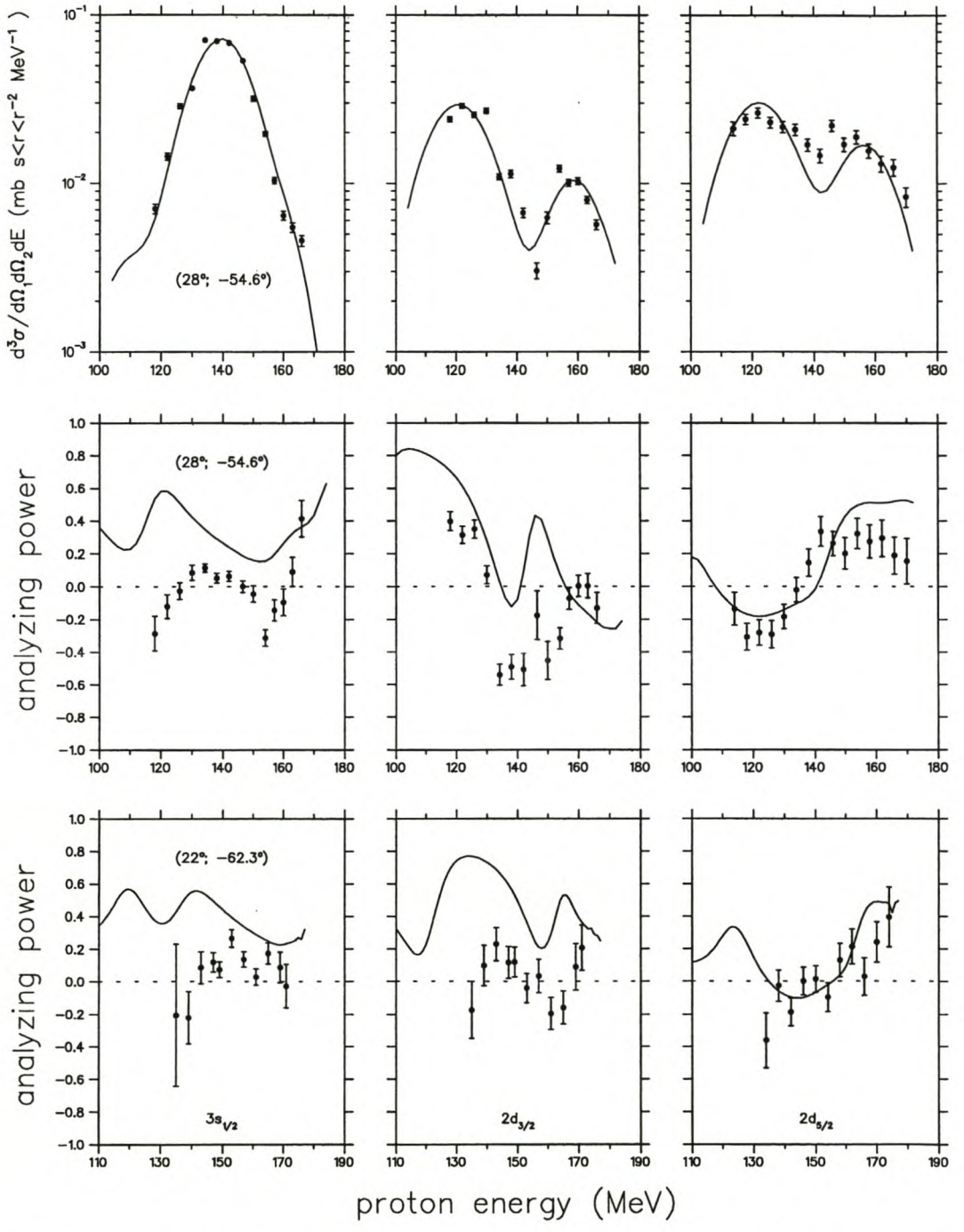

Figure 5.3: Energy-sharing analyzing power and cross-section results for the $^{208}Pb(p,2p)^{207}Tl$ reaction for the resolved $3s_{1/2}$ and $2d_{3/2}$ states. Calculations shown for the $2d_{5/2} + 1h_{11/2}$ experimental results are for the $2d_{5/2}$ state only. The details of the calculations are the same as in Fig. (5.1).

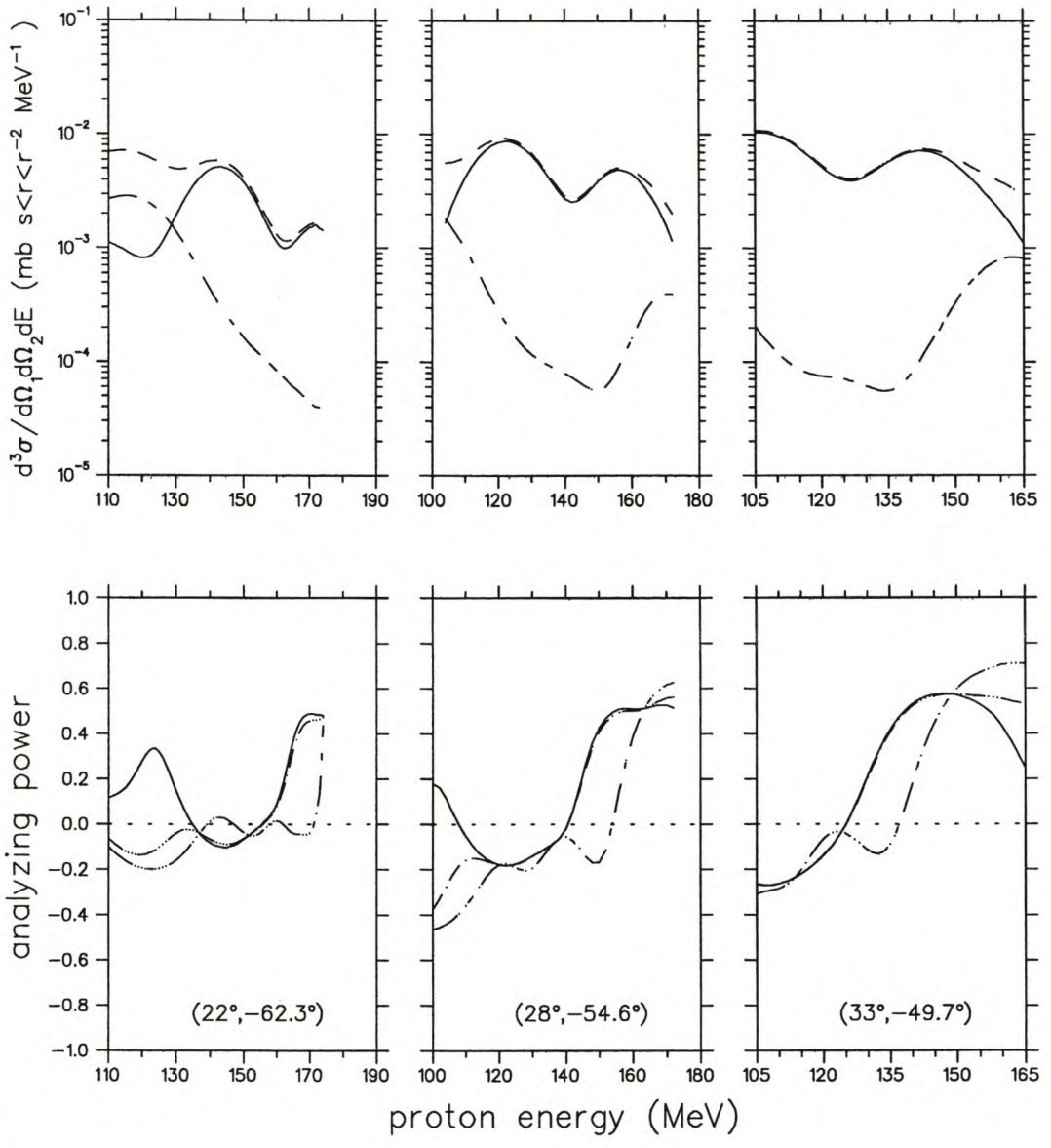

Figure 5.4: DWIA calculations for the cross-sections and analyzing powers of the $2d_{5/2}$ state (solid line), the $1h_{11/2}$ state (dot-dashed line) and combination of the two states (dashed line) for non-relativistic DWIA calculations with the free NN interaction and the Nadasen [Nad81] optical potential. The contribution of the $1h_{11/2}$ state on the combined $2d_{5/2} + 1h_{11/2}$ results is shown to be negligible.

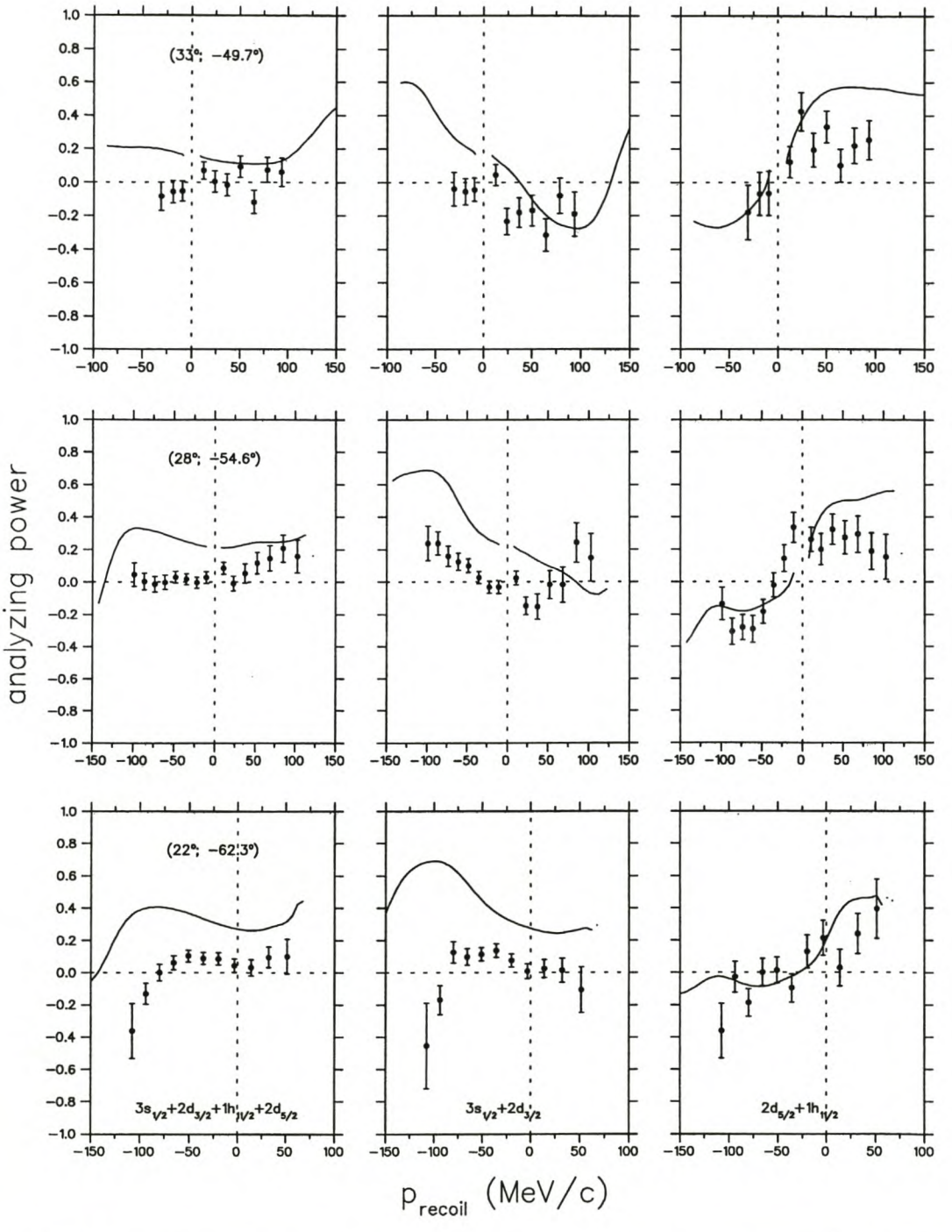

Figure 5.5: Analyzing power energy-sharing distributions of the unseparated results for the three sets of angle pairs as a function of the recoil momentum. The details of the calculations are the same as in Fig. (5.1).

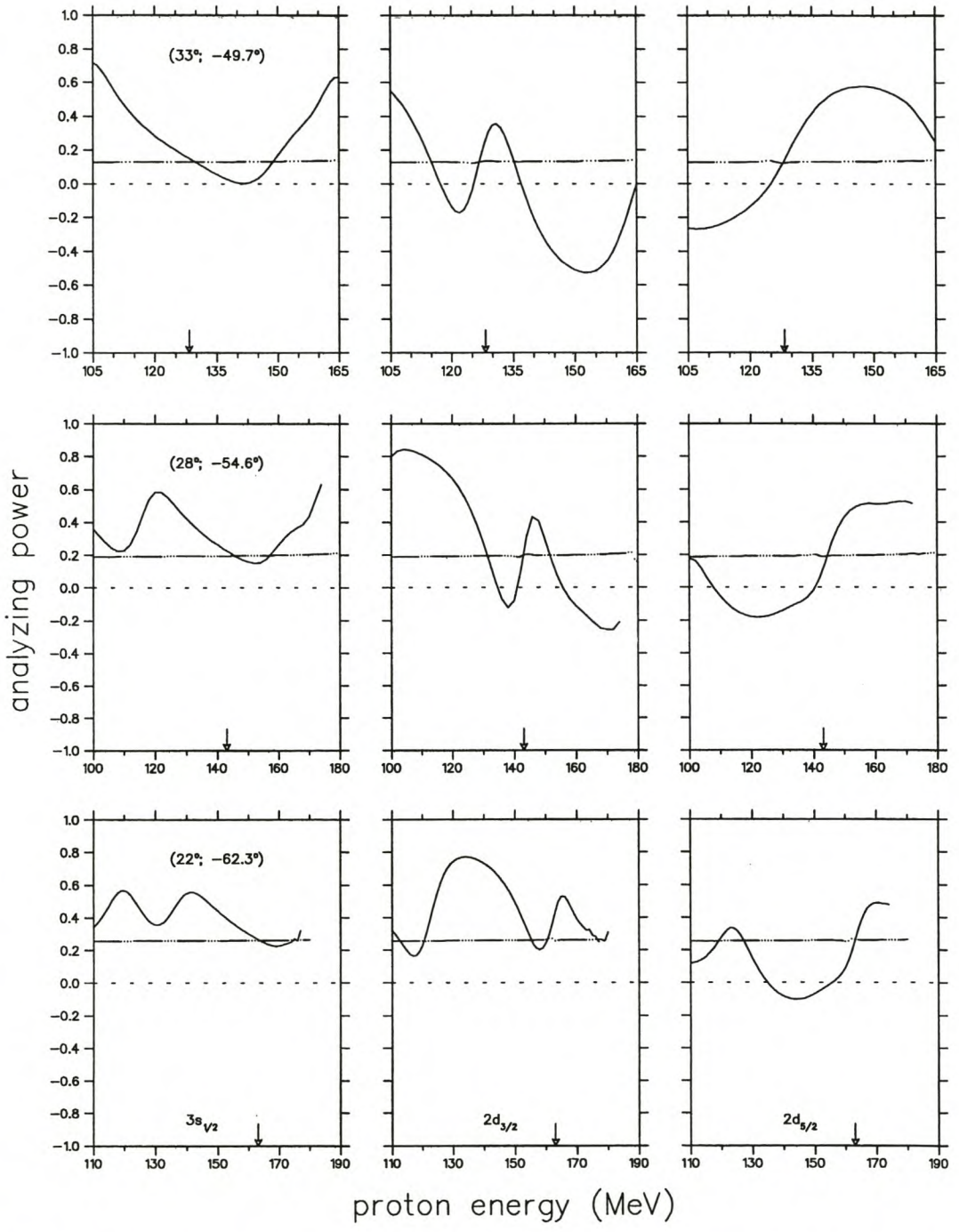

Figure 5.6: Analyzing power energy-sharing distributions for the DWIA calculation employing the free NN interaction and Nadasen [Nad81] OMP (solid line), and the equivalent PWIA calculation (dashed line). The arrows indicate the regions of minimum recoil.

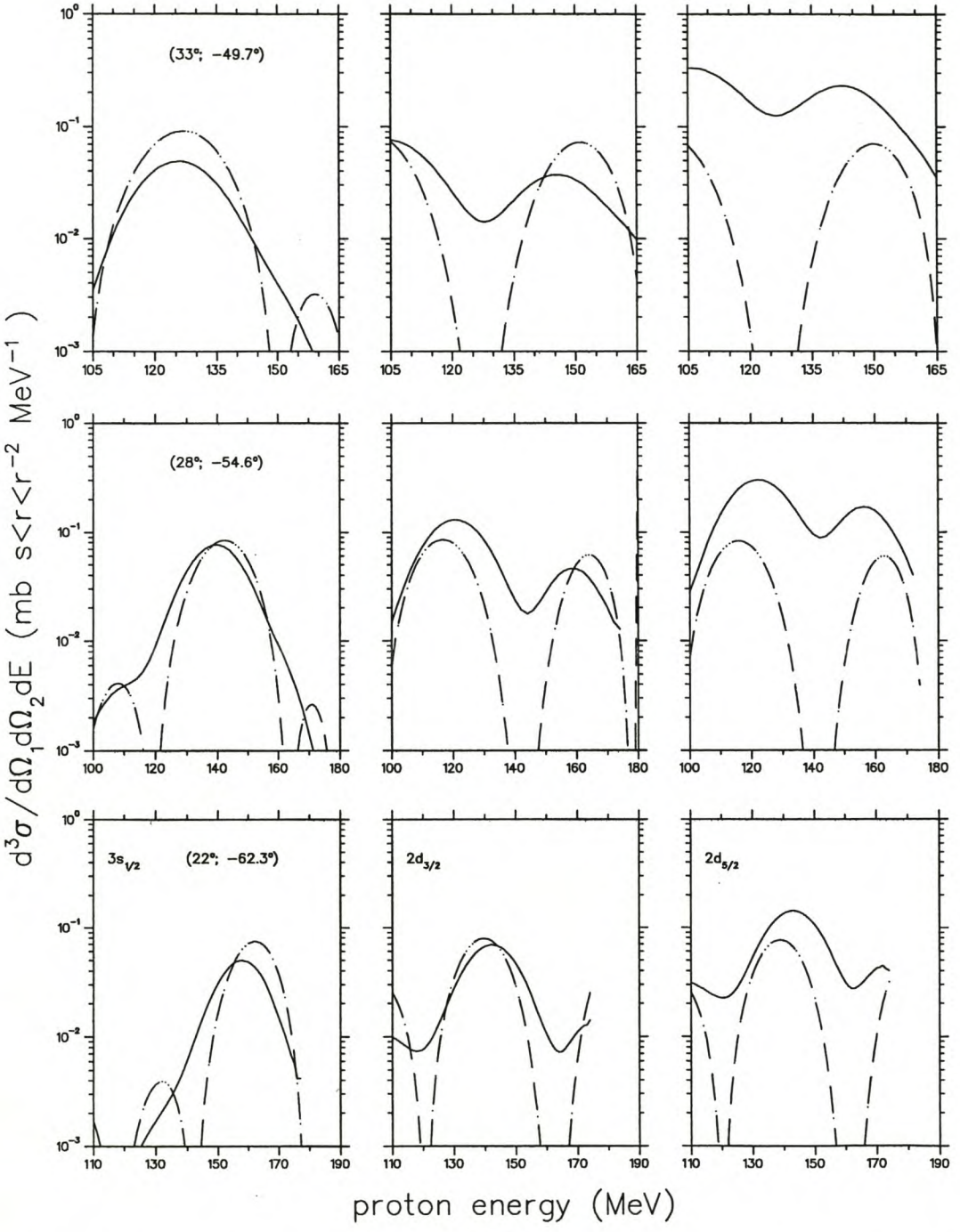

Figure 5.7: Cross-section energy-sharing distributions for the DWIA calculation employing the free NN interaction and Nadasen [Nad81] OMP (solid line), and the equivalent PWIA calculation (dashed line). The DWIA calculations are plotted with a normalization factor of 1. For comparison purposes the PWIA calculations are multiplied by a factor of 0.05.

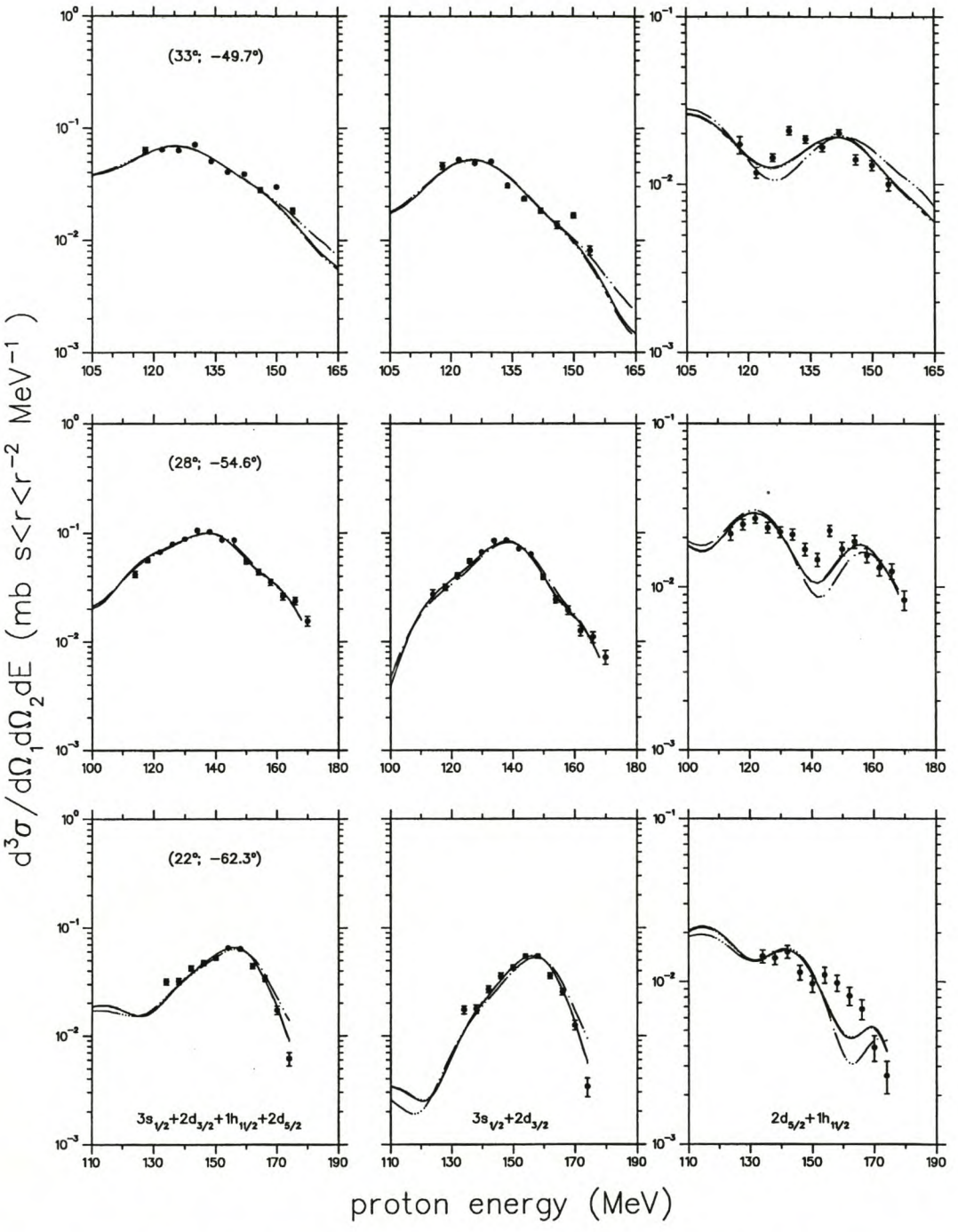

Figure 5.8: Energy-sharing cross-sections for the unresolved valence states. The curves represent DWIA predictions for the free NN interaction and distorting optical potential parameter sets of Schwandt [Sch82] (solid line), Nadasen [Nad81] (dashed line) and Madland [Mad87] (dot-dashed line). The DWIA calculations shown are plotted with the spectroscopic factors from Appendix A.

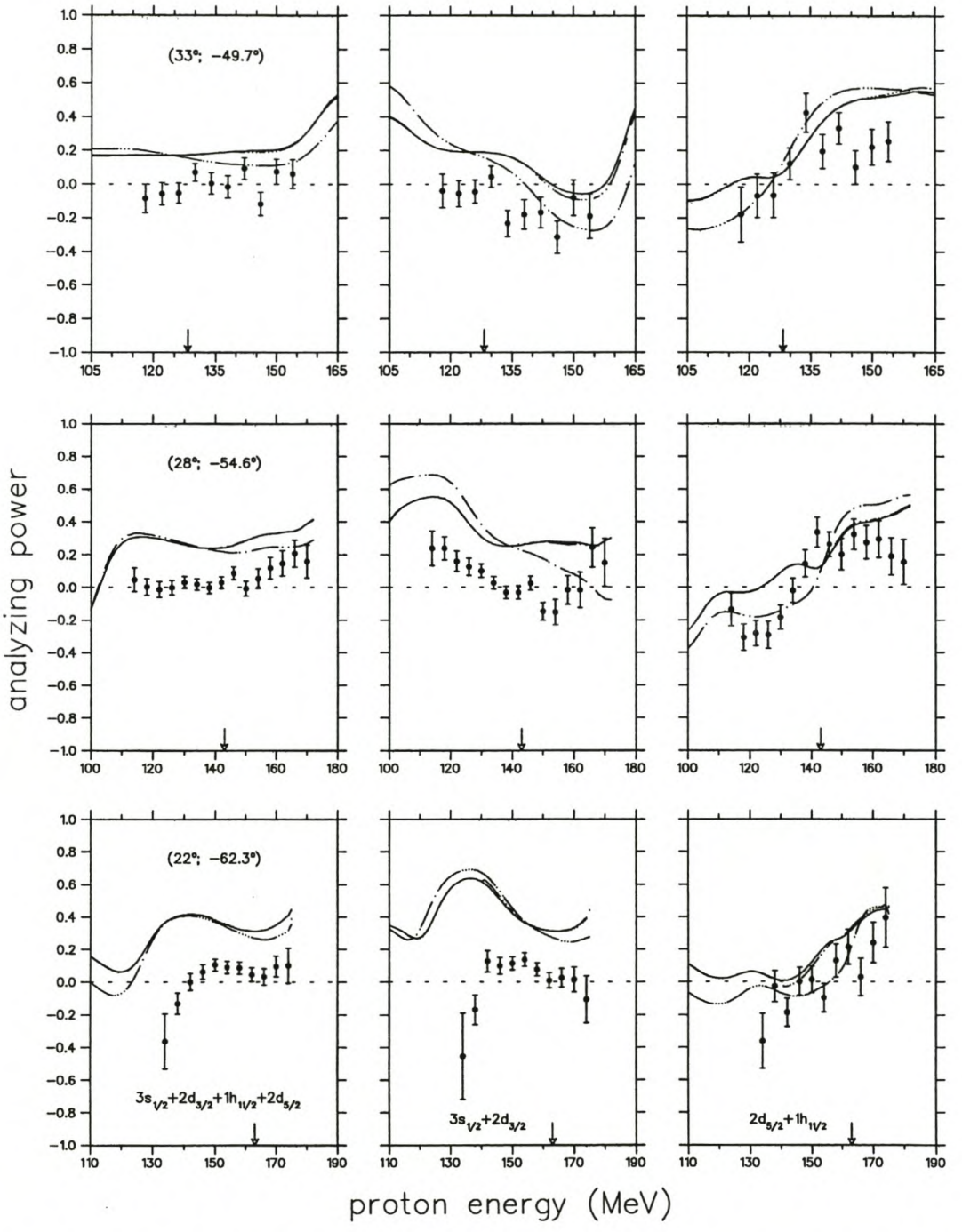

Figure 5.9: Energy-sharing analyzing powers for the unresolved valence states. The details of the calculations are the same as in Fig. (5.8).

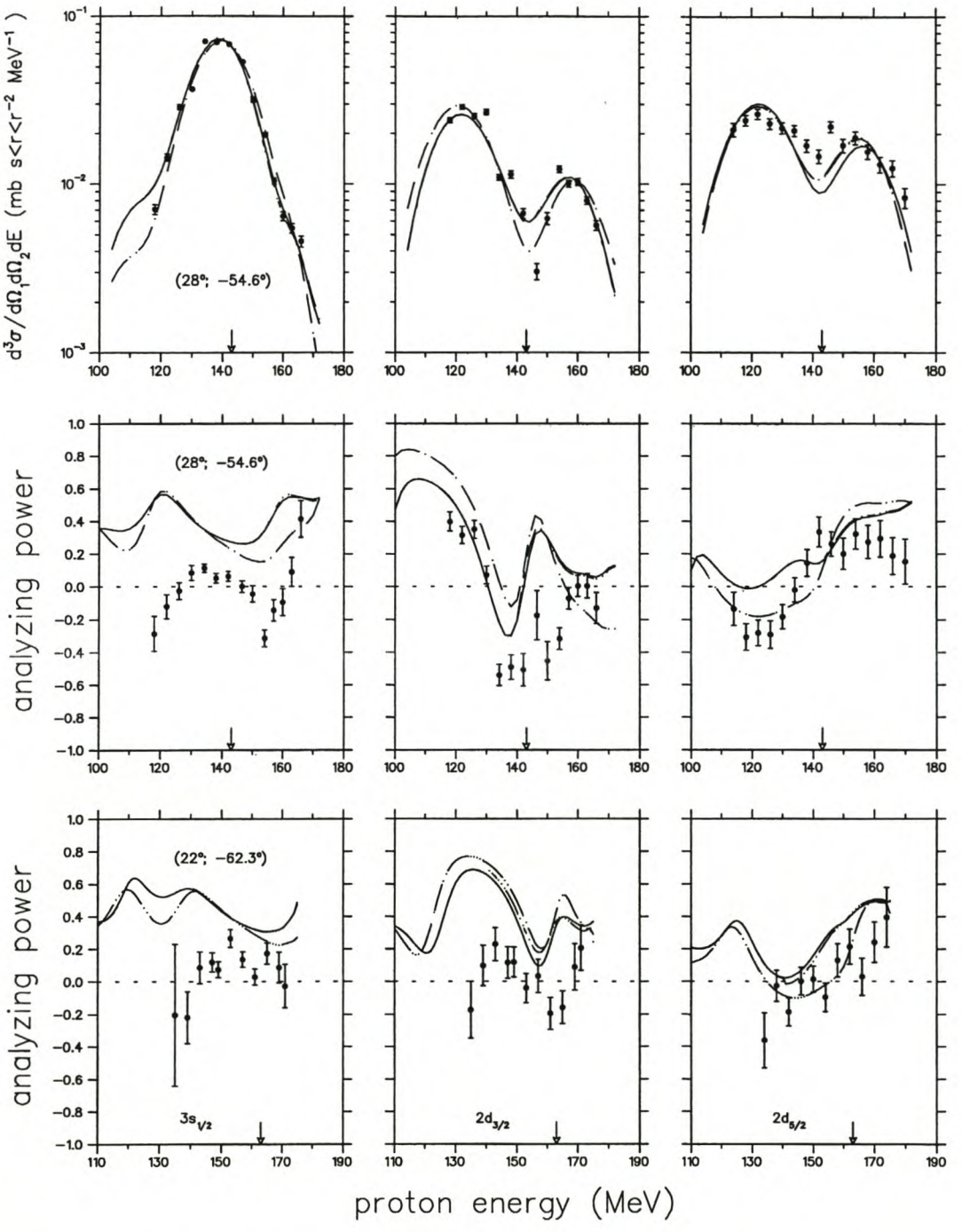

Figure 5.10: Analyzing power and cross-section energy-sharing distributions for the resolved $3s_{1/2}$ and $2d_{3/2}$ states. The curves represent DWIA predictions for free NN interaction for the distorting optical potential parameter sets of Schwandt [Sch82] (solid line), Nadasen [Nad81] (dashed line) and Madland (dot-dashed line).

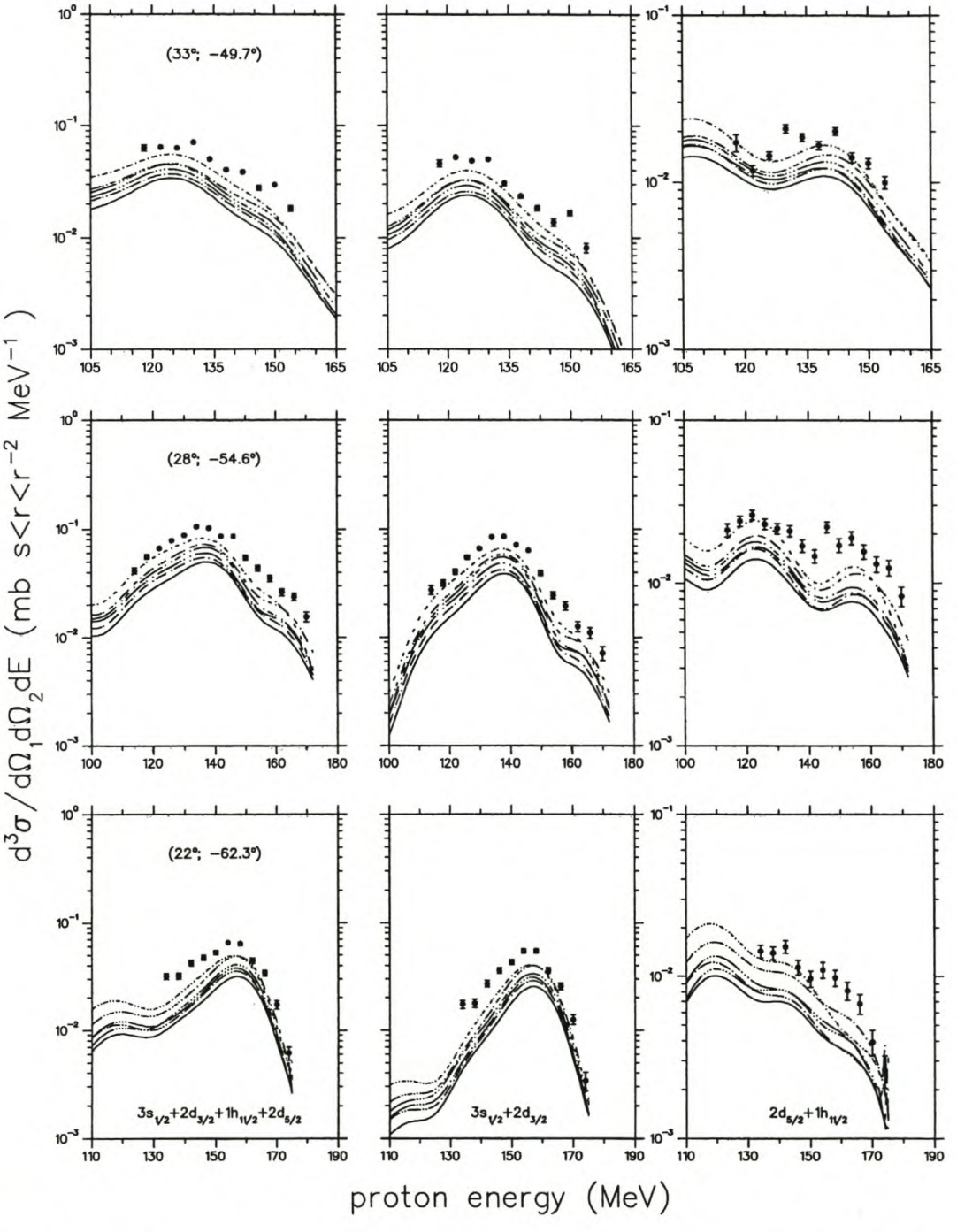

Figure 5.11: Cross-section energy-sharing distributions for the unresolved valence states. The curves represent DWIA predictions for free NN interaction for distorting optical potential parameter sets of Cooper [Coo93] EDAD1 (solid line), EDAD2 (dashed line), EDAD3 (dot-dashed line), EDAI (short dashed line), and Hama [Ham90] DHD (short dot-dashed line) and DH2D (dotted line). The DWIA calculations are arbitrarily scaled for display purposes. Actual spectroscopic factors, which would normalize the theoretical results properly, are available from Appendix A.

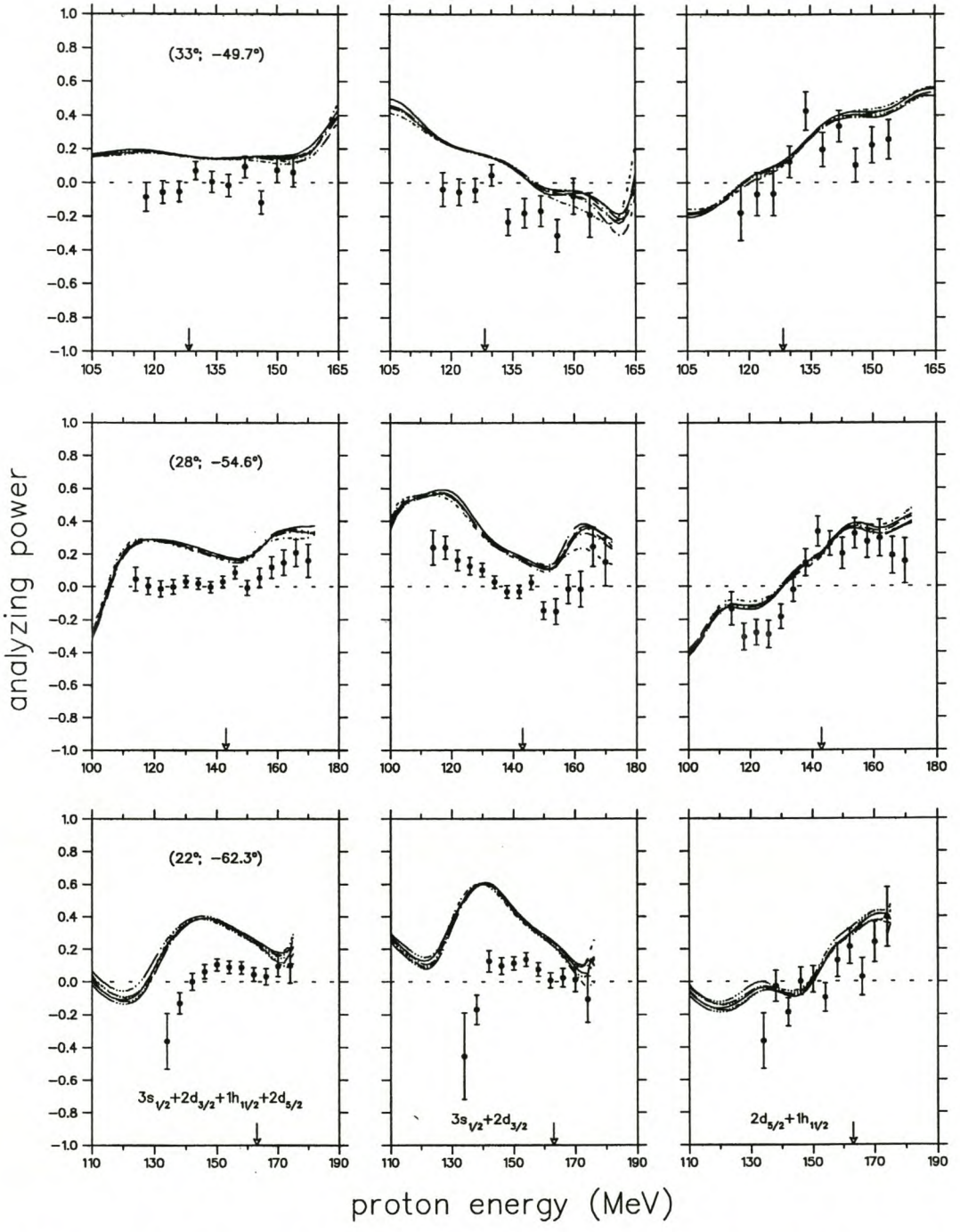

Figure 5.12: Analyzing power energy-sharing distributions for the unresolved valence states for DWIA calculations using DEB optical potentials. The details of the calculations are as in Fig. 5.11.

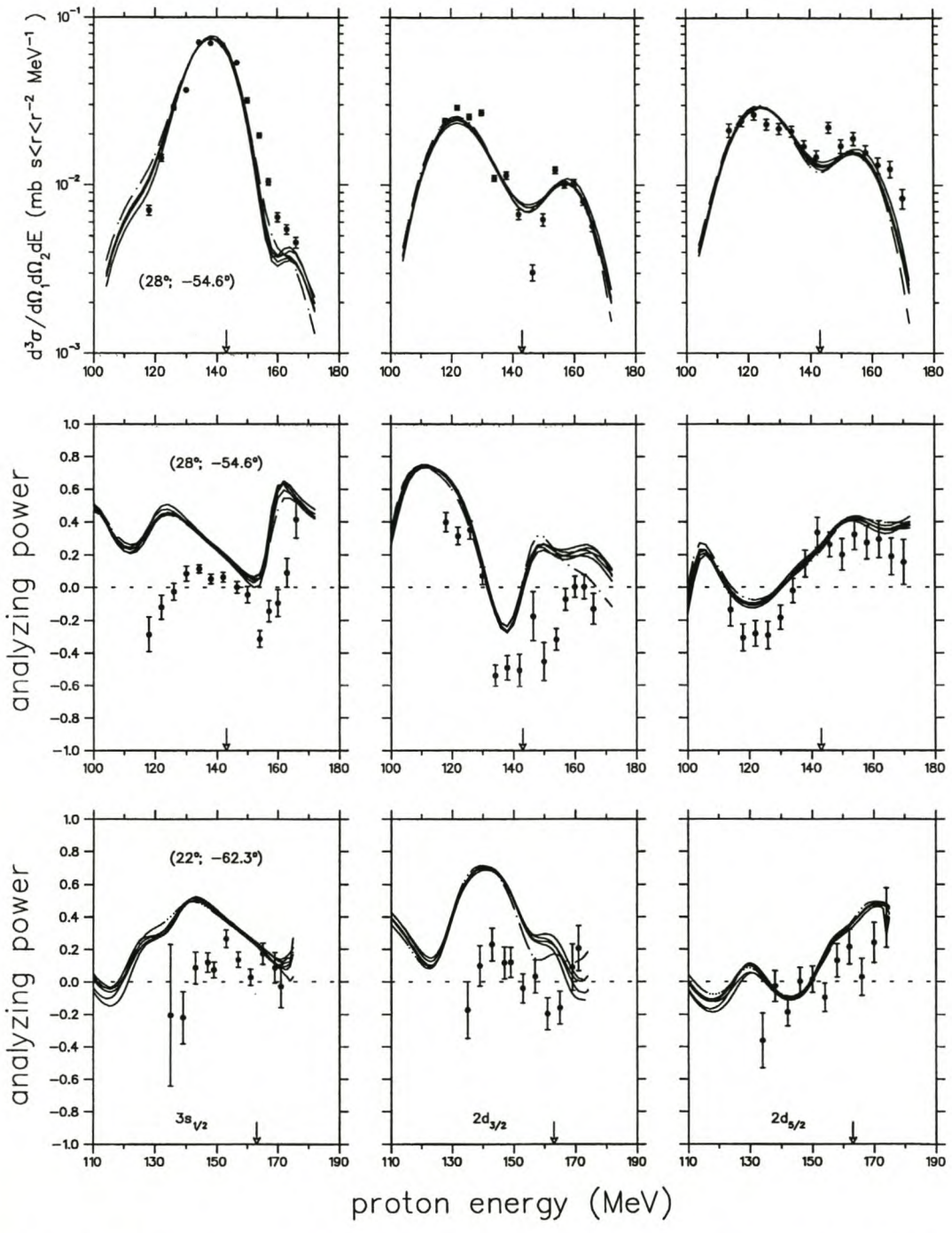

Figure 5.13: Analyzing power and cross-section energy sharing distributions for the resolved $3s_{1/2}$ and $2d_{3/2}$ states. The curves represent DWIA predictions for free NN interaction for distorting optical potential parameter sets of Cooper [Coo93] EDAD1 (solid line), EDAD2 (dashed line), EDAD3 (dot-dashed line), EDAI (short dashed line), and Hama [Ham90] DHD (short dot-dashed line) and DH2D (dotted line). The DWIA cross-section calculations shown are plotted using the spectroscopic factors from Appendix A.

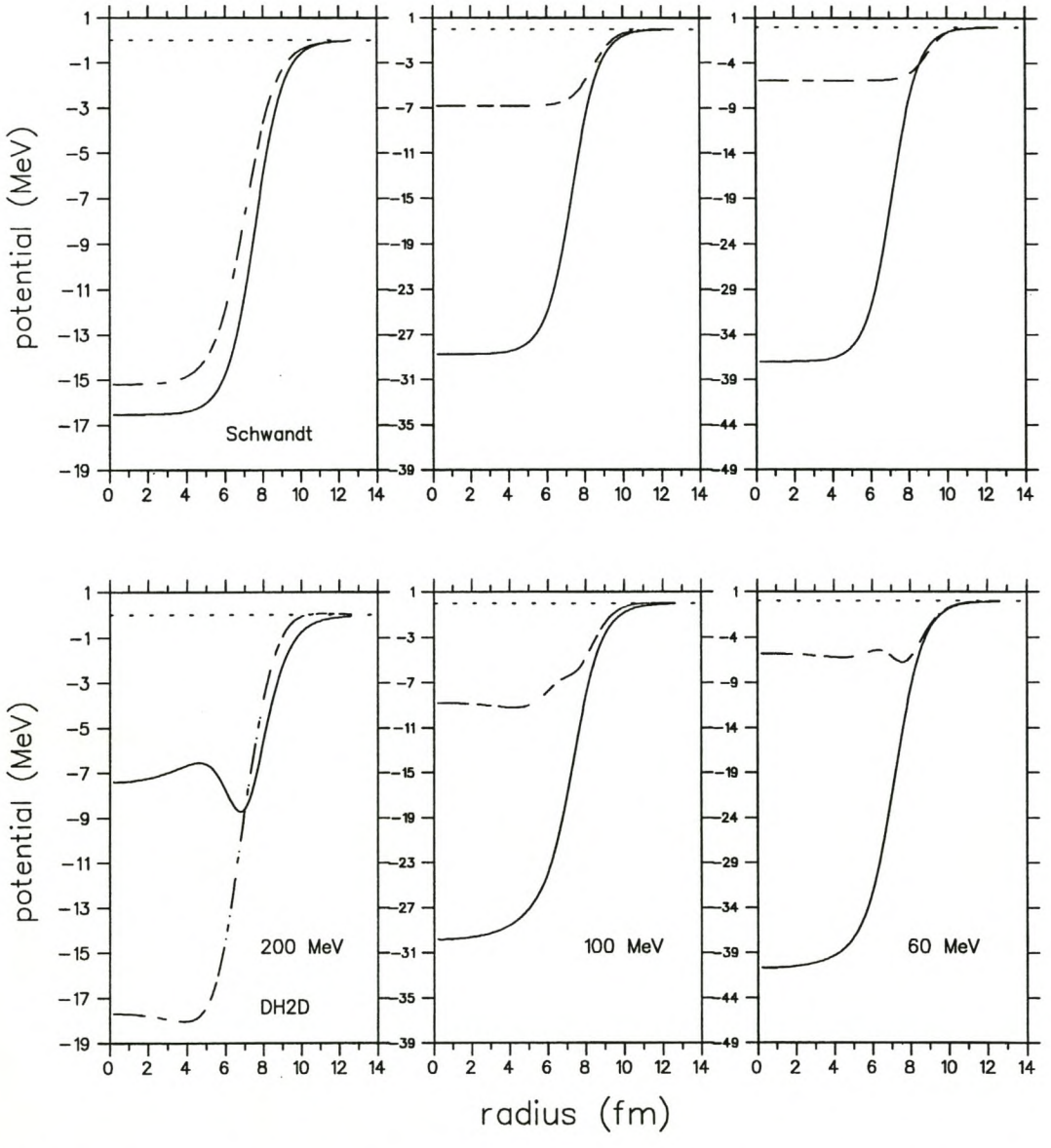

Figure 5.14: Relative contributions of the real (solid line) and imaginary (dot-dashed line) parts of the central potential for the Schwandt [Sch82] and Hama [Ham90] (DH2D) optical potential.

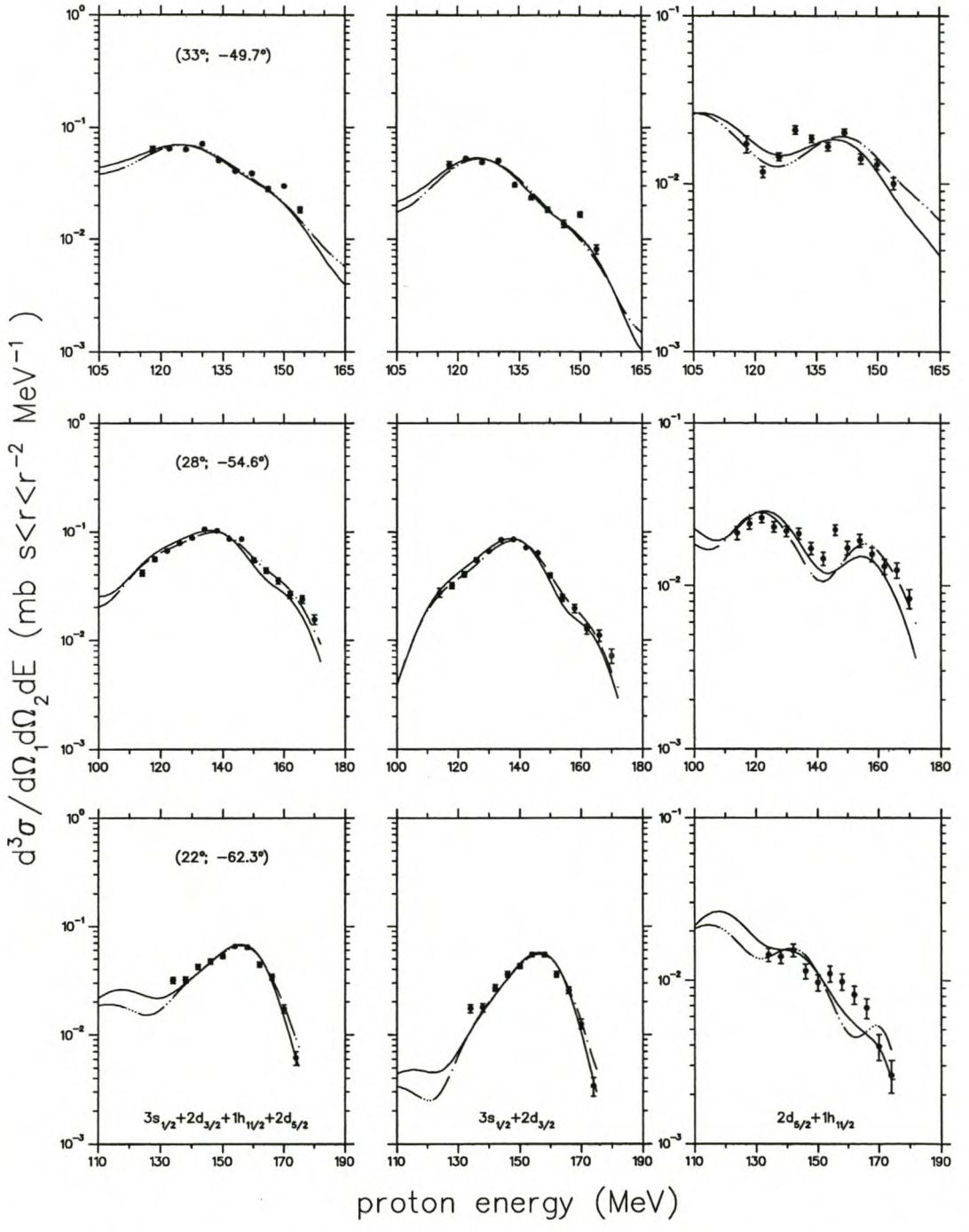

Figure 5.15: Cross-section energy-sharing distributions for the unresolved valence states. The curves represent DWIA predictions for free NN interaction for distorting optical potential parameter sets of Hama [Ham90] (DH2D) (solid line) and Schwandt [Sch82] (dashed line). The DWIA calculations shown are plotted with spectroscopic factors from Appendix A.

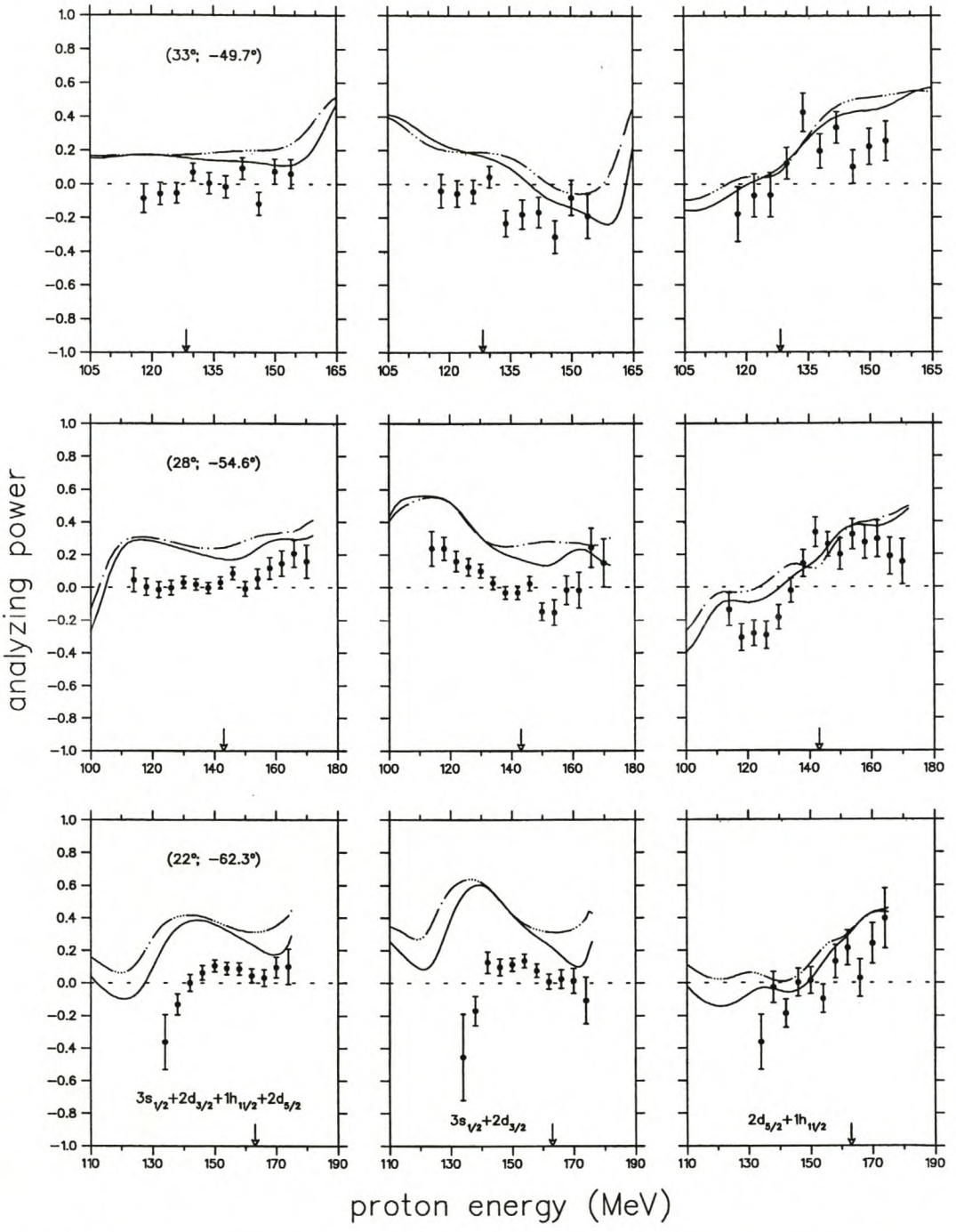

Figure 5.16: Analyzing power energy-sharing distributions for the unresolved valence states. The details on the calculations are the same as in Fig. 5.15.

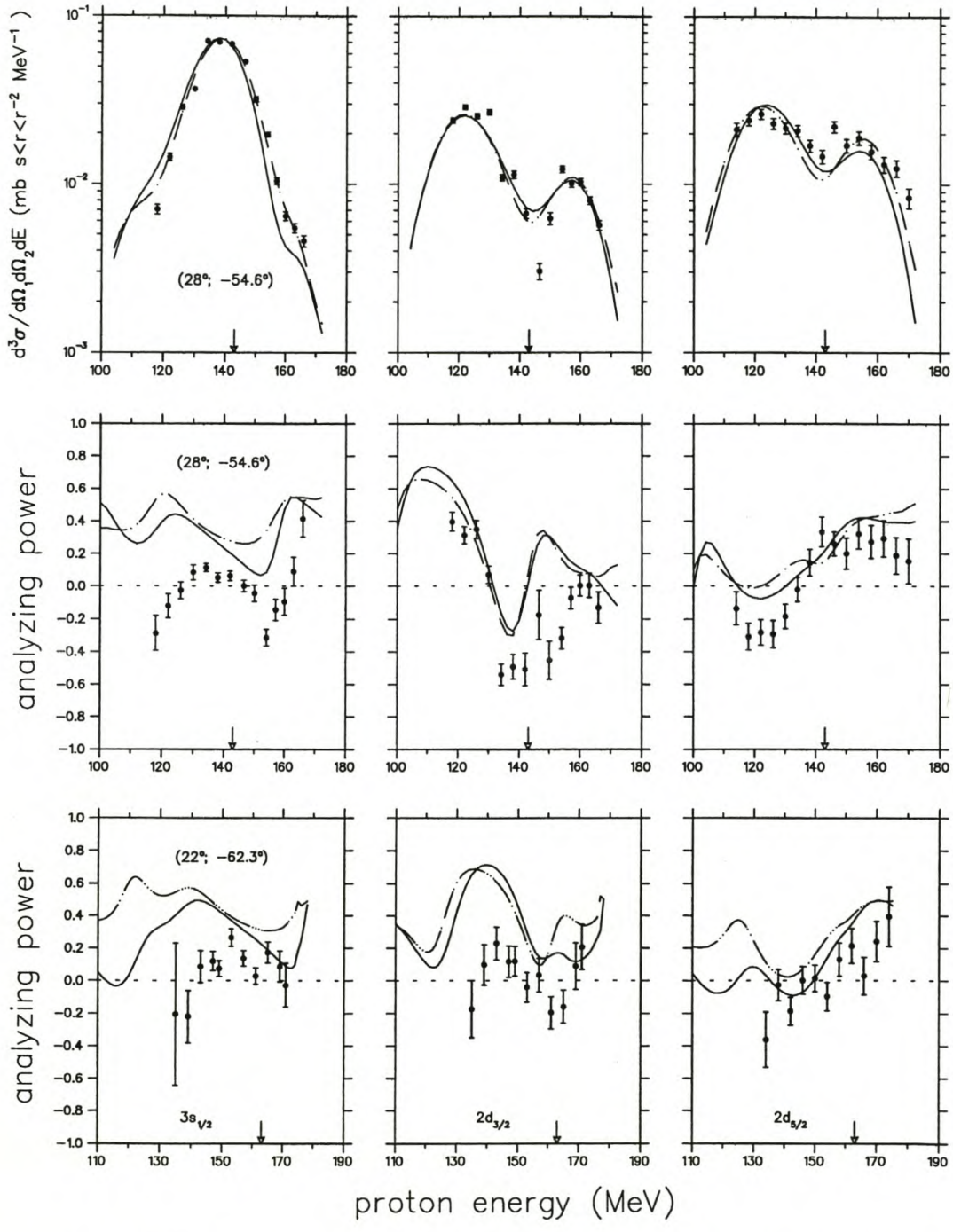

Figure 5.17: Analyzing power and cross-section energy-sharing distributions for the resolved $3s_{1/2}$ and $2d_{3/2}$ states. The curves represent DWIA predictions for free NN interaction for distorting optical potential parameter sets of Hama [Ham90] (DH2D) (solid line) and Schwandt [Sch82] (dashed line).

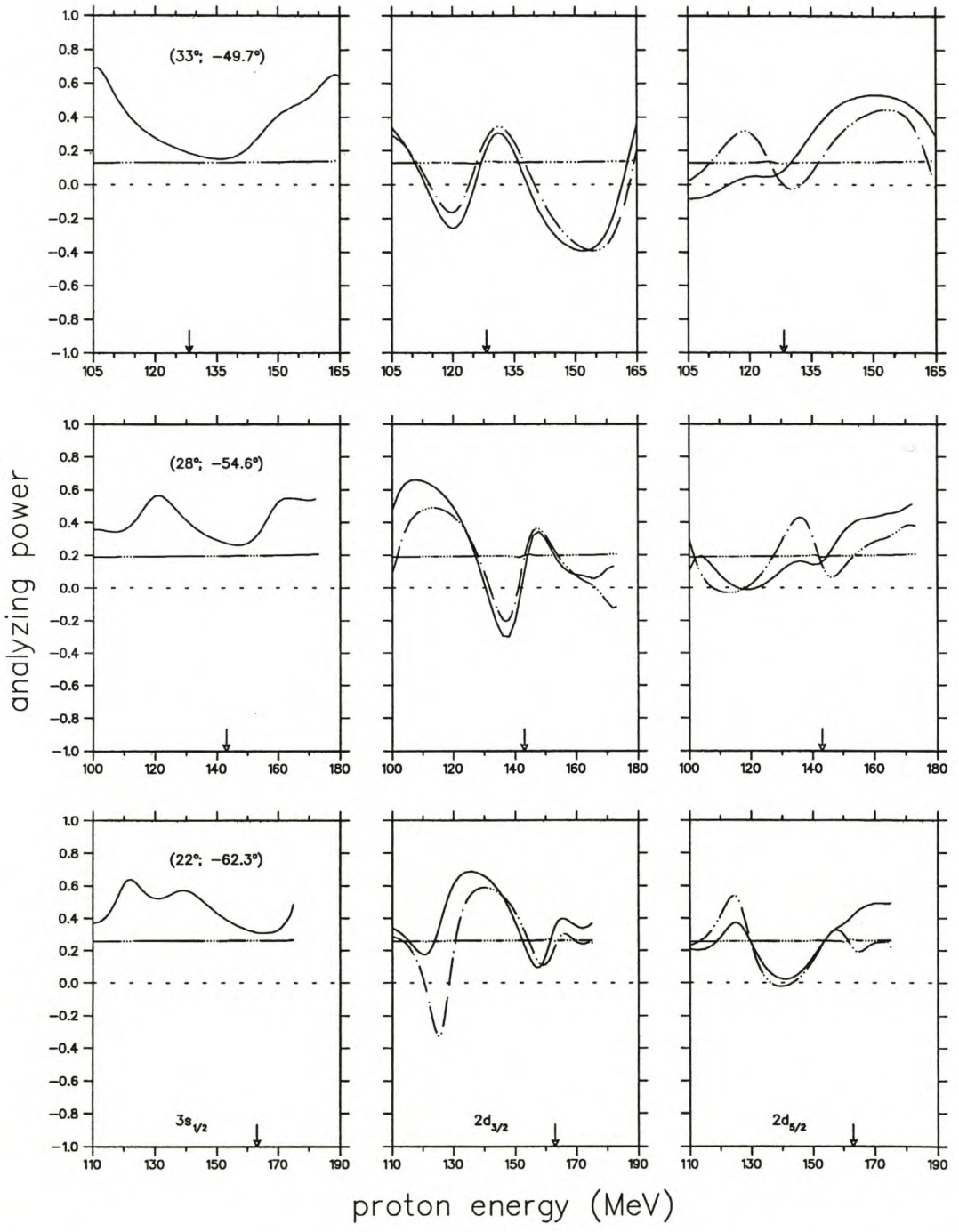

Figure 5.18: Analyzing power energy-sharing distributions for the ground state and first two excited valence states for the OMP of Schwandt [Sch82] and the free NN interaction (solid line), compared to the calculations with a modified optical potential where the spin-orbit terms are ignored (dashed line), and the PWIA calculation (dot-dashed line).

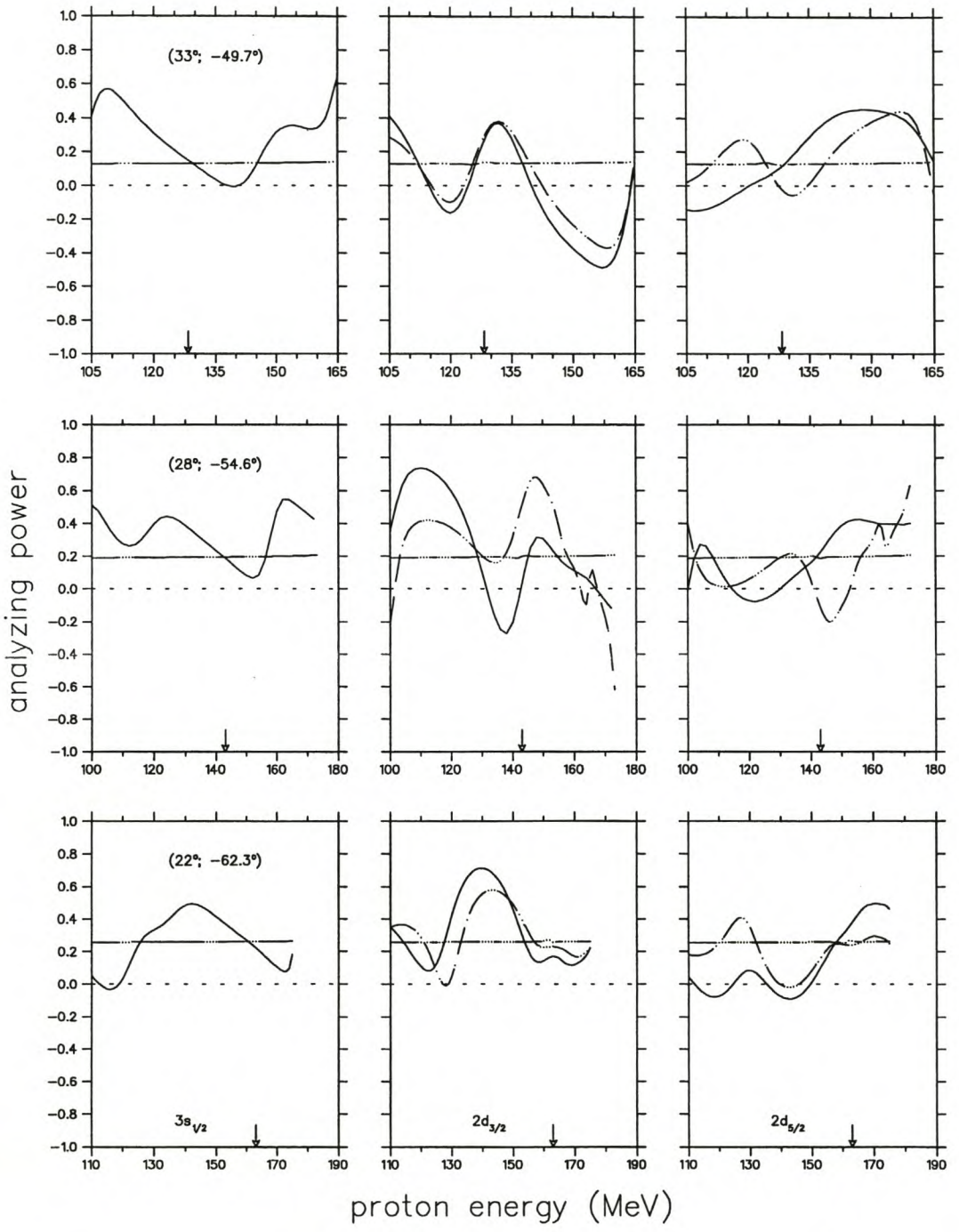

Figure 5.19: Analyzing power energy-sharing distributions for the ground state and first two excited valence states for the DH2D OMP of Hama [Ham90] and the free interaction (solid line), compared to calculations with a modified OMP where the spin-orbit terms are ignored (dashed line), and the PWIA calculation (dot-dashed line).

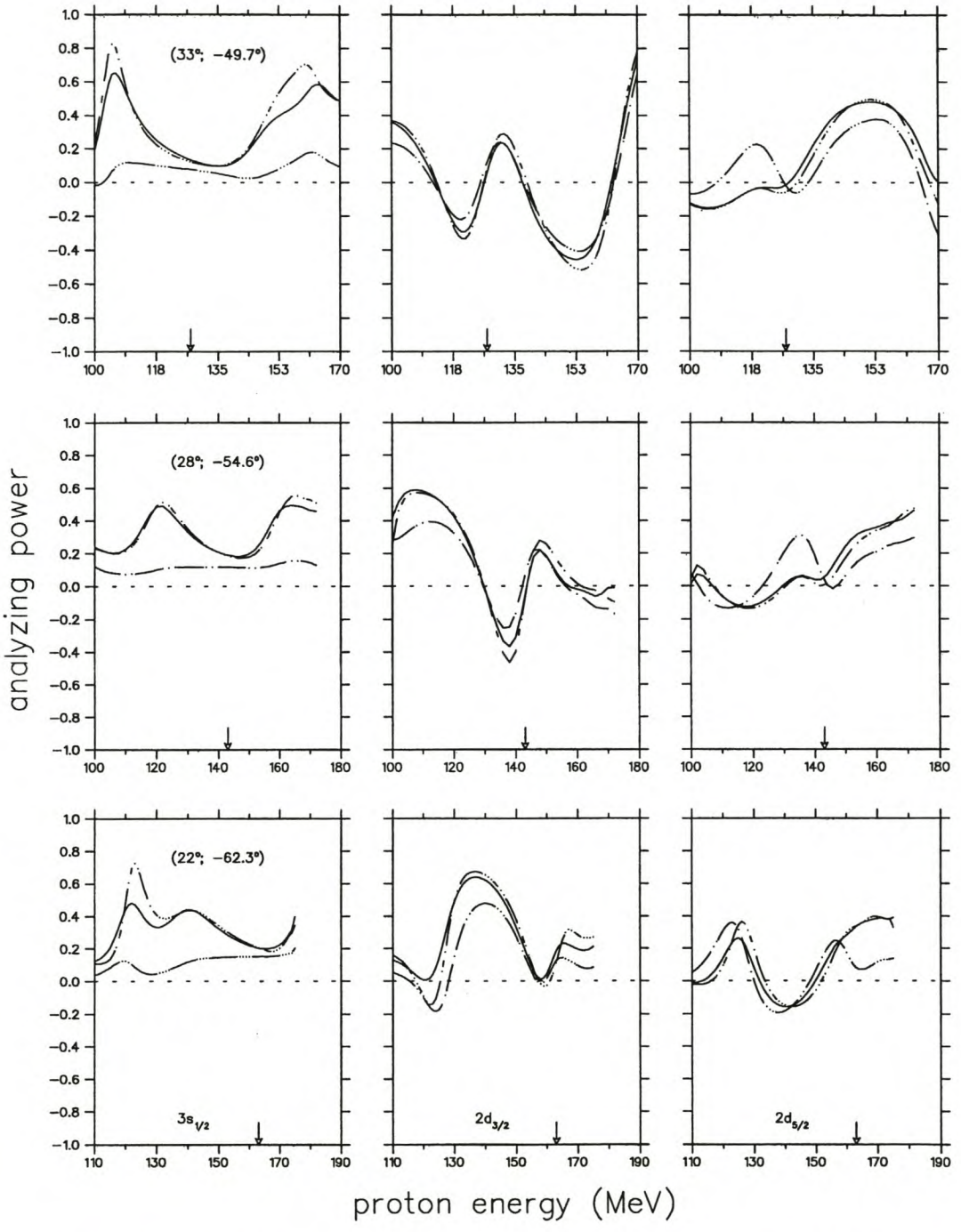

Figure 5.20: Analyzing power energy-sharing distributions for the ground state and first two excited valence states for the OMP of Schwandt [Sch82] and the Kelly [Kel94] effective interaction (solid line), compared to calculations where the spin-orbit interaction is neglected for the incoming projectile only (dashed line), and for the two outgoing protons only (dot-dashed line). The arrows indicates regions of minimum recoil.

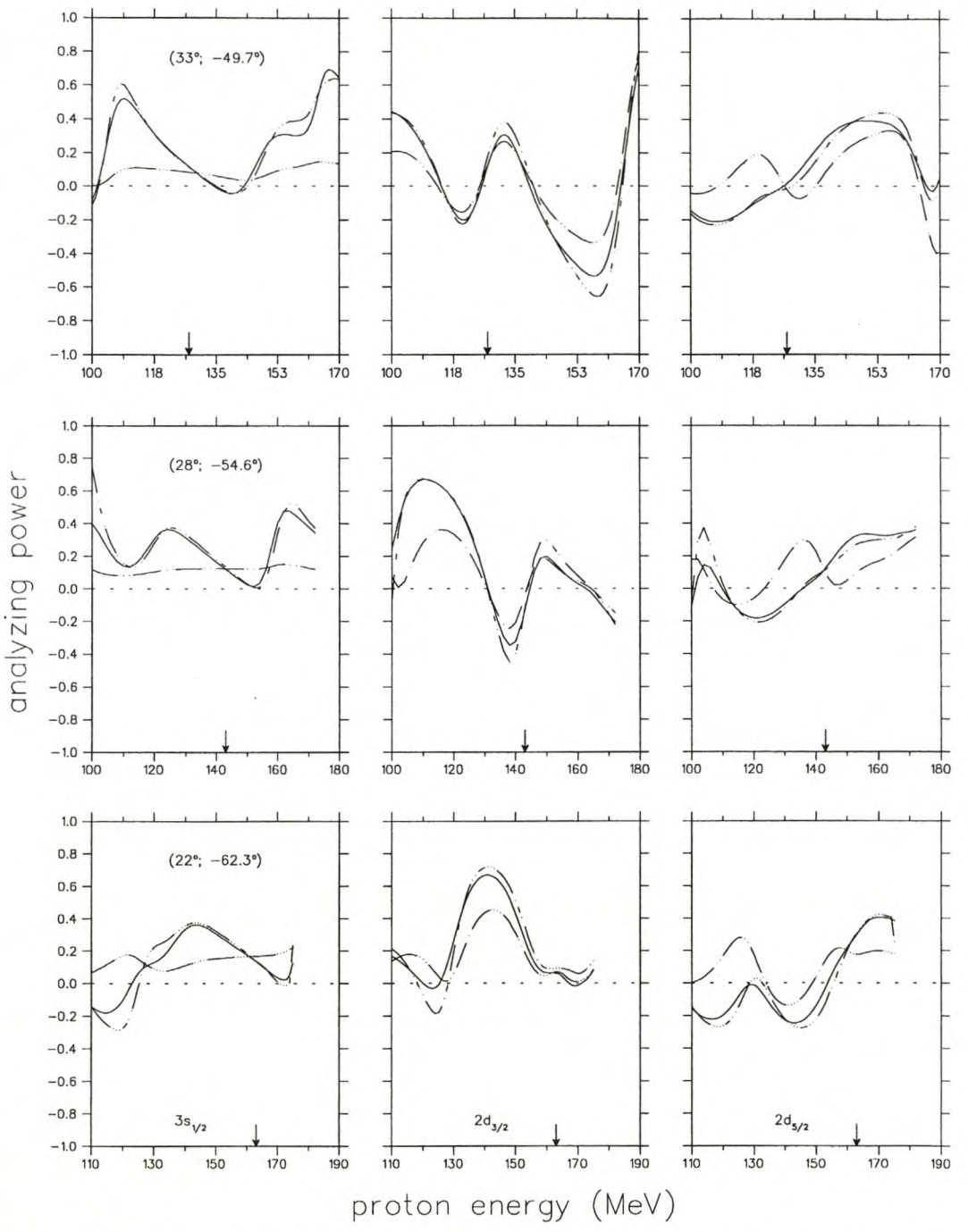

Figure 5.21: Analyzing power energy-sharing distributions for the ground state and first two excited valence states for the DH2D OMP of Hama [Ham90] and the Kelly [Kel94] effective interaction (solid line), compared to calculations where the spin-orbit interaction is neglected for the incoming projectile only (dashed line), and for the two outgoing protons only (dot-dashed line). The arrows indicates regions of minimum recoil.

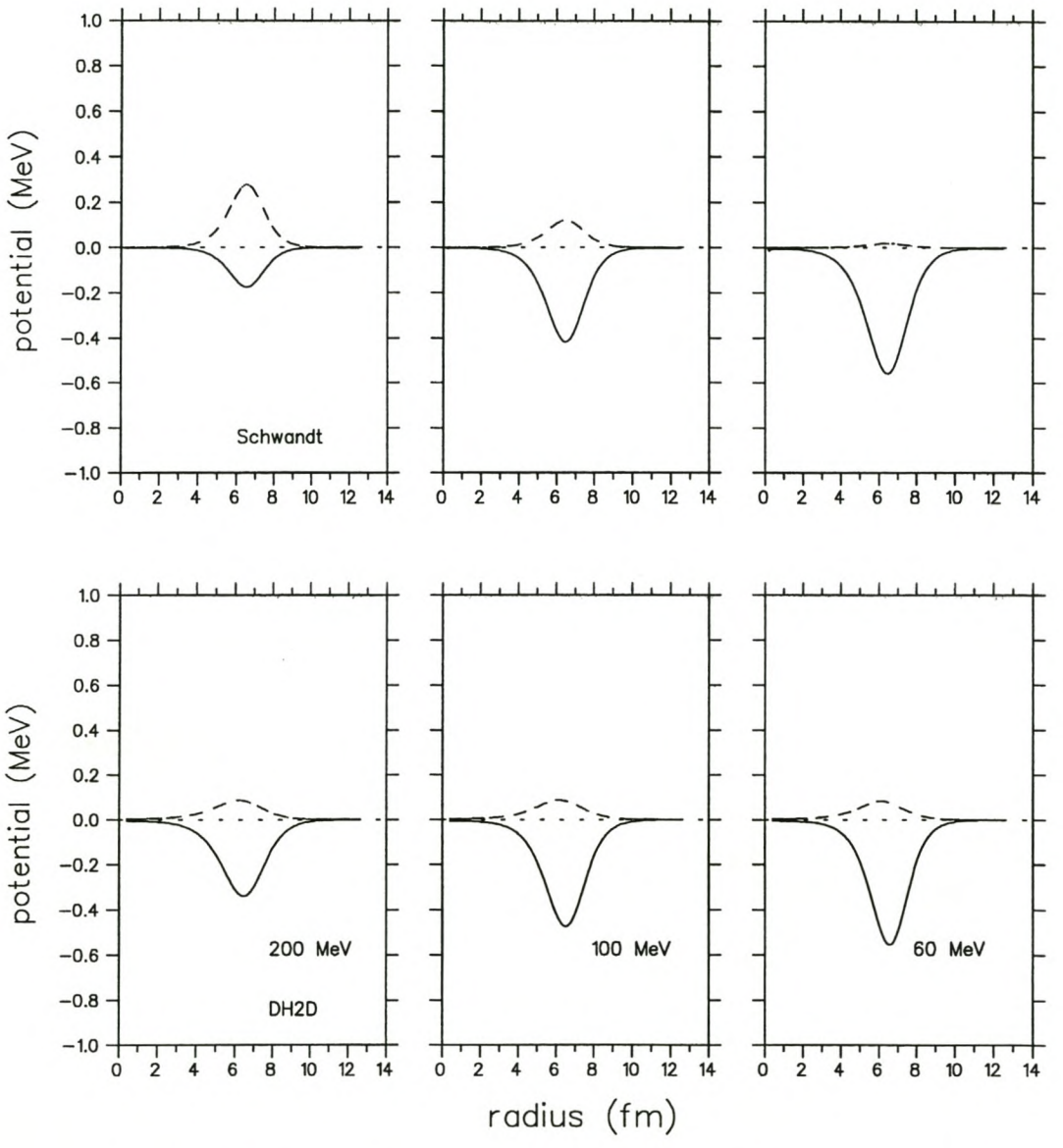

Figure 5.22: Relative contributions of the real (solid line) and imaginary (dashed line) parts of the spin-orbit potential for the Schwandt [Sch82] and Hama [Ham90] (DH2D) optical potential.

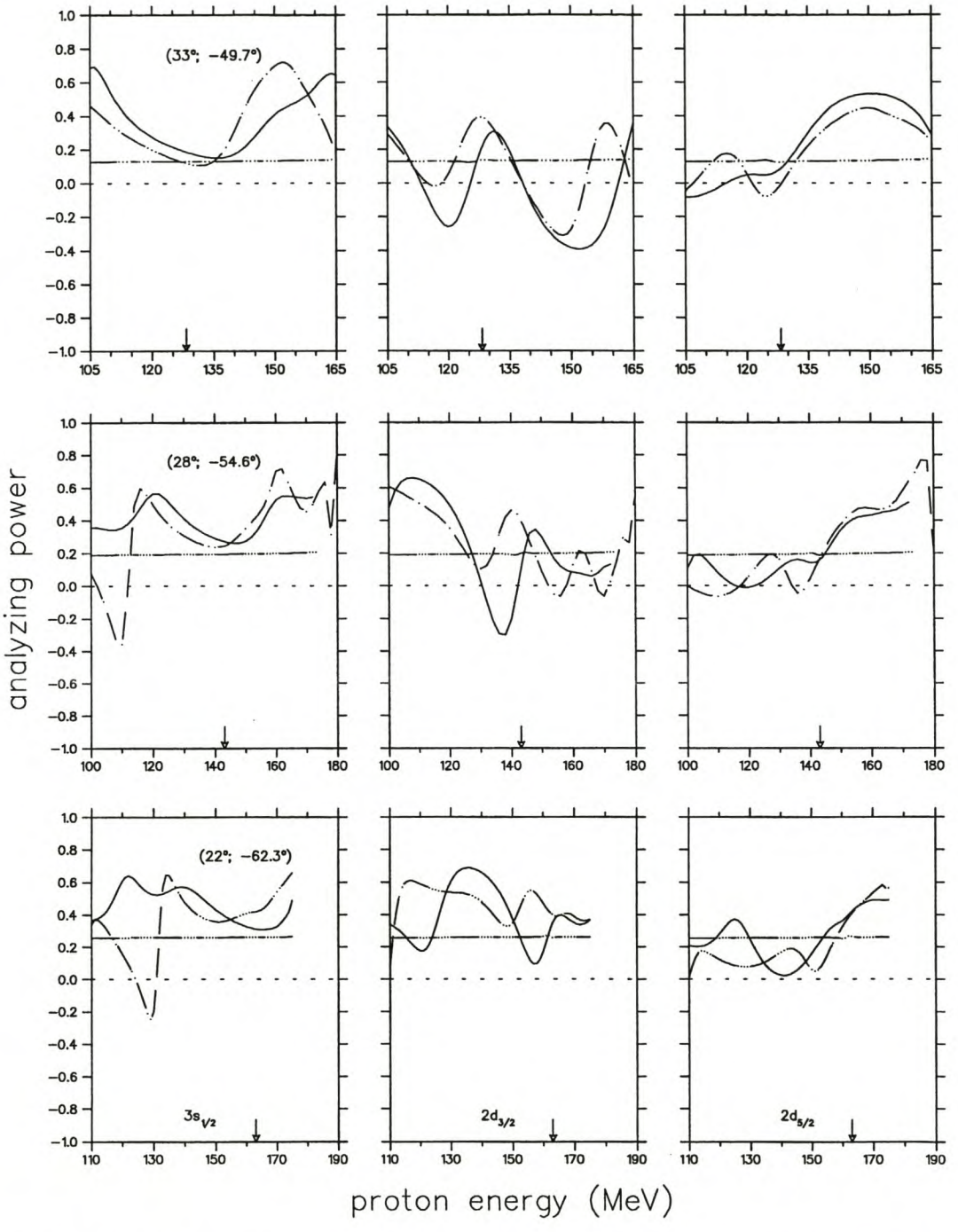

Figure 5.23: Calculated analyzing power energy-sharing distributions for the ground state and first two excited valence states for the OMP of Schwandt [Sch82] and the free NN interaction (solid line), compared to calculations with a modified optical potential where the central (real and imaginary) terms are ignored (dashed line), and the PWIA calculation (dot-dashed line).

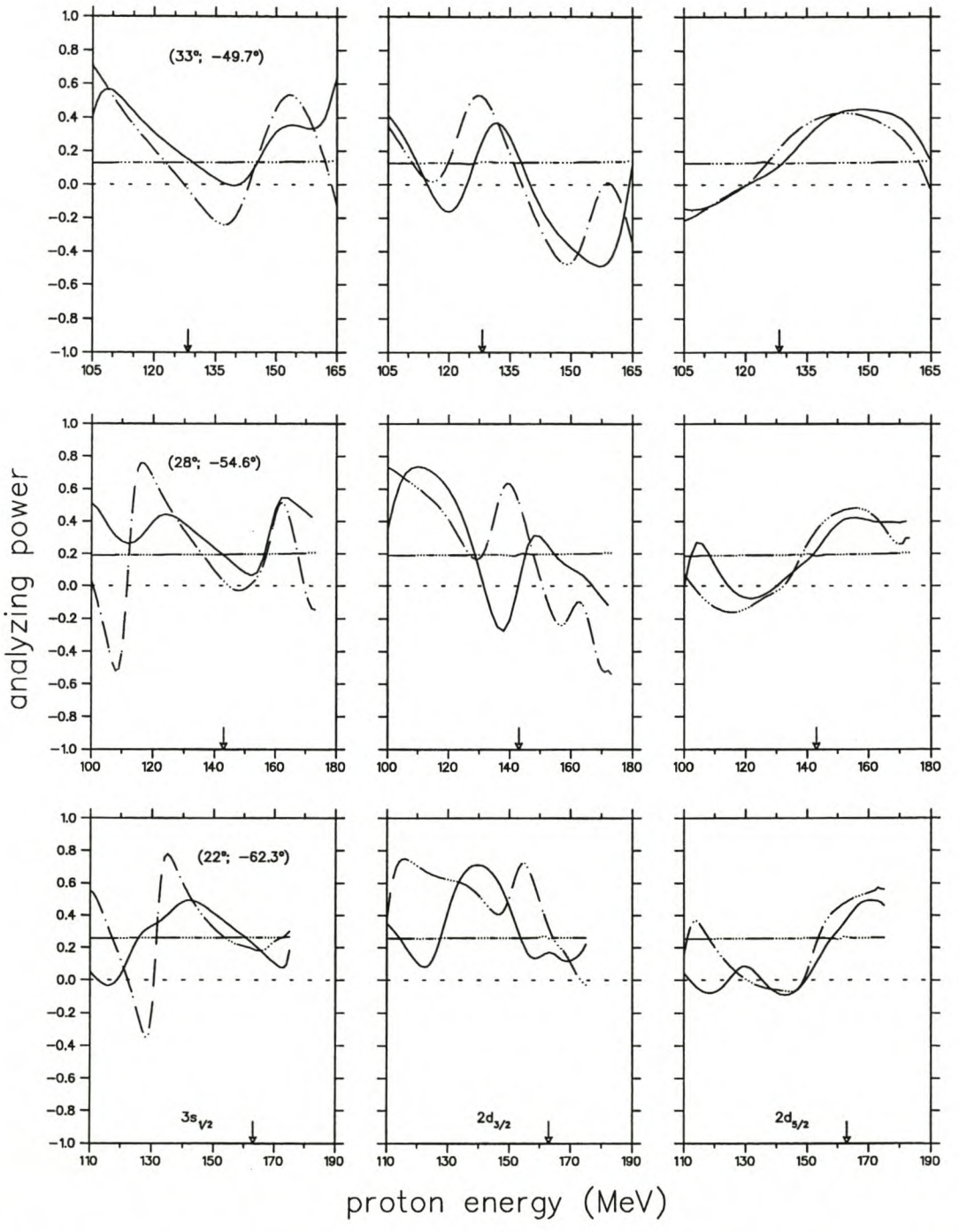

Figure 5.24: Calculated analyzing power energy-sharing distributions for the ground state and first two excited valence states for the DH2D Hama [Ham90] optical potential and the free NN interaction (solid line), compared to calculations with a modified version of the optical potential where the central (real and imaginary) terms are ignored (dashed line), and the PWIA calculation (dot-dashed line).

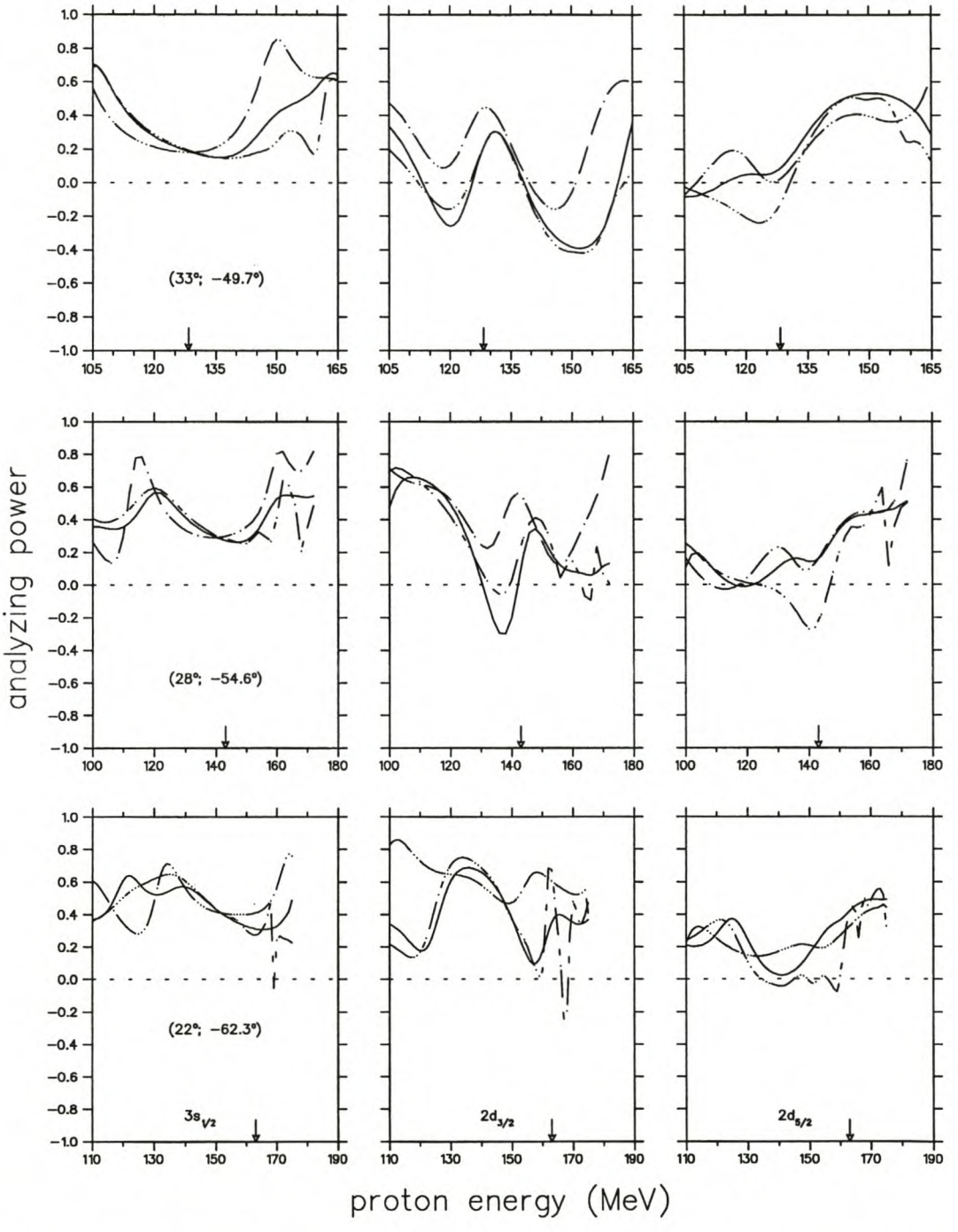

Figure 5.25: Calculated analyzing power energy-sharing distributions for the ground state and first two excited valence states for the optical potential of Schwandt [Sch82] and the free NN interaction (solid line), compared to calculations with a modified version of the optical potential where the real (dashed line) and imaginary (dot-dashed line) central terms of the optical potential are ignored.

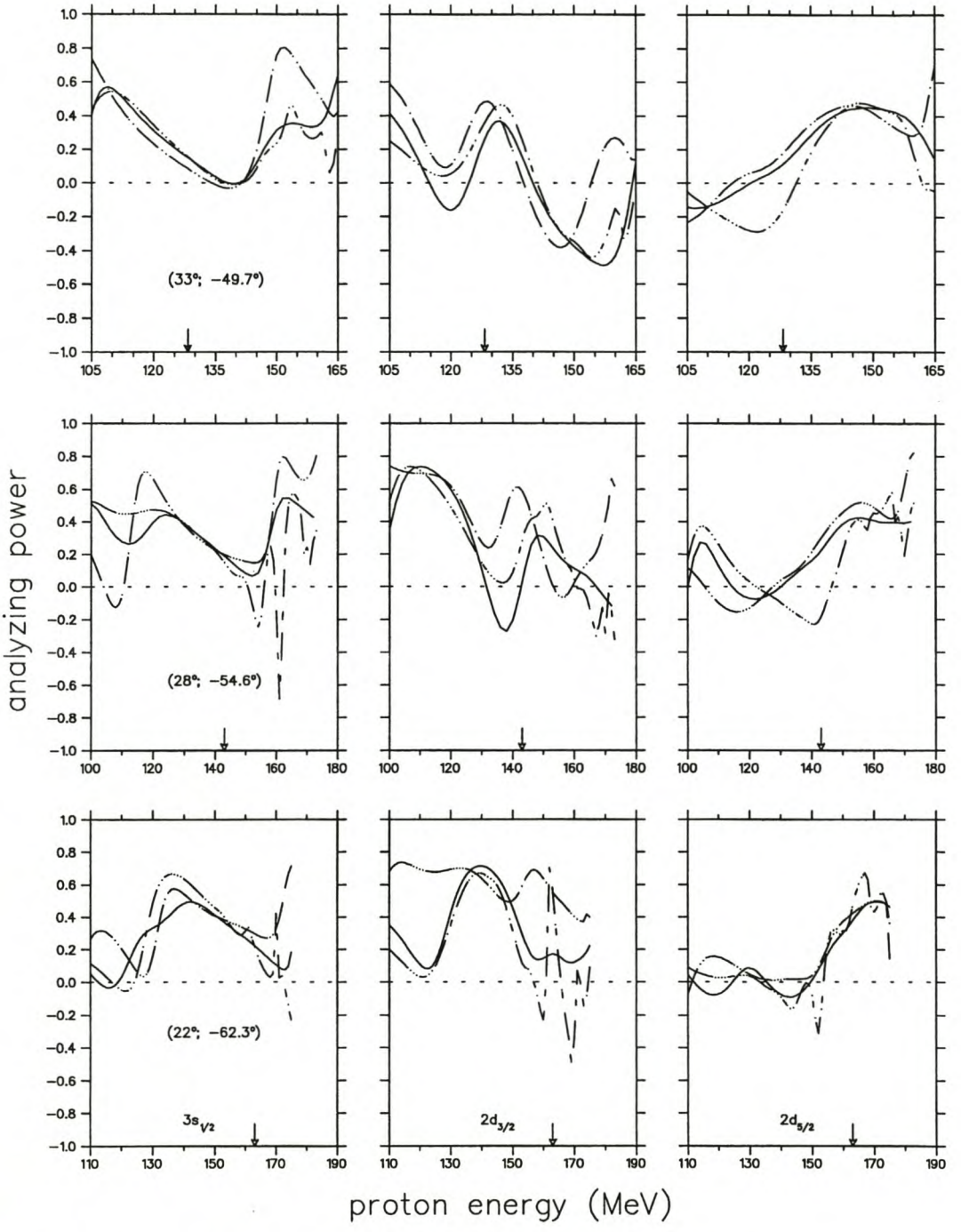

Figure 5.26: Calcualted analyzing power energy-sharing distributions for the $3s_{1/2}$, $2d_{3/2}$ and $2d_{5/2}$ states for the Hama [Ham90] (DH2D) OMP and the free interaction (solid line), compared to calculations with a modified version of the optical potential where the real (dashed line) and imaginary (dot-dashed line) central terms of the optical potential are ignored.

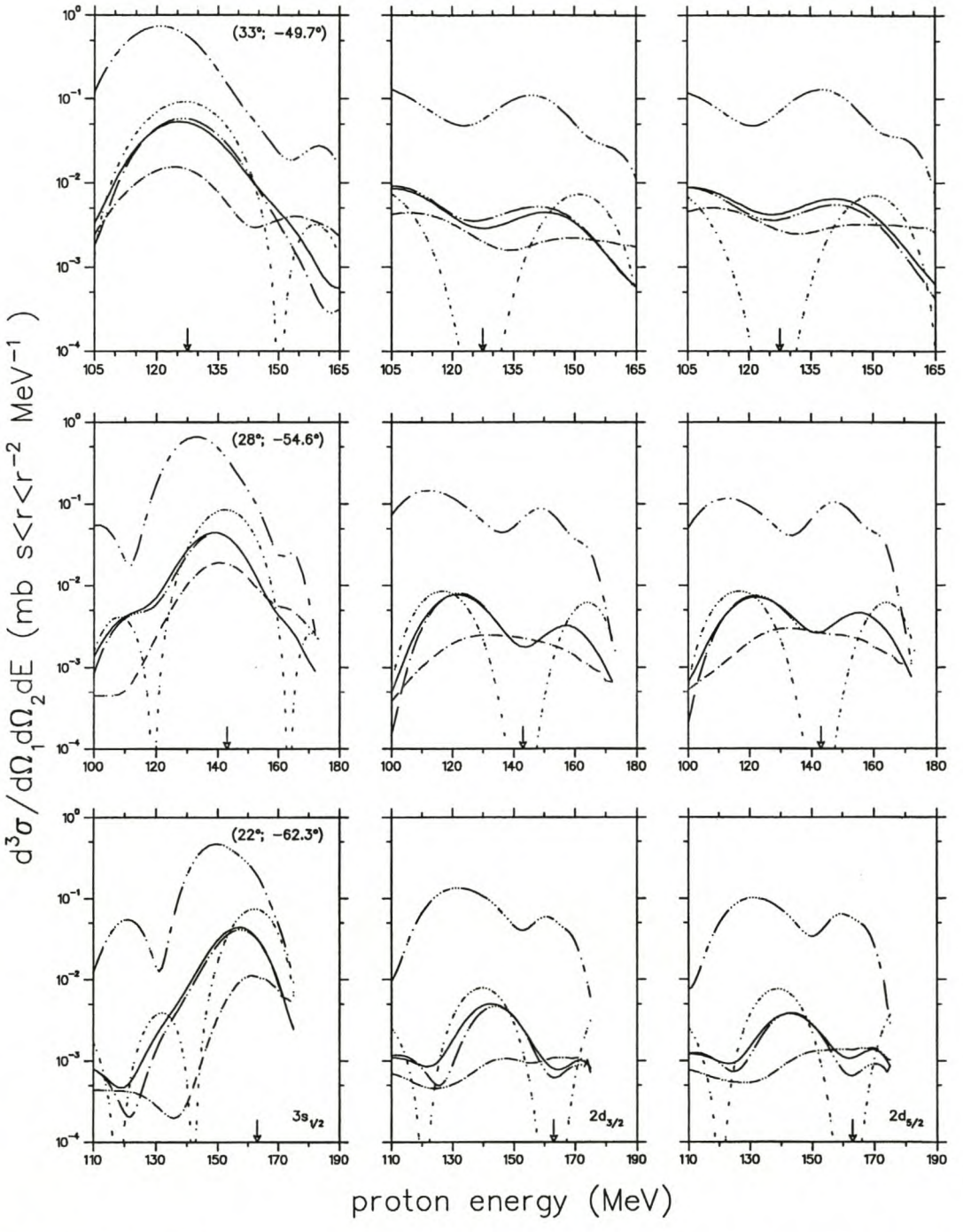

Figure 5.27: Calculated cross-section energy-sharing distributions for the $3s_{1/2}$, $2d_{3/2}$ and $2d_{5/2}$ states for the OMP of Schwandt [Sch82] and the free interaction (solid line), compared to calculations with modified versions of the optical potential where the spin-orbit terms (dashed line), the central (real and imaginary) potential terms (dot-dashed line) and the Coulomb interaction (medium-sized dashed line) are neglected. PWIA calculations are represened by the short dashed lines.

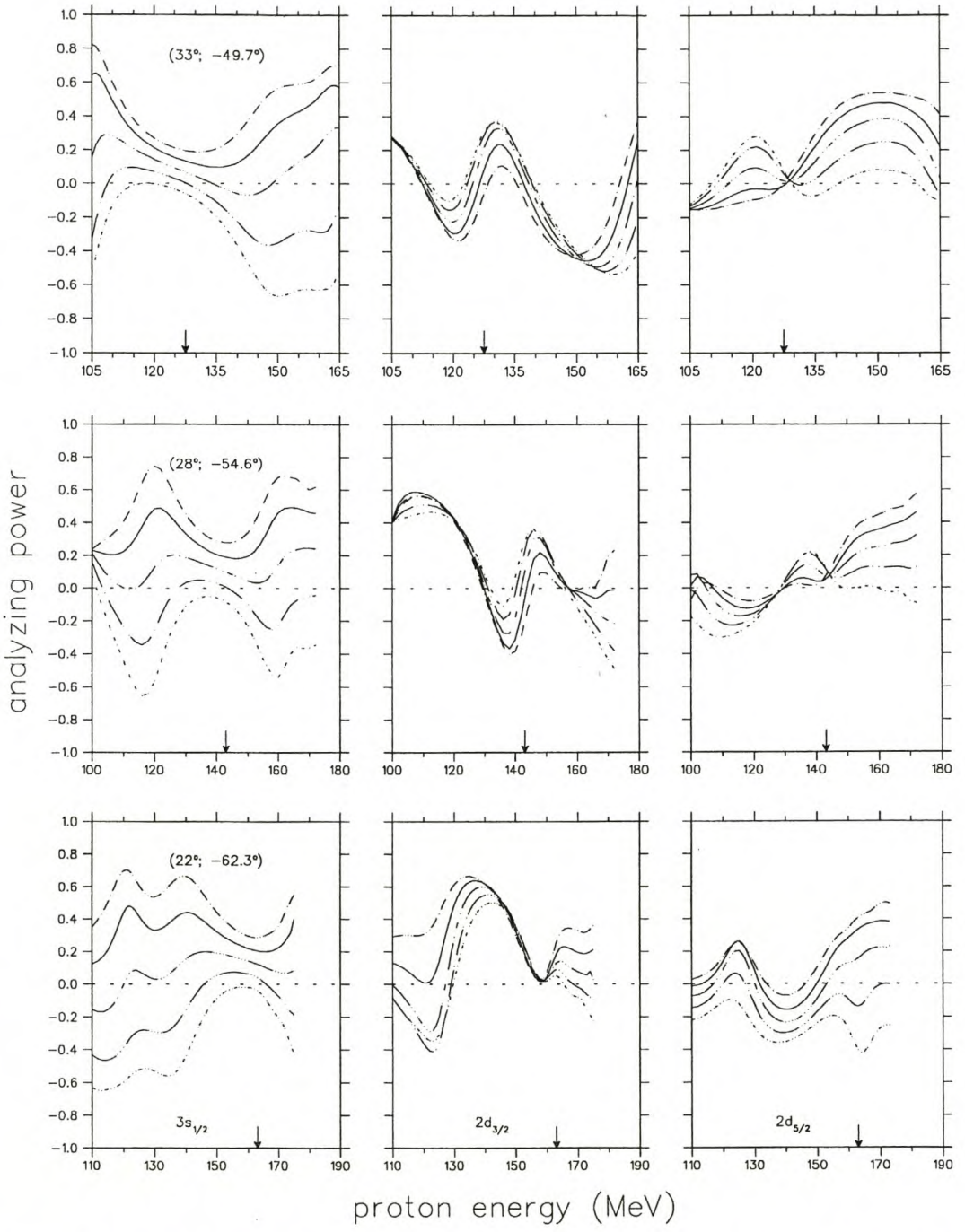

Figure 5.28: Calculated analyzing power energy-sharing distributions for the $3s_{1/2}$, $2d_{3/2}$ and $2d_{5/2}$ states for the OMP of Schwandt [Sch82] and the Kelly [Kel94] effective interaction (solid line), compared to calculations with a modified version of the imaginary part of the spin-orbit potential: $W'_{so}=-W_{so}$ (dashed line), $W'_{so}=0$ (dot-dashed line), $W'_{so}=2W_{so}$ (short dashed line) and $W'_{so}=-2W_{so}$ (dotted line).

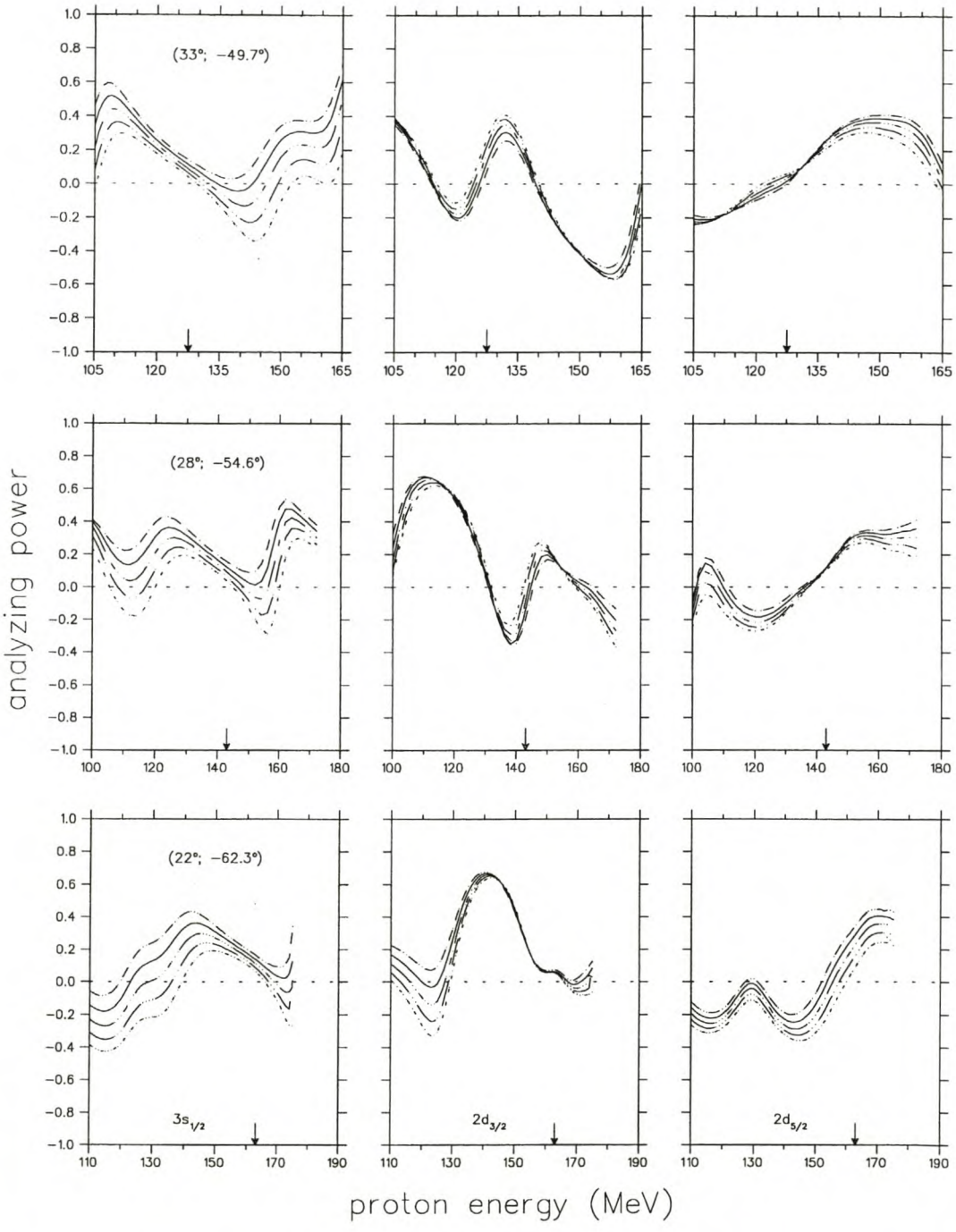

Figure 5.29: Calculated analyzing power energy-sharing distributions for the $3s_{1/2}$, $2d_{3/2}$ and $2d_{5/2}$ states for the OMP of Hama [Ham90] (DH2D) and the Kelly [Kel94] effective interaction (solid line), compared to calculations with a modified version of the imaginary part of the spin-orbit potential: W'_{so}=$-W_{so}$ (dashed line), W'_{so}=0 (dot-dashed line), W'_{so}=$2W_{so}$ (short dashed line) and W'_{so}=$-2W_{so}$ (dotted line).

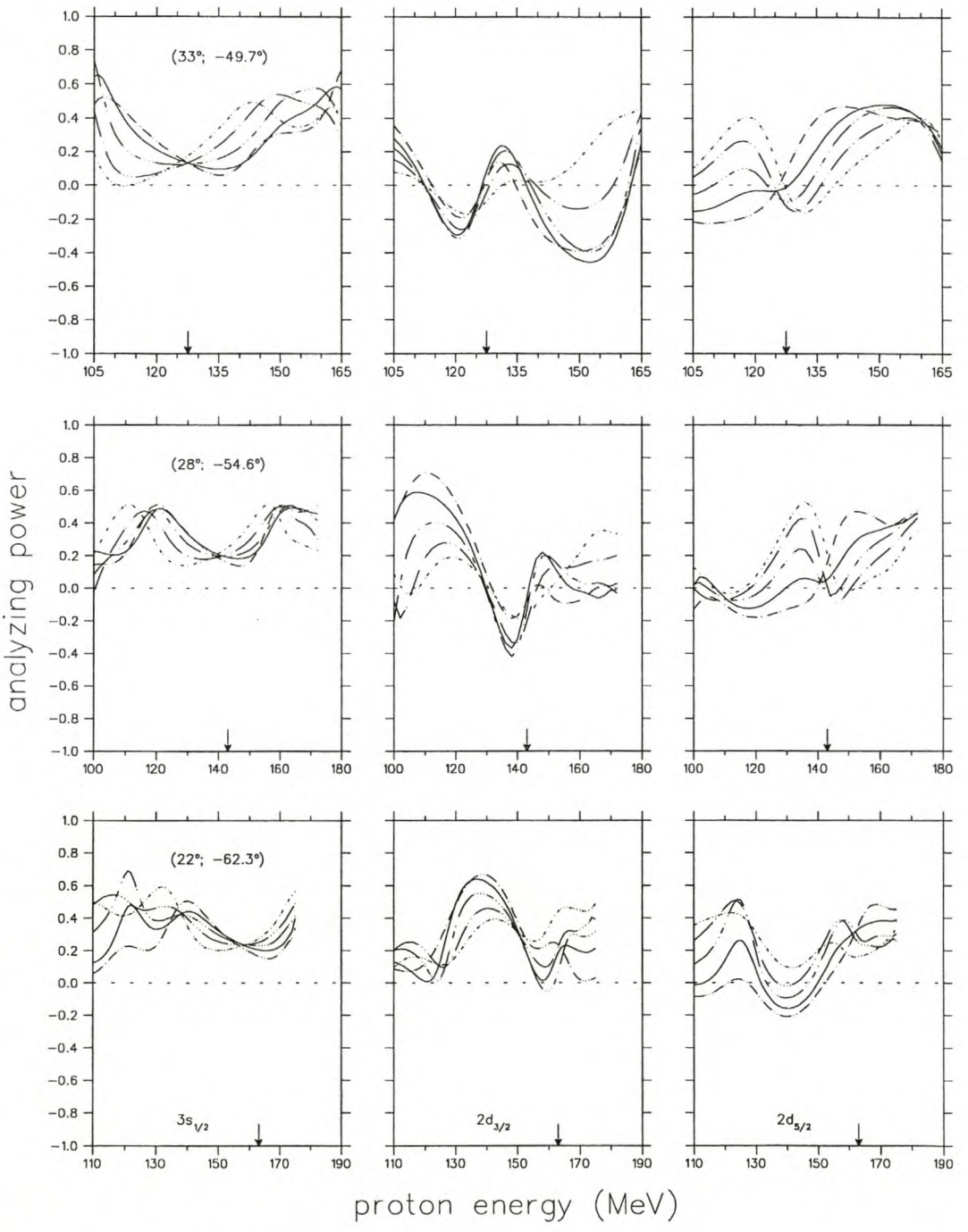

Figure 5.30: Calculated analyzing power energy-sharing distributions for the $3s_{1/2}$, $2d_{3/2}$ and $2d_{5/2}$ states for the OMP of Schwandt [Sch82] and the Kelly [Kel94] effective interaction (solid line), compared to calculations with a modified version of the imaginary part of the spin-orbit potential: V'_{so}=$-V_{so}$ (dashed line), V'_{so}=0 (dot-dashed line), V'_{so}=$2V_{so}$ (short dashed line) and V'_{so}=$-2V_{so}$ (dotted line).

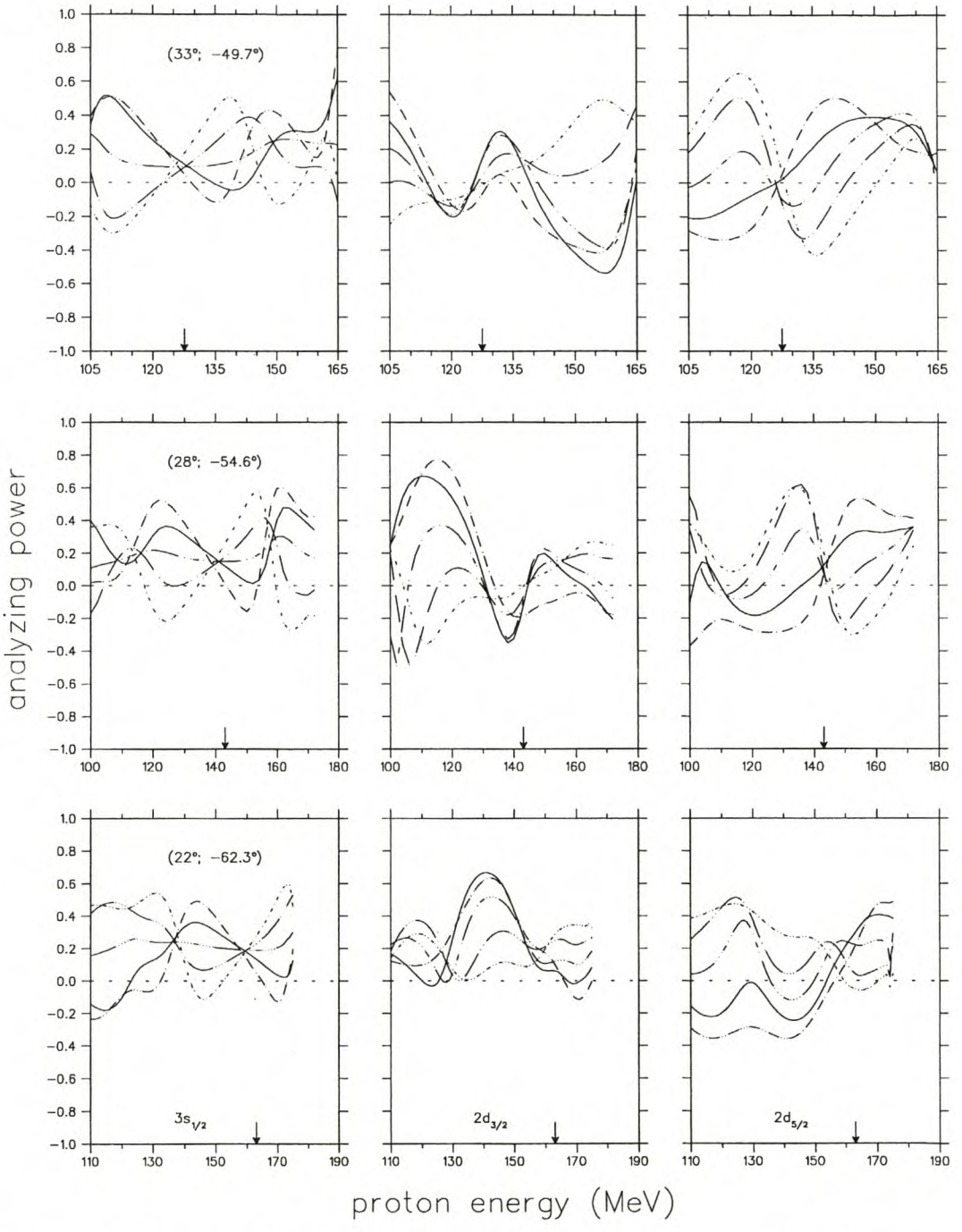

Figure 5.31: Calculated analyzing power energy-sharing distributions for the $3s_{1/2}$, $2d_{3/2}$ and $2d_{5/2}$ states for the OMP of Hama [Ham90] (DH2D) and the Kelly [Kel94] effective interaction (solid line), compared to calculations with a modified version of the imaginary part of the spin-orbit potential: V'_{so}=$-V_{so}$ (dashed line), V'_{so}=0 (dot-dashed line), V'_{so}=$2V_{so}$ (short dashed line) and V'_{so}=$-2V_{so}$ (dotted line).

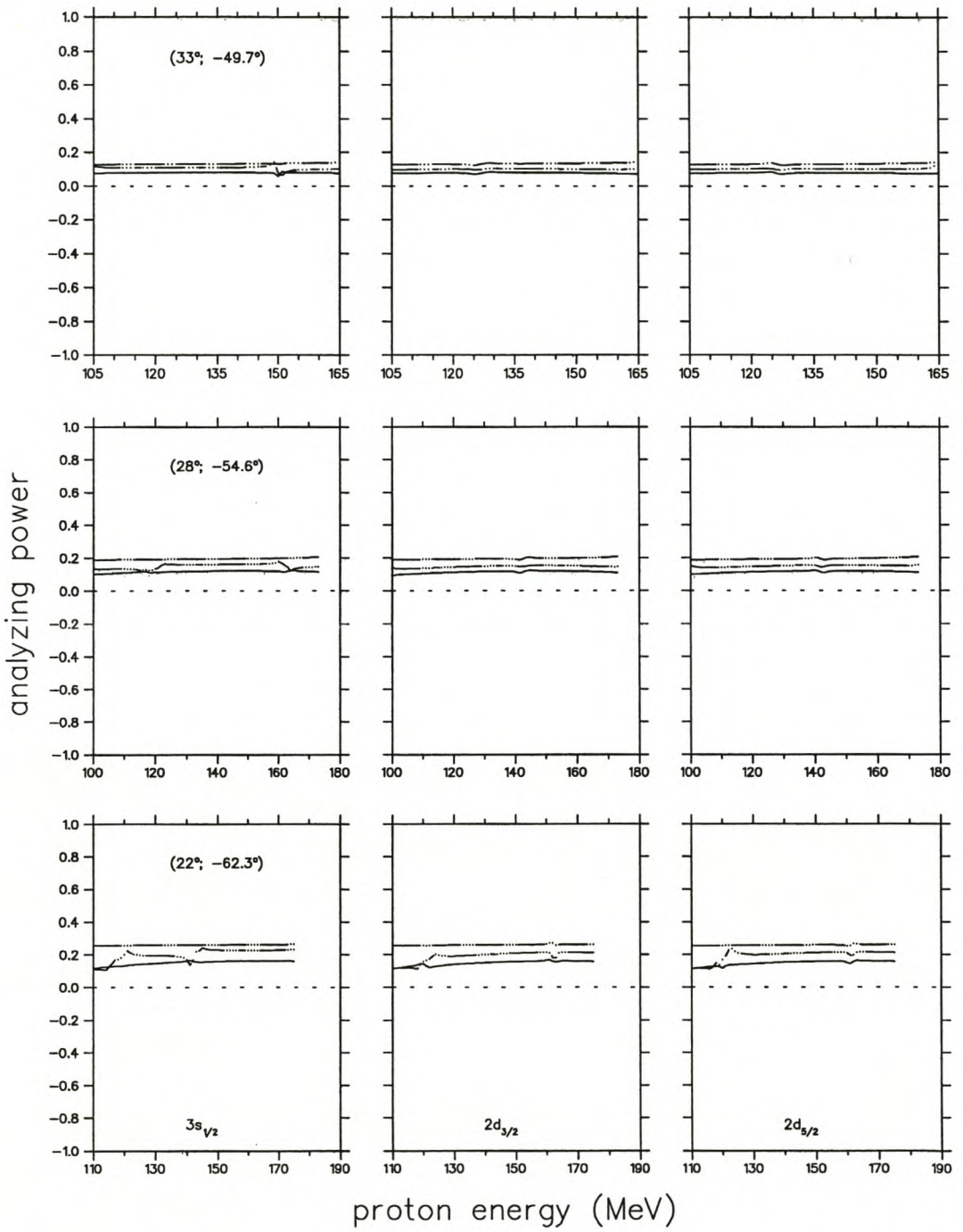

Figure 5.32: PWIA analyzing power energy-sharing distributions for the free (dashed line), Kelly [Kel94] effective (solid line) and Horowitz Iqbal [Hor86] (dot-dashed line) NN interaction.

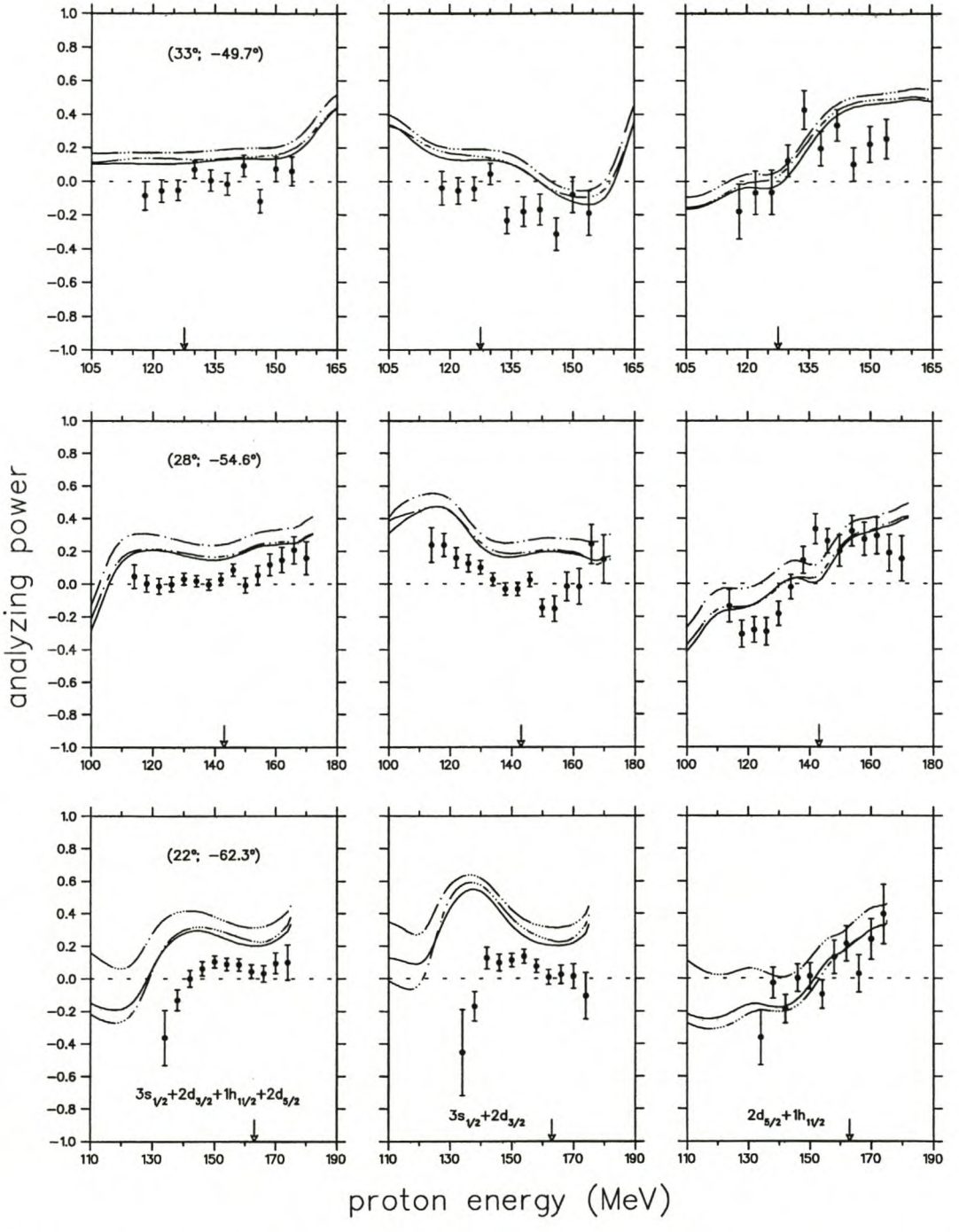

Figure 5.33: Analyzing power energy-sharing distributions for the unresolved valence states. The curves represent DWIA predictions for the optical potential parameter set of Schwandt [Sch82], utilizing the free NN interaction (dashed line) and the density dependent interactions of Kelly [Kel94] (solid line) and Horowitz and Iqbal [Hor86] (dot-dashed line).

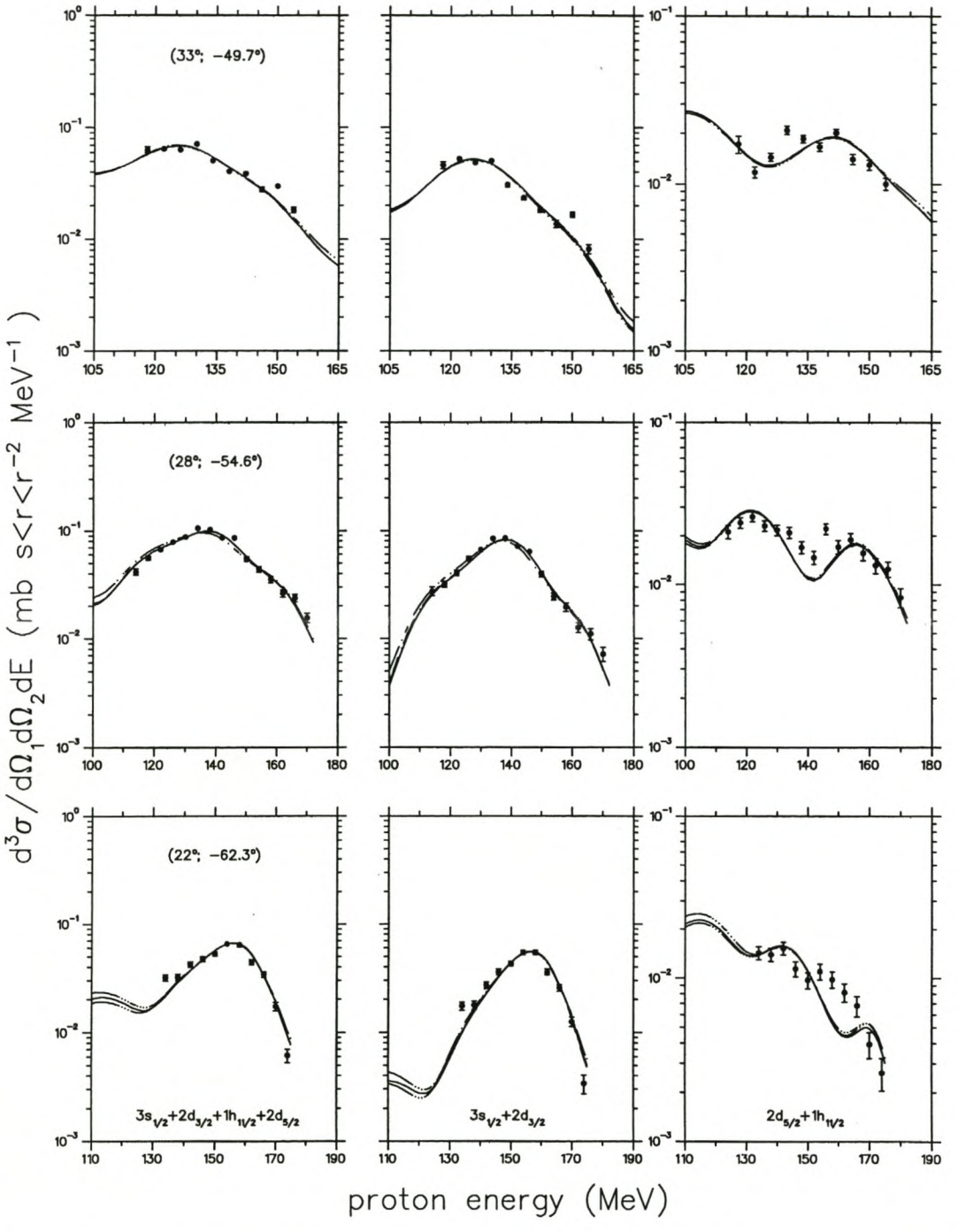

Figure 5.34: Cross-section energy-sharing distributions for the unresolved valence states. The details on the calculations are the same as in Fig. 5.33.

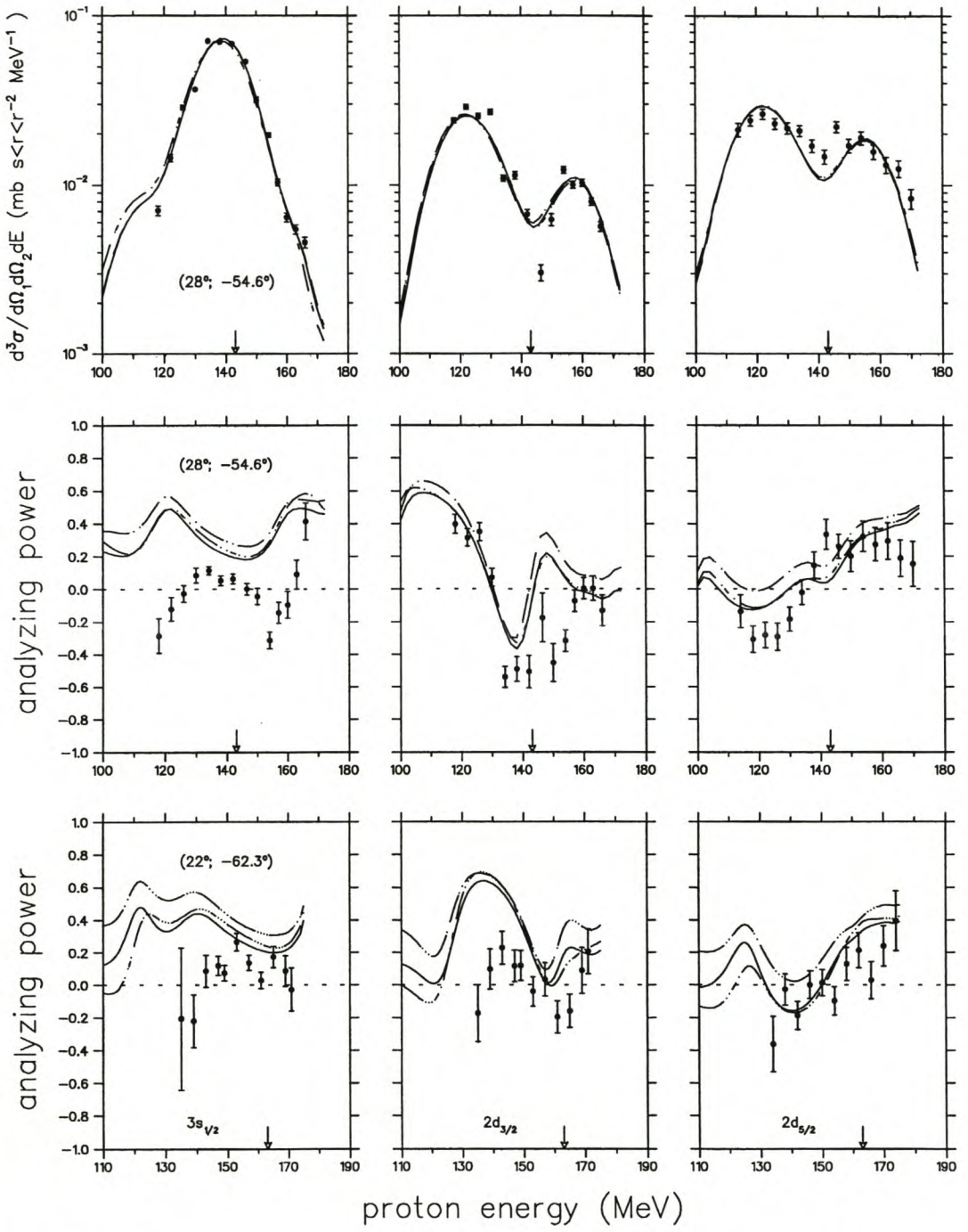

Figure 5.35: Cross-section and analyzing power energy-sharing distributions for for the resolved $3s_{1/2}$ and $2d_{3/2}$ states. The details on the calculations are as in Fig. 5.33.

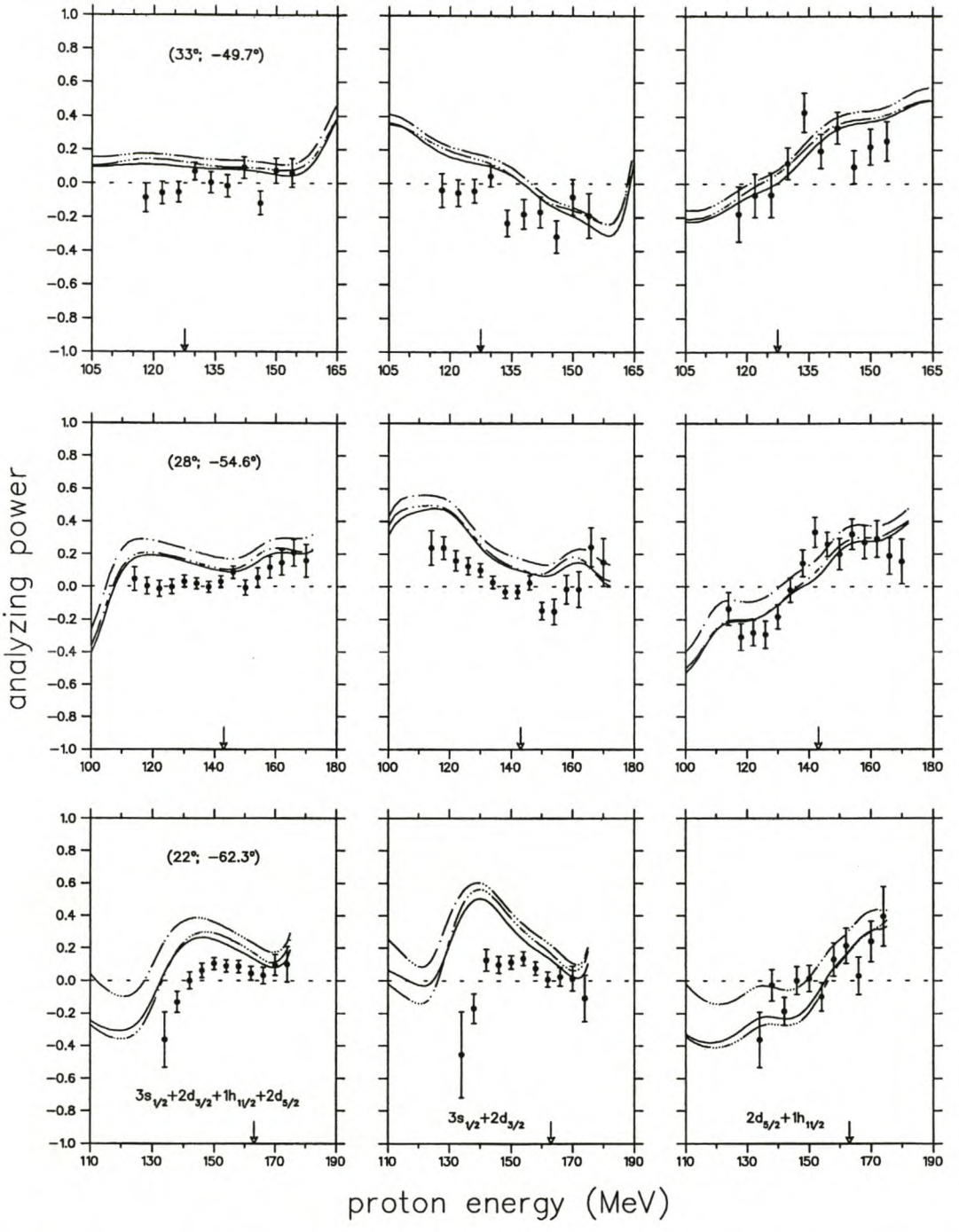

Figure 5.36: Analyzing power energy-sharing distributions for the unresolved valence states. The curves represent DWIA predictions for the second optical potential parameter set of Hama [Ham90] (DH2D), utilizing the free NN interaction (dashed line) and the density dependent interactions of Kelly [Kel94] (solid line) and Horowitz and Iqbal (dot-dashed line).

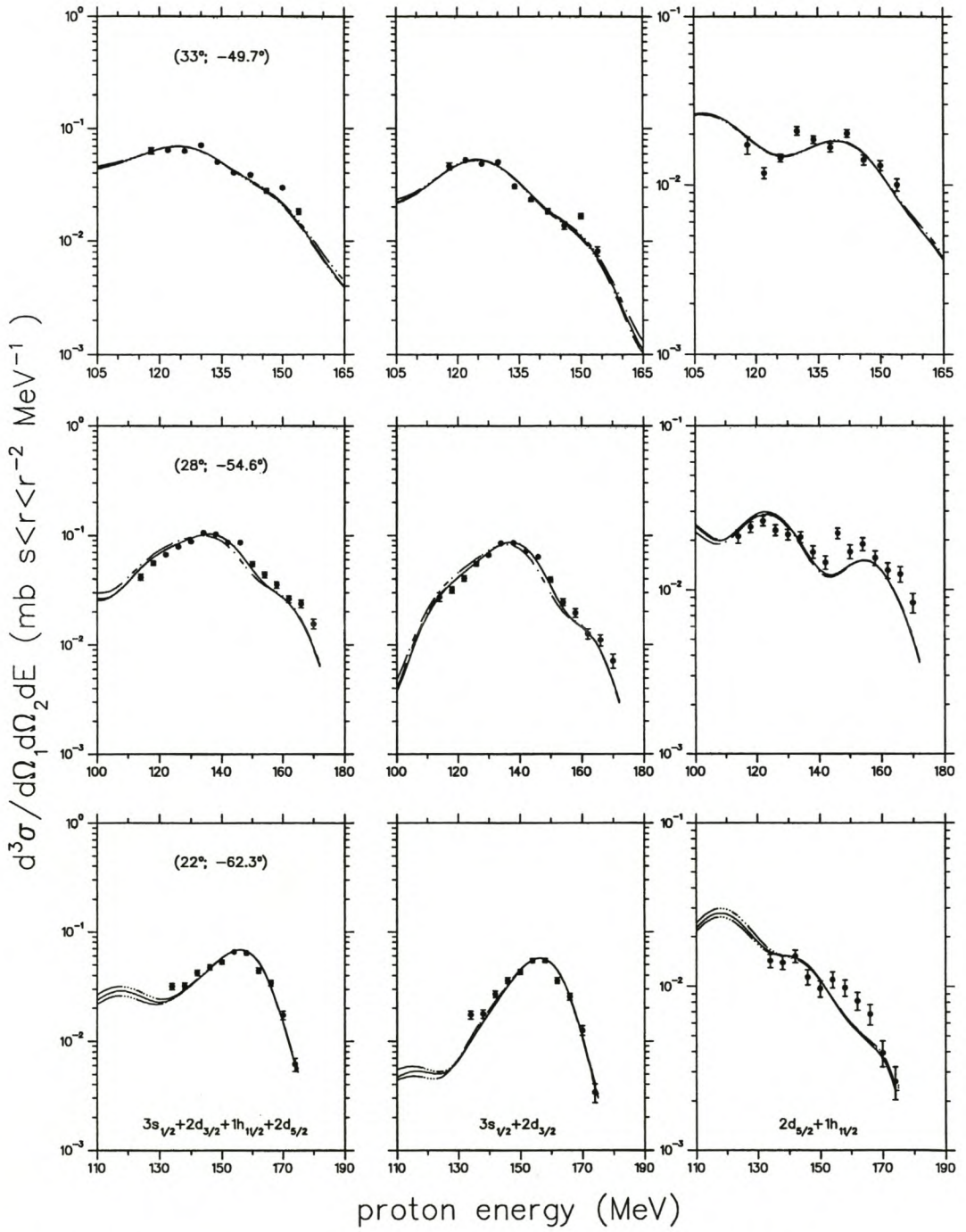

Figure 5.37: Cross-section energy-sharing distributions for the unresolved valence states. The details on the calculations are the same as in Fig. (5.36).

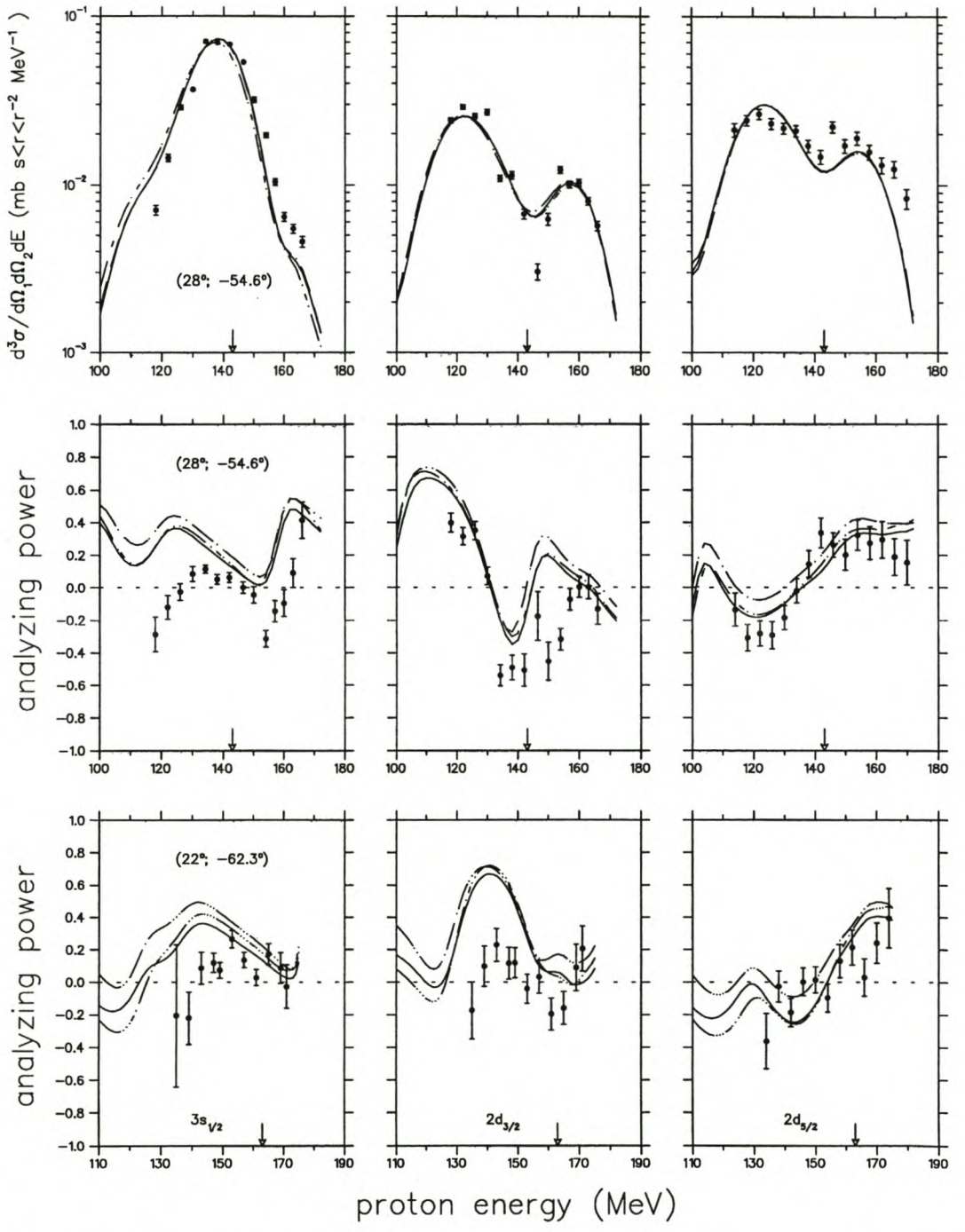

Figure 5.38: Cross-section and analyzing power energy-sharing distributions for the unresolved valence states. The details on the calculations are the same as in Fig. (5.36).

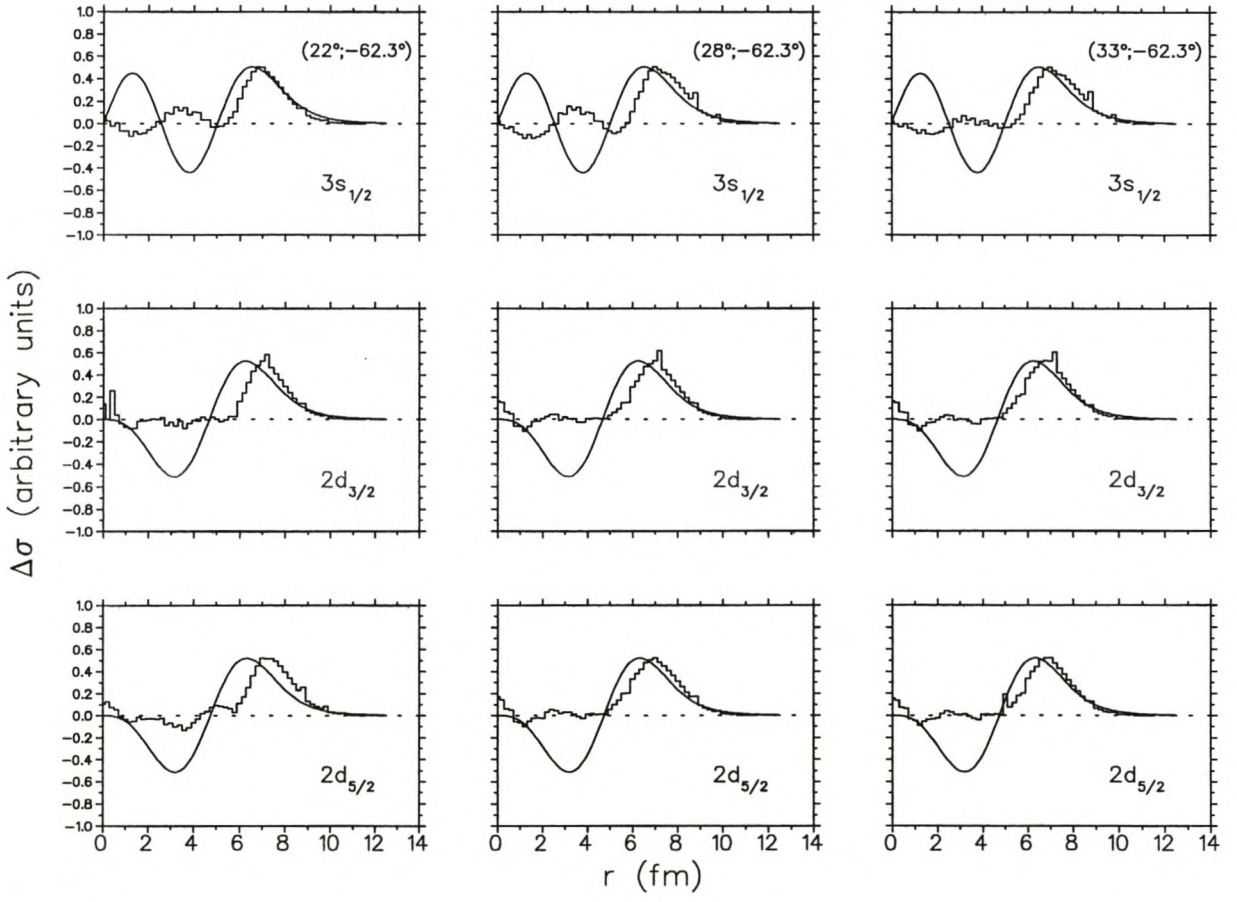

Figure 5.39: Histograms depicting the radial distribution of contributions to the DWIA cross-section ($\Delta\sigma$) at the quasi-free point for three valence states of ^{208}Pb. The smooth solid lines represent bound state radial wave functions.

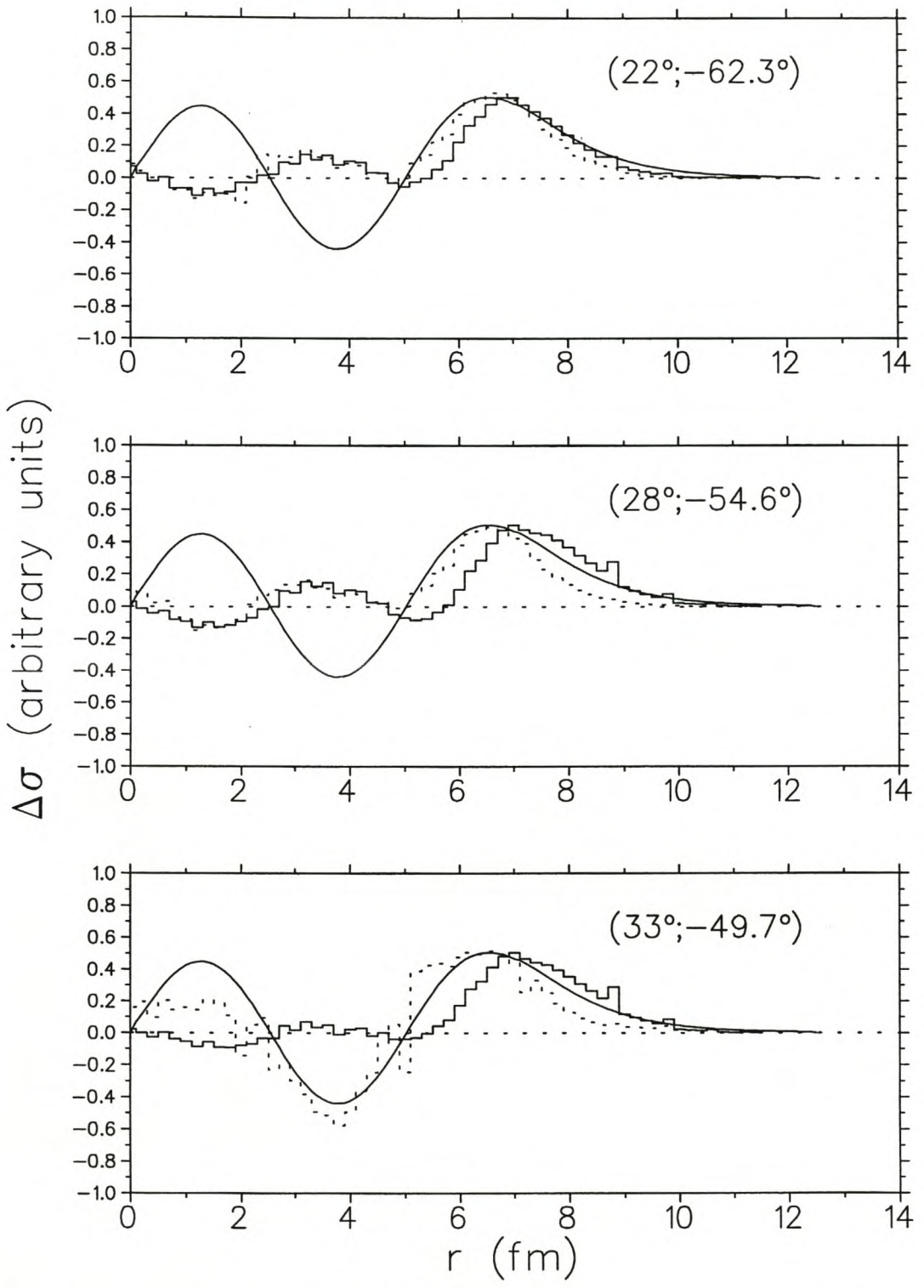

Figure 5.40: Histogram of $\Delta\sigma$, contrasting the radial distribution of contributions to the DWIA cross-section at the quasi-free point (solid line histogram) to that away from the quasi-free point (dotted line histogram). The smooth solid line represents bound state radial wave functions.

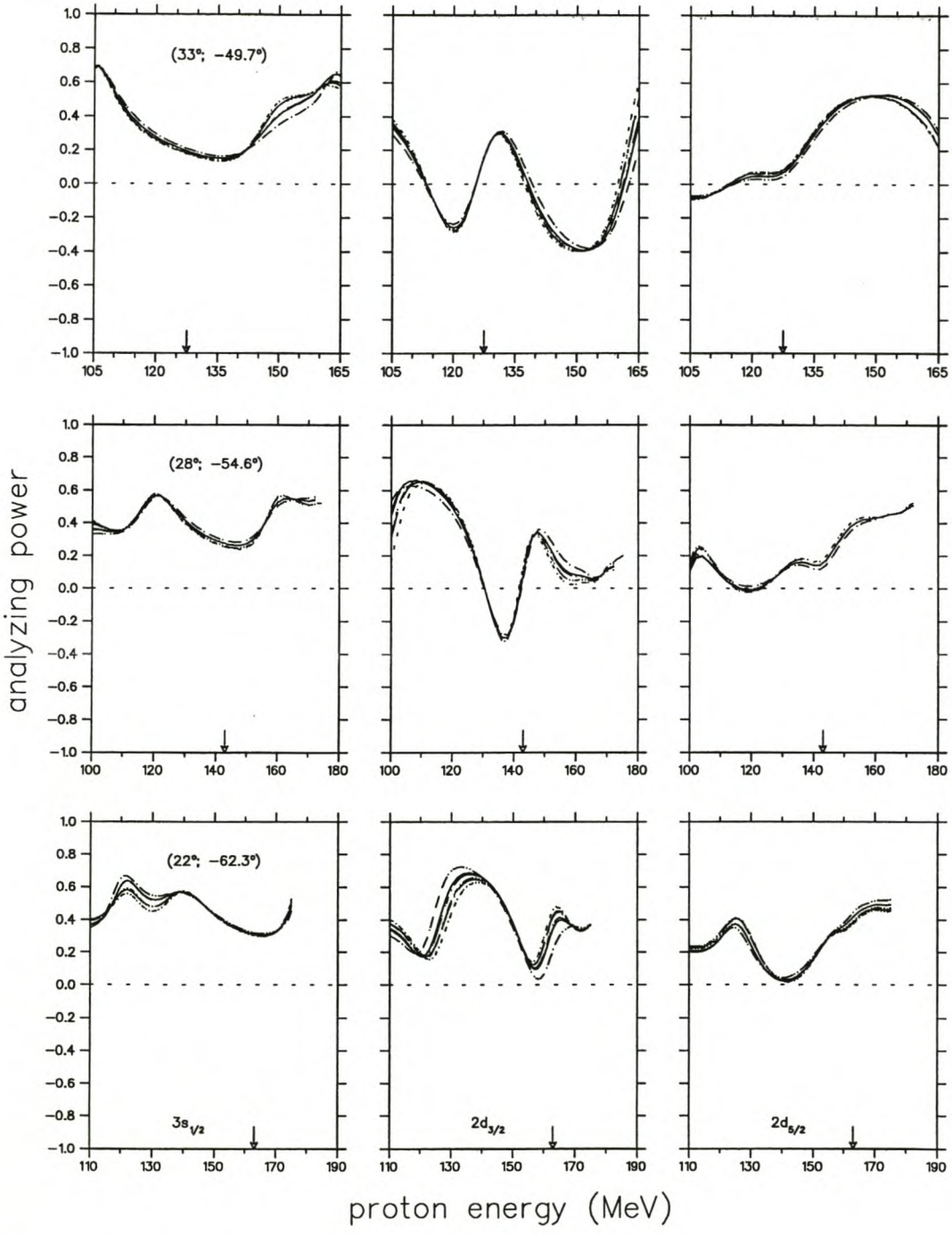

Figure 5.41: Analyzing power energy-sharing distributions for the free NN interaction and the Schwandt [Sch82] optical potential for six different bound state parameter sets: [Mah88] (big dot-dashed), [Ma91] (dotted line), [Cha83] (dashed line), [Qui88] (short dashed line), [Cow95] (solid line) and [Hor81] (short dot-dashed line).

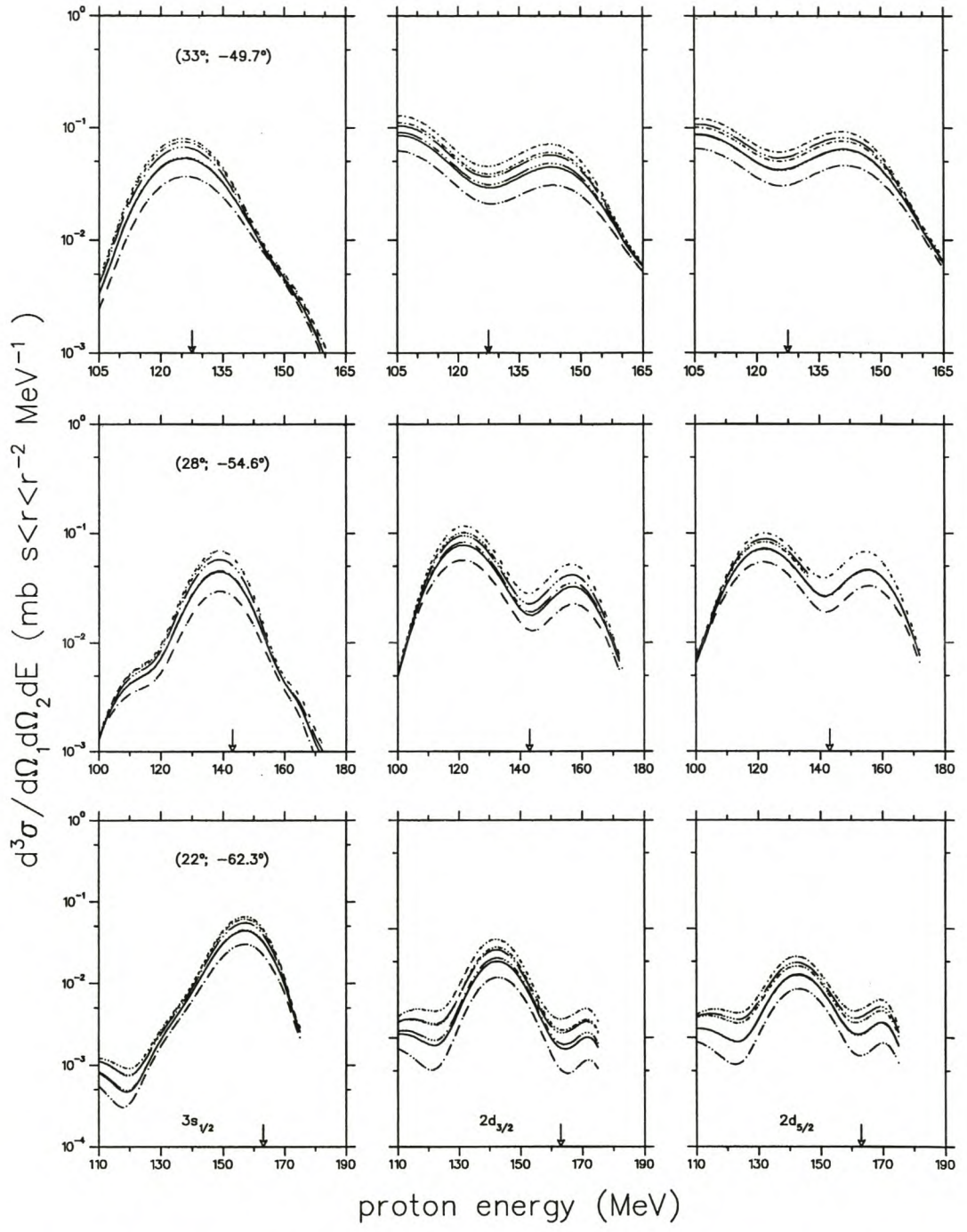

Figure 5.42: Cross-section energy-sharing distributions for the free NN interaction and the Schwandt [Sch82] optical potential for six different bound state parameter sets. The calculations are as in Fig. (5.41).

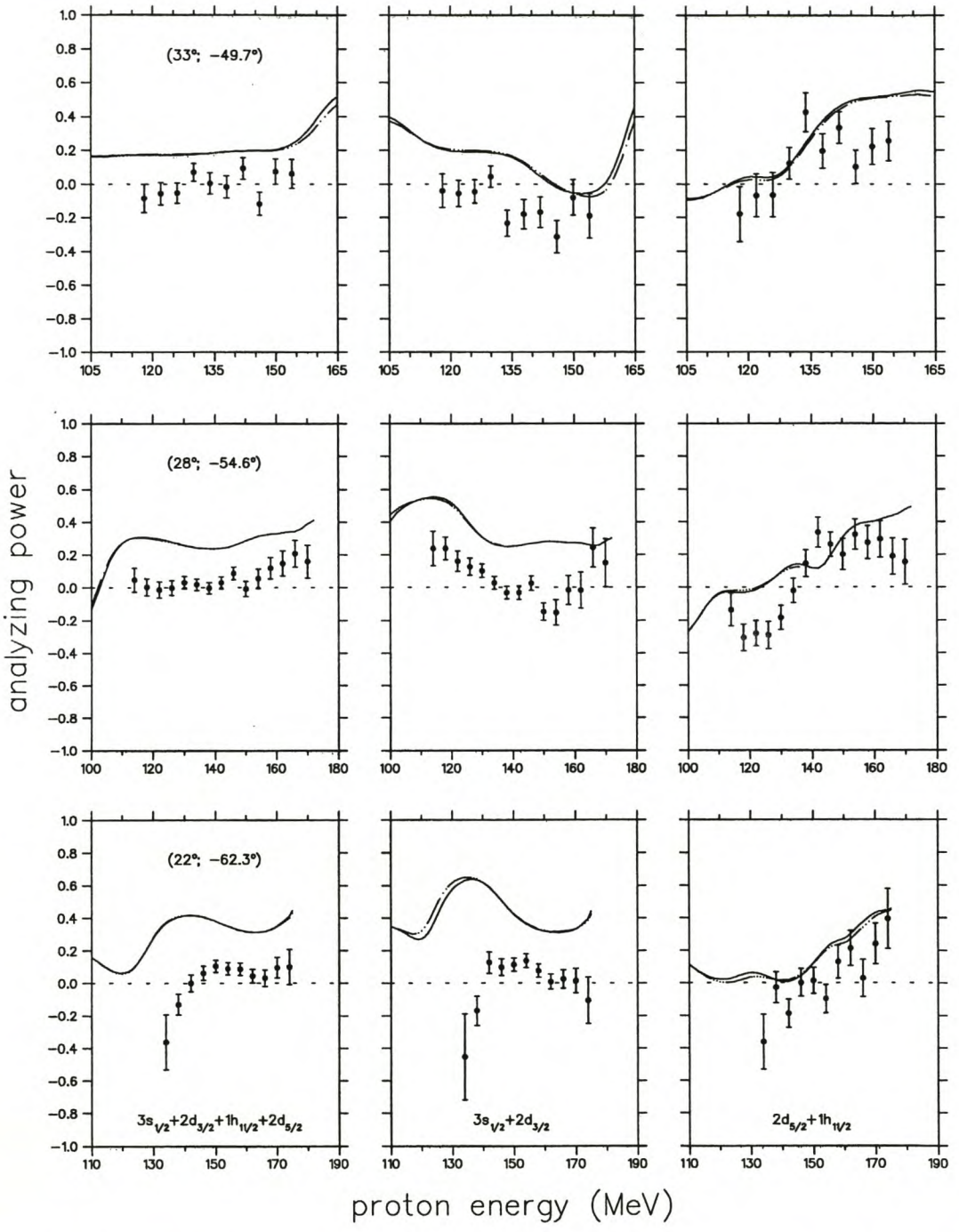

Figure 5.43: Analyzing power energy-sharing distributions for the free NN interaction and the Schwandt [Sch82] optical potential with non-locality for the distorted waves included (solid curve) and excluded (dashed curve).

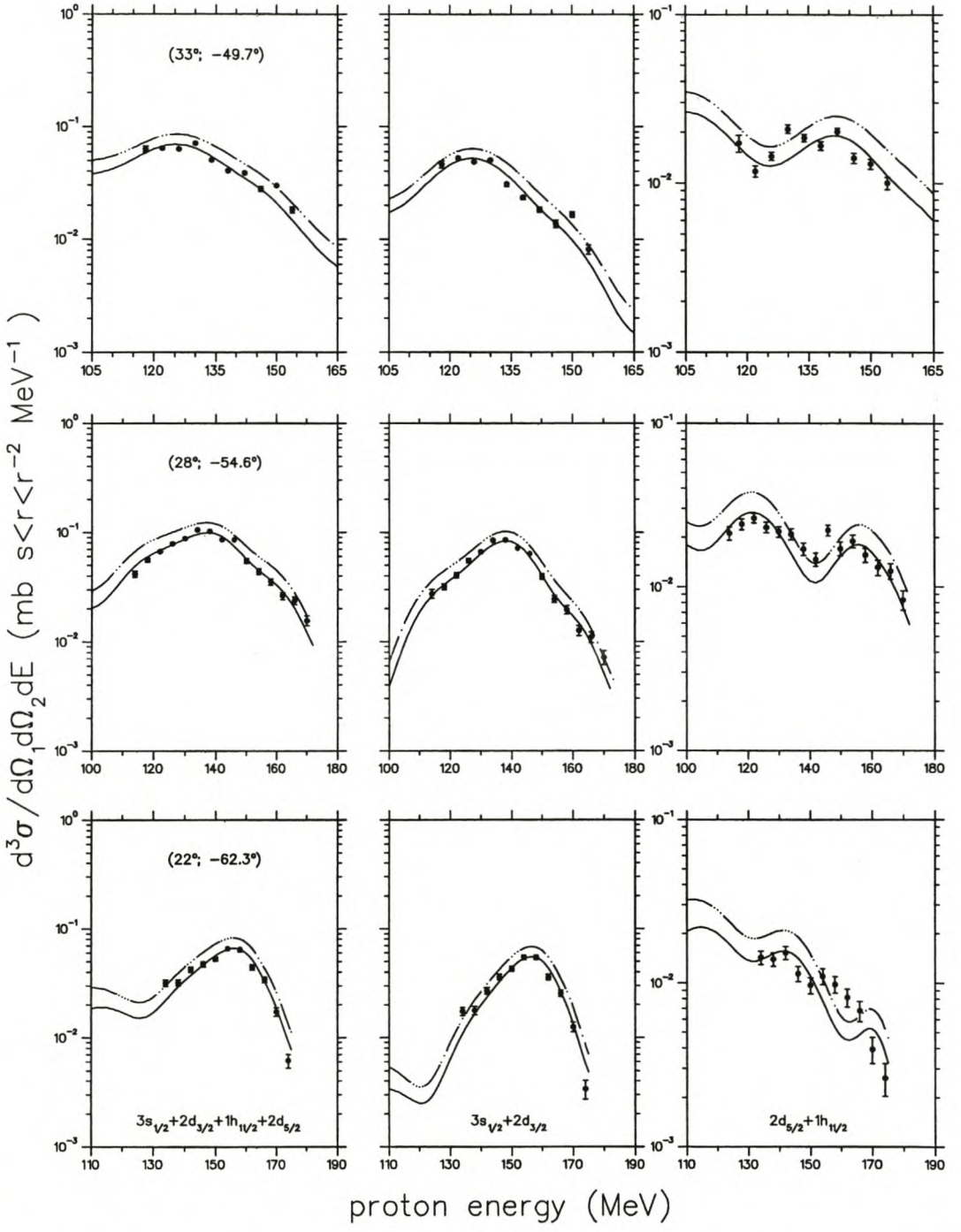

Figure 5.44: Cross-section energy-sharing distributions for the free NN interaction and the Schwandt [Sch82] optical potential with non-locality for the distorted waves included (solid curve) and excluded (dashed curve). Both calculations are plotted with the spectroscopic value calculated for non-locality included.

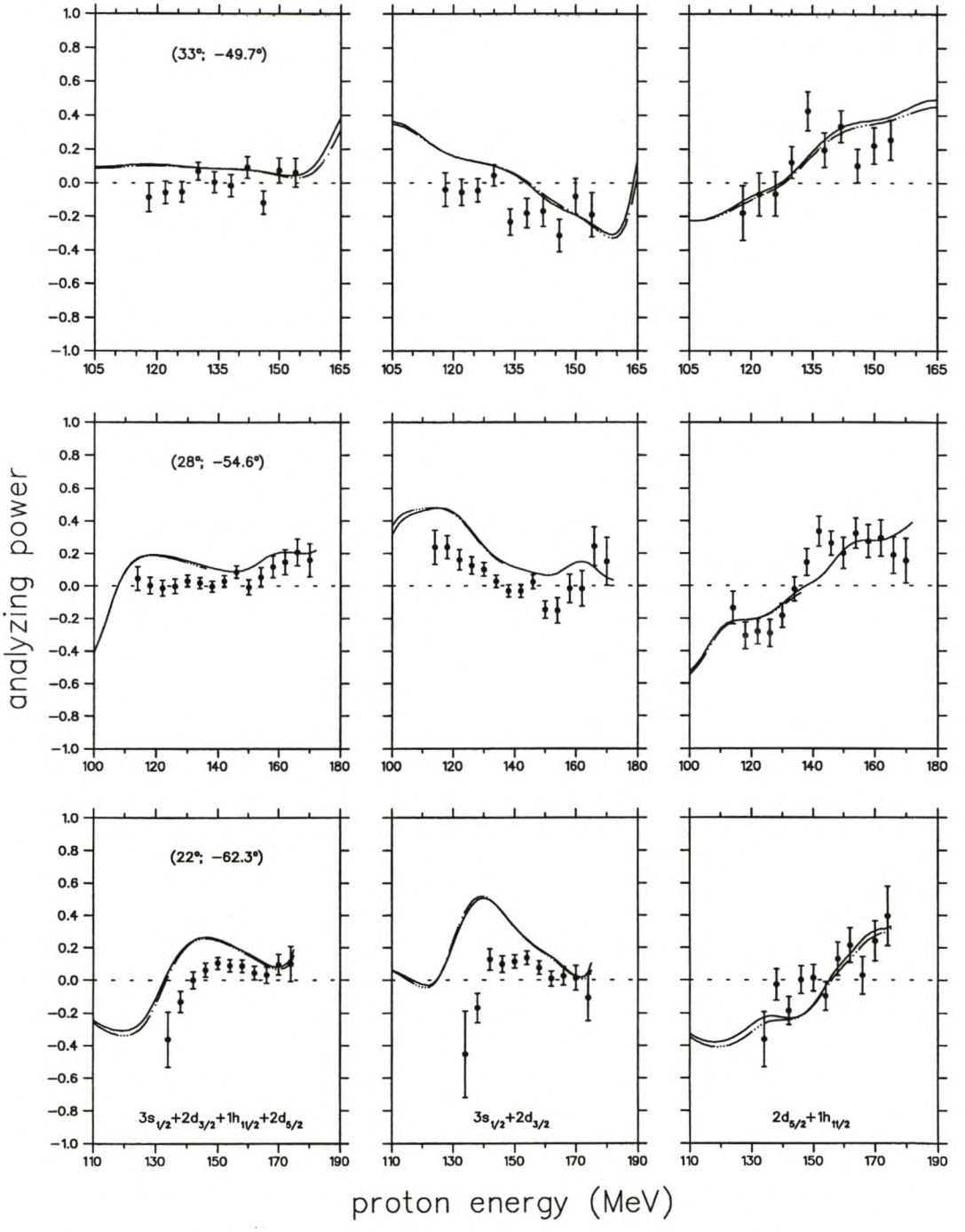

Figure 5.45: Analyzing power energy-sharing distributions for the Kelly [Kel94] NN interaction and the Hama [Ham90] optical potential, with non-locality for the distorted waves included (solid curve) and excluded (dashed curve).

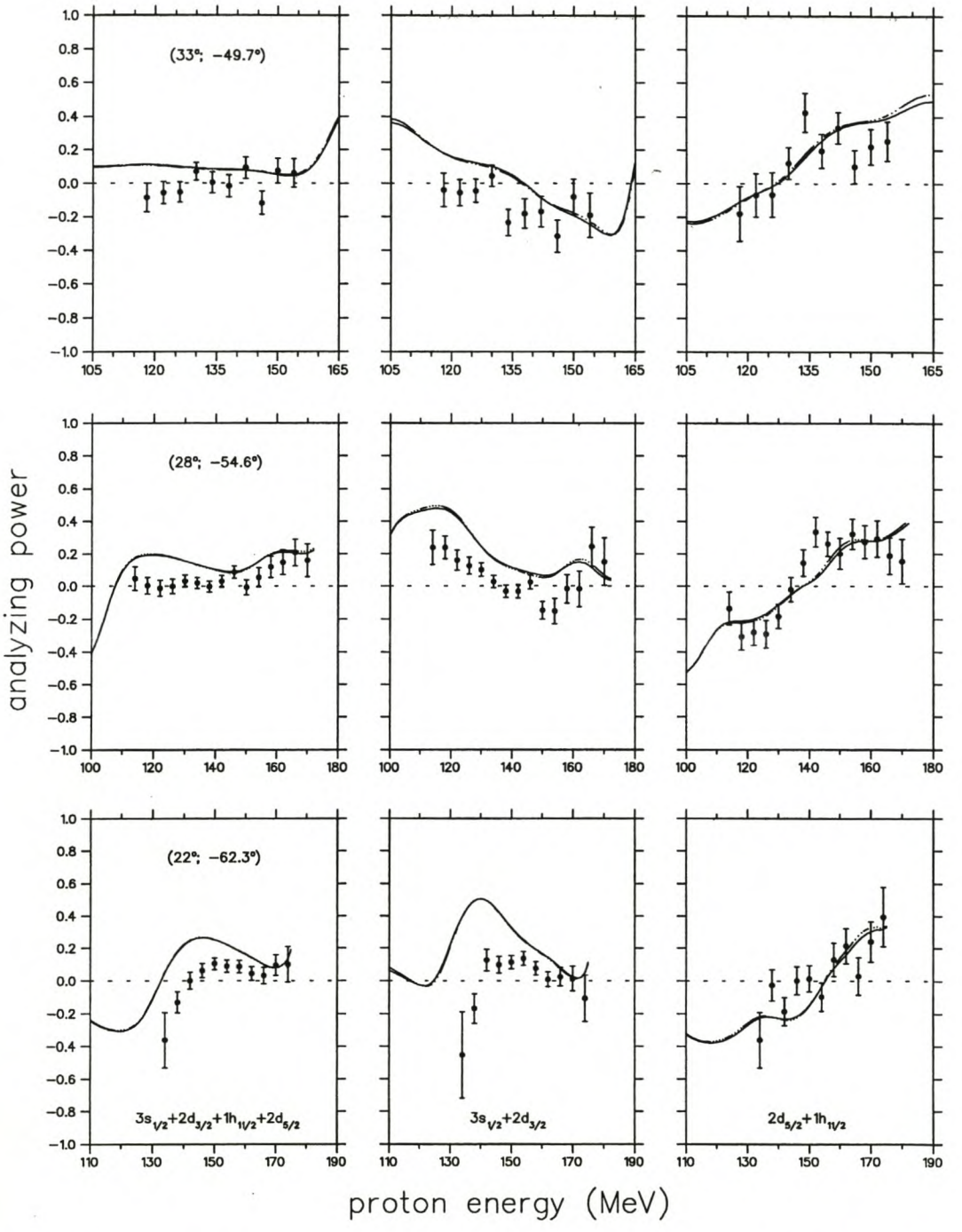

Figure 5.46: Analyzing power energy-sharing distributions for the Kelly [Kel94] NN interaction and the Hama [Ham90] optical potential, with non-locality for the distorted waves included (solid curve) and excluded (dashed curve) according to the contribution of the Darwin term.

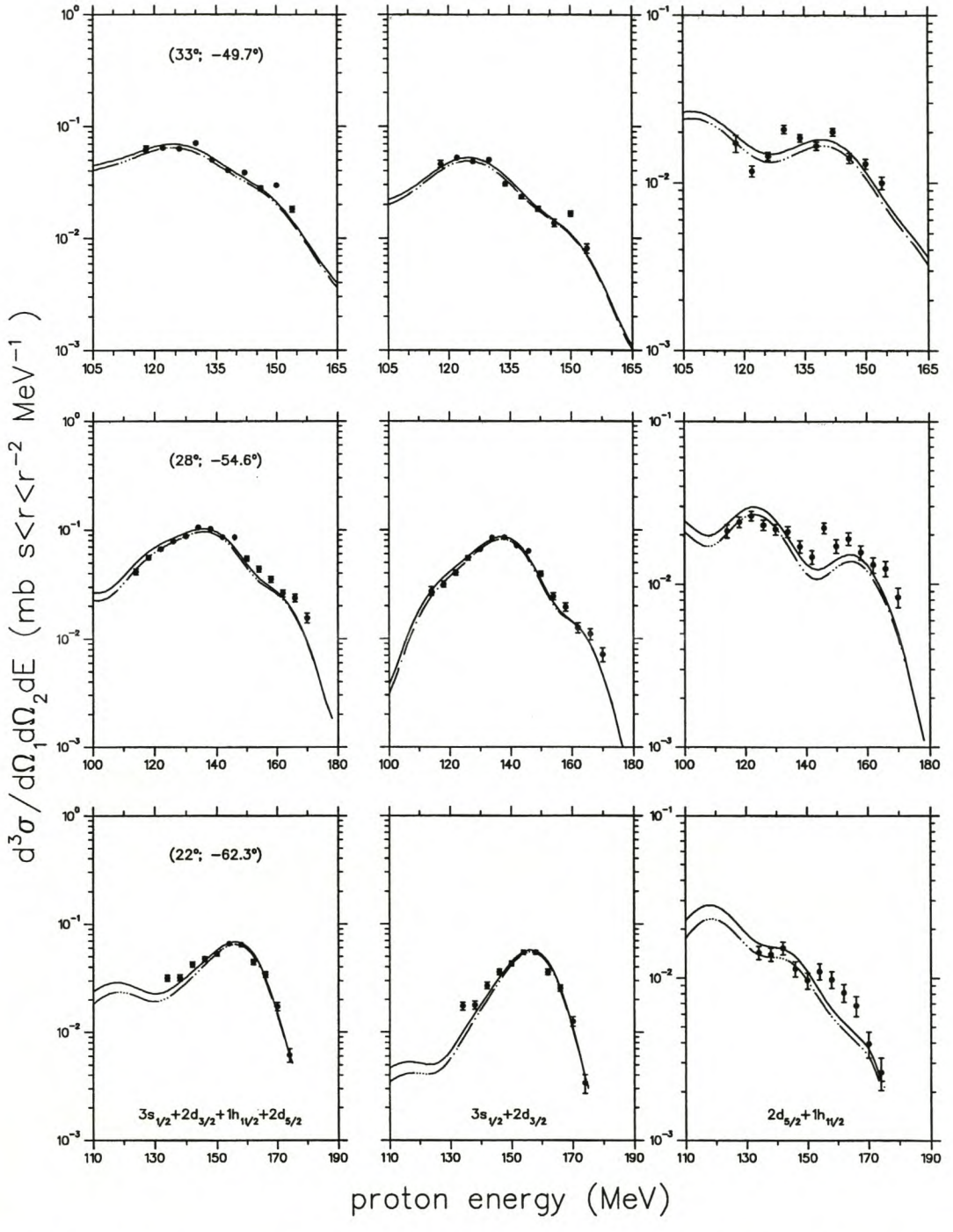

Figure 5.47: Cross-section energy-sharing distributions for the Kelly [Kel94] NN interaction and the Hama [Ham90] optical potential, with non-locality for the distorted waves included (solid curve) and excluded (dashed curve) according to the contribution of the Darwin term.

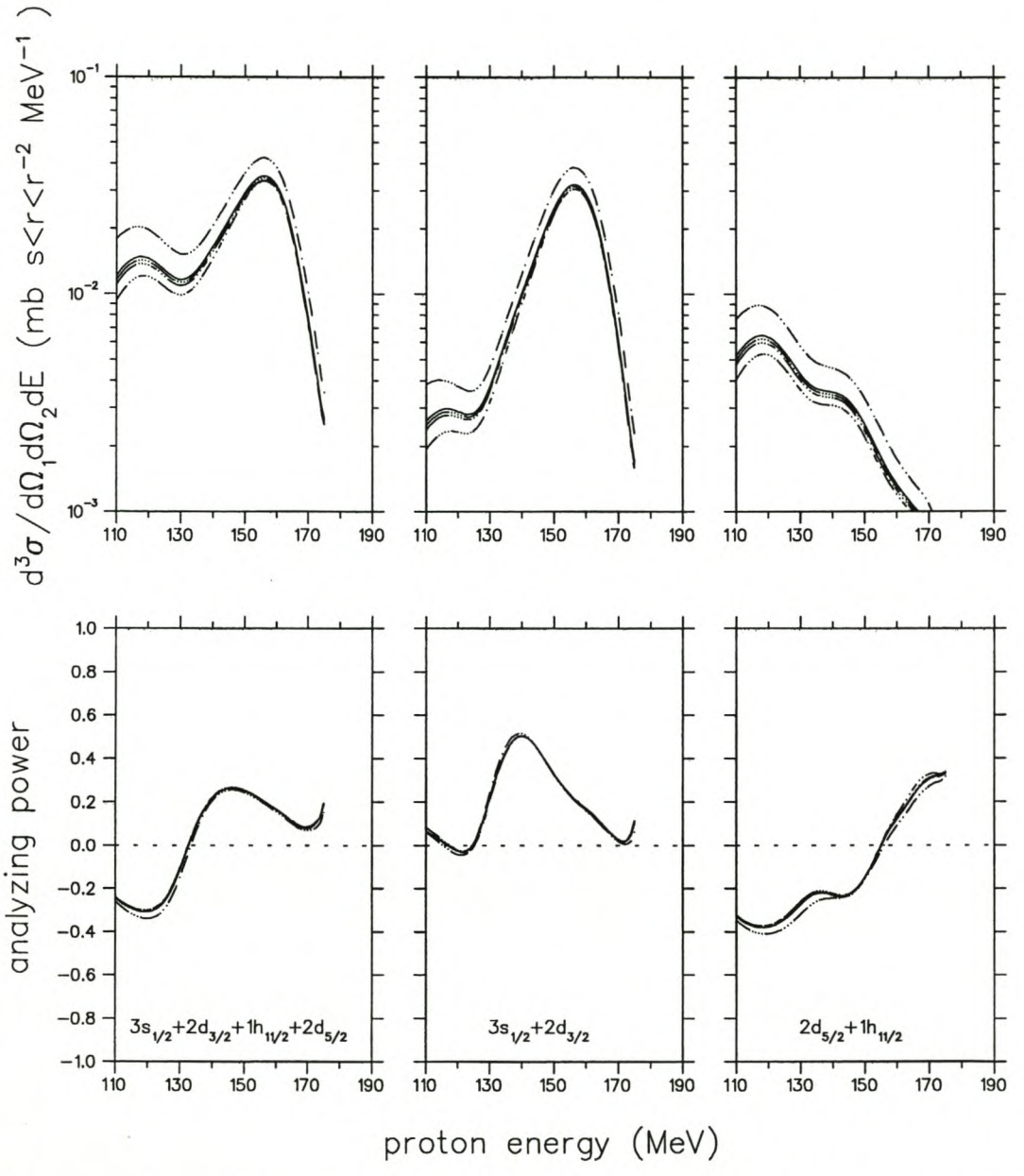

Figure 5.48: Analyzing power energy-sharing distributions for the Kelly [Kel94] NN interaction and the Hama [Ham90] optical potential, with non-locality for the distorted waves included via the Perey term [Per62] with $\beta = 0.85$ (solid curve), $\beta = 0.90$ (dashed curve), $\beta = 0.95$ (dot-dashed curve), $\beta = 1.00$ (short-dashed curve) and the Darwin term enabled (short dot-dashed curve). Cross-sections are plotted with a normalization factor of 1.

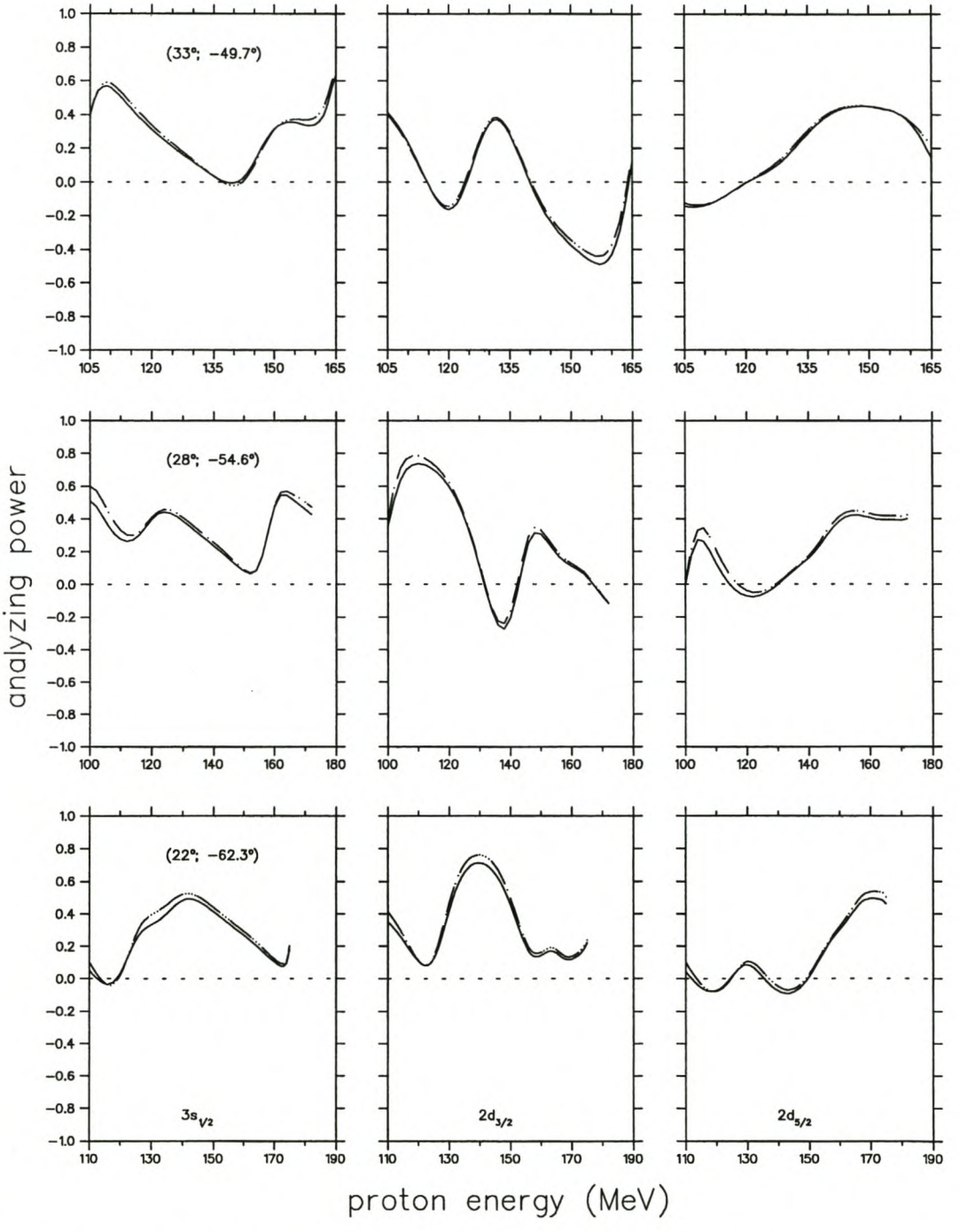

Figure 5.49: Analyzing power energy-sharing distributions for the initial energy prescription (dot-dashed line) and final energy prescription (solid line), representing DWIA calculations for free NN interaction and distorting optical potential parameter set of Hama [Ham90] (DH2D).

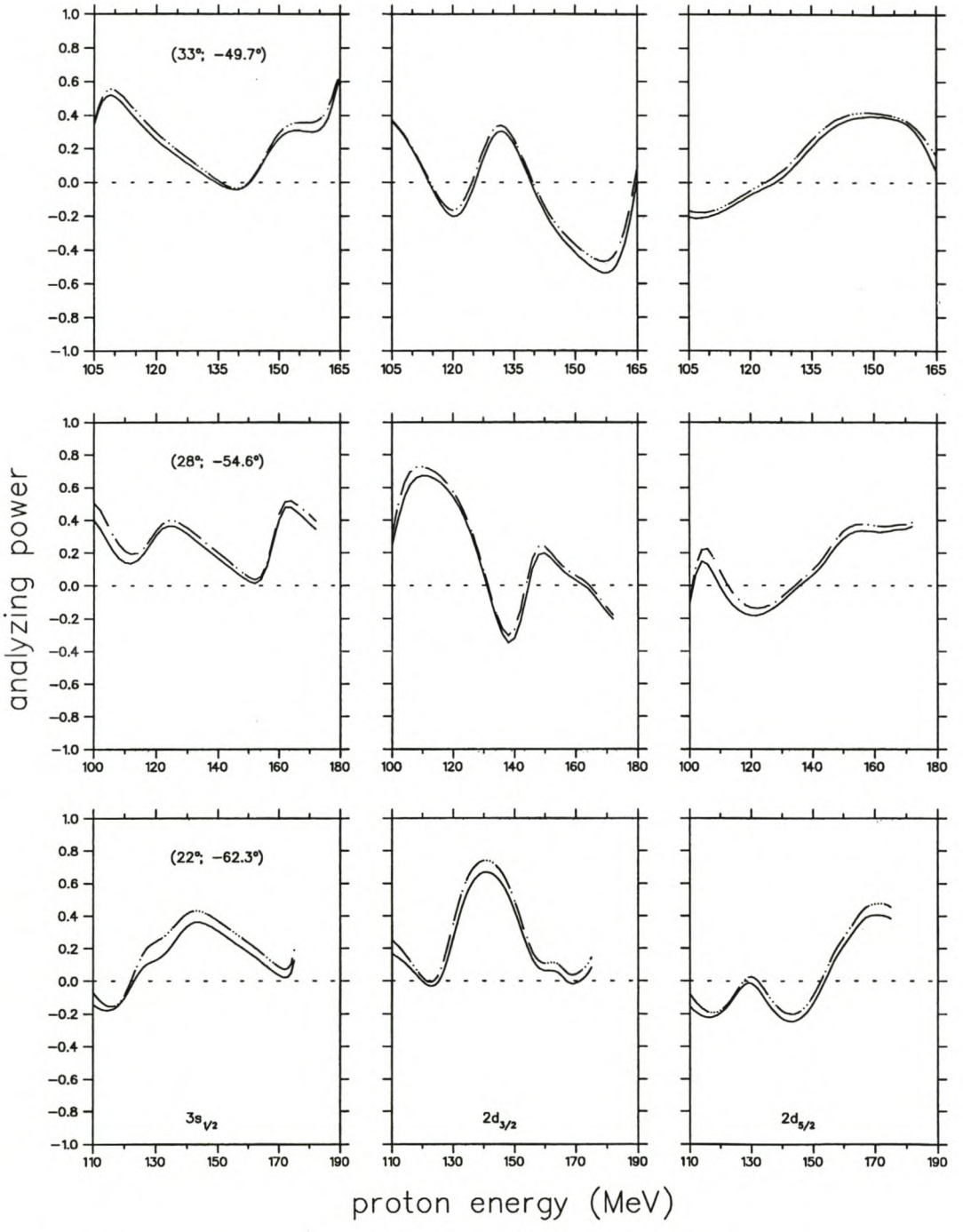

Figure 5.50: Analyzing power energy-sharing distributions for the initial energy prescription (dot-dashed line) and final energy prescription (solid line), representing DWIA calculations for the Kelly [Kel94] NN interaction for distorting optical potential parameter set of Hama [Ham90] (DH2D).

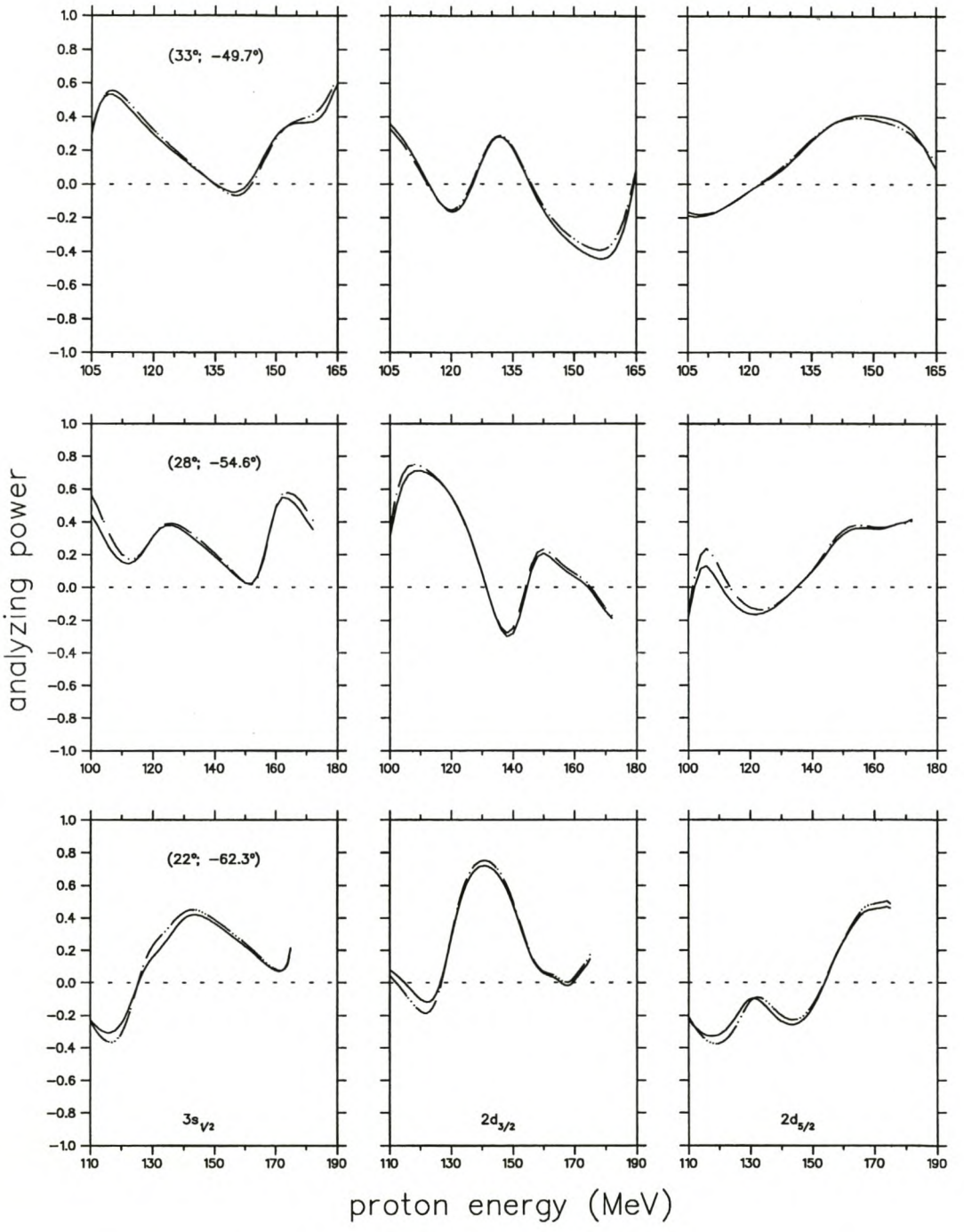

Figure 5.51: Analyzing power energy-sharing distributions for the initial energy prescription (dot-dashed line) and final energy prescription (solid line), representing DWIA calculations for the Horowitz Iqbal [Hor86] NN interaction for distorting optical potential parameter set of Hama [Ham90] (DH2D).

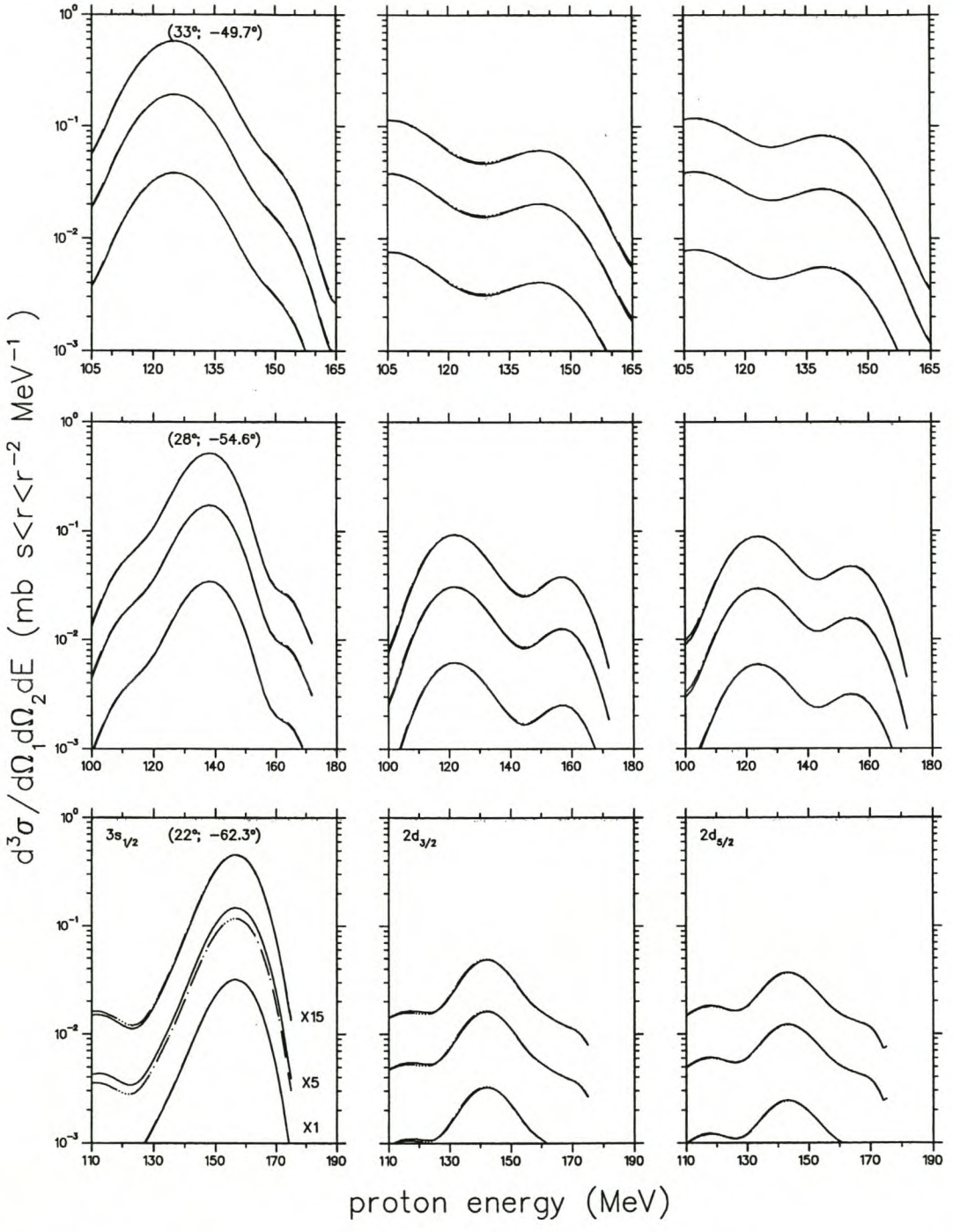

Figure 5.52: Cross-section energy-sharing distributions for the initial energy prescription (dashed line) and final energy prescription (solid line), representing DWIA calculations for the free NN interaction (×1), the Kelly [Kel94] empirical effective interaction (×5) and the Horowitz Iqbal [Hor86] interaction (×15). The optical potential parameter set of Hama [Ham90] (DH2D) was employed in the above calculations. Normalization factors (given in brackets) were chosen for display purposes.

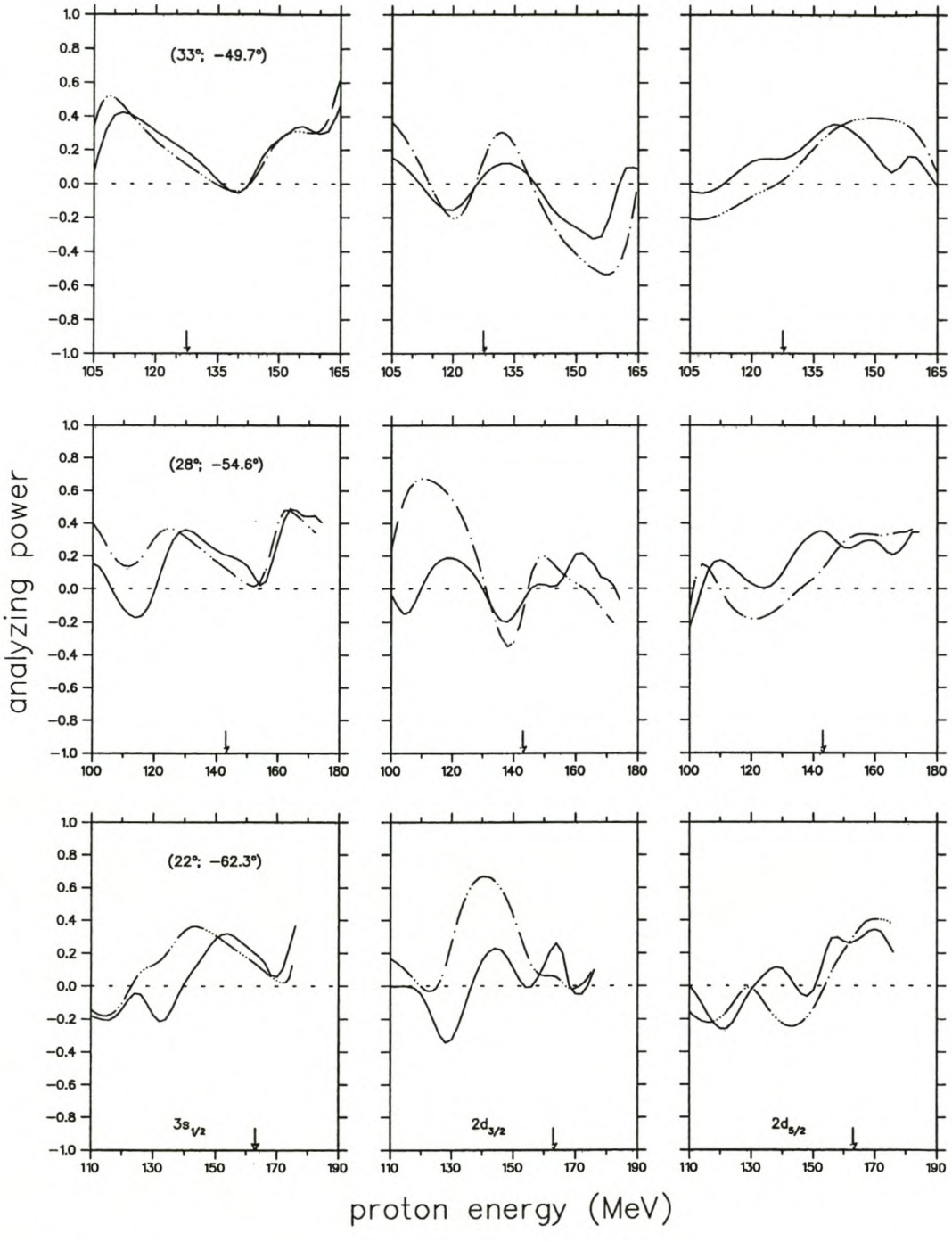

Figure 5.53: Analyzing power energy-sharing distributions for the optical potential of Hama [Ham90] (DH2D) and the Kelly [Kel94] effective interaction (solid line), compared to calculations made with the relativistic DWIA code of Mano (dashed lines).

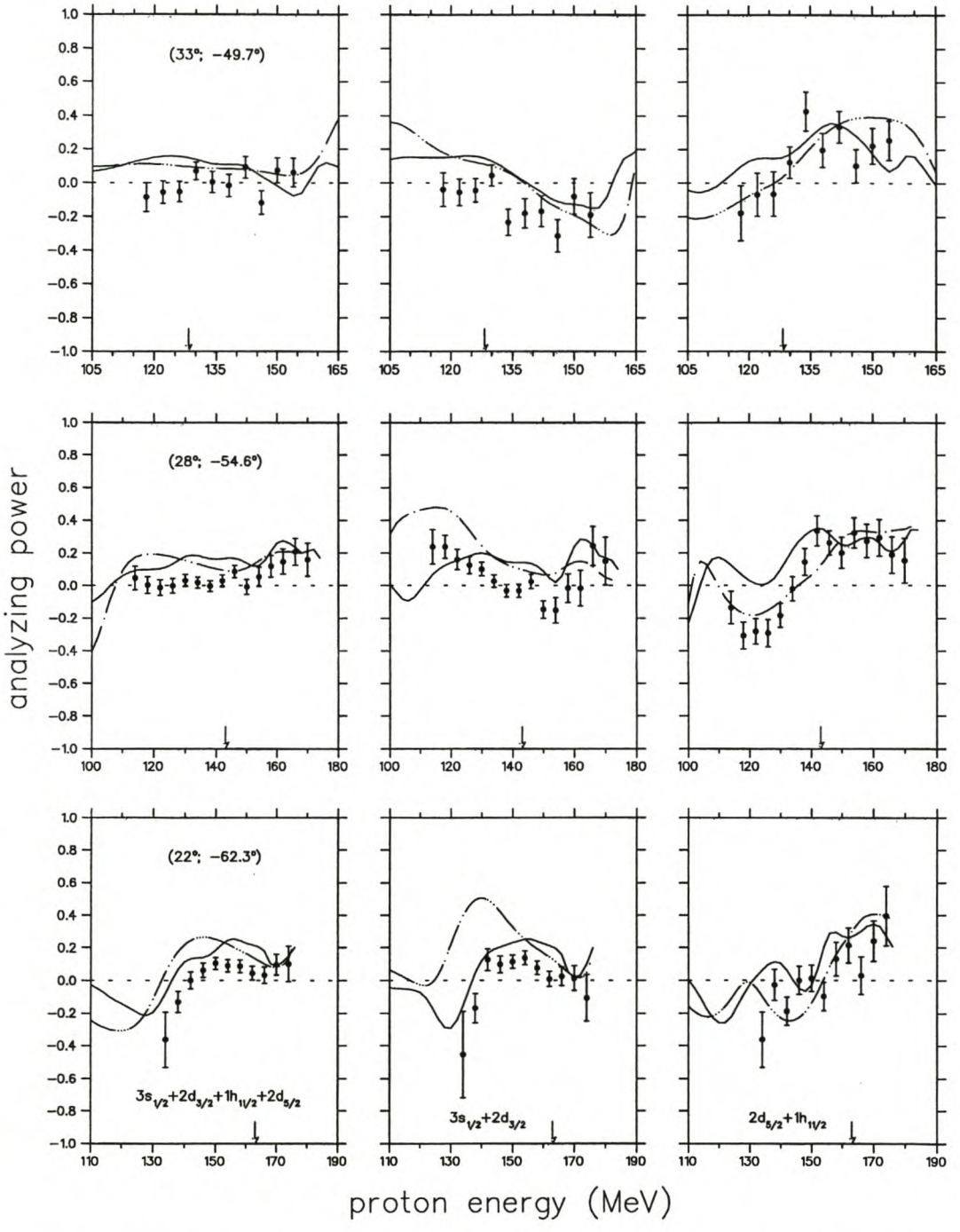

Figure 5.54: Analyzing power energy-sharing distributions for the unresolved valence states for the optical potential set of Hama [Ham90] (DH2D) and the Kelly [Kel94] effective interaction (solid line), compared to calculations made with the relativistic DWIA code of Mano (dashed line).

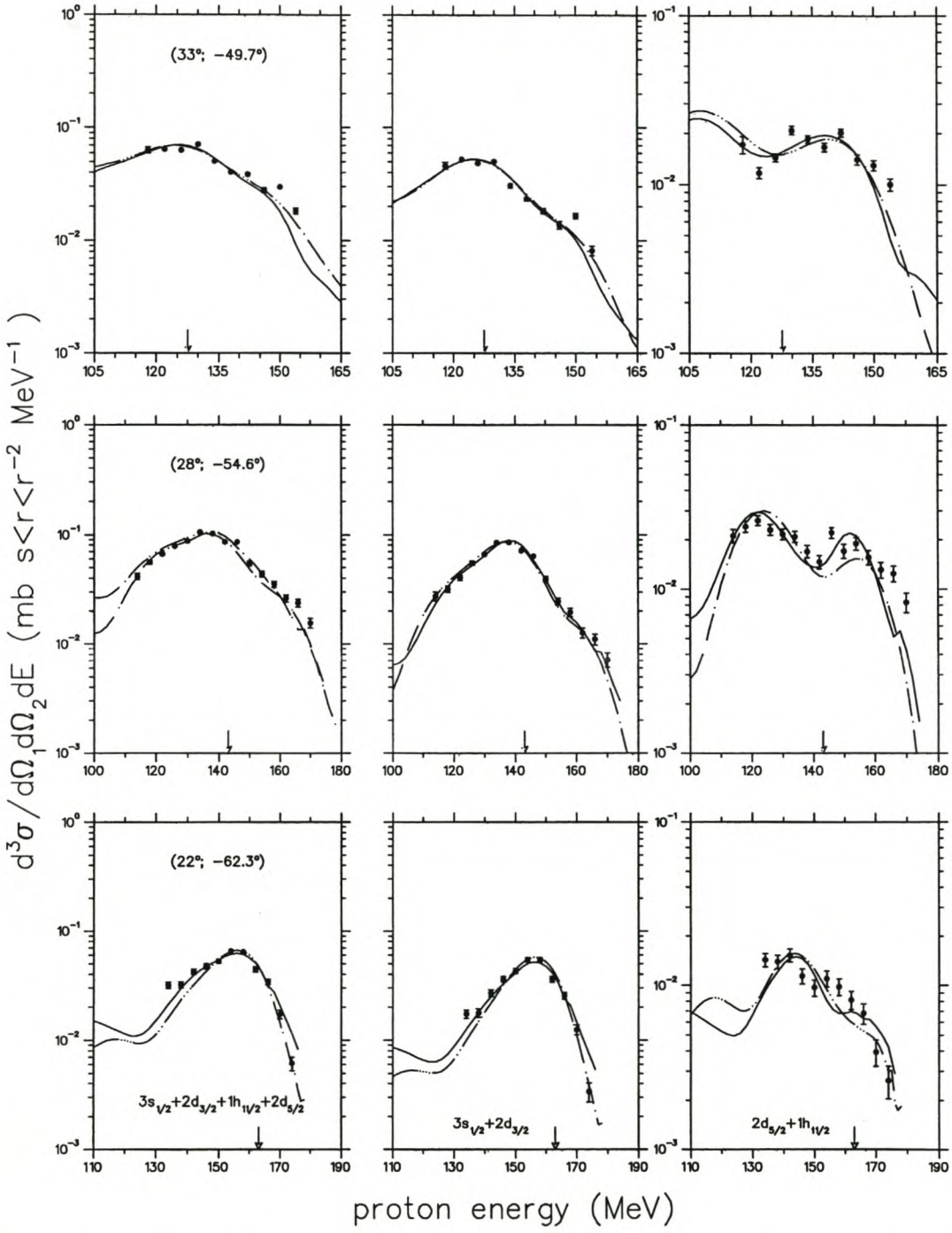

Figure 5.55: Cross-section energy-sharing distributions for the unresolved valence states for the optical potential set of Hama [Ham90] (DH2D) and the Kelly [Kel94] effective interaction (dashed line), compared to calculations made with the relativistic DWIA code of Mano (solid line).

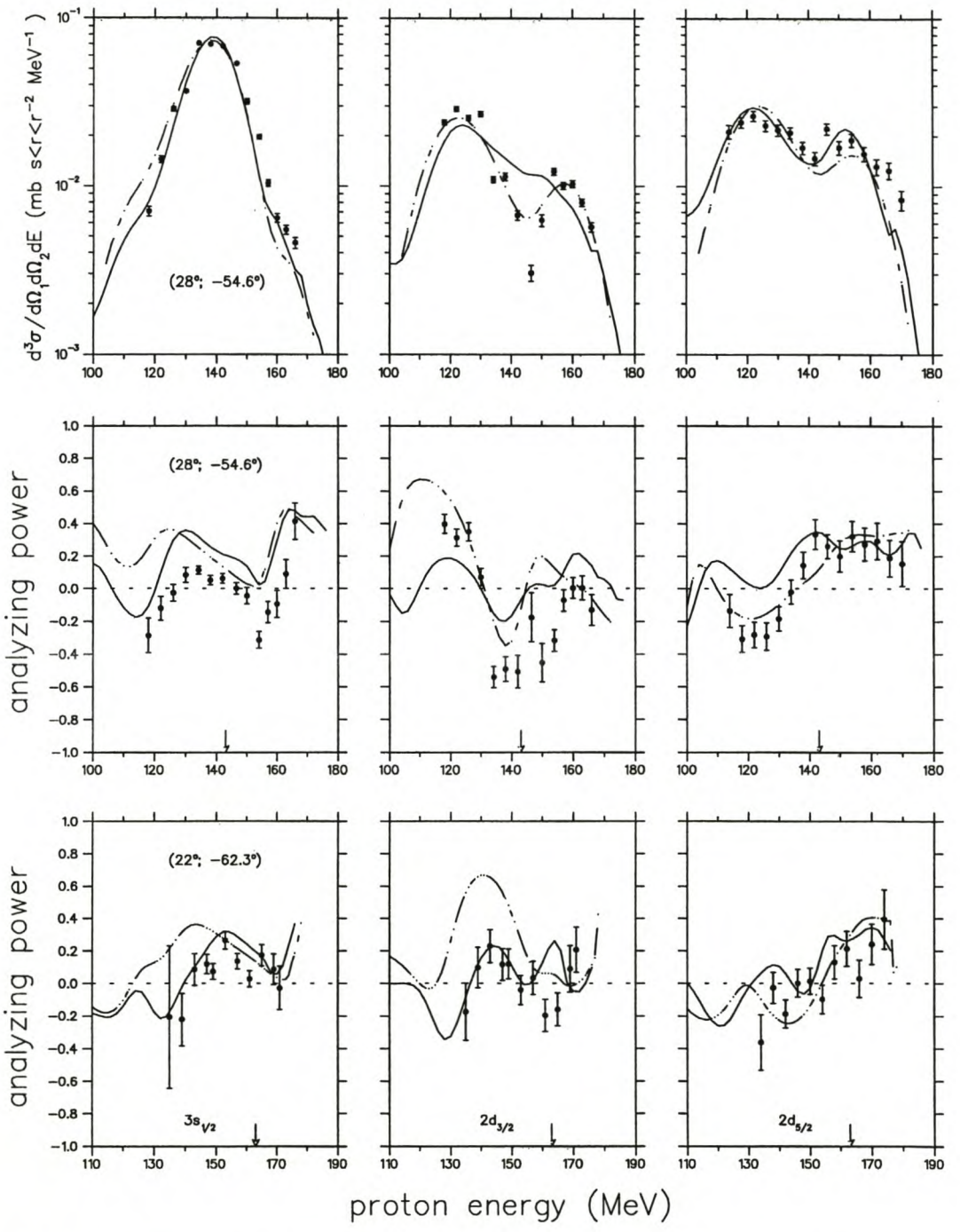

Figure 5.56: Analyzing power and cross-section energy-sharing distributions for the resolved $3s_{1/2}$ and $2d_{3/2}$ states. Calculations shown are for the optical potential of Hama [Ham90] (DH2D) and the Kelly [Kel94] effective interaction (dot-dashed line), compared to calculations made with the relativistic DWIA code of Mano (solid line).

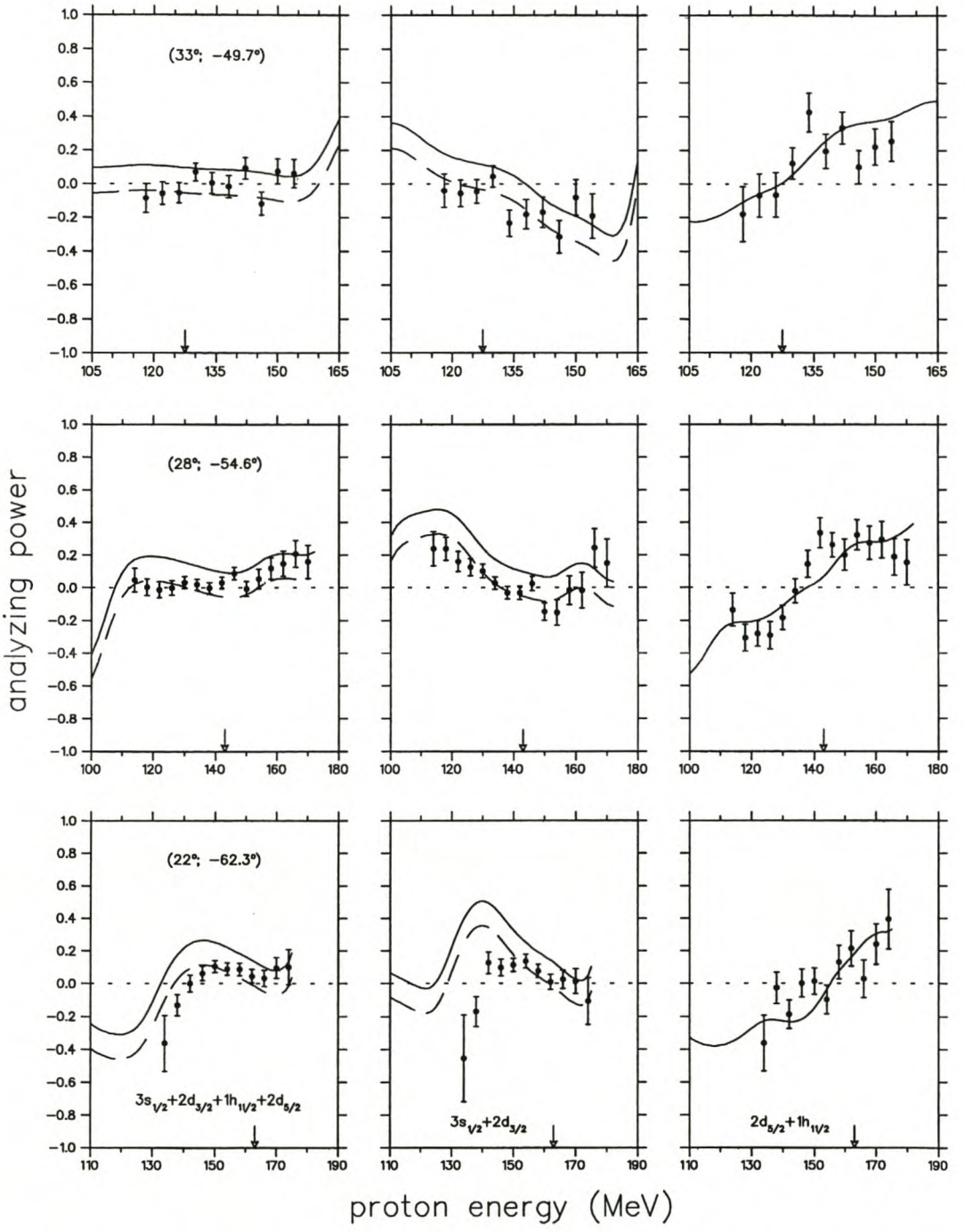

Figure 5.57: Analyzing power energy distributions for the unresolved valence states. The solid curves represent DWIA predictions for the second optical potential parameter set of Hama [Ham90] and the density dependent NN interaction of Kelly [Kel94]. The dashed lines represent the same DWIA calculation, shifted downwards by 0.15.

Chapter 6

Conclusion

It is known that the DWIA theoretical framework successfully predicts cross-sections for quasi-free proton knockout reactions over a wide energy range (76-600 MeV) for light and medium targets up to ^{40}Ca. The DWIA was also shown, somewhat surprisingly, to provide an accurate prediction of cross-sections and spectroscopic factors for proton knockout from a ^{208}Pb target at 200 MeV [Cow95] to a combination of 4 states in the ^{207}Tl final state. This success, in spite of severe distortion effects due to the heavy target, was interpreted as an indication of the valid theoretical treatment of the proton distortions within the DWIA framework. On the other hand, calculations of the analyzing power of the quasi-free proton knockout reaction for light to medium targets are problematic. At projectile energies $\geq$ 200 MeV, and especially for knockout from s-states, the analyzing power was found to be consistently lower than the standard DWIA predictions [Huf96, Hat97, Mil98, Nor98]. The introduction of density dependent NN interactions succeeded in reducing the discrepance between experiment and theory, but did not yield satisfactory agreement.

High resolution measurements for the $^{208}Pb(\vec{p},2p)^{207}Tl$ quasi-free proton knockout reaction performed in this study show, as expected, that the standard non-relativistic DWIA calculation yield good shape agreement for the cross-section results as well as satisfactory spectroscopic factors. However, A_y data for especially the $3s_{1/2}$ state exhibits a substantial reduction from the standard non-relativistic DWIA calculations. The inability of the DWIA to predict analyzing powers for light and medium targets is thus shown to persist in the high mass region.

One element of the DWIA calculation known to strongly affect the shape of the analyzing power is the optical potential used to generate the distortions of the proton wave functions. These distortions cause energy dependent modifications to the PWIA analyzing power, which can be identified as the analyzing power of the NN interaction. For s-state knockout the mod-

ification of the PWIA analyzing power is mainly due to the spin-orbit term of the optical potential, and more specifically due to the spin-orbit distortion of the projectile proton. It was furthermore shown that at the quasi-free point A_y displays minimal sensitivity to changes in the spin-orbit potential term, which indicates that the observed A_y discrepancy is unlikely to be due to sensitivity to the distorting potentials. The deviation of the analyzing power for the d-states from the PWIA value originates from both the spin-orbit potential terms as well as the effective initial spin polarization of the struck nucleon, the Maris effect. No adjustment, within reason, to the different potential parameters of either the phenomenological Schrödinger or Dirac equation based optical potentials could resolve the discrepancy between experiment and theory. Because the distortions can only alter the shape of the PWIA A_y, without reducing the PWIA benchmark analyzing power, it is concluded that in principle the description of the proton distortions cannot account for the lowering of the A_y. Initial arguments that the reduction in A_y as observed at the higher energies is likely to be ascribed to inaccuracies in the parameterization of the standard phenomenological Schrödinger optical potentials (known to fail at energies > 200 MeV [Bau98]) is thus shown to be unlikely.

It is clear that the mechanism required to improve agreement between experiment and theory must result in a reduced value for the calculated PWIA A_y over the whole recoil momentum range. Other facets of the DWIA, such as the sensitivity to the energy prescription of the NN interaction, as well as non-locality effects, were investigated and shown to play a negligible role. And since the wave functions used for the bound protons are consistent with results from $(e, e'p)$ studies, it is concluded that the problem is unlikely to be caused by the description of the bound state wave function.

From the radial localization of the DWIA cross-section it is seen that a non-negligible contribution to the reaction originates from inside the nuclear volume. Medium modification to the NN interaction is therefore a natural candidate in the search for mechanisms that cause changes in the A_y of the NN interaction. The insensitivity of the A_y of the $3s_{1/2}$-state at the quasi-free point to changes in the distorting potentials suggests that the quasi-free point is well-suited to access the NN interaction. In other words, an inadequate description of the density dependent NN interactions is expected to be revealed at the quasi-free point, where complications due to the distortions are minimal. The inclusion of density dependent NN-interactions exhibited the desired trend in reducing the theoretical calculations over the whole range of recoil momenta.

This reduction results in acceptable agreement between the theoretical prediction and experimental data for the $2d_{3/2}$ and $2d_{5/2}$ states, while the disagreement remains significant for the $3s_{1/2}$ state.

In order to ascertain whether a full relativistic calculation could provide a quick solution to the analyzing power problem, a naive relativistic DWIA calculation was performed. At a first glance the relativistic DWIA calculation seems to do much better than the non-relativistic calculations. However, where there is improvement regarding $3s_{1/2}$ data, agreement for the other states deteriorates. Furthermore, the reduction near the quasi-free point is as bad or worse as for the non-relativistic calculations. This indicates that the relativistic DWIA is not more successful than the non-relativistic DWIA. More calculations where density-dependence are introduced through the effective mass effect are however needed before an authoritive conclusion can be drawn concerning the success of the relativistic DWIA.

To summarize: From the *cross-section* results of the $^{208}Pb(\vec{p},2p)^{207}Tl$ reaction at an incident energy of 200 MeV, we conclude that the DWIA is a reasonable theoretical framework for the description of quasi-free proton scattering. However, discrepancies between experimental and theoretical *analyzing power* distributions indicate a need for refinements to the model. Furthermore, it is shown that a nuclear-matter density dependent description of the NN interaction inside the nuclear field is the only ingredient of the DWIA that allows an appropriate modification of the analyzing power. Available prescriptions for the introduction of a density dependence of the NN interaction are reasonably successful, but especially for knockout of protons from the s-state shell-model orbital, the problem is not fully resolved. Clearly, further investigation of the theoretical formulation of this density dependence is needed.

Appendix A

Experimental Data

A.1 Spectroscopic Factors

The spectroscopic factors S_{LJ} were extracted by normalising the theoretical calculations to the experimental data. The normalization was performed with the method of chi-square minimization [Leo87]. A full list of spectroscopic factors from this study is given in tables A.1 - A.7, illustrating the variation of the spectroscopic factors for different optical potentials (as described in section 2.4) and NN interaction types (see section 2.3), as well as between the non-relativistic DWIA and relativistic DWIA. As mentioned in section 5.1, the spectroscopic factors calculated for the combination of states are obtained by normalizing the combined theoretical cross-sections (refer to Eq. 5.2) to the experimental values, assuming that the main contribution to the combined cross-section is either from the s-state, as in the case of all states combined and for the combination of states $(3s_{1/2} + 2d_{3/2})$, or from the d-state for the combination of states $(2d_{5/2} + 1h_{11/2})$. Note that other than the spectroscopic factors in table 5.1, those presented in the following tables are not yet normalized to the $2j + 1$ limit.

It is seen that the DEB optical potentials yield spectroscopic factors that are somewhat larger than the traditional Schrödinger equation based optical potentials. This phenomena was also found by Arendse [Are97]. On the other hand the Nadasen [Nad81] potential generates the lowest values. It can be shown that for only 70% of the imaginary part of the DEB potential of Hama [Ham90] we can reproduce the spectroscopic factors as obtained with the Nadasen [Nad81] potential, without any drastic effect on the analyzing power results.

In his thesis Arendse [Are97] showed that for standard (i.e. for the non-relativistic DWIA and the free NN interaction) DWIA calculations the uncertainty of the spectroscopic value due to the use of different bound state parameter sets and optical potentials is $\sim$ 19%. By adding this to the systematic error of 7.8% we find that the following spectroscopic factors are in reasonable agreement with each other, as well as with those from the literature as listed in table 5.2.

	all			$3s_{1/2}$ + $2d_{3/2}$		
Optical model potential	free	Kelly	H&I	free	Kelly	H&I
Nadasen [Nad81]	1.11	1.20	1.14	0.98	1.07	1.02
Madland [Mad87]	1.32	1.44	1.38	1.19	1.30	1.26
Schwandt [Sch82]	1.32	1.44	1.38	1.18	1.30	1.25
Hama [Ham90] DP1	1.89	2.01	1.94	1.73	1.85	1.81
Hama [Ham90] DP2	1.82	1.95	1.88	1.67	1.79	1.75
Cooper [Coo93] EDAD1	2.44	2.61	2.53	2.23	2.40	2.35
Cooper [Coo93] EDAD2	2.46	2.62	2.54	2.25	2.42	2.36
Cooper [Coo93] EDAD3	2.28	2.40	2.32	2.04	2.20	2.15
Cooper [Coo93] EDAI	2.18	2.33	2.26	1.97	2.12	2.07

Table A.1: Spectroscopic factors for the angle pair (22°,-62.3°).

	$2d_{5/2}$ + $1h_{11/2}$			$2d_{5/2}$		
Optical model potential	free	Kelly	H&I	free	Kelly	H&I
Nadasen [Nad81]	2.71	2.76	2.62	3.18	3.28	3.19
Madland [Mad87]	3.30	3.40	3.25	4.04	4.29	4.24
Schwandt [Sch82]	3.40	3.51	3.34	4.21	4.49	4.41
Hama [Ham90] DP1	4.45	4.54	4.18	6.90	7.39	7.32
Hama [Ham90] DP2	4.24	4.33	4.04	6.36	6.81	6.79
Cooper [Coo93] EDAD1	5.72	5.86	5.51	7.39	8.48	8.44
Cooper [Coo93] EDAD2	5.79	5.93	5.53	8.31	8.95	8.89
Cooper [Coo93] EDAD3	6.00	5.44	5.07	7.78	8.35	8.31
Cooper [Coo93] EDAI	5.36	5.49	5.15	7.66	8.19	8.15

Table A.2: Spectroscopic factors for the angle pair (22°,-62.3°).

Optical model potential	all			$3s_{1/2}$ + $2d_{3/2}$			$3s_{1/2}$		
	free	Kelly	H&I	free	Kelly	H&I	free	Kelly	H&I
Nadasen [Nad81]	1.45	1.56	1.41	1.30	1.40	1.29	1.22	1.32	1.26
Madland [Mad87]	1.78	1.93	1.77	1.68	1.82	1.71	1.63	1.80	1.76
Schwandt [Sch82]	1.80	1.94	1.78	1.69	1.83	1.72	1.64	1.80	1.75
Hama [Ham90] DP1	2.61	2.82	2.63	2.53	2.74	2.64	2.40	2.65	2.62
Hama [Ham90] DP2	2.26	2.43	2.25	2.22	2.40	2.27	2.13	2.34	2.30
Cooper [Coo93] EDAD1	3.16	3.44	3.26	3.03	3.31	3.25	2.88	3.19	3.21
Cooper [Coo93] EDAD2	3.17	3.44	3.25	3.09	3.37	3.28	2.95	3.26	3.27
Cooper [Coo93] EDAD3	2.87	3.11	2.94	2.74	2.99	2.91	2.57	2.84	2.83
Cooper [Coo93] EDAI	2.82	3.05	2.87	2.70	2.94	2.84	2.58	2.84	2.83

Table A.3: Spectroscopic factors for the angle pair (28°,-54.6°).

Optical model potential	$2d_{3/2}$			$2d_{5/2}$ + $1h_{11/2}$			$2d_{5/2}$		
	free	Kelly	H&I	free	Kelly	H&I	free	Kelly	H&I
Nadasen [Nad81]	2.93	3.05	2.54	3.19	3.34	2.92	3.45	3.62	3.18
Madland [Mad87]	3.31	3.48	2.99	3.61	3.82	3.34	3.97	4.36	3.72
Schwandt [Sch82]	3.37	3.54	3.02	3.68	3.89	3.39	4.04	4.30	3.78
Hama [Ham90] DP1	4.71	5.02	4.36	5.05	5.34	4.69	5.94	6.37	5.68
Hama [Ham90] DP2	4.15	4.40	3.75	4.40	4.79	4.10	5.05	5.40	4.81
Cooper [Coo93] EDAD1	5.91	6.36	5.61	6.27	6.66	5.90	7.22	7.74	6.94
Cooper [Coo93] EDAD2	5.75	6.16	5.43	6.05	6.42	5.69	7.03	7.54	6.77
Cooper [Coo93] EDAD3	5.46	5.84	5.11	5.77	6.11	5.40	6.70	7.20	6.44
Cooper [Coo93] EDAI	5.21	5.56	4.86	5.59	5.92	5.23	6.42	6.87	6.13

Table A.4: Spectroscopic factors for the angle pair (28°,-54.6°).

Optical model potential	all			$3s_{1/2}$ + $2d_{3/2}$		
	free	Kelly	H&I	free	Kelly	H&I
Nadasen [Nad81]	0.84	0.89	0.76	0.70	0.74	0.63
Madland [Mad87]	1.02	1.09	0.93	0.88	0.94	0.80
Schwandt [Sch82]	1.04	1.11	0.94	0.89	0.96	0.81
Hama [Ham90] DP1	1.55	1.67	1.45	1.43	1.55	1.36
Hama [Ham90] DP2	1.31	1.42	1.23	1.19	1.29	1.12
Cooper [Coo93] EDAD1	1.78	1.93	1.69	1.61	1.76	1.55
Cooper [Coo93] EDAD2	1.79	1.95	1.71	1.64	1.80	1.59
Cooper [Coo93] EDAD3	1.65	1.79	1.56	1.50	1.64	1.44
Cooper [Coo93] EDAI	1.61	1.75	1.52	1.46	1.59	1.39

Table A.5: Spectroscopic factors for the angle pair (33°,-49.7°).

Optical model potential	$2d_{5/2}$ + $1h_{11/2}$			$2d_{5/2}$		
	free	Kelly	H&I	free	Kelly	H&I
Nadasen [Nad81]	2.58	2.79	2.33	2.77	2.99	2.50
Madland [Mad87]	2.80	3.02	2.53	3.00	3.23	2.72
Schwandt [Sch82]	2.88	3.10	2.60	3.08	3.32	2.79
Hama [Ham90] DP1	3.52	3.75	3.19	3.84	4.11	3.52
Hama [Ham90] DP2	3.17	3.38	2.87	3.40	3.64	3.10
Cooper [Coo93] EDAD1	4.27	4.58	3.92	4.61	4.95	4.26
Cooper [Coo93] EDAD2	4.13	4.43	3.80	4.46	4.78	4.12
Cooper [Coo93] EDAD3	3.39	4.21	3.59	4.25	4.56	3.91
Cooper [Coo93] EDAI	3.89	4.16	3.54	4.18	4.48	3.84

Table A.6: Spectroscopic factors for the angle pair (33°,-49.7°).

Angle pair	all states	$3s_{1/2} + 2d_{3/2}$	$3s_{1/2}$	$2d_{3/2}$	$2d_{5/2} + 1h_{11/2}$
(22°,-62.3°)	1.18	1.08	-	-	8.07
(28°,-54.6°)	1.64	1.54	1.76	4.08	10.7
(33°,-49.7°)	0.94	0.82	-	-	7.86.

Table A.7: Spectroscopic factors for the various angle pairs for the relativistic calculations.

A.2 Cross-section and Analyzing Power Data

Measured triple differential cross-section and analyzing power data for the $^{208}Pb(\vec{p},2p)^{207}Tl$ reaction at the three sets of angle pairs are listed below. The uncertainties quoted are the statistical errors calculated as outlined in section 4.7.2.

E_{K600} (MeV)	$\frac{d^3\sigma}{d\Omega_1 d\Omega_2 dE}$ (mb·sr^{-2}·MeV^{-1})	$\delta(\frac{d^3\sigma}{d\Omega_1 d\Omega_2 dE})$ (mb·sr^{-2}·MeV^{-1})	A_y	δA_y
134.0	3.17×10^{-2}	1.99×10^{-3}	-0.362	0.169
138.0	3.21×10^{-2}	2.01×10^{-3}	-0.132	6.46×10^{-2}
142.0	4.23×10^{-2}	2.31×10^{-3}	7.40×10^{-4}	5.18×10^{-2}
146.0	4.74×10^{-2}	2.44×10^{-3}	6.18×10^{-2}	4.27×10^{-2}
150.0	5.30×10^{-2}	2.57×10^{-3}	0.105	3.62×10^{-2}
154.0	6.57×10^{-2}	2.94×10^{-3}	9.01×10^{-2}	3.71×10^{-2}
158.0	6.42×10^{-2}	2.90×10^{-3}	8.64×10^{-2}	3.75×10^{-2}
162.0	4.45×10^{-2}	2.42×10^{-3}	4.47×10^{-2}	4.18×10^{-2}
166.0	3.41×10^{-2}	2.12×10^{-3}	3.23×10^{-2}	4.94×10^{-2}
170.0	1.73×10^{-2}	1.51×10^{-3}	9.61×10^{-2}	6.29×10^{-2}
174.0	6.14×10^{-3}	8.99×10^{-4}	0.101	0.108

Table A.8: Experimental results for all four states combined for the angle pair $(22°, -62.3°)$.

E_{K600} (MeV)	$\frac{d^3\sigma}{d\Omega_1 d\Omega_2 dE}$ (mb·sr^{-2}·MeV^{-1})	$\delta(\frac{d^3\sigma}{d\Omega_1 d\Omega_2 dE})$ (mb·sr^{-2}·MeV^{-1})	A_y	δA_y
114.0	4.15×10^{-2}	2.71×10^{-3}	4.64×10^{-2}	7.17×10^{-2}
118.0	5.60×10^{-2}	2.67×10^{-3}	3.53×10^{-3}	5.23×10^{-2}
122.0	6.69×10^{-2}	2.92×10^{-3}	-1.33×10^{-2}	4.79×10^{-2}
126.0	7.85×10^{-2}	3.17×10^{-3}	-1.26×10^{-3}	4.42×10^{-2}
130.0	8.78×10^{-2}	3.30×10^{-3}	3.10×10^{-2}	3.64×10^{-2}
134.0	0.105	3.61×10^{-3}	1.86×10^{-2}	3.33×10^{-2}
138.0	0.102	3.56×10^{-3}	-2.49×10^{-3}	3.37×10^{-2}
142.0	8.60×10^{-2}	3.27×10^{-3}	2.96×10^{-2}	3.68×10^{-2}
146.0	8.55×10^{-2}	3.26×10^{-3}	8.64×10^{-2}	3.70×10^{-2}
150.0	5.46×10^{-2}	2.60×10^{-3}	-7.77×10^{-3}	4.61×10^{-2}
154.0	4.39×10^{-2}	2.57×10^{-3}	5.37×10^{-2}	5.91×10^{-2}
158.0	3.53×10^{-2}	2.31×10^{-3}	0.118	6.62×10^{-2}
162.0	2.62×10^{-2}	1.99×10^{-3}	0.147	7.70×10^{-2}
166.0	2.37×10^{-2}	1.90×10^{-3}	0.207	8.15×10^{-2}
170.0	1.56×10^{-2}	1.53×10^{-3}	0.158	0.100

Table A.9: Experimental results for all four states combined for the angle pair $(28°, -54.6°)$.

E_{K600} (MeV)	$\frac{d^3\sigma}{d\Omega_1 d\Omega_2 dE}$ (mb·sr^{-2}·MeV^{-1})	$\delta(\frac{d^3\sigma}{d\Omega_1 d\Omega_2 dE})$ (mb·sr^{-2}·MeV^{-1})	A_y	δA_y
118.0	6.30×10^{-2}	3.91×10^{-3}	8.59×10^{-2}	8.55×10^{-2}
122.0	6.42×10^{-2}	1.46×10^{-3}	-5.75×10^{-2}	6.62×10^{-2}
126.0	6.30×10^{-2}	1.75×10^{-3}	-5.39×10^{-2}	6.10×10^{-2}
130.0	7.09×10^{-2}	2.08×10^{-3}	7.01×10^{-2}	5.22×10^{-2}
134.0	5.03×10^{-2}	1.69×10^{-3}	4.63×10^{-3}	6.29×10^{-2}
138.0	4.04×10^{-2}	1.46×10^{-3}	-1.67×10^{-2}	6.60×10^{-2}
142.0	3.86×10^{-2}	1.50×10^{-3}	9.23×10^{-2}	6.43×10^{-2}
146.0	2.78×10^{-2}	1.41×10^{-3}	-0.118	6.89×10^{-2}
150.0	2.97×10^{-2}	1.28×10^{-3}	7.31×10^{-2}	7.52×10^{-2}
154.0	1.83×10^{-2}	1.14×10^{-3}	6.01×10^{-2}	8.54×10^{-2}

Table A.10: Experimental results for all four states combined for the angle pair $(33°, -49.7°)$.

E_{K600} (MeV)	$\frac{d^3\sigma}{d\Omega_1 d\Omega_2 dE}$ (mb·sr^{-2}·MeV^{-1})	$\delta(\frac{d^3\sigma}{d\Omega_1 d\Omega_2 dE})$ (mb·sr^{-2}·MeV^{-1})	A_y	δA_y
134.0	1.74×10^{-2}	1.48×10^{-3}	-0.454	0.264
138.0	1.78×10^{-2}	1.50×10^{-3}	-0.170	9.04×10^{-2}
142.0	2.69×10^{-2}	1.84×10^{-3}	0.126	6.69×10^{-2}
146.0	3.59×10^{-2}	2.12×10^{-3}	9.82×10^{-2}	5.07×10^{-2}
150.0	4.30×10^{-2}	2.32×10^{-3}	0.113	4.10×10^{-2}
154.0	5.44×10^{-2}	2.67×10^{-3}	0.137	4.14×10^{-2}
158.0	5.45×10^{-2}	2.67×10^{-3}	7.54×10^{-2}	4.06×10^{-2}
162.0	3.59×10^{-2}	2.17×10^{-3}	8.65×10^{-3}	4.60×10^{-2}
166.0	2.55×10^{-2}	1.83×10^{-3}	2.42×10^{-2}	5.66×10^{-2}
170.0	1.25×10^{-2}	1.28×10^{-3}	1.44×10^{-2}	7.60×10^{-2}
174.0	3.39×10^{-3}	6.69×10^{-4}	-0.107	0.143

Table A.11: Experimental results for the combined $3s_{1/2}$ and $2d_{3/2}$ states for the angle pair $(22°, -62.3°)$.

E_{K600} (MeV)	$\frac{d^3\sigma}{d\Omega_1 d\Omega_2 dE}$ (mb·sr^{-2}·MeV^{-1})	$\delta(\frac{d^3\sigma}{d\Omega_1 d\Omega_2 dE})$ (mb·sr^{-2}·MeV^{-1})	A_y	δA_y
114.0	2.74×10^{-2}	2.59×10^{-3}	0.237	0.105
118.0	3.17×10^{-2}	2.00×10^{-3}	0.237	7.01×10^{-2}
122.0	4.05×10^{-2}	2.27×10^{-3}	0.159	6.17×10^{-2}
126.0	5.51×10^{-2}	2.65×10^{-3}	0.126	5.28×10^{-2}
130.0	6.62×10^{-2}	2.87×10^{-3}	0.101	4.20×10^{-2}
134.0	8.43×10^{-2}	3.23×10^{-3}	2.72×10^{-2}	3.72×10^{-2}
138.0	8.51×10^{-2}	3.25×10^{-3}	-3.19×10^{-2}	3.70×10^{-2}
142.0	7.15×10^{-2}	2.98×10^{-3}	-3.09×10^{-2}	4.03×10^{-2}
146.0	6.35×10^{-2}	2.81×10^{-3}	2.41×10^{-2}	4.28×10^{-2}
150.0	3.92×10^{-2}	2.20×10^{-3}	-0.147	5.47×10^{-2}
154.0	2.45×10^{-2}	1.91×10^{-3}	-0.153	7.90×10^{-2}
158.0	1.95×10^{-2}	1.71×10^{-3}	-1.65×10^{-2}	8.84×10^{-2}
162.0	1.26×10^{-2}	1.38×10^{-3}	-1.69×10^{-2}	0.110
166.0	1.10×10^{-2}	1.29×10^{-3}	0.243	0.120
170.0	7.15×10^{-3}	1.04×10^{-3}	0.150	0.148

Table A.12: Experimental results for the combined $3s_{1/2}$ and $2d_{3/2}$ states for the angle pair $(28°, -54.6°)$.

E_{K600} (MeV)	$\frac{d^3\sigma}{d\Omega_1 d\Omega_2 dE}$ (mb·sr^{-2}·MeV^{-1})	$\delta(\frac{d^3\sigma}{d\Omega_1 d\Omega_2 dE})$ (mb·sr^{-2}·MeV^{-1})	A_y	δA_y
118.0	4.60×10^{-2}	3.34×10^{-3}	-4.02×10^{-2}	0.100
122.0	5.24×10^{-2}	1.13×10^{-3}	-5.69×10^{-2}	7.85×10^{-2}
126.0	4.84×10^{-2}	1.53×10^{-3}	-4.99×10^{-2}	6.91×10^{-2}
130.0	5.02×10^{-2}	1.71×10^{-3}	4.39×10^{-2}	6.30×10^{-2}
134.0	3.08×10^{-2}	1.43×10^{-3}	-0.233	7.85×10^{-2}
138.0	2.37×10^{-2}	1.10×10^{-3}	-0.181	8.82×10^{-2}
142.0	1.84×10^{-2}	1.06×10^{-3}	-0.168	9.19×10^{-2}
146.0	1.37×10^{-2}	1.02×10^{-3}	-0.315	9.77×10^{-2}
150.0	1.66×10^{-2}	8.79×10^{-4}	-8.10×10^{-2}	0.107
154.0	8.12×10^{-3}	7.40×10^{-4}	-0.191	0.133

Table A.13: Experimental results for the combined $3s_{1/2}$ and $2d_{3/2}$ states for the angle pair $(33°, -49.7°)$.

E_{K600} (MeV)	$\frac{d^3\sigma}{d\Omega_1 d\Omega_2 dE}$ (mb·sr^{-2}·MeV^{-1})	$\delta(\frac{d^3\sigma}{d\Omega_1 d\Omega_2 dE})$ (mb·sr^{-2}·MeV^{-1})	A_y	δA_y
134.0	1.43×10^{-2}	1.34×10^{-3}	-0.362	0.169
138.0	1.40×10^{-2}	1.32×10^{-3}	-2.72×10^{-2}	9.53×10^{-2}
142.0	1.53×10^{-2}	1.39×10^{-3}	-0.187	8.61×10^{-2}
146.0	1.14×10^{-2}	1.20×10^{-3}	1.95×10^{-3}	8.36×10^{-2}
150.0	9.70×10^{-3}	1.10×10^{-3}	1.39×10^{-2}	8.11×10^{-2}
154.0	1.10×10^{-2}	1.20×10^{-3}	-9.72×10^{-2}	8.79×10^{-2}
158.0	9.80×10^{-3}	1.13×10^{-3}	0.130	0.101
162.0	8.14×10^{-3}	1.03×10^{-3}	0.213	0.107
166.0	6.76×10^{-3}	9.41×10^{-4}	2.91×10^{-2}	0.114
170.0	3.93×10^{-3}	7.19×10^{-4}	0.240	0.125
174.0	2.63×10^{-3}	5.88×10^{-4}	0.394	0.183

Table A.14: Experimental results for the combined $2d_{5/2}$ and $1h_{11/2}$ states for the angle pair $(22°, -62.3°)$.

E_{K600} (MeV)	$\frac{d^3\sigma}{d\Omega_1 d\Omega_2 dE}$ (mb·sr^{-2}·MeV^{-1})	$\delta(\frac{d^3\sigma}{d\Omega_1 d\Omega_2 dE})$ (mb·sr^{-2}·MeV^{-1})	A_y	δA_y
114.0	2.12×10^{-2}	1.94×10^{-3}	-0.137	0.101
118.0	2.41×10^{-2}	1.75×10^{-3}	-0.308	8.17×10^{-2}
122.0	2.63×10^{-2}	1.83×10^{-3}	-0.282	7.79×10^{-2}
126.0	2.30×10^{-2}	1.72×10^{-3}	-0.292	8.33×10^{-2}
130.0	2.17×10^{-2}	1.63×10^{-3}	-0.184	7.37×10^{-2}
134.0	2.09×10^{-2}	1.61×10^{-3}	-2.03×10^{-2}	7.46×10^{-2}
138.0	1.70×10^{-2}	1.45×10^{-3}	0.145	8.32×10^{-2}
142.0	1.47×10^{-2}	1.34×10^{-3}	0.335	9.18×10^{-2}
146.0	2.21×10^{-2}	1.65×10^{-3}	0.261	7.39×10^{-2}
150.0	1.71×10^{-2}	1.61×10^{-3}	0.201	9.60×10^{-2}
154.0	1.89×10^{-2}	1.69×10^{-3}	0.322	9.28×10^{-2}
158.0	1.57×10^{-2}	1.54×10^{-3}	0.273	0.101
162.0	1.31×10^{-2}	1.41×10^{-3}	0.293	0.111
166.0	1.25×10^{-2}	1.37×10^{-3}	0.189	0.112
170.0	8.34×10^{-3}	1.12×10^{-3}	0.154	0.137

Table A.15: Experimental results for the combined $2d_{5/2}$ and $1h_{11/2}$ states for the angle pair $(28°, -54.6°)$.

E_{K600} (MeV)	$\frac{d^3\sigma}{d\Omega_1 d\Omega_2 dE}$ (mb·sr^{-2}·MeV^{-1})	$\delta(\frac{d^3\sigma}{d\Omega_1 d\Omega_2 dE})$ (mb·sr^{-2}·MeV^{-1})	A_y	δA_y
118.0	1.72×10^{-2}	2.04×10^{-3}	-0.180	0.164
122.0	1.17×10^{-2}	8.72×10^{-4}	-6.92×10^{-2}	0.127
126.0	1.43×10^{-2}	7.66×10^{-4}	-6.58×10^{-2}	0.132
130.0	2.08×10^{-2}	1.18×10^{-3}	0.121	9.38×10^{-2}
134.0	1.85×10^{-2}	9.71×10^{-4}	0.426	0.115
138.0	1.66×10^{-2}	9.53×10^{-4}	0.194	0.103
142.0	2.01×10^{-2}	1.06×10^{-3}	0.333	9.42×10^{-2}
146.0	1.40×10^{-2}	9.63×10^{-4}	0.100	0.100
150.0	1.30×10^{-2}	9.18×10^{-4}	0.222	0.107
154.0	1.00×10^{-2}	8.53×10^{-4}	0.255	0.117

Table A.16: Experimental results for the combined $2d_{5/2}$ and $1h_{11/2}$ states for the angle pair $(33°, -49.7°)$.

E_{K600} (MeV)	$\frac{d^3\sigma}{d\Omega_1 d\Omega_2 dE}$ (mb·sr^{-2}·MeV^{-1})	$\delta(\frac{d^3\sigma}{d\Omega_1 d\Omega_2 dE})$ (mb·sr^{-2}·MeV^{-1})	A_y	δA_y
135.0	-	-	-0.206	0.436
139.0	-	-	-0.221	0.161
143.0	-	-	8.63×10^{-2}	9.82×10^{-2}
147.0	-	-	0.119	5.88×10^{-2}
149.0	-	-	7.34×10^{-2}	4.82×10^{-2}
153.0	-	-	0.265	5.40×10^{-2}
157.0	-	-	0.137	4.58×10^{-2}
161.0	-	-	2.83×10^{-2}	4.97×10^{-2}
165.0	-	-	0.173	6.54×10^{-2}
169.0	-	-	8.74×10^{-2}	9.41×10^{-2}
171.0	-	-	-2.84×10^{-2}	0.134

Table A.17: Experimental results for the separated $3s_{1/2}$ state for the angle pair $(22°, -62.3°)$.

E_{K600} (MeV)	$\frac{d^3\sigma}{d\Omega_1 d\Omega_2 dE}$ (mb·sr^{-2}·MeV^{-1})	$\delta(\frac{d^3\sigma}{d\Omega_1 d\Omega_2 dE})$ (mb·sr^{-2}·MeV^{-1})	A_y	δA_y
118.0	7.06×10^{-3}	4.77×10^{-4}	-0.287	0.106
122.0	1.44×10^{-2}	6.80×10^{-4}	-0.120	7.33×10^{-2}
126.0	2.86×10^{-2}	9.57×10^{-4}	-2.59×10^{-2}	5.18×10^{-2}
130.0	3.67×10^{-2}	1.08×10^{-3}	8.50×10^{-2}	4.57×10^{-2}
134.22	7.07×10^{-2}	1.23×10^{-3}	0.113	2.39×10^{-2}
138.0	6.97×10^{-2}	1.47×10^{-3}	5.17×10^{-2}	2.89×10^{-2}
142.0	6.82×10^{-2}	1.45×10^{-3}	6.29×10^{-2}	2.92×10^{-2}
146.5	5.36×10^{-2}	1.38×10^{-3}	1.81×10^{-3}	3.52×10^{-2}
150.0	3.18×10^{-2}	1.15×10^{-3}	-4.45×10^{-2}	4.94×10^{-2}
154.0	1.96×10^{-2}	6.95×10^{-4}	-0.314	5.17×10^{-2}
157.0	1.04×10^{-2}	4.70×10^{-4}	-0.144	6.49×10^{-2}
160.0	6.43×10^{-3}	3.71×10^{-4}	-9.51×10^{-2}	8.22×10^{-2}
163.0	5.47×10^{-3}	3.43×10^{-4}	8.95×10^{-2}	8.97×10^{-2}
166.0	4.57×10^{-3}	3.42×10^{-4}	0.414	0.111

Table A.18: Experimental results for the separated $3s_{1/2}$ state for the angle pair $(28°, -54.6°)$.

E_{K600} (MeV)	$\frac{d^3\sigma}{d\Omega_1 d\Omega_2 dE}$ (mb·sr^{-2}·MeV^{-1})	$\delta(\frac{d^3\sigma}{d\Omega_1 d\Omega_2 dE})$ (mb·sr^{-2}·MeV^{-1})	A_y	δA_y
135.0	-	-	-0.175	0.174
139.0	-	-	9.73×10^{-2}	0.123
143.0	-	-	0.229	0.102
147.0	-	-	0.116	9.66×10^{-2}
149.0	-	-	0.119	9.27×10^{-2}
153.0	-	-	-4.02×10^{-2}	9.04×10^{-2}
157.0	-	-	3.24×10^{-2}	0.102
161.0	-	-	-0.197	9.78×10^{-2}
165.0	-	-	-0.160	0.101
169.0	-	-	8.92×10^{-2}	0.143
171.0	-	-	0.206	0.138

Table A.19: Experimental results for the separated $2d_{3/2}$ state for the angle pair $(22°, -62.3°)$.

E_{K600} (MeV)	$\frac{d^3\sigma}{d\Omega_1 d\Omega_2 dE}$ (mb·sr^{-2}·MeV^{-1})	$\delta(\frac{d^3\sigma}{d\Omega_1 d\Omega_2 dE})$ (mb·sr^{-2}·MeV^{-1})	A_y	δA_y
118.0	2.41×10^{-2}	8.71×10^{-4}	0.397	5.79×10^{-2}
122.0	2.88×10^{-2}	9.55×10^{-4}	0.314	5.24×10^{-2}
126.0	2.55×10^{-2}	8.97×10^{-4}	0.350	5.59×10^{-2}
130.0	2.69×10^{-2}	9.26×10^{-4}	6.99×10^{-2}	5.34×10^{-2}
134.22	1.09×10^{-2}	4.82×10^{-4}	-0.541	6.51×10^{-2}
138.0	1.14×10^{-2}	5.91×10^{-4}	-0.493	7.58×10^{-2}
142.0	6.68×10^{-3}	4.53×10^{-4}	-0.508	9.92×10^{-2}
146.5	3.02×10^{-3}	3.27×10^{-4}	-0.177	0.149
150.0	6.24×10^{-3}	5.06×10^{-4}	-0.453	0.117
154.0	1.22×10^{-2}	5.48×10^{-4}	-0.318	6.55×10^{-2}
157.0	1.00×10^{-2}	4.63×10^{-4}	-7.31×10^{-2}	6.58×10^{-2}
160.0	1.03×10^{-2}	4.70×10^{-4}	2.98×10^{-3}	6.51×10^{-2}
163.0	7.96×10^{-3}	4.14×10^{-4}	3.84×10^{-3}	7.40×10^{-2}
166.0	5.68×10^{-3}	3.76×10^{-4}	-0.132	9.46×10^{-2}

Table A.20: Experimental results for the separated $2d_{3/2}$ state for the angle pair $(28°, -54.6°)$.

Appendix B

Energy Resolution and Target Thickness

Sufficient energy resolution to achieve complete online separation of proton knockout from the different valence states of ^{208}Pb was not attained. Straggling and other effects due to the finite thickness of the target ultimately limited the experimental energy resolution.

Quasi-free knockout events from the 7.7 mg·cm^{-2} thick ^{208}Pb target yielded peaks in the binding energy spectrum with an average FWHM ~480 keV, which is quite considerable when compared to the 351 keV that separates the $3s_{1/2}$ ground state from the $2d_{3/2}$ first excited state of ^{207}Tl. The inherent energy resolution of the 1998 experimental setup, disregarding effects due to the ^{208}Pb target thickness, was found on average to be FWHM ~327 keV. This was inferred from the elastic $H(p,p)$ scattering peak in the binding energy spectrum for a 0.5 mg·cm^{-2} thick $(CH_2)_n$ target.

It was therefore decided that a much thinner target, constrained at the lower boundary by the limited intensity of the available proton beam, would be used for the second round of measurements in 2000. Together with improved detector calibration techniques the new 0.74 mg·cm^{-2} thick ^{208}Pb yielded peaks in the binding energy spectrum for quasi-free proton knockout from ^{208}Pb with an average FWHM ~310 keV. Calculations in the following sections are shown to account for these figures.

B.1 Thick Target Energy Resolution

Straggling calculations were performed according to the description of ionization loss in thin absorbers by Vavilov [Leo87, Vav57]. An absorber is considered to be thin if the ionization losses are much smaller than the initial energy of the particles, or equivalently when the absorbing layer is thin in comparison with the particle range [Shu67]. The 7.7 mg·cm^{-2} thick ^{208}Pb target is considered to meet this requirement, since the range of a 200 MeV proton in ^{208}Pb is ~ 4.6 cm, which is ~6700 times thicker than the ^{208}Pb target. It is furthermore also assumed that:

- The individual energy transfers are sufficiently large such that the electrons may be treated as free. In effect this means that small energy transfers from so-called *distant* collisions are ignored, and that the energy structure of the electron shell of the atoms of the stopping media are ignored.
- The decrease in the velocity of the of the particle is negligible.

In the Gaussian limit (i.e. where the tail to the high energy side of the energy loss probability distribution is negligible) the variance of the energy loss distribution is given as

$$\sigma^2 = \frac{\xi^2}{\kappa}\frac{1-\beta^2}{2}\ , \tag{B.1}$$

where ξ denotes the mean energy loss as calculated with the Bethe-Bloch formula, and the quantity κ is given by the ratio $\frac{\xi}{W_{\max}}$, where

$$\begin{aligned} W_{\max} &= \frac{2m_e c^2\beta^2\gamma^2}{1+2\frac{m_e}{M}\sqrt{1+\beta^2\gamma^2}+\left(\frac{m_e}{M}\right)^2}\ , \\ &\simeq 2m_e c^2\beta^2\gamma^2 \qquad (M \gg m_e) \end{aligned} \tag{B.2}$$

represents the maximum energy transfer to an electron in a single collision. The quantity m_e denotes the electron mass and M is the mass of the particle traversing the medium. β and γ are the standard relativistic quantities.

If it is assumed that the 200 MeV proton traverses the whole length of the target before a quasi-free knockout reaction occurs, the variance of the energy loss distribution due to energy straggling follows from Eq. (B.1), where $\xi = 0.02$ MeV, $\beta = 0.566$ and $W_{\max} = 0.482$ MeV, so that

$$\sigma^2 = \frac{\xi^2}{\kappa}\frac{1-\beta^2}{2} = 3.28\times10^{-3}\ \text{MeV}^2\ .$$

The contribution to the FWHM of the binding energy peak is therefore $= 0.1348$ MeV. In a different scenario we assume the interaction takes place in the front of the target[1]. The total effect of straggling on the energy resolution in the binding energy spectrum will then be the contribution of straggling of both protons added in quadrature. This is now calculated for a typical case where a 60 MeV proton is detected in the *Ge*-detector and a 130 MeV proton in the K600 detector. For a 60 MeV proton we have that $\xi = 0.04$ MeV, $\beta = 0.342$ and

[1] In this and all following calculations the effective increase in target thickness due to nonzero detection angles are assumed to be negligible.

$W_{\max} = 0.135$ MeV, resulting in FWHM = 114.7 keV. For a 130 MeV proton $\xi = 0.027$, $\beta = 0.478$ and $W_{\max} = 0.304$ MeV, so that FWHM= 132 keV. Therefore we have

$$FWHM_{straggling} = \sqrt{132^2 + 115^2} = 175 \text{ keV} .$$

Another factor that must be incorporated in the energy resolution calculations is the energy difference associated with the quasi-free proton knockout interaction occuring in the front and the back of the target foil. The least energetic proton that would still reach the *Ge*-detector (a proton of kinetic energy ~12.5 MeV), having had an interaction at the first ^{208}Pb-surface, would have energy loss in the target of ~118 keV. The other proton ($E_{K600} \sim 180$ MeV) will loose about 20 keV when passing through the ^{208}Pb target. On the other hand, a projectile proton that interacts at the back of the target will first lose 20 keV, and then the interaction will take place at 200 MeV-20 keV. It can thus be said that the quasi-free reaction in the front of the target will occur at an energy ~ 118 keV less than the events at the back of the target. In other word, the distribution in the binding energy spectrum due to events that occur in front of the target is shifted relative to the events that happen at the back of the target by 118 keV.

In order to calculate the intrinsic energy resolution of the experimental setup, the contribution of straggling in the $(CH_2)_n$ target must be subtracted from the the resolution found for the elastic hydrogen scattering peak in the binding energy spectrum. For similar scenarios as calculated for the ^{208}Pb target we calculate the straggling for a 200 MeV proton and a 60 + 130 MeV pair of protons. Both the 130 and 200 MeV experience negligible energy loss in the 0.5 mg·cm^{-2} thick $(CH_2)_n$ target. For a 60 MeV proton $\xi = 0.005$ MeV, $\beta = 0.342$, $W_{\max} = 0.135$ MeV so that $\sigma^2 = 2.98 \times 10^{-4}$ MeV^2 and FWHM = 41 keV. The energy resolution found with the $(CH_2)_n$ target was FWHM=330 keV. Thus it follows that in the worst case scenario (i.e. a 60 + 130 MeV proton pair) the FWHM yielded by the setup independent of the target thickness is

$$\begin{aligned} FWHM_{setup} &= \left((FWHM_{CH_2})^2 - (FWHM_{straggling-proton1})^2 - (FWHM_{straggling-proton2})^2\right)^{1/2} \\ &= 327 \text{ keV} . \end{aligned}$$

A measure of the expected resolution in the binding energy spectrum for the thick target is therefore calculated by taking the sum of the squares of the intrinsic resolution of the experimental setup and the maximum straggling effects, adding to that the mistake due to interaction

at two target surfaces linearly:

$$\begin{aligned} FWHM_{total} &= \left((FWHM_{exp-setup})^2 + (FWHM_{straggling-proton1})^2 + (FWHM_{straggling-proton2})^2\right)^{1/2} \\ &\quad + FWHM_{2-surfaces} \\ &= \sqrt{(327)^2 + (132)^2 + (115)^2} + 118 = 489 \text{ keV} \\ &\simeq FWHM_{exp} = 480 \text{ keV} . \end{aligned}$$

B.2 Thin Target Energy Resolution

For the 0.74 mg·cm^{-2} thick ^{208}Pb target and the maximum straggling effect (arising due to 60 and 130 MeV protons) it follows from straggling calculations that for a 60 MeV proton $\xi = 0.005$, $\beta = 0.342$, $W_{\max} = 0.135$ MeV, and therefore FWHM = 41 keV. Negligible energy loss for the 130 MeV proton results in FWHM = 0. Using similar arguments as in the previous section (FWHM$_{CH_2}$=300 keV) it follows that the energy resolution of the valence peaks in the binding energy spectrum should be

$$\begin{aligned} FWHM_{total} &= \left((FWHM_{exp-setup})^2 + (FWHM_{straggling-proton1})^2 + (FWHM_{straggling-proton2})^2\right)^{1/2} \\ &\quad + FWHM_{2-surfaces} \\ &= \sqrt{(297)^2 + (41)^2} + 5 = 305 \text{ keV} \\ &\simeq FWHM_{exp} = 310 \text{ keV} . \end{aligned}$$

Bibliography

[Abd79] I. Abdul-Jalil and D.F. Jackson, *J. Phys.* **G5** (1979) 1699.

[Ant81] L. Antonuk, P. Kitching, C.A. Miller, D.A. Hutcheon, W.J. McDonald, G.C. Neilson and W.C. Olsen, *Nucl. Phys.* **A370** (1981) 389.

[Are97] G.J. Arendse, Ph.D. thesis, University of Stellenbosch, (1997), unpublished.

[Arn86] R.A. Arndt and D. Roper, Virginia Polytechnic Institute and State University Scattering Analysis Interactive Dial-In Program (SAID), Solution WI86, *http : //said.phys.vt.edu/said_branch.html.*

[Bau98] E. Bauge, J.P. Delaroche and M. Girod, *Phys. Rev.* **C58** (1998) 1118.

[Ber62] T. Berggren, G.E. Brown and G. Jacob, *Phys. Lett.* **1** (1962) 88.

[Ber77] W. Bertozzi, M.V. Hynes, C.P. Sargent, C. Cresswell, P.C. Dunn, A. Hirsch, M. Leitch, B. Norum, F.N. Rad and T. Sasanuma, *Nucl. Instrum. Methods* **141** (1977) 457.

[Bha85] R. Bhattacharye, *Z. Phys.* **A322** (1985) 1060.

[Bho74] R.K. Bhowmik, C.C. Chang, P.G. Roos and H.D. Holgren, *Nucl. Phys.* **A226** (1974) 365.

[Bla93] L.C. Bland, Proceedings of the 8^{th} mini-conference on *Correlations in Hadronic Systems* (1993) 64.

[Bob94] I. Bobeldijk, M. Bouwhuis, D.G. Ireland, C.W. de Jager, E. Jans, N. de Jonge, W-J. Kasdorp, J. Konijn, L. Lapiks, J.J. van Leeuwe, R.L.J. van der Meer, G.J.L. Nooren, E. Passchier, M. Schroevers, G. van der Steenhoven, J.J.M. Steijger, J.A.P. Theunissen, M.A. van Uden, H. de Vries, R. de Vries, P.K.A. de Witt Huberts, H.P. Blok, H.B. van den Brink, G.E. Dodge, M.N. Harakeh, W.H.A. Hesselink, N. Kalantar-Nayestanaki, A. Pellegrino, C.M. Spaltro, J.A. Templon, R.S. Hicks, J.J. Kelly and C. Marchand, *Phys. Lett.* **73** (1994) 2684.

[Bob95] I. Bobeldijk, Ph.D. thesis, University of Utrecht, (1995), unpublished.

[Car84] T.A. Carey, K.W. Jones, J.B. McClelland, J.M. Moss, L.B. Rees, N. Tanaka and A.D. Bacher, *Phys. Rev. Lett.* **53** (1984) 144.

[Car96] R.F. Carlson, *Atomic Data and Nuclear Data Tables* **63** (1996) 93.

[Car99] D.S. Carmen, L.C. Bland, N.S. Chant, T. Gu, G.M. Huber, J. Huffman, A. Klyachko, B.C. Markham, P.G. Roos, P. Schwandt and K. Solberg, *Phys. Rev.* **C59** (1999) 1869.

[Car99a] D.S. Carmen, L.C. Bland, N.S. Chant, T. Gu, G.M. Huber, J. Huffman, A. Klyachko, B.C. Markham, P.G. Roos, P. Schwandt and K. Solberg, *Phys. Lett.* **B452** (1999) 8.

[Cha52] O. Chamberlain and E. Segrè, *Phys. Rev.* **87** (1952) 81.

[Cha77] N.S. Chant and P.G. Roos, *Phys. Rev.* **C15** (1977) 57.

[Cha79] N.S. Chant, P. Kitching, P.G. Roos and L. Antonuk, *Phys. Rev. Lett.* **43** (1979) 495.

[Cha83] N.S. Chant and P.G. Roos, *Phys. Rev.* **C27** (1983) 1060.

[Cha98] N.S. Chant and P.G. Roos, Program THREEDEE, University of Maryland, unpublished.

[Cia83] G. Ciangaru, C.C. Chang, H.D. Holmgren, A. Nadasen, P.G. Roos, A.A. Cowley, S. Mills, P.P. Singh, M.K. Saber and J.R. Hall, *Phys. Rev.* **C27** (1983) 1360.

[Coo89] E.D. Cooper and O.V. Maxwell, *Nucl. Phys.* **A493** (1989) 468.

[Coo93] E.D. Cooper, S. Hama, B.C. Clark and R.L. Mercer, *Phys. Rev.* **C47** (1993) 297.

[Cow80] A.A. Cowley, C.C. Chang, H.D. Holmgren, J.D. Silk, D.L. Hendrie, R.W. Koontz, P.G. Roos, C. Samanta and J.R. Wu, *Phys. Rev. Lett.* **45** (1980) 1930.

[Cow91] A.A. Cowley, J.J. Lawrie, G.C. Hillhouse, D.M. Whittal, S.V. Förtsch, J.V. Pilcher, F.D. Smit and P.G. Roos, *Phys. Rev.* **C44** (1991) 329.

[Cow95] A.A. Cowley, G.J. Arendse, J.A. Stander, W.A. Richter, *Phys. Lett.* **B359** (1995) 300.

[Cow97] A.A. Cowley, G.J. Arendse, S.V. Förtsch, G.C. Hillhouse, J.J. Lawrie, R. Neveling, R.T. Newman, W.A. Richter, F.D. Smit, J.A. Stander, G.F. Steyn and S.M. Wyngaardt, NAC Research Proposal, Nr. PR15c, 1997.

[Dud81] J. Dudek, Z. Szymanski and T. Werner, *Phys. Rev.* **C23** (1981) 920.

[Eng81] H.A. Enge, *Nucl. Instrum. Methods* **187** (1981) 1.

[Eps80] M.P. Epstein, D.J. Margaziotis, J. Simone, D.K. Hasell, B.K.S. Koene, B.T. Murdoch, W.T.H. van Oers, J.M. Cameron, L.G. Greeniaus, G.A. Moss, J.G. Rogers and A.W. Stetz, *Phys. Rev. Lett.* **44** (1980) 20.

[Fou00] D. Fourie, private communication, National Accelerator Centre, (2000).

[For92] S.V. Förtsch, Ph.D. thesis, University of Pretoria, (1992), unpublished.

[Fra75] R. Frascaria, P.G. Roos, M. Morlet, N. Marty, A. Willis, V. Comparat and N. Fujiwara, *Phys. Rev.* **C12** (1975) 243.

[Fra85] M.A. Franey and W.G. Love, *Phys. Rev.* **C31** (1985) 488.

[Ham90] S. Hama, B.C. Clark, E.D. Cooper, H.S. Sherif and R.L. Mercer, *Phys. Rev.* **C41** (1990) 2737.

[Hae74] W. Haeberli, *Nuclear Spectroscopy and Reactions: Part A*, edited by J. Cerny, Academic Press, New York, (1974), 151.

[Hat97] K. Hatanaka, M. Kawabata, N. Matsuoka, Y. Mizuno, S. Morinobu, M. Nakamura, T. Noro, A. Okihana, K. Sagara, K. Takahisa, H. Takeda, K. Tamura, M. Tanaka, S. Toyama, H. Yamazaki and Y.Yuasa, *Phys. Rev. Lett.* **78** (1997) 1014.

[Hau91] O. Häusser, M.C. Vetterli, R.W. Fergerson, C. Glashausser, R.G. Jeppeson, R.D. Smith, R. Abegg, F.T. Baker, A. Celler, R.L. Helmer, R. Henderson, K. Hicks, M.J. Iqbal, K.P. Jackson, K.W. Jackson, J. Lisanti, J. Mildenberger, C.A. Miller, R.S. Sawafta and S. Yen, *Phys. Rev.* **C43** (1991) 230.

[Hen74] D.L. Hendrie, *Nuclear Spectroscopy and Reactions: Part A*, edited by J. Cerny, Academic Press, New York, (1974), 365.

[Hil60] P. Hillman, H. Tyŕen and Th.A.J. Maris, *Phys. Rev. Lett* **5** (1960) 107.

[Hil99] G.C. Hillhouse, Ph.D. thesis, University of Stellenbosch, (1999), unpublished.

[Hor81] C.J. Horowitz and B.D. Serot, *Nucl. Phys.* **A368** (1981) 503.

[Hor85] C.J. Horowitz, *Phys. Rev.* **C31** (1985) 1340.

[Hor86] C.J. Horowitz and M.J. Iqbal, *Phys. Rev.* **C33** (1986) 2059.

[Hor88] C.J. Horowitz and D.P. Murdock, *Phys. Rev.* **C37** (1988) 2032.

[Hor91] C.J. Horowitz, D.P. Murdock and B.D. Serot, *Computational Nuclear Physics 1, Nuclear Structure*, Springer Verlag, Heidelberg, (1991).

[Hos68] N. Hoshizaki, *Suppl. Prog. Theo. Phys.* **42** (1968) 107.

[Huf96] J.D. Huffman, Ph.D. thesis, University of Maryland, (1996), unpublished.

[Ike95] Y. Ikebata, *Phys. Rev.* **C52** (1995) 890.

[Jac66] G. Jacob and A.J. Maris, *Rev. Mod. Phys.* **38** (1966) 121.

[Jac73a] G. Jacob and A.J. Maris, *Rev. Mod. Phys.* **45** (1973) 6.

[Jac73] G. Jacob, A.J. Maris, C. Schneider and M.R. Teodoro, *Phys. Lett.* **45B** (1973) 181.

[Jac76] G. Jacob, A.J. Maris, C. Schneider and M.R. Teodoro, *Nucl. Phys.* **A257** (1976) 517.

[Jack65] D.F. Jackson and T. Berggren, *Nucl. Phys.* **62** (1965) 353.

[Jack76] D.F. Jackson, *Nucl. Phys.* **A257** (1976) 221.

[Jin92] Y. Jin, S.D. Onley and L.E. Wright, *Phys. Rev.* **C45** (1992) 1311.

[Kan90] N. Kanayama, Y. Kudo, H. Tsunoda and T. Wakasugi, *Prog. Theo. Phys.* **83** (1990) 540.

[Kel80] J.J. Kelly, W. Bertozzi, T.N. Buti, F.W. Hersman, C. Hyde, M.V. Hynes, B. Norum, F.N. Rad, A.D. Bacher, G.T. Emery, C.C. Foster, W.P. Jones, D.W. Miller, B.L. Berman, W.G. Love and F. Petrovich, *Phys. Rev. Lett.* **45** (1980) 2012.

[Kel89b] J.J. Kelly, *Phys. Rev.* **C39** (1989) 2120.

[Kel89a] J.J. Kelly, W. Bertozzi, T.N. Buti, J.M. Finn, F.W. Hersman, C. Hyde-Wright, M.V. Hynes, M.A. Kovash, B. Murdock, B.E. Norum, B. Pugh, F.N. Rad, A.D. Bacher, G.T. Emery, C.C. Foster, W.P. Jones, D.W. Miller, B.L. Berman, W.G. Love, J.A. Carr and F. Petrovich, *Phys. Rev.* **C39** (1989) 1222.

[Kel94] J.J. Kelly, *Phys. Rev.* **C49** (1994) 1315.

[Ker59] A.K. Kerman, H. McManus and R.M. Thaler, *Ann. Phys.* **8** (1959) 551.

[Kit76] P. Kitching, C.A. Miller, D.A. Hutcheon, A.N. James, W.J. McDonald, *Phys. Rev. Lett.* **37** (1976) 1600.

[Kit80] P. Kitching, C.A. Miller, W.C. Olsen, D.A. Hutcheon, W.J. McDonald and A.W. Stetz, *Nucl. Phys.* **A340** (1980) 423.

[Kit82] P. Kitching, *AIP Conf. Proc.*, Vol.97 (1982) 232.

[Kit85] P. Kitching, W.J. McDonald, A.J. Maris and C.A.Z. Vasconcellos, *Adv. Nucl. Phys.* **15** (1985) 43.

[Kno89] G.F. Knoll, *Radiation Detection and Measurement*, John Wiley & Sons, New York, (1989).

[Koz89] R. Kozack and D.G. Madland, *Phys. Rev.* **C39** (1989) 1461.

[Kre95] G. Krein, Th.A.J. Maris, B.B. Rodrigues and E.A. Veit, *Phys. Rev.* **C51** (1995) 2646.

[Kud86] Y. Kudo and K. Miyazaki, *Phys. Rev.* **C34** (1986) 1192.

[Kud88] Y. Kudo, N. Kanayama and T. Wakasugi, *Phys. Rev.* **C38** (1988) 1126.

[Kud89] Y. Kudo, N. Kanayama and T. Wakasugi, *Phys. Rev.* **C39** (1989) 1162.

[Kul71] S. Kullander, F. Lemeilleur, P.U. Renberg, G. Landaud, J.Yonnet, B. Fagerstrom, A. Johansson and G. Tibell, *Nucl. Phys.* **A173** (1971) 357.

[Leo87] W.R. Leo, *Techniques for Nuclear and Particle Physics Experiments*, Springer Verlag, Berlin, (1987).

[Li94] P. Li, Ph.D. thesis, Indiana University, (1994), unpublished.

[Lim64a] K.L. Lim and I.E. McCarthy, *Phys. Rev. Lett.* **13** (1964) 446.

[Lim64b] K.L. Lim and I.E. McCarthy, *Phys. Rev.* **133** (1964) B1006.

[Lim66] K.L. Lim and I.E. McCarthy, *Nucl. Phys.* **88** (1966) 433.

[Lov81] W.G. Love and M.A. Franey, *Phys. Rev.* **C24** (1981) 1073.

[Ma83] Z.Y. Ma and J. Wambach, *Nucl. Phys.* **A402** (1983) 275.

[Ma91] Z.Y. Ma and J. Wambach, *Phys. Lett.* **256B** (1991) 1.

[Mad87] D.G. Madland, Los Alamos National Laboratory Report LA-UR 87-3382, (1987), unpublished.

[Mah88] C. Mahaux and R. Sartor, *Nucl. Phys.* **A481** (1988) 381.

[Mah89] C. Mahaux and R. Sartor, *Nucl. Phys.* **A503** (1989) 525.

[Mah91] C. Mahaux and R. Sartor, *Adv. Nucl. Phys.* **20** (1991) 1.

[Man98] J. Mano and Y. Kudo, *Prog. Theor. Phys.* **100** (1998) 91.

[Man99] J. Mano and Y. Kudo, *Nuclear Responses and Medium Effects*, Universal Academy Press Inc., Tokyo, (1999) 176.

[Man00] J. Mano, Program RELP2P, unpublished.

[Mar58] Th.A.J. Maris, P. Hillman and H.Tyren, *Nucl. Phys.* **7** (1958) 1.

[Mar59] Th.A.J. Maris, *Nucl. Phys.* **9** (1959) 557.

[Mar82] D.J. Margaziotis, M.B. Epstein, W.T.H. van Oers, D.K. Hasell, R. Abegg, G.A. Moss, L.G. Greeniaus, J. Cameron and A.W. Stetz, *Phys. Rev.* **C25** (1982) 2873.

[Mar93] M.J. Martin, *Nuclear Data Tables* **70** (1993) 315.

[Mar98] Y. Mardor, J. Aclander, J. Alster, D. Barton, G. Bunce, A. Carroll, N. Christensen, H. Courant, S. Durrant, S. Gushue, S. Heppelmann, E. Kosonovsky, I. Mardor, M. Marshak, Y. Makdisi, E.D. Minor, I. Navon, H. Nicholson, E. Piasetzky, T. Roser, J. Russell, C.S. Sutton, M. Tanaka, C. White and J-Y Wu, *Phys. Lett.* **B437** (1998) 257.

[Max90] O.V. Maxwell and E.D. Cooper, *Nucl. Phys.* **A513** (1990) 584.

[Max93] O.V. Maxwell and E.D. Cooper, *Nucl. Phys.* **A565** (1993) 740.

[Max94] O.V. Maxwell and E.D. Cooper, *Nucl. Phys.* **A574** (1994) 819.

[Max96] O.V. Maxwell and E.D. Cooper, *Nucl. Phys.* **A603** (1996) 441.

[McD90] J.P. McDermott, *Phys. Rev. Lett.* **65** (1990) 1991.

[McE57] J.C. McEwen, W.M. Gibson and P.J. Duke, *Phil. Mag.* **2** (1957) 231.

[McN83] J.A. McNeil, L. Ray and S.J. Wallace, *Phys. Rev.* **C27** (1983) 2123.

[Mea69] D.F. Measday and C. Richard-Serre, *Nucl. Instrum. Methods* **76** (1969) 45.

[Mey82] H.O. Meyer, Scientific and Technical Report, Indiana University Cyclotron Facility, (1982) 183.

[Mil90] C.A. Miller, *Proc. 7th Int. Conf. on polarization phenomena in nuclear physics*, Paris, 1990, edited by A. Boudard and Y. Terrien, [*Colloq. Phys. Suppl.* **51**, C6 (1990) 595].

[Mil98] C.A. Miller, K.H. Hicks, R. Abegg, M. Ahmad, N.S. Chant, D. Frekers, P.W. Green, L.G. Greeniaus, D.A. Hutcheon, P. Kitching, D.J. Mack, W.J. McDonald, W.C. Olsen, R. Schubank, P.G. Roos and Y. Ye, *Phys. Rev.* **C57** (1998) 1756.

[Nad81] A. Nadasen, P. Schwandt, P.P. Singh, W.W. Jacobs, A.D. Bacher, P.T. Debevec, M.D. Kaitchuck and J.T. Meek, *Phys. Rev.* **C23** (1981) 1023.

[Nev98] R. Neveling, M.Sc. thesis, University of Stellenbosch, (1998), unpublished.

[Nev99] R. Neveling, A.A. Cowley, G.J. Arendse, J. Bezuidenhout, S.V. Förtsch, G.C. Hillhouse, J.J. Lawrie, R.T. Newman, W.A. Richter, F.D. Smit, J.A. Stander, G.F. Steyn and S.M. Wyngaardt, NAC Research Proposal, Nr. PR15d, 1999.

[New96] R.T. Newman, Ph.D. thesis, University of Cape Town, (1996), unpublished.

[Nor86] T. Noro, H. Sakai, N. Matsuoka, H. Ito, M. Nakamura, S. Shimoura and M. Yosoi, Research Center for Nuclear Physics, Osaka University, Annual Report, (1986), 55.

[Nor98] T. Noro, T. Baba, K. Hatanaka, M. Ito, M. Kawabata, N. Matsuoka, Y. Mizuno, S. Morinobu, M. Nakamura, A. Okihana, K. Sagara, H. Sakaguchi, K. Takahisa, H. Takeda, A. Tamii, K. Tamura, M. Tanaka, S. Toyama, H. Yamazaki, Y. Yuasa, Y. Yoshido and M. Yosoi, *Nucl. Phys.* **A629** (1998) 324c.

[Nor99] T. Noro, H. Akimune, H. Akiyoshi, I. Daito, H. Fujimura, K. Hatanaka, F. Ihara, T. Ishikawa, M. Itoh, M. Kawabata, T. Kawabata, Y. Maeda, N. Matsuoka, S. Morinobu, M. Nakamura, E. Obayashi, A. Okihana, K. Sagara, H. Sakaguchi, H. Takeda, T. Taki, A. Tamii, K. Tamura, H. Yamazaki, Y. Yoshido, M. Yoshimura and M. Yosoi, Nuclear Responses and Medium Effects, Universal Academy Press Inc., Tokyo, (1999) 167.

[Oer82] W.T.H. van Oers, B.T. Murdoch, B.K.S. Koene, D.K. Hasell, R. Adbegg, D.J. Margaziotis, M.P. Epstein, G.A. Moss, L.G. Greeniaus, J.M. Greben, J.M. Cameron, J.G. Rogers and A.W. Stetz, *Phys. Rev.* **C25** (1982) 390.

[Pan84] V.R. Pandharipande, C. Papanicolas and J. Wambach, *Phys. Rev. Lett.* **53** (1984) 1133.

[Per62] F. Perey and B. Buck, *Nucl. Phys.* **32** (1962) 353.

[Per69] C.F. Perdrisat, L.W. Swenson, P.C. Gugelot, E.T. Boschitz, W.K. Roberts, J.S. Vincent and J.R. Priest, *Phys. Rev.* **187** (1969) 1201.

[Pil89] J.P. Pilcher, Ph.D. thesis, University of Cape Town, (1989), unpublished.

[Pug71] H.G. Pugh, P.G. Roos, A.A. Cowley, V.K.C. Cheng and R. Woody, *Phys. Lett.* **46B** (1973) 192.

[Qui86] E.N.M. Quint, J.F.J. van den Brand, J.W.A. den Herder, E. Jans, P.H.M. Keizer, L. Lapikás, G. van der Steenhoven, P.K.A. de Witt Huberts, S. Klein, P. Grabmayr, G.J. Wagner, H. Nann, B. Frois and D. Goutte, *Phys. Rev. Lett.* **57** (1986) 186.

[Qui88] E.N.M. Quint, Ph.D. thesis, University of Amsterdam, (1988), unpublished.

[Ray90] L. Ray, *Phys. Rev.* **C41** (1990) 2816.

[Red70] E.F. Redish, G.J. Stephenson and G.M. Lerner, *Phys. Rev.* **C2** (1970) 1665.

[Roy70] D. Royer, M. Arditi, L. Bimbot, H. Doubre, N. Frascaria, J.P. Garron and M. Riou, *Nucl. Phys.* **A158** (1970) 516.

[Sak94] Sakurai, *Modern Quantum Mechanics (Revised Edition)*, Addison Wesley, (1994).

[Sam81] C. Samanta, Ph.D. thesis, University of Maryland, (1981), unpublished.

[Sam86] C. Samanta, N.S. Chant, P.G. Roos, A. Nadasen, J. Wesick and A.A. Cowley, *Phys. Rev.* **C34** (1986) 1610.

[Sat83] G.R. Satchler, *Direct Nuclear Reactions*, Claredon Press, Oxford, (1983).

[Sch71] P. Schwandt, T.B. Clegg and W. Haeberli, *Nucl. Phys.* **A163** (1971) 432.

[Sch82] P. Schwandt, H.O. Meyer, W.W. Jacobs, A.D. Bacher, S.E. Vidgor, M.D. Kaitchuck and T.R. Donoghue, *Phys. Rev.* **C26** (1982) 55.

[Sei93] H. Seifert, J.J. Kelly, A.E. Feldman, B.S. Flanders, M.A. Khandaker, Q. Chen, A.D. Bacher, G.P.A. Berg, E.J. Stephenson, P. Karen, B.E. Norum, P. Welch and A. Scott, *Phys. Rev.* **C47** (1993) 1615.

[Shu67] P. Shulek, B.M. Golovin, L.A. Kulyukina, S.V. Medved and P. Pavlovich, *Sov. Journal Nucl. Phys.* **4** (1967) 3, 400.

[Sho98] V.B. Shostak, G.P. Palkin, N.I. Woloshin, V.P. Likhachev, J.D.T. Arruda-Neto, M.T.F. da Cruz and M.N. Martins, *Nucl. Phys.* **A643** (1998) 3.

[Sho99] V.B. Shostak, G.P. Palkin, N.I. Woloshin, V.P. Likhachev, M.N. Martins and J.D.T. Arruda-Neto, *Phys. Rev.* **C61** (1999) 024601.

[Ste97] S.W. Steyn, Ph.D. thesis, University of Stellenbosch, (1997), unpublished.

[Tyr58] H. Tyŕen, P. Hillman and Th.A.J. Maris, *Nucl. Phys.* **7** (1958) 10.

[Tyr66] H. Tyŕen, S. Kullander, O. Sundberg, R. Ramachandran and T. Berggren , *Nucl. Phys.* **79** (1966) 321.

[Udi93] J.M. Udìas, P. Sarriguren, E. Moya de Guerra, E. Garrido and J.A. Caballero, *Phys. Rev.* **C48** (1993) 2731.

[Udi95] J.M. Udìas, P. Sarriguren, E. Moya de Guerra, E. Garrido and J.A. Caballero, *Phys. Rev.* **C51** (1995) 3246.

[Var91] R.L. Varner, W.J. Thompson, T.L. McAbee, E.J. Ludwig and T.B. Clegg, *Physics Reports* **201** (1991) 57.

[Vav57] P.V. Vavilov, *Soviet Phys. JETP* **5** (1957) 749.

[Ven00] B. van der Ventel, G.C. Hillhouse and P.R. de Kock, *Phys. Rev.* **C62** (2000) 024609.

[Wag90] G.J. Wagner, *Prog. Part. Nucl. Phys.* **24** (1990) 17.

[Whi90] D.M. Whittal, A.A. Cowley, J.V. Pilcher, S.V. Förtsch, F.D. Smit and J.J. Lawrie, *Phys. Rev.* **C42** (1990) 309.

[Wil55] J.M. Wilcox and B.J. Moyer, *Phys. Rev.* **99** (1955) 875.

[Woo82] P.W. Woods, R. Chapman, J.N. Mo, P. Skensved, J.A. Kuehner, *Phys. Lett.* **116B** (1982) 320.

[Wyn98] S.M. Wyngaardt, M.Sc. thesis, University of Stellenbosch, (1998), unpublished.

[Yo94] N.R. Yoder, *IUCF VME Data Acquisition System User Information*, Indiana University Cyclotron Facility, (1994), unpublished.